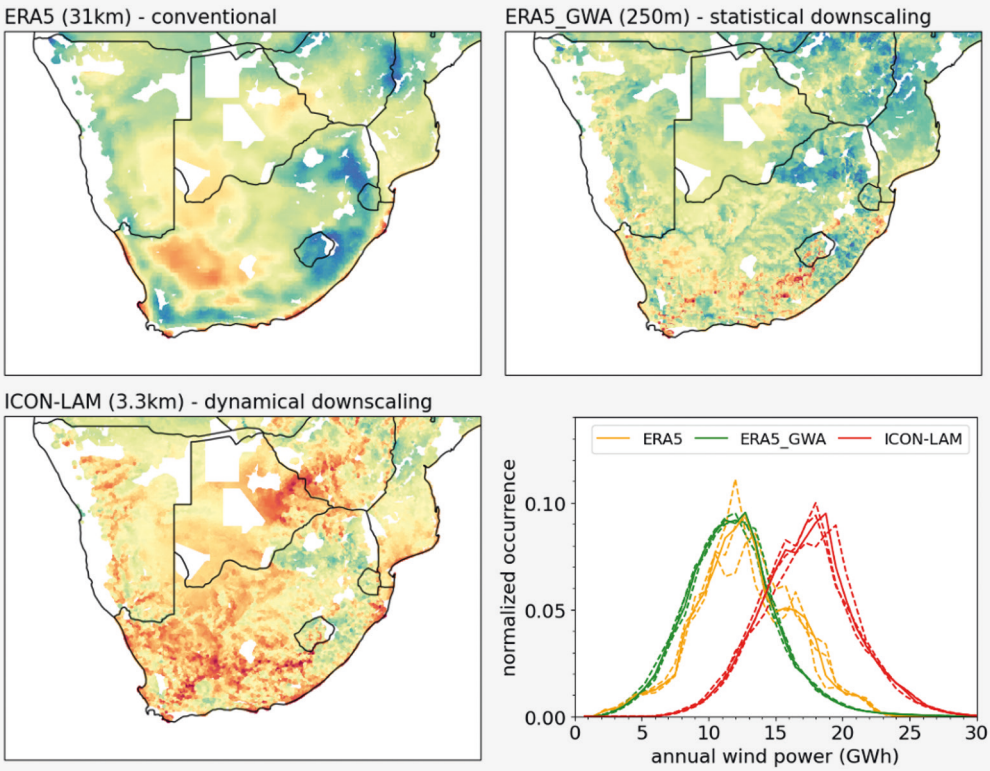

Variable renewable energy potential estimates based on high-resolution regional atmospheric modelling over southern Africa

Shuying Chen

Energie & Umwelt / Energy & Environment
Band / Volume 662
ISBN 978-3-95806-822-3

Mitglied der Helmholtz-Gemeinschaft

JÜLICH
Forschungszentrum

Schriften des Forschungszentrums Jülich
Reihe Energie & Umwelt / Energy & Environment Band / Volume 662

Forschungszentrum Jülich GmbH
Institut für Bio- und Geowissenschaften (IBG)
Agrosphäre (IBG-3)

Variable renewable energy potential estimates based on high-resolution regional atmospheric modelling over southern Africa

Shuying Chen

Schriften des Forschungszentrums Jülich
Reihe Energie & Umwelt / Energy & Environment Band / Volume 662

ISSN 1866-1793 ISBN 978-3-95806-822-3

Bibliografische Information der Deutschen Nationalbibliothek.
Die Deutsche Nationalbibliothek verzeichnet diese Publikation in der
Deutschen Nationalbibliografie; detaillierte Bibliografische Daten
sind im Internet über http://dnb.d-nb.de abrufbar.

Herausgeber und Vertrieb:	Forschungszentrum Jülich GmbH Zentralbibliothek, Verlag 52425 Jülich Tel.: +49 2461 61-5368 Fax: +49 2461 61-6103 zb-publikation@fz-juelich.de www.fz-juelich.de/zb
Umschlaggestaltung:	Grafische Medien, Forschungszentrum Jülich GmbH
Druck:	Grafische Medien, Forschungszentrum Jülich GmbH
Copyright:	Forschungszentrum Jülich 2025

Schriften des Forschungszentrums Jülich
Reihe Energie & Umwelt / Energy & Environment, Band / Volume 662

D 82 (Diss. RWTH Aachen University, 2025)

ISSN 1866-1793
ISBN 978-3-95806-822-3

Vollständig frei verfügbar über das Publikationsportal des Forschungszentrums Jülich (JuSER)
unter www.fz-juelich.de/zb/openaccess.

Contents

Contents I
List of Figures IV
List of Tables XI
List of Acronyms XII
Abstract 1
Zusammenfassung 3
Chapter 1. Introduction 5
Chapter 2. Theory 10
2.1 Atmospheric model ICON 10
2.2 Renewable energy model RESKit 12
2.2.1 RESKit wind workflow 12
2.2.2 RESKit solar workflow 13
Chapter 3. Convection-permitting ICON-LAM simulations for renewable energy potential estimates over southern Africa 15
3.1 Introduction 15
3.2 Materials and methods 19
3.2.1 Study area 19
3.2.2 Numerical model and experiment design 21
3.2.3 Observational data sets 23
3.2.4 In-situ observations quality control 25
3.2.5 Evaluation methods 27
3.3 Results and discussion 29
3.3.1 Seasonal mean comparison 29
3.3.2 Simulated wind speed evaluation 31
3.3.3 Simulated solar irradiance evaluation 38
3.3.4 Simulated precipitation and 2 m air temperature evaluation 43
3.4 Summary and conclusions 44
Chapter 4. Higher onshore wind energy potentials revealed by kilometre-scale atmospheric modelling 46
4.1 Introduction 46

4.2 Data and methods 47
4.2.1 Wind Speed Data and Height Scaling 47
4.2.2 Wind Power Calculation 48
4.2.3 Wind Speed Evaluation and Wind Power Comparison 49
4.3 Results 50
4.3.1 Comparison of Simulated 60 m Wind Speeds from ERA5 and ICON-LAM to Observations 50
4.3.2 Contrasts in Wind Power Generation Driven from ERA5 and ICON-LAM Over Weather Mast Locations 51
4.3.3 Spatially Distributed Wind Energy Potential 52
4.4 Discussion and conclusions 55
Chapter 5. High-resolution atmospheric modelling reveals lower costs for renewable energy systems in southern Africa 57
5.1 Introduction 57
5.2 Materials and methods 59
5.2.1 Meteorological data sets 59
5.2.2 The wind and solar power calculation and the REP estimation 60
5.2.3 Spatially resolved electricity demand and time series for 2050 61
5.2.4 Energy systems modelling 63
5.3 Results 64
5.3.1 ICON-LAM reveals higher onshore wind and similar open-field solar PV energy potential 64
5.3.2 Lower annual costs in energy systems derived from ICON-LAM 66
5.3.3 Spatially varied costs and design of energy systems using different meteorological inputs 70
5.3.4 ICON-LAM: Increased wind and reduced solar energy contribution for meeting demand over time 71
5.4 Discussion and conclusions 76
Chapter 6. Discussion, conclusions, and outlook 79
6.1 Discussion 79
6.2 Conclusions 81
6.3 Outlook 82
Appendix 85
A. Appendix A 85

B. Appendix B 89
B.1 Data preparation for wind speed evaluation and wind energy potential estimation . 89
B.2 Details of wind turbine technologies used to simulate wind power over weather mast locations 90
B.3 Evaluation of wind speeds at the different wind speed ranges of the wind turbine's power curve 91
B.4 Comparison of simulated wind power to measured wind power for three provinces in South Africa 95
B.5 Comparison of CF time series, annual and average CF derived from different wind speed products 101
B.6 Exploration of the frequency distribution of simulated wind speeds and its derived CFs across eligible wind turbine placements country by country 104
B.7 The estimated wind power over eligible placements across southern Africa 107
C. Appendix C 109
Acknowledgements 119
Bibliography 120

List of Figures

Figure 3.1 Top: Long-term (1998-2017) mean wind speed [m s^{-1}] at 100m height. Bottom: Long-term (1994/1999/2007 (depending on the region) to 2018) mean of daily totals of horizontal global irradiance. Data sources: Global wind (GWA, 2019) and solar (GSA, 2019) atlas. 20

Figure 3.2 Full ICON-LAM model domain including the boundary relaxation zone with model topography (GLOBE30) and ground meteorological stations as used in this study of the TAHMO (purple squares), SASSCAL WeatherNet (red circles) and NCEI Global Hourly - Integrated Surface Database (black triangles) meteorological station networks. 21

Figure 3.3 Average sfcWind [m s^{-1}] (top multi-panel) and rsds [W m^{-2}] (lower multi-panel) for the period 2017 to 2019 and austral winter (JJA) (upper row) and austral summer (DJF) (lower row), for ERA5 (1st column), driving ICON-GL (2nd column), ICON-LAM (3rd column), and the reference data (4th column), OSB-CDR for sfcWind, SARAH-3 for rsds. The sfcWind of ICON-GL is derived from the lowest model level (10 m) of u and v and the rsds of ICON-GL is not available. All the datasets are presented on their respective native grids. 30

Figure 3.4 Spatial distribution of MAE, ME, R, and PSS of hourly sfcWind for the period 2017 to 2019 at ground meteorological stations. Statistics are calculated comparing simulated sfcWind by ICON-LAM and observed sfcWind by ground meteorological stations. Symbols identify different observational networks. Rectangles: TAHMO, circles: SASSCAL_WN, triangles: NCEI_ISD. The symbol sizes represent the number of valid measurement days during 2017 to 2019. 32

Figure 3.5 Summary statistics of the metrics presented in Figure 3.4 per meteorological station network and combined. Each box-whisker plot shows the minimum, 0.25 percentile, median, 0.75 percentile, and maximum values of each evaluation measure per network, and in addition the mean (white dashed line) and the outliers (black diamonds). Yellow dots: individual data points (one dot corresponds to one station in Figure 3.4), n is the number of stations with valid data. 33

Figure 3.6 Overview of sfcWind characteristics, ICON-LAM vs meteorological station observations, for three selected stations (rows) for hourly 10 m wind speed [m s^{-1}]. Columns from left to right: scatter plots, percentile plots, histograms (bin width 1 m s^{-1}), monthly mean annual cycles, and the location of each station. Colours in the scatter plots: point density estimated by a Gaussian Kernel (brighter colour means higher density). Percentiles in the percentile plot are at every 1% interval. Histogram plot has a bin size of 1 m s^{-1}. 35

Figure 3.7 Average diurnal cycle of hourly sfcWind [m s^{-1}] at three selected stations (rows). Results are shown for in-situ observations (blue line) and ICON-LAM simulations (orange line) for the period 2017 to 2019 (all-year), austral winter (JJA), and austral summer (DJF) (columns). 36

Figure 3.8 Differences in 3-hourly sfcWind [m s^{-1}] between (ICON-LAM minus OSB-CDR) for corresponding percentiles (0.05, 0.25, 0.5, 0.75, 0.95) over the ocean for the

period 2017 to 2019. The mean difference is also plotted. 37
Figure 3.9 As in Figure 3.4, but for daytime hourly rsds [W m^{-2}] under sky conditions of all-sky, clear-sky, and cloudy-sky (rows). The last column "% days of 1095" indicates the percentage of days out of the full three years (1095 days) that are available with the corresponding sky condition over each station. 39
Figure 3.10 As in Figure 3.5, but for the summary statistics of the metrics presented in Figure 3.9. 39
Figure 3.11 As in Figure 3.6, but for daytime hourly rsds statistics [W m^{-2}] and histogram plot has a bin size of 30 [W m^{-2}]. 40
Figure 3.12 Average diurnal cycles for hourly rsds [W m^{-2}] at three selected stations (rows). Results are shown for in-situ observations (blue line) and ICON-LAM simulations (orange line) under all-sky, clear-sky, and cloudy-sky conditions (columns). "No.days" is the number of days found with the corresponding sky condition. ... 41
Figure 3.13 As in Figure 3.8, but for daytime hourly rsds [W m^{-2}]. 42
Figure 4.1 Comparison of simulated 60 m wind speeds from ERA5 (EAR5_ori and ERA5_GWA) and ICON-LAM against weather mast observations: a) ME, b) MAE, c) R, and d) PSS. Dashed lines correspond to the average of the respective metric per dataset. The pie charts indicate the temporal data coverage of 60 m observed wind speeds for each weather mast; dark grey indicates the percentage of available data from 2017 to 2019. The masts are labelled according to their identifier in the Wind Atlas of South Africa (2010); weather mast "WM04" has no data from 2017 to 2019 and is therefore not included in the comparison. For the mast locations see Figure 4.2b. 51
Figure 4.2 a) Locations of the weather masts (red dots) with topography over the entire study area and ICON-LAM model domain. b) As in a), but zoomed into the area where the masts (with index) are located. c) Averaged CFs from 2017 to 2019 over weather mast locations estimated from ERA5_ori, ERA5_GWA, and ICON-LAM under two wind turbine technologies of H60m and HOpt. 52
Figure 4.3 Averaged CF of 2017 to 2019 for each eligible wind turbine placement across southern Africa derived from a) ICON-LAM, c) ERA5_ori, and e) ERA5_GWA and their relative differences in CF of d) (ICON-LAM minus ERA5_ori) / ERA5_ori and f) (ICON-LAM minus ERA5_GWA) / ERA5_GWA. The frequency distributions of spatially distributed 3-year (solid lines) and annually (dashed lines) averaged CFs across all eligible placements derived from three wind speed products are shown in b) with a CF bin size of 0.025. 54
Figure 5.1 a) Projected total hourly electricity demand for 2050 for the entire southern Africa and those countries that are fully or partly covered by the ICON-LAM model domain, b) Same as in a) but zoomed in for countries with relatively lower electricity demand (Ishmam, unpublished yet). 62
Figure 5.2 Hourly electricity demand time series for a) southern Africa, b) South Africa, and c) Western Cape as projected for 2050, with days of the year aggregated by month shown on the x-axis and hours of the day shown on the y-axis. Please note the

different scales of the colour bars used in the figure. 63
Figure 5.3 Comparison of estimated 2017-2019 average annual total power derived from ERA5_ori, ERA5_GWA/_GSA, and ICON-LAM simulated by the RESKit model wind and solar workflows across all eligible wind turbine and solar PV panel placements in southern Africa. Black lines are country borders and grey lines are provinces in southern Africa used as energy system nodes in the study. Names of the countries and provinces included in this study are shown in Figure C.1 and Table C.1. All maps are made up of multiple colour-coded site-specific information, where each data point represents one wind turbine (total 1.8 million turbines) in Figure 5.3a, 5.3c, and 5.3e and one area of solar PV panels (total 0.74 million km^2 panels) in Figure 5.3b, 5.3d, and 5.3f, visually appearing as continuous data fields. 65
Figure 5.4 The energy system's total annual cost (Billion Euros) (blue bar) and the installed capacity (GW) of wind energy, solar energy, and battery (respective orange bars from left to right) for the cost-optimized regional energy system derived from different meteorological products for the three weather reference years a) 2017, b) 2018, and c) 2019. The first column contains all data points, while the second column zooms in on a range from 0 to 1 billion Euros and 0 to 10 GW capacity for a better presentation of the data. Each box extends from the first quartile (25th percentile) to the third quartile (75th percentile) of the data, with the median shown as a solid line inside. The whiskers are set at 1.5 times the interquartile range (IQR, the difference between the 75th and 25th percentiles) above the 75th percentile and below the 25th percentile, i.e., a box ends at ± 1.5*IQR. Data points are marked as outliers if they exceed the range defined by two whiskers. Dashed lines are the averages of all underlying data points for the corresponding box plots. 68
Figure 5.5 Annual operational characteristics, including full load hours (FLH, [hours]) (1st row), levelized cost of electricity (LCOE, cents per kilowatt-hour [€/kWh]) (2nd row), potential utilization rate (3rd row), and curtailment rate (4th row), for onshore wind (1st column), open-field PV (2nd column), and battery (3rd column) technologies used in cost-optimized energy systems designed from different meteorological datasets. Please note that terminology changes when it comes to battery technology. The (dis)charge frequency is the total energy delivered by the battery divided by its capacity, and the levelized cost of storage is the total annual cost of the battery divided by the total energy delivered by the battery. A blank subplot indicates that the corresponding metric does not apply to that particular technology. For the description of the components of boxplots please refer to Figure 5.4..... 69
Figure 5.6 The costs and design of cost-optimized energy systems in southern Africa derived from meteorological data sets of ICON-LAM (1st row), ERA5_adpt (2nd row), and ERA5_ori (3rd row) based on 2017. For the other years, the reader is directed to Figure C.3 and C.4. Energy systems optimized with ERA5 data sets are depicted as relative differences compared to results obtained from ICON-LAM. The regions

coloured in white indicate that a cost-optimized energy system incorporating wind, solar, and battery technologies is not feasible in that region without connections to neighbouring regions. 71

Figure 5.7 The time series subset of the cost-optimized energy system of the province Western Cape derived from three different meteorological data sets based on the 2017 weather year. The orange solid line represents the total power generation in the energy system, which is made up of contributions from open-field PV (solar energy) in the red solid line, onshore wind energy in the green solid line, and batteries in the blue solid line. The electricity demand, or energy sink, is presented in the brown solid line. The maximum harvestable solar and wind energy generation is shown in the red and green dashed lines, respectively. 73

Figure 5.8 The projected 2050 daily total electricity demand of the southern African provinces (numbers), where a feasible cost-optimized energy system can be built. The colour bar on the right of the figure, with a different scale, is used exclusively for the electricity demand of South African provinces. This is necessary due to the large difference in electricity demand between provinces from South Africa and other Southern African countries considered in this study. All provinces are arranged by country and sorted ascending by name index, i.e., their identical GID numbers, which are shown in the ticks on the x axis. For the correspondence between the identical GID numbers and the exact province, please refer to Table C.1, column "Province code (GID_1 code)". 74

Figure 5.9 The time series comparison of daily demand (with reference to the 2050 demand projection) fraction met by wind, solar, and battery technologies in the cost-optimized energy systems derived from meteorological data sets ICON-LAM, ERA5_adpt, and ERA5_ori for 2017. The 1st column is the result derived from ICON-LAM, and the 2nd and 3rd columns are the comparison of ICON-LAM to the ERA5 variants, ICON-LAM minus ERA5_adpt and ICON-LAM minus ERA5_ori, respectively. The structure of the x- and y-axis of each subplot in this figure is the same as in Figure 5.8, i.e., the y-axis contains the day of the year, and the x-axis shows different provinces grouped by country; the country names are abbreviated (Table C.1) for better visualization. In the "ICON-LAM" column, only positive or 0 values are present in the "Wind" and "Solar" rows, meaning the corresponding fraction of electricity demand is met; both positive and negative values are present in the "Battery" row, indicating battery discharge and charge, respectively. In the columns "ICON-LAM - ERA5_adpt" and "ICON-LAM - ERA5_ori" positive and negative values represent the comparison between ICON-LAM and ERA5 for each technology. The results for years 2018 and 2019 are shown in Figures C.5 and C.6. 76

Figure A.1 Average total precipitation [mm month^{-1}] (top multi-panel) and 2 m air temperature [°C] (lower multi-panel) for the period 2017 to 2019 and austral winter (JJA) (upper row) and austral summer (DJF) (lower row), for ERA5 (1st column), driving ICON-GL (2nd column), ICON-LAM (3rd column), and the reference data (4th column),

GPM for pr, and CRU for tas. The tas of ICON-GL is based on the lowermost model level (10 m) of air temperature. All the datasets are presented on their respective native grids. 85
Figure A.2 Spatial distribution of a) MAE and b) ME of monthly precipitation [mm] from 2017 to 2019 from ICON-LAM compared with ground meteorological stations. 86
Figure A.3 Precipitation comparison: 0.95 percentile of daily precipitation [mm day^{-1}] (1st column), daily precipitation in austral winters [mm day^{-1}] (2nd column), daily precipitation in austral summers [mm day^{-1}] (3rd column), and monthly mean precipitation [mm $month^{-1}$] (4th column) from ICON-LAM (1st row) and GPM (2nd row); difference ICON-LAM minus GPM (3rd row), for the years from 2017 to 2019. Simulated precipitation from ICON-LAM is resampled to the GPM grid using conservative remapping. 86
Figure A.4 Spatial distribution of MAE, ME, R, and PSS of hourly air temperature at 2 m height for the period from 2017 to 2019. Statistics are calculated for simulated air temperature by ICON-LAM compared with ground meteorological stations. Rectangles are stations from the TAHMO network, circles are SASSCAL_WN stations, and triangles represent NECI_ISD stations. The symbol size represents the number of valid measurement days. 87
Figure A.5 For three selected stations hourly 2 m air temperature statistics [°C] are shown (one row per station). The columns from left to right show: scatter plot, percentile plot, histograms, mean annual cycles, and spatial location. In these plots ICON-LAM simulated values are compared with measurements. Colours in the scatter plot represent the point density estimated by the Gaussian Kernel, the brighter the colour is, the higher the density is. Percentiles for every 1% are plotted in the percentile plot. The histogram plot has a bin size of 1 [°C]. 88
Figure B.1 Spatial distribution of wind turbine hub heights used in the HOpt wind turbine setting across all 1.8 million eligible wind turbine placements in southern Africa. Note that values are plotted for each of the 1.8 million placements, providing eventually a continuous map; white spots are areas where no wind turbine placement is possible according to (Franzmann et al., 2023; Ishmam et al., 2024; Winkler et al., 2025). 90
Figure B.2 The exemplary power curve used in this study for determining different investigated wind speed ranges in the wind speed evaluation. 92
Figure B.3 As in Figure 4.1, but for the observed 60 m wind speed in the range of the 3 m s^{-1} cut-in to the 25 m s^{-1} cut-out wind speeds, concentrating on the usable wind speed range for wind turbines. 93
Figure B.4 As in Figure B.3, but for the observed 60 m wind speed in the range of 3 m s^{-1} to 11 m s^{-1} wind speeds, concentrating on the wind speed range during the ramping phase of a wind turbine's power curve. Note the nearly equal mean PSS values of ERA5_GWA and ICON_LAM. 94
Figure B.5 As in Figure B.3, but for the observed 60 m wind speed in the range of 11 m s^{-1} to 25 m s^{-1} wind speeds, concentrating on the wind speed range from the rated wind

speed to the cut-out wind speed of a wind turbine's power curve. Note that ERA5_ori, ERA5_GWA, and ICON-LAM all experience negative R at mast number 19 of -0.06, -0.07, and -0.04, respectively. 94
Figure B.6 As in Figure B.3, but for the observed 60 m wind speeds that cannot be harvested by the wind turbine—wind speeds outside the cut-in (3 m s^{-1}) and cut-out (25 m s^{-1}) wind speed range of the wind turbine's power curve. Note the extended y-axis range in subplot a) and the nearly equal mean MAE values of ERA5_GWA and ICON_LAM as well as the nearly equal mean R values of ERA5_ori and ERA5_GWA in subplot c). 95
Figure B.7 Spatial distribution of 25 wind farms in South Africa in 2019. 96
Figure B.8 Frequency distributions of measured (OBS) and simulated CFs from ERA5_ori, ERA5_GWA, and ICON-LAM with a bin size of 0.025 for three provinces in South Africa (Northern Cape, Western Cape, and Eastern Cape). Averaged CF are presented next to the legend of each product. 100
Figure B.9 As in Figure B.8, but for the corresponding wind speed frequency distribution with bin size of 1 m s^{-1}. 100
Figure B.10 Comparison of time series of estimated CFs between ICON-LAM-based and ERA5-based wind energy potentials for all 1.8 million eligible wind turbine placements in southern Africa; 1st column ICON-LAM vs ERA5_ori; 2nd column ICON-LAM vs ERA5_GWA for ME, MAE, R, and DCCA. White spots are areas where no wind turbine placement is possible according to (Franzmann et al., 2023; Ishmam et al., 2024; Winkler et al., 2025). 102
Figure B.11 Differences (3rd column) of averaged CF derived from ICON-LAM (1st column) and ERA5_ori (2nd column) mapped across all the eligible wind turbine placements southern Africa for the years 2017, 2018, and 2019, and 3 years average. 103
Figure B.12 As in Figure B.11, but for the ERA5_GWA. 104
Figure B.13 As in Figure B.8, but over the eligible wind turbine placements for seven countries in southern Africa. 106
Figure B.14 As in Figure B.13, but for the corresponding wind speed frequency distribution with bin size of 1 m s^{-1} over the eligible wind turbine placements for seven countries in southern Africa. 107
Figure B.15 As in Figure 4.3, but for the estimated average annual total power for 2017-2019, simulated by the RESKit model with the HOpt wind turbine, across all eligible wind turbine placements in southern Africa. The used bin size of power in subplot b) is 0.75 GWh. 108
Figure C.1 Location of the 65 fully covered provinces by the ICON-LAM domain over southern Africa. Provincial boundaries are coloured purple and country boundaries are coloured black. For country names and the reference of the indexed province name to the full name, readers are forwarded to Table C.1. 109
Figure C.2 As in Figure 5.3, but comparison of the capacity factor. 110
Figure C.3 As in Figure 5.6 but based on the weather year 2018. 115
Figure C.4 As in Figure C.3 but for the weather year 2019. 116

Figure C.5 As in Figure 5.9 but based on the weather year 2018. 117
Figure C.6 As in Figure C.5 but for the weather year 2019. 118

List of Tables

Table 3.1 Summary of data used in this chapter. 23
Table 3.2 Three selected representative stations with location, altitude, and the altitude of the corresponding ICON-LAM grid cell. 34
Table 5.1 Key parameters of anticipated advanced wind turbine and PV panel technologies. Note that all simulated wind turbines have deviating parameters from the baseline configuration that lead to a maximum wind resource harvesting efficiency. 61
Table B.1 Wind turbine technologies details for the 60 m hub height wind turbine H60m, the baseline wind turbine H130m, and the optimal wind turbine HOpt over weather mast locations. H60m is included to quantify the impact of the different data sets on wind energy potential calculation for the observation height of the weather masts. H130m represents the wind turbine development in 2035 and it is used as the baseline turbine to derive HOpt turbine parameters in the RESKit model. 90
Table B.2 Detailed information on the 2019 wind farms in South Africa. The comparison of the province's installed capacity, derived from The Wind Power (black) and REDIS (blue), is shown in the rows next to each province. 97
Table C.1 Information on all provinces in southern Africa fully covered by this study and their feasibility to build a cost-optimized energy system. 111

List of Acronyms

AGL Above Ground Level

CF Capacity Factor

CFL Courant–Friedrichs–Lewy (CFL) condition

CMIP Coupled Model Intercomparison Project

CORDEX Coordinated Regional Climate Downscaling Experiment

CPCM Convection-Permitting Climate Modelling

CRU Climatic Research Unit

DWD Deutscher Wetterdienst (German Weather Service)

ECMWF European Centre for Medium-Range Weather Forecasts

ERA5 ECMWF Reanalysis v5

FLH Full Load Hours

GHI Global Horizontal Irradiance

GPM Global Precipitation Measurement

GWA Global Wind Atlas

GSA Global Solar Atlas

HPC High Performance Computing

IEC International Electrotechnical Commission

IFS Integrated Forecasting System

ICON the ICOsahedral Nonhydrostatic model

ICON-GL the global deterministic ICON-NWP forecasts (DWD initialized analysis)

ICON-LAM the ICOsahedral Nonhydrostatic model in its Limited Area Mode

IC Initial Condition

ITCZ Inter-Tropical Convergence Zone

LBC Lateral Boundary Condition

LCOE Levelized Cost Of Electricity

ME Mean Error

MAE Mean Absolute Error

NCEI National Centers for Environmental Information

NGFS Network for Greening the Financial System

NOAA National Oceanic and Atmospheric Administration

NWP Numerical Weather Prediction

OBS OBServation

OSB-CDR Ocean Surface Bundle Climate Data Record

PBL Planetary Boundary Layer

PDF Probability Density Function

PV PhotoVoltaic

PSS Perkins Skill Score

R Pearson correlation coefficient

REP Renewable Energy Potential

RESKit Renewable Energy Simulation toolkit for Python

RCM Regional Climate Model

SICZ South Indian Convergence Zone

SASSCAL Southern African Science Service Centre for Climate Change and Adaptive Land Management

SARAH Surface Solar Radiation Data Set - Heliosat

SDGs Sustainable Development Goals

TAHMO Trans-African Hydro-Meteorological Observatory

TKE Turbulent Kinetic Energy

UTC Universal Time Coordinated

VRE Variable Renewable Energy

WCRP World Climate Research Programme

WEP Wind Energy Potential

WMO World Meteorological Organization

Abstract

Africa is the world's least electrified continent, home to three-quarters of the global population without electricity. Electricity generation in African countries today relies heavily on fossil fuels and hydropower, despite the continent's abundant potential for the most widely accessible renewable energy sources—wind and solar, as Africa is the sunniest continent in the world and has many windy sites. Africa is also very vulnerable to climate change due to relatively low levels of local socio-economic development. Renewable energy is recognized as an important solution for Africa to address both climate change mitigation and electricity access. Reliable and highly resolved information on Renewable Energy Potential (REP) is imperative to support renewable power plant expansion. However, existing meteorological data sets over Africa used for REP estimates are often characterized by relatively coarse spatial resolution, data gaps in space and time, and general data quality issues. This challenges the reliability and accuracy of existing REP estimates, as well as the modelling of energy systems that include renewable energy.

To overcome the existing meteorological data set challenges for renewable energy applications in Africa, the ICOsahedral Nonhydrostatic (ICON) Numerical Weather Prediction (ICON-NWP) model in its Limited Area Mode (ICON-LAM) is implemented and run over southern Africa as a prototype for the continent. The ICON model is configured in a hindcast dynamical downscaling setup at a convection-permitting 3.3 km spatial resolution. The simulation time span covers contrasting solar and wind weather years from 2017 to 2019. To assess the suitability of the novel simulations for REP estimates, the simulated hourly 10 m wind speed (sfcWind) and hourly surface solar irradiance (rsds) are extensively evaluated against a large compilation of in-situ observations, satellite, and composite data products. ICON-LAM reproduces the spatial patterns, temporal evolution, the variability, and absolute values of sfcWind sufficiently well, albeit with a slight overestimation and a mean bias (mean error (ME)) of 1.12 m s^{-1} over land. Likewise the simulated rsds with an ME of 50 W m^{-2} well resembles the observations.

In this work, the simulated 60 m wind speeds (ws60m) from the ICON-LAM simulation and the often-used 31 km-resolution ERA5 reanalysis are also evaluated against measurements at 18 weather masts. The wind power calculated from these simulated wind speed data sets is also compared with measurements at existing wind farms in South Africa. The estimated wind energy potential (WEP) based on ICON-LAM and ERA5 are finally compared using an innovative approach with 1.8 million eligible wind turbine placements over southern Africa. Results show ERA5 underestimates ws60m with a Mean Error (ME) of -1.8 m s^{-1} (-27%). In contrast, ICON-LAM shows a ME of -0.1 m s^{-1} (-1.8%), resulting in a much higher average WEP by 48% compared to ERA5. A combined Global Wind Atlas-ERA5 product reduces the ws60m underestimation of ERA5 to -0.3 m s^{-1} (-4.7%), but shows a similar average WEP compared to ERA5 resulting from the WEP spatial heterogeneity. ICON-LAM also reproduces the observed wind power better than the others, further consolidating the reliability of its derived WEP. Underestimating wind energy yields may hinder the expansion of wind energy,

as less economic performance is expected, which underlines the importance of highly resolved meteorological data.

Increasing the share of renewable energy in African energy systems is imperative and urgent to address climate change mitigation and access to electricity. This thesis also investigates the impact of the high-resolution ICON-LAM simulations on energy system modelling for southern Africa. An energy system design, encompassing wind energy, solar energy, and battery storage, is derived exemplarily to meet 100% of the local electricity demand, cost-optimized, for each administrative province in southern Africa. Different meteorological data sets, including ICON-LAM as well as the commonly used ERA5 and its variant, are utilized and compared to derive cost-optimized energy systems. The results show significant differences in the wind energy potentials derived from different meteorological data sets, while similar solar energy potentials are found. Cost-optimized energy systems when using ICON-LAM meteorological inputs require less total annual cost (approx. 14%) and battery capacity (approx. 13%) compared to the other energy system solutions using different meteorological input datasets. This suggests that the cost of renewable energy systems may have been overestimated in the past, potentially also hindering its local development. The study further emphasizes the importance of using high-resolution, alternative, atmospheric modelling data sets as a decisive input for energy system modelling.

Overall, our results show that the ICON model is able to reproduce the renewable energy related variables and basic atmospheric flows in southern Africa. Compared to other commonly used data sets, the ICON simulations reveal higher wind energy potentials, and cost-optimized energy systems based on these simulations require lower total annual costs and battery capacity. These findings are critical for local renewable energy development, as renewable energy potentials may have long been underestimated and the costs of building renewable energy-based energy systems overestimated in southern Africa. Further tuning of physical parameterization schemes specifically for southern Africa may improve the performance of the ICON simulation. Adapting a more sophisticated energy system that includes the real-world power grid and various energy-using sectors may also improve the accuracy of the energy system modelling performed in this study.

Zusammenfassung

Afrika ist der am wenigsten elektrifizierter Kontinent der Welt und beherbergt drei Viertel der Weltbevölkerung ohne Strom. Die Stromerzeugung in den afrikanischen Ländern hängt größtenteils von fossilen Brennstoffen und Wasserkraft ab, obwohl der Kontinent über ein großes Potenzial für die am leichtesten zugänglichen erneuerbaren Energiequellen verfügt - Wind- und Solarenergie, da Afrika der sonnenreichste Kontinent der Welt ist und über viele windreiche Standorte verfügt. Außerdem ist Afrika aufgrund des geringen sozioökonomischen Entwicklungsstandes der Bevölkerung sehr anfällig für den Klimawandel. Erneuerbare Energien gelten als wichtige Lösung für Afrika, um sowohl den Fortschritt des Klimawandels zu verlangsamen als auch den Zugang zu Elektrizität zu erhöhen. Zuverlässige und hochaufgelöste Informationen über das Potenzial erneuerbarer Energien (REP) sind unerlässlich, um den Ausbau erneuerbarer Kraftwerke zu unterstützen. Bestehende meteorologische Datensätze über Afrika, die für REP-Schätzungen verwendet werden, sind jedoch häufig durch eine relativ grobe räumliche Auflösung, räumliche und zeitliche Datenlücken und allgemeine Probleme mit der Datenqualität gekennzeichnet. Dies stellt eine Herausforderung für die Zuverlässigkeit und Genauigkeit der bestehenden REP-Schätzungen sowie für die Modellierung von Energiesystemen miterneuerbaren Energien.

Um die bestehenden Herausforderungen mit meteorologischen Datensätzen für Anwendungen im Bereich der erneuerbaren Energien in Afrika zu überwinden, wurde das ICOsahedral Nonhydrostatic (ICON) Numerical Weather Prediction (ICON-NWP) Modell in seinem Limited Area Mode (ICON-LAM) implementiert und über dem südlichen Afrika als Prototyp für den Kontinent angewandt. Das ICON-Modell wird in einem dynamischen Hindcast-Downscaling-Setup mit einer konvektionsgeeigneten räumlichen Auflösung von 3,3 km konfiguriert. Die Simulationszeitspanne umfasst unterschiedliche Sonnen- und Windjahre von 2017 bis 2019. Um die Eignung der neuartigen Simulationen für REP-Schätzungen zu beurteilen, werden die simulierte stündlich aufgelößte 10-m-Windgeschwindigkeit (sfcWind) und die stündliche Oberflächensonneneinstrahlung (rsds) ausführlich anhand einer großen Sammlung von In-situ-Beobachtungen, Satelliten- und zusammengesetzten Datenprodukten bewertet. ICON-LAM reproduziert die räumlichen Muster, die zeitliche Entwicklung, die Variabilität und die absoluten Werte von sfcWind ausreichend gut, wenn auch mit einer leichten Überschätzung und einer mittleren Abweichung (mittlerer Fehler (ME)) von 1,12 m s^{-1} über Land. Auch das simulierte rsds mit mittlerer Abweichung von 50 W m^{-2} bildet die Beobachtungen gut nach.

In dieser Arbeit werden die simulierten 60-m-Windgeschwindigkeiten (ws60m) aus der ICON-LAM-Simulation und der häufig verwendeten ERA5-Reanalyse mit 31 km Auflösung auch anhand von Messungen an 18 Wettermasten bewertet. Die aus diesen simulierten Windgeschwindigkeitsdatensätzen berechnete Windleistung wird auch mit Messungen an bestehenden Windparks in Südafrika verglichen. Das geschätzte Windenergiepotenzial (WEP) auf der Grundlage von ICON-LAM und ERA5 wird schließlich anhand eines innovativen Ansatzes mit 1,8 Millionen geeigneten Windturbinenplatzierungen im südlichen Afrika verglichen. Die Ergebnisse zeigen, dass ERA5 ws60m mit einem mittleren Fehler (ME) von -

1,8 m s^{-1} (-27%) unterschätzt. Im Gegensatz dazu zeigt ICON-LAM einen ME von -0,1 m s^{-1} (-1,8%), was zu einem um 48% höheren durchschnittlichen WEP im Vergleich zu ERA5 führt. Ein kombiniertes Global Wind Atlas-ERA5 Produkt reduziert die Unterschätzung des ws60m von ERA5 auf -0.3 m s^{-1} (-4.7%), zeigt allerdings einen ähnlichen durchschnittlichen WEP im Vergleich zu ERA5, was auf die räumliche Heterogenität des WEP zurückzuführen ist. ICON-LAM reproduziert auch die beobachtete Windenergie besser als die anderen Modelle, was die Zuverlässigkeit der abgeleiteten WEP weiter untermauert. Eine Unterschätzung der Windenergieerträge kann den Ausbau der Windenergie behindern, da eine geringere wirtschaftliche Leistung erwartet wird, was die Bedeutung hoch aufgelöster meteorologischer Daten unterstreicht.

Die Erhöhung des Anteils erneuerbarer Energien in den afrikanischen Energiesystemen ist zwingend erforderlich und dringend notwendig, um den Klimawandel abzumildern und den Zugang zu Elektrizität zu gewährleisten. In dieser Arbeit wurden auch die Auswirkungen der hochauflösenden ICON-LAM-Simulationen auf die Modellierung des Energiesystems im südlichen Afrika untersucht. Ein Energiesystem, das Windenergie, Solarenergie und Batteriespeicher umfasst, wird so kostenoptimiert, dass 100% des lokalen Strombedarfs für jede Provinz im südlichen Afrika gedeckt werdenn. Verschiedene meteorologische Datensätze, darunter ICON-LAM sowie der üblicherweise verwendete ERA5-Datensatz und seine Varianten, werden verwendet und verglichen, um kostenoptimierte Energiesysteme abzuleiten. Die Ergebnisse zeigen signifikante Unterschiede in den Windenergiepotenzialen, die aus den verschiedenen meteorologischen Datensätzen abgeleitet wurden, während für die Solarenergie ähnliche Potenziale gefunden wurden. Kostenoptimierte Energiesysteme, die aus ICON-LAM abgeleitet wurden, erfordern im Vergleich zu den anderen weniger jährliche Gesamtkosten (ca. 14%) und Batteriekapazität (ca. 13%). Dies deutet darauf hin, dass die Kosten für erneuerbare Energiesysteme in der Vergangenheit möglicherweise stark überschätzt wurden, was ihre lokale Entwicklung behindert hat. Dies unterstreicht die Bedeutung der Verwendung hochauflösender, physikalisch konsistenter atmosphärischer Modellierungsdatensätze für die Modellierung von Energiesystemen.

Insgesamt zeigen unsere Ergebnisse, dass das ICON-Modell in der Lage ist, die mit erneuerbaren Energien verbundenen Variablen und die grundlegenden atmosphärischen Strömungen im südlichen Afrika zu reproduzieren. Im Vergleich zu anderen üblicherweise verwendeten Datensätzen zeigen die ICON-Simulationen ein höheres Windenergiepotenzial, und kostenoptimierte Energiesysteme, die auf diesen Simulationen basieren, erfordern geringere jährliche Gesamtkosten und Batteriekapazitäten. Diese Ergebnisse sind für die Entwicklung erneuerbarer Energien vor Ort von entscheidender Bedeutung, da die Potenziale erneuerbarer Energien im südlichen Afrika lange Zeit unterschätzt und die Kosten für den Bau von Energiesystemen auf der Grundlage erneuerbarer Energien überschätzt wurden. Eine weitere Abstimmung der physikalischen Parametrisierungsschemata speziell für das südliche Afrika könnte die Leistung der ICON-Simulation verbessern. Die Anpassung eines anspruchsvolleren Energiesystems, das das reale Stromnetz und verschiedene energieverbrauchende Sektoren umfasst, könnte die Genauigkeit der in dieser Studie durchgeführten Modellierung des Energiesystems ebenfalls verbessern.

Chapter 1. Introduction

Over the past 100 years, fossil fuels have enormously powered our world, playing a crucial role in enhancing the quality of life for billions of people around the world (Epstein, 2014; Hall, 2017). However, burning carbon-rich fossil fuels releases massive amounts of greenhouse gases—carbon dioxide (CO_2), nitrous oxide (N_2O), methane (CH_4), and water vapor (H_2O)—into the atmosphere, making the burning of carbon-rich fossil fuels the primary cause of the increased concentration of greenhouse gases compared to pre-industrial levels (Hafner et al., 2018; Raupach & Fraser, 2011). These greenhouse gases emitted by human activities have been identified as the most significant driver of observed climate change since the mid-20th century (Arias et al., 2021). Nowadays, many of the observed climate changes, such as rising global temperatures and extreme weather events, are unprecedented in thousands or hundreds of thousands of years, with widespread, rapid, and intensifying trends that pose significant threats (Intergovernmental Panel on Climate Change, 2021).

To mitigate climate change and avoid exhausting unsustainable fossil fuels, many countries have pledged to achieve carbon neutrality by gradually phasing out fossil fuels and significantly increasing the use of renewable energy (Zhou, 2023). Several grand and impactful policies have been initiated by countries around the world, such as the Green Deal from the European Commission (European Commission, 2019), the Carbon Peak and Carbon Neutrality in China (Wang et al., 2021), and net zero emission target set by America (The White House, 2021).

African countries present special cases. As the least electrified continent, Africa is home to three-quarters of the global population without electricity—about 600 million people in 2022—a number that has returned to historic highs due to the energy crisis and the COVID-19 pandemic (International Energy Agency, 2022). Meanwhile, Africa is the fastest-growing continent in terms of population, with one-fourth of the global population projected to be African by 2050 (Siegel, 2021). This rapid population growth may further deepen the current electricity supply gap if effective interventions are not implemented.

Despite contributing very little to the increased greenhouse gases in the atmosphere—only about 4% (Ayompe et al., 2021)—Africa is marked as the most vulnerable region to climate change (Caretta et al., 2022), primarily due to the limited capacity to buffer themselves from disasters. Mitigation actions and/or strategies for addressing climate changes are therefore even more urgent to plan and to execute in Africa. Renewable energy is widely recognized as one of the paramount solutions for Africa (Oyewo et al., 2023). Renewable energy helps reduce Africa's carbon footprint, at the same time, bringing electricity to the continent. Abundant untapped renewable energy potentials exist in Africa (Amir & Khan, 2021; Hafner et al., 2018), making renewable energy a viable solution to bridge the electricity supply gap. Furthermore, the distributed renewable energy in the form of local mini-grids connected or stand-alone power plants also provides a cost-effective solution to reach considerable amounts of rural Africans, when connecting them through building a traditional centralized power grid is economically unrealistic (International Energy Agency, 2022).

In 2023, Africa produced 869.65 terawatt-hours of electricity, with 76% coming from fossil fuels and only 24% from renewable energy (Ember, 2024). Despite being the sunniest continent (Duah & Asamoah, 2018), only 3% of Africa's electricity is generated by solar energy. Hydropower is the most heavily used renewable energy technology in Africa, accounting for 17% of the total electricity generation. Achieving a balance between addressing energy poverty to support African economic growth using fossil fuel-fired power plants, while also pursuing decarbonization, poses a significant challenge for African countries. However, large installations of renewable energy power plants are expected in Africa's near future and many African countries have already been increasingly adopting clean energy initiatives to harness the vast Renewable Energy Potential (REP) (Adelaja, 2020).

Wind and solar energy are the most widely accessible renewable energy technologies, compared to others like biomass, hydropower, and geothermal energy (López Prol & Schill, 2021). Due to their dependence on weather conditions, they are categorized as variable renewable energy (Schaber et al., 2012). Variable renewable energy technologies are the renewable energy sources that are focused on in this thesis. Global wind (GWA, 2019) and solar (GSA, 2019) atlas indicate higher wind and solar energy potentials in both northern and southern parts of Africa. Given its proximity to Europe, dedicated efforts have been made to analyse northern Africa's REP also in terms of import options for Europe (Benasla et al., 2018; Trieb et al., 2016). In this study, we focus on southern Africa as a prototype for the entire continent to help harness the potential and increase access to electricity for local benefits.

According to the latest estimates, the technical potential of open-field solar photovoltaic energy is approximately 97 TWpeak and onshore wind energy 14 TWpeak (Ishmam et al., 2024; Winkler et al., 2025) in the Southern African Science Service Centre for Climate Change and Adaptive Land Management (SASSCAL) countries Angola, Botswana, Namibia, South Africa, and Zambia. SASSCAL countries now heavily rely on coal-fired power (South Africa and Botswana) and hydropower (Namibia, Angola, and Zambia) (Ember, 2024), despite the existence of many sunny and windy sites, as can be deduced from energy potential maps (GWA, 2019; GSA, 2019; Ishmam et al., 2024; Winkler et al., 2025). To identify these high potential sites to expand the current renewable energy installation, reliable and highly resolved REP information is imperative.

However, using meteorological data sets for REP estimates over Africa is currently challenging. Due to data scarcity, coarse global reanalysis products like the state-of-the-art global reanalysis ERA5 (Hersbach et al., 2020), which has a spatial resolution of 31 km, are frequently employed to derive REP maps in Africa (Bloomfield et al., 2022; Jánosi et al., 2021). Meteorological data sets with coarse spatial resolution may be useful for broad-scale analysis and general trend identification. However, significant variations within a grid cell are averaged out in these data sets, making them inadequate for high-resolution applications that require great local detail. Statistical downscaling methods are sometimes used to overcome the coarse spatial resolution issue in REP-related applications over Africa (Sterl et al., 2022). However, its limited representation of physical processes typically results in an inability to capture local weather or

climate phenomena, extremes, and emerging patterns under changing climatic conditions, despite being computationally efficient (Xu et al., 2019; L. Zhang et al., 2020). High-resolution, physically consistent data sets for REP estimates are missing, and the impact of using high-resolution versus coarse-resolution data sets on REP estimates remains unknown. In addition to REP information, which is usually expressed in long-term averages over many years, power time series are also crucial for optimizing renewable energy systems. Unfortunately, global wind and solar energy potential atlases typically do not include time-varying REP information (GWA, 2019; GSA, 2019).

Regional dynamical downscaling is a well-known way to bridge the gap between available but coarse model-based data and the high-resolution data needed in practice (Tapiador et al., 2020). It involves a physically consistent simulation of atmospheric processes at a regional scale, achieving higher spatial resolution (hereafter regional atmospheric modelling) (Giorgi, 2020). Coarser simulations from a larger or global model domain often serve as the initial and time-varying (lateral) boundary conditions (Caldwell et al., 2009; Laprise, 2008) in regional atmospheric modelling. When the horizontal grid spacing is reduced to below 4 km, regional atmospheric modelling is considered convection-permitting (Prein et al., 2015). Recent overviews (Giorgi, 2019; Lucas‐Picher et al., 2021; Prein et al., 2015; Schär et al., 2020) have documented the advantages of high-resolution convection-permitting atmospheric modelling, which include more realistic depiction of surface terrain and better resolution of atmospheric dynamics and interactions between atmosphere and land surface.

This study aims to help close the power supply gap in Africa by producing reliable and highly resolved estimates of REP for wind and solar energy. It is hypothesized that reliable and highly resolved REP estimates can be achieved by using convection-permitting kilometre-scale, physically consistent model-based data sets with wind and solar energy potential modelling. A high-resolution regional atmospheric model is set up at a convection-permitting scale of 3.3 km with the ICOsahedral Non-hydrostatic (ICON) model (Zängl et al., 2015) over southern Africa. ICON is a state-of-the-art atmospheric modelling system and is currently in operational use for weather forecasting at several national weather services. A model comparison study shows that ICON has good forecasting skill scores (Magnusson et al., 2022). The wind and solar REPs are estimated using the Renewable Energy Simulation toolkit (RESKit) model (Ryberg, 2020; Ryberg et al., 2019) based on the meteorological data set simulated by the ICON model. The RESKit model has been used and proven to be trustworthy in several energy system modelling-related works (Patil et al., 2022; Pena Sanchez et al., 2021; Pueblas et al., 2023). This study then compares the estimated wind and solar REPs with available alternatives—ERA5 and its variant—over southern Africa, highlighting differences based on the high-resolution, physically consistent model-based data set. Further investigations explore the impacts on energy systems design using this simulated high-resolution data set compared to others.

The overarching goals of this PhD thesis are to:

(1) implement and execute high-resolution regional atmospheric modelling using the ICON model over southern Africa, and conduct a thorough evaluation of the simulation's performance in reproducing renewable energy-related variables as well as basic weather/climate variables, comparing them against observations.

(2) evaluate the simulated wind speed at the wind turbine hub height and the calculated wind power by comparing them to measurements, then calculate the spatially distributed wind energy potential based on the ICON simulations and compare it to other widely used wind energy potential products.

(3) investigate the impact of the high-resolution data set from ICON simulations on energy systems modelling. This investigation places special emphasis on the cost of building a cost-optimized energy system, the design of such a system, and the operational time series.

Chapter 2 provides an overview of the models used in this study. It comprises the basic introduction and specifics of the atmospheric model ICON, as well as detailed information about the wind and solar power simulation workflows in the RESKit model.

Chapter 3 deals with the dedicated ICON high-resolution atmospheric modelling for renewable energy applications over southern Africa. It first gives a review about the available meteorological data sets that have been used or can be used for wind and solar REP estimates. It then examines the advantages, disadvantages, limitations, and applicability of these data sets across the African continent, categorized by the data sets' type. This chapter also details the configurations of the dedicated regional atmospheric modelling for REP estimates using the ICON model in Limited Area Mode (ICON-LAM). Comprehensive spatial and temporal evaluation procedures are conducted for the ICON-LAM outputs of surface wind speed and surface solar irradiance, and the simulation performance of ICON-LAM is compared and discussed with other data sets. The basic weather/climate variables of air temperature and precipitation are also briefly examined in the evaluation as, to the best of our knowledge, this is the first time the ICON model has been run regionally over southern Africa.

Chapter 4 focuses on examining the simulation performance of the ICON model when applied to wind energy. Compared to the surface wind speed, the wind energy industry is more interested in the wind speed at upper atmosphere heights, where the rotors of the wind turbines are located. The simulated wind speed from ICON-LAM, ERA5, and ERA5's variant are evaluated against the wind speed measured by weather masts at 60 m, which is the highest available wind speed measurement height in southern Africa. Wind power simulation using the RESKit model based on the evaluated wind speed products are performed over existing wind farms in South Africa and validated against measurements. Wind energy potentials are further estimated by RESKit using an innovative approach adopted from a state-of-the-art work with 1.8 million eligible wind turbine placements employed in southern Africa and are compared between different wind speed driven products.

Chapter 5 shifts the focus to energy system modelling and aims to investigate the implications

of the ICON simulations for determining the cost-optimized energy system in southern Africa. The wind and solar energy potentials calculated by the RESKit model based on different meteorological products are compared using eligible power plant placements in southern Africa. Under the assumption of perfect power transmission from power plants to consumers, the shares of wind energy, solar energy, and battery storage in the energy system are designed in the way that the total available system power could meet 100% of the local electricity demand—the projected electricity demand for the year 2050—in a cost-optimized way for each province in southern Africa. The different costs and designs of these cost-optimized energy systems derived from different meteorological data sets are analysed and compared. Investigations into the operational time series of the cost-optimized energy system, in terms of the met electricity demand shares from wind energy, solar energy, and batteries, are further conducted and compared based on different driven meteorological data sets.

Finally, Chapter 6 discusses and concludes the main findings, and provides an outlook for necessary future research.

Chapter 2. Theory

2.1 Atmospheric model ICON

Atmospheric motions are governed by three fundamental physical principles: conservation of mass, conservation of momentum (Newton's second law), and conservation of energy (Holton & Hakim, 2013). These principles lead to the basic governing equations of atmospheric motion: the continuity equation, the equation of motion, the first law of thermodynamics, and the equation of state. Modelling the Earth's atmosphere requires solving these governing equations, which describe the dynamics and thermodynamics of the atmosphere. Numerical Weather Prediction (NWP) is an initial value problem where the initial state of the atmosphere is used with prognostic equations to predict the state of the atmosphere at some time in the future. The simulation of the atmosphere therefore emphasizes two aspects: the initial state and the prognostic equations solving, and both aspects are very active in research today. One way to better sample the initial state of the atmosphere is to assimilate as many observations as possible, while multiple ways exist to approximate the solution to prognostic equations.

The mathematical equations of atmospheric dynamics and thermodynamics that govern atmospheric motion are nonlinear partial differential equations and cannot be solved exactly by analytical methods (Strikwerda, 2004) except in a few idealized cases (Pielke Sr, 2013). NWP may obtain the approximate solution of the motion equations using spectral methods, which approximate the solution as a sum of certain basis functions (e.g., Fourier series is a sum of sinusoids), and/or the finite difference methods, which discretize the differential equations into partial derivatives and approximate each one using algebraic equations with finite differences (Strikwerda, 2004). Even with the capacity of today's supercomputers, the weather forecast runs only about two weeks into the future because the density and quality of the assimilated observations and the chaotic nature of solving the partial differential equations introduce forecast errors that double every five days (Weickmann et al., 2007).

Depending on the simulated scale, an atmospheric model can predict or reproduce microscale phenomena such as boundary layer eddies and tornadoes, sub-microscale turbulent flows over buildings, as well as large-scale synoptic and global flows. The horizontal coverage of a model is either global, for the entire Earth, or regional, for a limited area of the Earth. With a century of development in NWP beginning in the 1920s (Lynch, 2008), atmospheric models have evolved from relatively simple models with strong assumptions such as thermotropic and barotropic models (Gates, 1955) to sophisticated hydrostatic and non-hydrostatic models (Jacobson, 2002), along with continuously increasing computational power.

Hydrostatic atmospheric models replace the vertical momentum equation with the hydrostatic equilibrium under the assumption that the upward pressure gradient force is balanced by the downward gravitational pull of the Earth (Hargreaves, 1992), assuming a complete equilibrium between the gravity force and the pressure force in the atmosphere. This assumption filters out the vertically moving acoustic waves from the vertical momentum equation, thus significantly reducing model simulation time. It is a good approximation for synoptic and sub-synoptic

scales of motion. Hydrostatic equilibrium has been used successfully in the European Centre for Medium-Range Weather Forecasts (ECMWF) NWP model for 30 years back to 2010 (Wedi & Malardel, 2010), however, it fails when the horizontal grid spacing becomes finer and when the model has to resolve motions with similar horizontal and vertical scales, typically at the 10 km horizontal scale resolved on a grid spacing of the order of 2 km (Wedi & Malardel, 2010). In these cases of higher spatial resolution, a non-hydrostatic model is required, where no hydrostatic equilibrium is assumed and the vertical momentum equation is solved explicitly, although the computational time is considerably increased. The calculation time step and its upper limit implied by Courant–Friedrichs–Lewy (CFL) condition (Gnedin et al., 2018) for a non-hydrostatic model shall be adjusted accordingly.

The German Weather Service (DWD) is one of only 14 weather service centers in the world that operates a global NWP model (DWD, 2024), and the ICOsahedral Nonhydrostatic (ICON) model is their current NWP model. The ICON modelling framework (Zängl et al., 2015) is being developed primarily by DWD and the Max Planck Institute for Meteorology (MPI-M) to provide a unified set for the next generation global NWP and climate modelling system. The governing equations of the ICON model are fully compressible non-hydrostatic with a two-component system of dry air and water, where water can be present in all three phases (Prill et al., 2022).

The ICON model equips an unstructured triangular horizontal grid (Wan et al., 2013). The triangular grid structure is derived from an icosahedron and projected onto a sphere, resulting in 20 equilateral spherical triangles. Each individual global ICON grid is identified as RnBk, where “n” represents the number of divisions along the edges of the original icosahedron, followed by “k” subsequent edge bisections. Most of the variables in the ICON model are calculated based on the circumcentres of the triangles, while the horizontal velocity components are given at the edge midpoints (Prill et al., 2022).

The vertical coordinates of the atmospheric models can be divided into three main classes: constant-height coordinates with a constant height interval propagated vertically, constant-pressure coordinates with a constant pressure propagated vertically, and terrain-following coordinates (sigma-coordinate) based on either pressure or height that follow the contour of the land without a constant interval. Implementing a terrain-following coordinate clearly benefits the simulation of the lower boundary conditions, but it compromises the numerical accuracy of the horizontal pressure gradient at the same geometric height surface (Choi & Klemp, 2021). To mitigate this drawback, the hybrid terrain-following coordinate combines sigma-coordinates with constant-pressure or constant-height coordinates, such as the hybrid pressure/sigma vertical coordinate called the eta-coordinate used in the ECMWF Integrated Forecasting System (IFS). In non-hydrostatic models, the geometric height-varying vertical coordinate is preferred to the pressure-based coordinate (Prill et al., 2022). Two height-based terrain-following vertical coordinates hybrid Gal-Chen (Gal-Chen & Somerville, 1975; Klemp, 2011; Simmons & Burridge, 1981) and SLEVE (Leuenberger et al., 2010; Schär et al., 2002) are available in the ICON model.

In the NWP models, the solution of the prognostic equations is based on a spatial and temporal grid. Processes that can be resolved explicitly at this grid scale (gridscale processes) do not include all existing phenomena in the atmosphere or at the surface. For a realistic simulation, processes with a spatio-temporal scale below the model grid resolution (sub-gridscale processes) require additional representations or so-called physical parameterizations. The ICON model provides 8 types of physical parameterizations for sub-gridscale processes of solar and thermal radiation, cloud microphysics, convection, cloud cover, turbulent transfer, non-orographic gravity wave drag, orographic drag, and land surface (including sea ice and lake models). These physical parameterization schemes are continuously updated to reflect the latest developments in the scientific publications.

2.2 Renewable energy model RESKit

The Renewable Energy Simulation toolkit for Python (RESKit) is an open-source model (GitHub repository, 2019) developed by the Institute of Climate and Energy Systems - Jülich Systems Analysis (ICE-2), Forschungszentrum Jülich GmbH (Ryberg, 2020; Ryberg et al., 2019). It is capable of estimating the power time series of onshore and offshore wind turbines as well as open-field solar photovoltaic systems, using the technical specifications of the respective wind and solar energy applications. Several weather data sets and their corresponding calibrations derived from validation of simulated power against observations can be used within the RESKit model. The RESKit model is able to simulate renewable energy systems in the context of singular units, but with the proper parallelization configuration, millions of individual turbines and photovoltaic systems can be simulated in a matter of minutes (on the right hardware). Output from the RESKit model usually aids in the simulation of renewable energy systems and serves as input to the broader-scale energy system design models (Caglayan et al., 2021; Ortiz-Imedio et al., 2021; Patil et al., 2022).

2.2.1 RESKit wind workflow

The wind workflow of the RESKit model deals with the wind power calculation over wind turbine locations. Necessary input parameters are the locations of the wind turbines with longitude and latitude records and the wind turbine technology used for each wind turbine with hub height, rotor diameter, and capacity.

The RESKit model extracts weather variables of 2 m air temperature, surface pressure, and 100 m wind speed from the selected weather product at the wind turbine locations for wind power calculation. Spatial interpolations of nearest, bilinear, and cubic methods are available to derive weather variables at the specific wind turbine locations.

The wind turbine harnesses the wind resource and generates power by extracting the kinetic energy of the wind, specifically by converting the transverse motion of the wind into turbine rotation. The wind speed at the hub height of the wind turbine is used to approximate the speed of the air filled in the cross-sectional area of the turbine rotor; it is logarithmically extrapolated from the 100 m wind speed, as 100 m is the most representative hub height for modern wind

turbines (von Krauland et al., 2021).

The power curve in the RESKit model, which relates wind turbine power output in unit watt to wind speed, is approximated by the wind turbine's specific power, defined as the installed capacity per rotor swept area. Typically, the power curve of a wind turbine is given with respect to a standard air density of 1.225 kg m^{-3} (Carta & Mentado, 2007), which corresponds to the standard atmospheric conditions of sea level pressure (1013 hPa) and 15 °C temperature. An air density correction procedure is therefore applied to adjust the real-world wind speeds to the standard air density conditions as proposed by the International Electrotechnical Commission (IEC) 61400-12 (Turbines—Part, 2005).

If a wind turbine consistently generated power at a given wind speed according to its power curve, then converting wind speed to wind power would be fairly straightforward. However, wind turbines respond stochastically to wind speed in the real world, meaning that the power curve can only serve as a summary estimate of the turbine's generation (Ryberg et al., 2019). The underlying reasons for this variability are diverse, as documented in Ryberg et al. (2019a), including factors such as reduced aerodynamics efficiency caused by turbulence in the wind, large wind speed gradients existing across the turbine rotor, and the wind speed fluctuations exceeding the turbine response time. To account for this stochastic response, the final power curve used in the RESKit model is convoluted with a Gaussian kernel (Ryberg et al., 2019).

2.2.2 RESKit solar workflow

The versatile solar photovoltaic technology offers many configurations for a solar photovoltaic power system. Depending on the installation surface, it can be an open-field or rooftop solar photovoltaic system. Here, this thesis focuses only on the open-field solar photovoltaic system. The solar photovoltaic power is calculated using the solar workflow in the RESKit model (Ryberg, 2020). The necessary inputs besides weather variables are location and capacity of a solar photovoltaic system.

Weather variables of global horizontal irradiance, direct horizontal irradiance, surface wind speed, surface pressure, surface air temperature, and surface dew temperature at the location of the solar photovoltaic system are considered in the RESKit model solar workflow calculation. Similar to the wind workflow, several spatial interpolation methods, i.e., nearest, bilinear, and cubic, are available to interpolate weather variables to the solar plant locations.

To calculate solar power output, RESKit first determines the solar position, i.e., the solar azimuth and apparent zenith angle, based on the longitude/latitude, local time, and altitude above sea level according to the NREL SPA algorithm (Reda & Andreas, 2004). The apparent solar zenith angle considers the refraction or bending of the sun's rays as they pass through the Earth's atmosphere, compared to the solar zenith angle, which is the "true" zenith angle but at the top of the atmosphere (Labriji et al., 2022). The total solar irradiance at the top of the solar modules—the plane of the array—is then calculated considering the solar irradiance components of the solar beam and the sky diffuse solar irradiance using the solar position with

the sky diffuse irradiance model Perez (Perez et al., 1990). As the efficiency of the solar photovoltaics is temperature dependent (Dubey et al., 2013), the solar module temperature is estimated in RESKit using the surface wind speed, surface air temperature, and the global irradiance at the plane of the array. The solar power output of the solar modules is subsequently calculated based on the total solar irradiance at the plane of the array and the module temperature using the interpolated single diode approximation (Jain & Kapoor, 2004; King et al., 2004; Wenham et al., 2013).

In addition, there are many factors that affect the solar photovoltaic system performance and imply losses. A literature screening indicates that there is a lack of a general overview on a global scale that includes all solar photovoltaic system losses and their approximate magnitudes (not shown). Probably due to the complexity of the system and the current high rate of development in the industry, most studies focus on a specific loss such as soiling (Dehghan et al., 2022), mismatching (Dhass et al., 2022), inverter loss (Good & Johnson, 2016; Nagarajan et al., 2019), or wiring (Ekici & Kopru, 2017). Overall introductions of the system losses are available, but the typical loss values are not documented (Saeed & Zohaib, 2022) or the loss values are calculated and verified based on abundant field records from one location (Hashemi et al., 2021). Also, other studies (Kumar et al., 2019; Mejia et al., 2014; Mejia & Kleissl, 2013; Raj et al., 2016) examine some system losses in a specific case, raising questions about their representativeness, and studies (Anis & Nour, 1995; Bucciarelli Jr, 1984; Schaub et al., 1994) may be too old for a strongly developing industry.

Given the ambiguity of quantifying losses for solar photovoltaic systems in the literature, this thesis applies a recommendation and/or experience from the solar photovoltaic industry (Aurora Solar, 2023), which is different from (Ryberg, 2020). They (Aurora Solar, 2023) suggest annual solar photovoltaic system losses of 0.5% from connection, 1.5% from light-induced degradation, 2% from wiring, 2% from soiling, and 3% from system availability, with a total suggested annual loss of 8.7%. Considering the severe dusty conditions in many parts of southern Africa, we follow their suggestion and increase the soiling loss to a maximum of 4%, for a total system loss of 10.7%.

Chapter 3. Convection-permitting ICON-LAM simulations for renewable energy potential estimates over southern Africa

*adapted from: Chen, S., Poll, S., Hendricks Franssen, H. J., Heinrichs, H., Vereecken, H., & Goergen, K. (2024). Convection‐permitting ICON‐LAM simulations for renewable energy potential estimates over Southern Africa. Journal of Geophysical Research: Atmospheres, 129(6), e2023JD039569. https://doi.org/10.1029/2023JD039569

3.1 Introduction

The African continent is one of the focus areas when it comes to global efforts in mitigating the adverse impacts of climate change (Blunden & Boyer, 2022; Trisos et al., 2022). Though African societies have contributed little to global climate change, generating less than 4% of global greenhouse gas emissions (Ayompe et al., 2021), the African continent is identified as a highly vulnerable region (Caretta et al., 2022). The slow expansion of a basic electrical grid infrastructure hinders national economic development (Sarkodie & Adams, 2020), which may further reinforce adverse climate change impacts on African people. According to a report by the International Energy Agency in 2021, there are still around 580 million people in Sub-Saharan Africa lacking access to electricity in 2019, which accounts for three-quarters of the global population without reliable supply of electricity (International Energy Agency, 2021).

It is broadly accepted that renewable energy technologies are vital for a greenhouse gas neutral energy system (Fetting, 2020; Potrč et al., 2021; Yuan et al., 2022). This is especially true for Africa, given the large untapped REP existing over the African continent (Amir & Khan, 2021; Hafner et al., 2018). In this context our focus is on wind (primarily onshore) and solar power renewable energies. The transformation from a mainly fossil or nuclear fuelled energy system towards a renewable energy dominated energy system requires reliable information about the exact available REPs in space and time (McKenna et al., 2022).

In order to produce reliable REP estimates, the spatio-temporal variation of wind speed and solar irradiance needs to be well captured, and therefore the underlying atmospheric physics has to be accurately simulated. Near-surface winds, that wind turbines use to generate electricity, are controlled by the background wind field, planetary boundary layer (PBL) mixing, and surface friction (He et al., 2010). With respect to photovoltaic technology, less than 50% of the top of the atmosphere solar radiation is transmitted to the surface on average due to atmospheric processes (absorption, scattering, and reflection) influenced by cloud cover and atmospheric particles (e.g., aerosols) as well as the surface properties such as albedo and topography (Wald, 2018). Concerning resolution, for instance, the spatial resolution of 300 m to 3 km corresponds to PBL turbulence and near-surface flows (Pryor et al., 2020), and with a temporal resolution of at least one hour the diurnal cycle of PBL growth and decay can be captured (Yuanjie Zhang et al., 2020). Under highly fluctuating cloud cover and hence solar irradiance, a sub-hourly temporal resolution is necessary (Roy et al., 2021). Based on these requirements, we hereafter give an overview of meteorological datasets that are available and that have been used or are of potential use as inputs for REP estimates.

The Global Wind (GWA, 2019) and Solar (GSA, 2019) Atlases (Figure 3.1) are wide-spread sources of information for REP assessments. The latest versions of these global atlases at the time of writing in 2023-06 provide long-term averages of wind and solar information and their generation potentials under certain plant technical parameters at a spatial resolution of nominally 250 m. However, what is additionally needed are also time series of renewable energy potentials to design an energy system that assures a secure energy supply at all times (Caglayan et al., 2021; Lund et al., 2015).

Meteorological observations at weather stations, e.g., from the regional basic synoptic network, feeding into World Meteorological Organization (WMO), are available for long time spans and many locations. They provide local point-scale weather information for the past (He & Kammen, 2014; Ramirez-Vergara et al., 2023), while especially wind might show a pronounced spatial variability (Santos-Alamillos et al., 2014; Yu et al., 2015), and both wind and solar might show pronounced changes in the future related to climate change (Yang et al., 2022). Data from meteorological station networks often serve as ground truth in REP-related model validations or as assimilated observations in forecasts and reanalyses (Valmassoi et al., 2023).

Satellite observation-derived data products have become widely used in REP assessments and recently also as input to statistical approaches such as machine learning, semi-empirical, or physics-based models (Edwards et al., 2022; Medina-Lopez et al., 2021). For example, a study (Elsner, 2019) provided off-shore wind energy potential estimates for the African coastal areas by using the satellite-based Blended Sea Winds (BSW) data set with spatial resolution of 0.25° and temporal resolution of 6-hourly. In (Neher et al., 2020) the SARAH-2 satellite data product with 30-min temporal and 0.05° spatial resolution was used to derive the solar energy potential for West Africa. Nevertheless, satellite-derived products face shared challenges due to observation gaps in space and time caused by satellite routines, atmospheric noise from clouds and aerosols, and the need for accurate retrieval algorithms (Huang et al., 2019; Weissman et al., 2012).

Data from global or regional weather forecast or climate models can be used to provide multi-decadal, gap-free, homogeneous, and physically consistent datasets, also at wind turbine hub height and for arbitrary spatial domains. To assess REP, datasets are available through hindcast simulations or atmospheric reanalysis. Another application is to forecast renewable energy outputs as a function of weather conditions (Meenal et al., 2022), or to investigate future climate change impacts on REP and power production (Pryor et al., 2020).

Reanalyses, that combine observations with model simulations through data assimilation algorithms and synthesising a coherent set of surface and vertical atmospheric data (Kalnay, 2003), are frequently used for wind and solar REP estimates. The ERA5 at 31 km resolution and hourly outputs (Hersbach et al., 2020), its predecessor ERA-Interim at 79 km and three-hourly outputs (Dee et al., 2011), or the MERRA-2 at about 50 km (Gelaro et al., 2017) are examples for global reanalyses that are used in the context of renewable energy planning and

potential assessments for different spatial domains (Caglayan, Ryberg, et al., 2019; Jurasz et al., 2021; Ryberg et al., 2019; Yuhu Zhang et al., 2020). Many studies have addressed the suitability of these or similar reanalysis datasets for REP assessments, and depending on the study site and dataset, even lower resolution data are considered as suitable inputs (Doddy Clarke et al., 2021; Kanwal et al., 2022); for certain studies the reanalyses systematically underestimate wind speeds (Tahir et al., 2018). In general, higher temporal as well as spatial resolutions in model outputs lead to better agreement with observations (Michael R. Davidson & Dev Millstein, 2022; Samal, 2021).

A study (Frank et al., 2020) showed the added value of very high resolution regional reanalyses. COSMO-REA6 (Bollmeyer et al., 2015) for Europe at 6 km and COSMO-REA2 (Wahl et al., 2017) for Central Europe at 2 km, COSMO-REA2 performs better in the representation of extreme temporal wind speed changes at typical wind turbine hub height, which is often underestimated in coarser-resolution reanalyses (ERA-Interim, MERRA-2), when compared to tower measurements. In a COSMO-REA6 and ERA5 global solar irradiance (GHI) comparison with synoptic station and satellite data (Urraca et al., 2018), they concluded that in areas with high variability of surface solar irradiance in coastal areas and mountains the high-resolution reanalysis agrees closer with satellite observations.

In a study evaluating GHI from reanalysis and satellite products (Sawadogo, Bliefernicht, Fersch, Salack, Guug, Diallo, et al., 2023), they compared ERA5 and MERRA-2 reanalysis products with CAMS and SARAH-2 satellite products, using 37 in-situ measurements from western Africa. The study found that satellite data outperform reanalysis data under distinct sky conditions. Additionally, both data sources have a larger error of more than 150 W m^{-2} (root mean squared error) under cloudy skies than under clear skies. Another study (Mabasa et al., 2021) conducted an evaluation of GHI using two reanalyses (ERA5 and MERRA-2) and three satellite-based datasets (SOLCAST, CAMS, and SARAH-2) against 13 radiometric observations in South Africa. The study found that both types of datasets overestimate GHI, with less discrepancy observed in satellite-based GHI compared to reanalysis-based GHI.

Global climate models are also used for REP analysis (Devis et al., 2018), but by dynamically downscaling coarser resolution (global) weather/climate models, high-resolution regional models add value through a better representation of surface properties and dynamical processes (Giorgi, 2019; Laprise, 2008; Rummukainen, 2015), making them well suited as inputs to downstream impact studies, e.g., to REP assessment of wind power resources (Pryor et al., 2020). Using regional climate scenarios from the World Climate Research Programme's (WCRP) Coordinated Regional Climate Downscaling Experiment (CORDEX) initiative at 12 km resolution, e.g., studies (Moemken et al., 2018; Tobin et al., 2016) found a tendency in some areas towards a decrease of wind energy potentials due to climate change, and, e.g., a study (Vautard et al., 2014) identified only a limited climatic impact by large-scale wind farms on the atmosphere. In reanalysis-driven long hindcast time series from Regional Climate Model (RCM) runs at 24 km grid spacing (Geyer et al., 2015), they concluded for wind energy potentials over the North Sea that time series are characterized by a large interannual

variability, short observational time series as well as near-surface wind speed to hub height transformations may lead to large biases in the REP estimates. In a study (Sawadogo et al., 2021) used 25 km spatial resolution CORDEX-CORE initiative runs over Africa; the ERA5-driven evaluation runs reproduce observations reasonably well; in future climate projections, simulations indicate an increase in solar irradiance and wind speed.

RCM simulations at convection-permitting (CP) or km-scale resolution (below 4 km) add yet again value in comparison to conventional RCM simulations as recently summarised by (Lucas‐Picher et al., 2021) or (Schär et al., 2020), offering information at stakeholder-relevant scales (Gutowski et al., 2020; Senior et al., 2021). Studies in West Africa have assessed the key role of explicit convection in simulating monsoon systems (Birch et al., 2014; Marsham et al., 2013). CP climate modelling (CPCM) over the whole African continent (Kendon et al., 2019; Stratton et al., 2018) demonstrated that the CP model is able to realistically capture hourly rainfall characteristics and, e.g., notably reduce the dry austral winter average rainfall biases in West Africa. Such CP simulations require large computational resources (Prein et al., 2015) and have been routinely only used in numerical weather prediction (NWP) (Chamberlain et al., 2014; Lean et al., 2008) over parts of Africa. To date, the only pan-African CPCM simulation is with the Met Office Unified Model (Kendon et al., 2019; Stratton et al., 2018), covering 10-year historical and future time span at 4.5 km resolution.

In this context, our objective is to produce a high-resolution dataset over southern Africa from dedicated atmospheric simulations to be used for REP assessments. We choose southern Africa as the study domain due to the high demand for a reliable electricity supply and favourable solar and wind conditions. Simulations are done with the ICOsahedral Nonhydrostatic (ICON) Numerical Weather Prediction (ICON-NWP) model in its Limited Area Mode (ICON-LAM) (Zängl et al., 2015). ICON is the operational forecast model of multiple national weather services and as a state-of-the-art modelling system is feasible to not only run for NWP but also for climate applications (Pham et al., 2021). In a multi-model comparison (Magnusson et al., 2022), ICON shows good forecasting skill scores. In this study, ICON-LAM dynamically downscales the initialized analysis product of the German Weather Service (DWD), based on the global deterministic ICON-NWP forecasts dataset (hereafter ICON-GL), from a spatial grid spacing of 13 km to a convection-permitting resolution of 3.3 km, without parameterized deep convection. Simulations cover the time span from January 2017 to December 2019 with contrasting first-order meteorological drivers for a REP assessment. Simulated wind speed at 10 m height (sfcWind), surface solar irradiance (rsds), precipitation (pr), and air temperature at 2 m height (tas) from ICON-LAM setup are evaluated using ground meteorological stations as well as satellite and composite products. The goal is to demonstrate the potential of a physically consistent hindcast simulation with a km-scale NWP model in reproducing meteorological fields of sfcWind and rsds with high fidelity. This new dataset can then serve in ensuing case studies (i) as an alternative input dataset to REP estimations and hence as a potential input to renewable energy planning (Akinbami et al., 2021), and (ii) as a high-resolution test dataset for the study region that helps to determine in comparison with conventionally used data sources (such as coarse-resolution reanalysis) what the added value can be for REP analysis and what

is in fact needed in terms of meteorological input data.

3.2 Materials and methods

3.2.1 Study area

According to the Global Wind (GWA, 2019) and Solar (GSA, 2019) Atlas (Figure 3.1), southern as well as northern Africa have large wind and solar REP. Due to its proximity to Europe, REP of northern Africa has been assessed, e.g., by studies (Benasla et al., 2018; Trieb et al., 2016). We however choose southern Africa as our study area, where renewable energies might be exploited for the benefit of electricity supply for the sub-Saharan African countries.

Our study area and model domain extends from 16º S to 38º S, and 9º E to 39º E (Figure 3.2). Most of the area experiences semi-arid conditions with a wet season during austral summer, while along the southern coast it rains throughout the whole year, the western part receives winter rainfall (Engelbrecht et al., 2015; Weldon & Reason, 2014). Precipitation in the northern part of the model domain is mostly linked to the southernmost position of the Inter-Tropical Convergence Zone (ITCZ) (Waliser & Gautier, 1993), while the southern part of the area is affected by tropical-temperate climatic zone interactions (Todd et al., 2004) embedded in the South Indian Convergence Zone (SICZ) (Cook, 2000). Surrounded by the cold upwelling Benguela ocean current at the western and the warm Agulhas current along the eastern coastlines, the thermal gradients and evaporation over the nearby oceans strongly influence this region (Weber et al., 2017).

The topography of southern Africa is characterized by a narrow coastal plain and the inland Plateau, with the “horse-shoe-shaped” great escarpment situated in between (Moore et al., 2009). This complex topography strongly influences local weather conditions and climate. It triggers mesoscale convective systems in the eastern part (Blamey & Reason, 2009; Laing & Fritsch, 1997), and influences the intra-seasonal variability of the maize growing season (Tadross, Hewitson, et al., 2005), and the beginning of the austral summer rainy season (Tadross, Jack, et al., 2005).

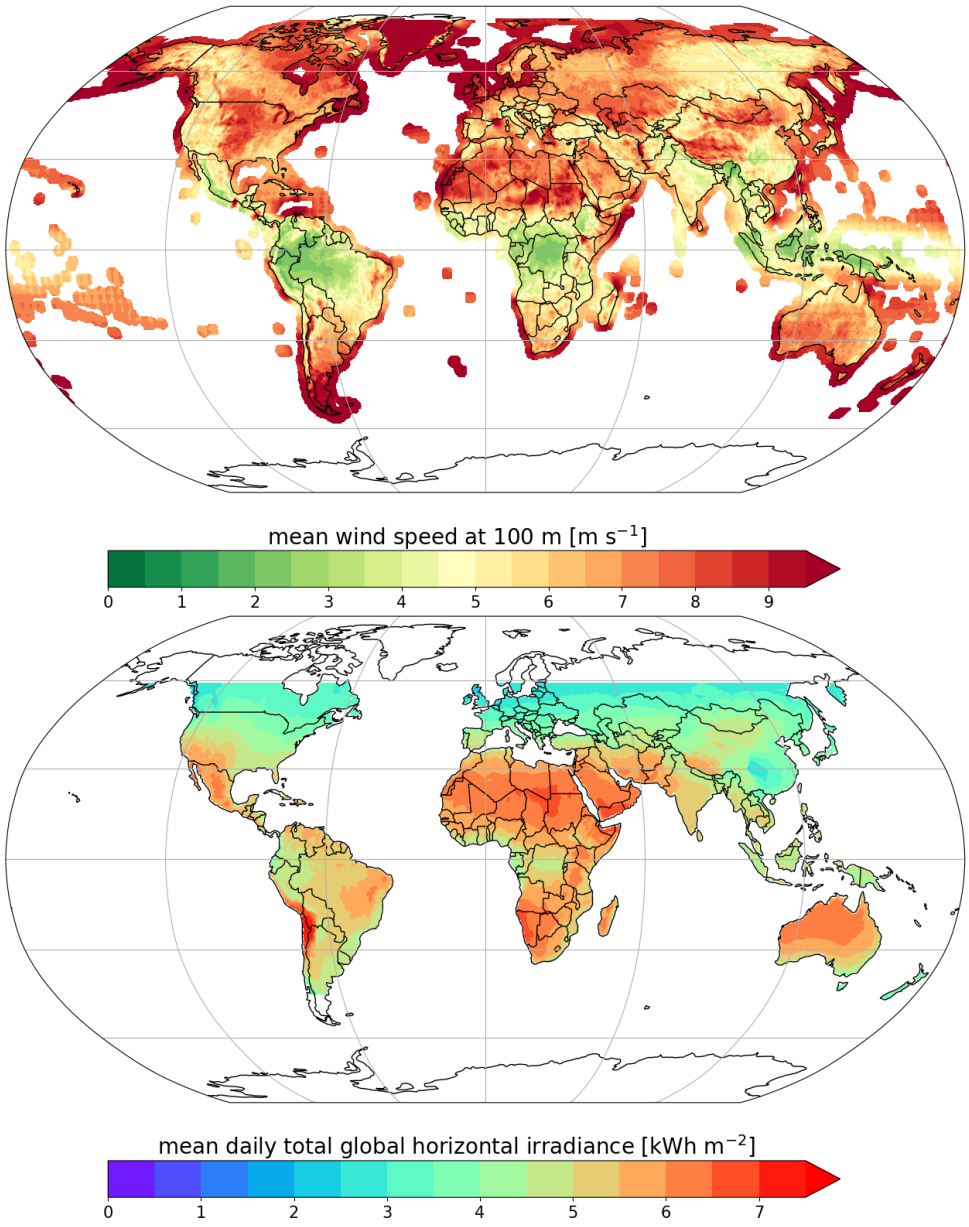

Figure 3.1 Top: Long-term (1998-2017) mean wind speed [m s^{-1}] at 100m height. Bottom: Long-term (1994/1999/2007 (depending on the region) to 2018) mean of daily totals of horizontal global irradiance. Data sources: Global wind (GWA, 2019) and solar (GSA, 2019) atlas.

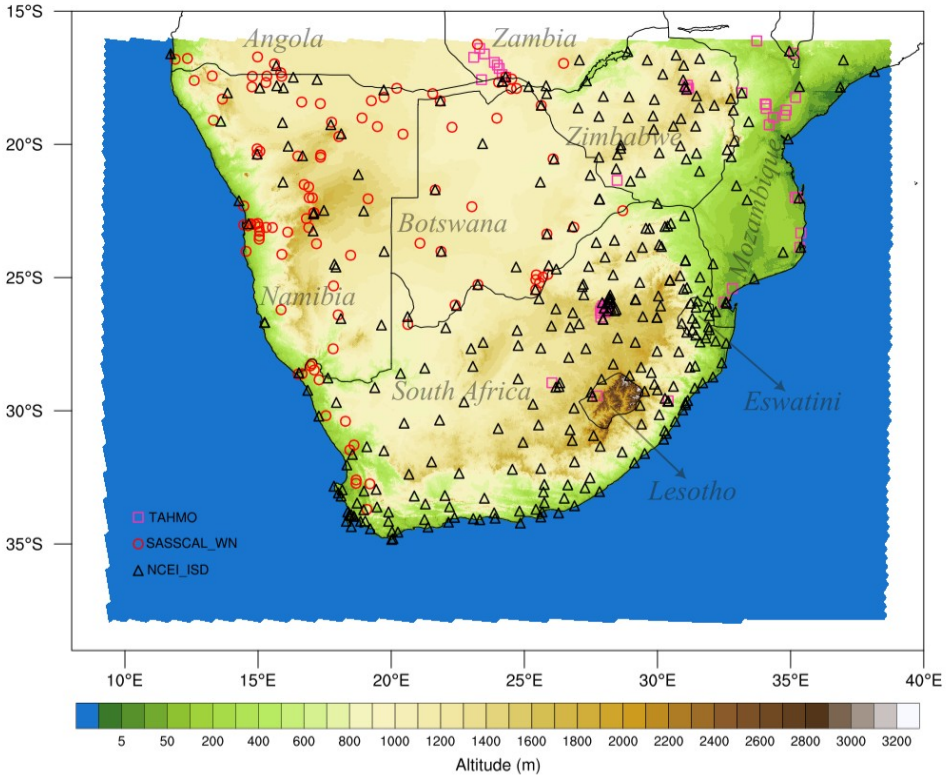

Figure 3.2 Full ICON-LAM model domain including the boundary relaxation zone with model topography (GLOBE30) and ground meteorological stations as used in this study of the TAHMO (purple squares), SASSCAL WeatherNet (red circles) and NCEI Global Hourly - Integrated Surface Database (black triangles) meteorological station networks.

3.2.2 Numerical model and experiment design

3.2.2.1 ICON model version

The ICON modelling framework (Zängl et al., 2015) is developed by the German Weather Service (Deutscher Wetterdienst, DWD) and the Max-Planck-Institute for Meteorology (MPI-M) and other partners to build a unified next-generation (global) Numerical Weather Prediction (NWP) and climate modelling system. The ICON model can be used for simulations at a variety of spatial and temporal scales (Heinze et al., 2017; Hohenegger et al., 2023). To achieve this, different model modes exist, which can be divided into the NWP, the climate mode ECHAM, and the large-eddy simulation physics packages (Pham et al., 2021). ICON-NWP is used for operational global and regional forecasts by the DWD. ICON-CLM is a recently realised mode (Pham et al., 2021) built upon ICON-NWP in a limited-area mode (ICON-LAM) and facilitates a suite of technical infrastructures for regional climate applications. Here, we make use of the ICON model release version 2.6.4 (so-called “common release” as of 2021-09-29) ICON-NWP

in limited area mode (ICON-LAM).

3.2.2.2 Model setup and configuration

The ICON-LAM triangular horizontal grid used here has a high spatial resolution of approximately 3.3 km with total 649,392 triangular cells centred at (24° E, -27° S) (ICON grid identifier: R3B09). The used vertical height-based terrain-following coordinate system SLEVE (Leuenberger et al., 2010; Schär et al., 2002) has 65 levels with a model top at 22 km; the lowermost vertical level is located at a height of 10 m above the land surface.

In this study, ICON-LAM is used in a one-way single nest dynamical downscaling setup. The Initial and hourly Lateral Boundary Conditions (ICs and LBCs) are from the DWD initialized analysis as part of the DWD global ICON weather forecast (13 km, R3B07 ICON grid). The high-resolution triangular grid cells (R3B09) of the 3.3 km domain are exactly inscribed in the 13 km global grid cells (R3B07), following the sub-triangle generation rule of the ICON model mesh. The LBCs relaxation zone is 14 grid cells and is discarded in the presentation of the results. To keep our ICON-LAM hindcast simulations close to the assimilated synoptic atmospheric state of the driving global NWP, the model's atmosphere is reinitialized at 6-day intervals. In details, day 6 of the preceding time slice overlaps with day 1 of the current time slice, which is used as a spin-up day and discarded later; day 2 until day 6 of each time slice are concatenated with each other, leading to a slight inconsistency in the atmospheric fields every 120hrs. The land surface and subsurface are run transient, i.e., they are restarted from the model's previous state. This way, subsurface storage terms, such as soil moisture, which affect the land-atmosphere coupling can freely develop over time in the high-resolution nest.

The model setup (e.g., grid and nesting approach) and configuration (e.g., physics settings) used here has been adopted from the operational weather forecast of DWD, for Germany and surrounds at a convection-permitting resolution. This so-called ICON-D2 implementation currently uses the ecRad (Hogan & Bozzo, 2018) radiation scheme, the diagnostic Probability Density function (PDF) cloud cover scheme, a single-moment scheme for cloud microphysics and precipitation (Doms et al., 2011; Seifert, 2008), the prognostic turbulent kinetic energy (TKE) scheme (Raschendorfer, 2001) for vertical diffusion and transfer (turbulent transfer), and the land surface model TERRA (Schrodin & Heise, 2001; Schulz et al., 2016) with up to 3 (+ 3 for three additional "water" tiles of open water, lake, and sea-ice) dominant land tiles considered per grid cell in combination with the Flake lake scheme (Mironov, 2005), and sea-ice scheme (Mironov et al., 2012). As simulations are done on convection-permitting scale, deep convection parameterization is switched off. Five main aerosol species (sea salt, soil dust, organic aerosol, sulfate aerosol, and black carbon) are considered by ICON's radiation scheme, based on the spatially distributed long-term mean monthly aerosol annual cycle from the Tegen climatology (Tegen et al., 1997). ICON-LAM output intervals for wind and solar energy-related variables are 15 minutes with instantaneous values, for other variables output is hourly.

The static surface parameters are extracted from the external variable database of the ICON model auxiliary system ExtPar. Model topography is based on the Global Land One-km Base

Elevation Project at 30 arc seconds (GLOBE30). Land cover is taken from the Global Land Cover Map for 2009 at 10 arc seconds (GlobCover 2009). The Digital Soil Map of the World at 5 arc seconds (DSMW) is used to classify soil types, and the Global Lake Database at 30 arc seconds (GLDB) for the lake data.

3.2.2.3 Simulation time span

The global ICON-NWP operational forecasts that are used as ICs and LBCs for our ICON-LAM model runs are available since 2015. On the basis of the ERA5 reanalysis (Hersbach et al., 2020) a simulation period from 2017 to 2019 is chosen (data not shown). It is representative for an average year as well as contrasting meteorological conditions with respect to wind and solar REP to serve as a basis for a robust energy system analysis. Total surface global solar irradiance of the year 2019 was recognized as generally higher than the 30 years average, the year 2017 lower, and the year 2018 close to average. The annual average wind speed at 100m compared with the 30 years average also shows a clear difference between these three years, although with more spatial heterogeneity and less obvious as for radiation. The concrete simulation time span is 2016-12-31UTC00H to 2020-01-01UTC00H. The 1st day in each 6 days reinitialization interval is treated as a spin-up day and would be discarded, therefore, we set one additional day at the beginning of the simulation time span to solve the data-lacking issue for the 1st day of the very 1st time slice.

3.2.3 Observational data sets

Table 3.1 lists all the datasets used in this study as an overview.

Table 3.1 Summary of data used in this chapter.

Abbreviation used in the text	Variables description	Spatial resolution	Temporal resolution	Dataset type	Source (URLs), last visited on 2024-01-03
OBS	10 m wind speed, surface solar irradiance, 2 m air temperature, and precipitation	point	sub- to multi-hourly	ground meteorological station	SASSCAL_WN: https://sasscalweathernet.org/, TAHMO: https://tahmo.org/, and NCEI_ISD: https://www.ncei.noaa.gov/products/land-based-station/integrated-surface-database
OSB-CDR	10 m wind speed over global ice-free oceans	0.25°, ~ 25 km	3-hourly	satellite	NOAA: https://doi.org/10.7289/V55T3HH0
SARAH-3	Surface solar irradiance	0.05°, ~ 5 km	30-minute	satellite	CM SAF: https://doi.org/10

					.5676/EUM_SAF_CM/SARAH/V003
CRU	2 m air temperature over all land domains of the world except Antarctica	0.5°, ~ 50 km	monthly	composite product	UEA: https://crudata.uea.ac.uk/cru/data/hrg/
GPM	Precipitation	0.1°, ~ 10 km	30-minute	satellite (successor of TRMM)	NASA: https://pps.gsfc.nasa.gov/
ERA5	10 m wind speed, surface solar irradiance, 2 m air temperature, and precipitation	~ 31 km	hourly	ECMWF reanalysis	ECMWF: https://doi.org/10.24381/cds.adbb2d47
ICON-GL	10 m wind speed and 2 m air temperature	~ 13 km	hourly	DWD initialized analysis	DWD - PAMORE archive: https://www.dwd.de/EN/ourservices/pamore/pamore.html
ICON-LAM	10 m wind speed, surface solar irradiance, 2 m air temperature, and precipitation	~ 3.3 km	15-minute except hourly with pr	simulated in this study	this study

3.2.3.1 Meteorological ground station networks

Data from two local meteorological station networks and one global hourly in-situ surface integrated database (OBS) have been used for model evaluation purposes: The Southern African Science Service Centre for Climate Change and Adaptive Land Management (SASSCAL) is a joint initiative of Angola, Botswana, Namibia, South Africa, Zambia, and Germany in response to the challenges of global climate change. SASSCAL is monitoring the weather in southern Africa by a meteorological station network called SASSCAL WeatherNet (hereafter SASSCAL_WN). The second local network is the Trans-African Hydro-Meteorological Observatory (hereafter TAHMO), TAHMO aims to develop a dense network of hydro-meteorological monitoring stations in sub-Saharan Africa. The third in-situ dataset

comes from the National Centers for Environmental Information (NCEI) and contains a global hourly integrated surface database (hereafter NCEI_ISD) collected from numerous sources over the world. NCEI_ISD does not provide rsds and pr observation in our study area. Figure 3.2 shows the location of each weather station used from the three networks. The station data is used at an hourly temporal resolution.

3.2.3.2 Satellite and composite data sets

Apart from the aforementioned in-situ observations, we also incorporate satellite and composite datasets for the evaluation of different variables. Currently, station observations such as buoys over the oceanic part of the study domain are unavailable. We therefore use the National Oceanic and Atmospheric Administration (NOAA) Ocean Surface Bundle Climate Data Record (OSB-CDR) (Clayson et al., 2016) for ICON-LAM sfcWind evaluation over the oceans. OSB-CDR provides sfcWind over global ice-free oceans from passive microwave sensor data. It has a grid spacing of 0.25° with a temporal resolution of 3 hours and a continuous spatial coverage.

Satellite driven rsds observations have been widely used to evaluate climate model simulations (Bichet et al., 2019; Sawadogo et al., 2021; Tang et al., 2019). Surface Solar Radiation Parameters edition 3 (SARAH-3) (Pfeifroth et al., 2023) is the successor of the SARAH-2 (Pfeifroth et al., 2017), which has been proved to provide viable solar energy assessment data over Africa (Mabasa et al., 2021; Sawadogo, Bliefernicht, Fersch, Salack, Guug, Diallo, et al., 2023); SARAH-3 is provided by the European Organisation for the Exploitation of Meteorological Satellites (EUMETSAT) Satellite Application Facility on Climate Monitoring (CM SAF). It provides rsds based on geostationary satellite observations with a half hourly temporal resolution and a high spatial resolution of 0.05°, covering an area from -65°E to 65°E and -65°N to 65°N. SARAH-3 data at an hourly temporal resolution is used to evaluate ICON-LAM rsds output.

The Climatic Research Unit Timeseries CRU TS V4.06 (Harris et al., 2020) provides monthly mean tas at 0.5° resolution for all land areas, except Antarctica. We compare the monthly tas between ICON-LAM and CRU.

The Global Precipitation Measurement mission (GPM) (Huffman et al., 2015) is a global observation mission for pr and snow; it is the successor of the Tropical Rainfall Measuring Mission (TRMM). GPM with a spatial resolution of 0.1° and a temporal resolution of 30 minutes has been shown to outperform TRMM (Zhang et al., 2018) over mountainous area. From GPM we utilise hourly pr for the ICON-LAM evaluation.

3.2.4 In-situ observations quality control

Before using the in-situ observations of rsds and sfcWind and – to a lesser extent tas and pr (see Figure A.1 to A.5) – for validation, a quality control related pre-processing is necessary. We first unify the variable names and physical units from different networks and standardise the observations' recording time zones to Universal Time Coordinated (UTC). In a next step

implausible or out-of-range observations are then excluded. With rsds, the Baseline Surface Radiation Network (BSRN) quality control tests (Long & Dutton, 2010) are applied to the rsds observations; we use the BSRN's physically possible limits test, and the BSRN's extremely rare limits test; due to the lack of the necessary observed solar irradiance components (direct normal irradiance and diffuse horizontal irradiance) the BSRN closure test cannot be used. After that, we discard stations with more than 70% missing hourly observations over the 3-years period. Finally, 217 (87 of SASSCAL_WN, 27 of TAHMO, and 103 of NCEI_ISD), 96 (70 of SASSCAL_WN, 26 of TAHMO), 106 (86 of SASSCAL_WN, 20 of TAHMO), and 212 (88 of SASSCAL_WN, 28 of TAHMO, and 96 of NCEI_ISD) stations remain with sfcWind, rsds, pr, and tas measurements, respectively. No gap-filling technique is used to fill the missing observations, the evaluation applies only to the available observation time steps of each in-situ station.

From the 96 stations that provide rsds observations, 13 stations show dubious constant nighttime rsds values in the range of 3 to 70 W m^{-2}. These offsets constitute at the same time the minimum values per station. Per station a nighttime average offset is therefore subtracted from the time series. The Ineichen and Perez (Ineichen & Perez, 2002) clear sky model with a global coverage of monthly climatological Linke turbidity from pvlib (Holmgren et al., 2018) is used to check maxima and diurnal cycles of each corrected station rsds time series; otherwise, we would lose about 13% of our rsds validation sites. As this study focuses on the evaluation of simulated daytime rsds, an additional location and day-of-the-year specific sunrise and sunset check of the rsds observations is also done based on simulated ICON-LAM rsds.

The installed height of the sensor devices is especially important for the sfcWind evaluation procedure. Most of the stations from aforementioned networks meet common meteorological observation standards (World Meteorological Organization, 2021), i.e., 1.25 m to 2 m for air temperature observations, 10 m for wind speed, surface solar irradiance within a range of 1m to 2 m, and precipitation at 0.5 m to 1 m. In the TAHMO network, however, different weather sensors are integrated into a combined device to reduce maintenance costs and all the observed variables are recorded at 2 metres height. A further scaling procedure to extrapolate observed TAHMO network wind speed from 2 m to 10 m height is therefore needed. There are several scaling methods with associated advantages and disadvantages, discussion in this regard is out of the scope of the current study. Simplified extrapolations are the theoretically derived log law (assuming a neutrally stratified atmosphere) (Upstill‐Goddard et al., 1990; Yu et al., 1984) and the empirically derived power law (Hellmann, 1919). We compared the use of log law and power law here, and found that the log law unrealistically amplifies 2 m wind speed to 10 m especially for large wind speeds (data not shown). Therefore, the power law procedure is used in our wind speed scaling, see equation (3.1):

$$WS_H = WS_{ref}\left(\frac{H}{H_{ref}}\right)^{\alpha} \qquad (3.1)$$

WS_{ref} is the wind speed at the reference hight H_{ref} (here 2 m), while WS_H is the wind speed of

interest at height *H* (here 10 m). The α of power law is derived by following the approach in a study (Tizgui et al., 2017), incorporating roughness length as used in the ICON-LAM simulations for the closest model grid cell to the station.

3.2.5 Evaluation methods

This study aims to construct reliable and highly resolved meteorological information for downstream robust REP estimates. We focus on wind and solar energy as those renewable energy sources are considered as most important to achieve greenhouse gas neutral energy systems. We therefore conduct a model evaluation of sfcWind and rsds and on the hourly temporal resolution for it is necessary in the REP application field to capture the wind speed and solar irradiance fluctuations, leading also to a very strict model-to-observations evaluation. Aside from REP-related variables, tas and pr are also included in the evaluation, being the most basic variables considered in model evaluations (Ban et al., 2021; Kotlarski et al., 2014) and also being the fact that to our knowledge the model is run for the first time in the km-scale setup over southern Africa. Three observation networks are used here in order to include as many stations as possible.

Most of the in-situ observations are recorded at an hourly basis while the ICON-LAM simulation output is available every 15 minutes (for a later use in REP analysis). In line with the observations, the evaluation procedures use an hourly temporal scale. Only pr is investigated on a monthly scale given the scarce pr events over large semi-arid and arid parts of the study area. While simulated datasets provide 15min instantaneous sfcWind estimates, in-situ observations report mean sfcWind for 5, 10, 30, or 60 minutes periods depending on the available recordings and station operator. We always compare hourly mean sfcWind by averaging existing in-situ sub-hourly sfcWind and by averaging simulated ICON-LAM 15min sfcWind. For stations that reported hourly instantaneous values of tas and of rsds, a comparison between observations and ICON-LAM simulations was made for the hourly instantaneous values. For rsds, additionally, nighttime observations (equal to 0 W m^{-2}) were discarded from the analysis. As ICON-LAM accurately simulates sunrise and sunset, the nighttime rsds can be determined precisely.

The evaluation is carried out at the point and area scales. The nearest ICON-LAM generic model grid value to a station location is used for comparison. Even though we are working at a high resolution of 3.3 km and most of the stations are approximately at the same altitude above mean sea level as the grid cells, the comparison of a simulated value representative of a grid cell and a point measurement can still be affected by surface heterogeneity. We therefore apply a lapse rate of 0.0065 °C m^{-1} to the ICON-LAM simulated tas to account for the possible discrepancy in altitude between the model grid cell and the observation station, following examples from studies (Chen et al., 2019; Heikkilä et al., 2011).

For the statistical comparison, we use the mean error (*ME*),

$$ME = \frac{1}{N}\sum_{i=1}^{N}(M_i - O_i) = \bar{M} - \bar{O} \quad (3.2)$$

the mean absolute error (*MAE*),

$$MAE = \frac{1}{N}\sum_{i=1}^{N}|M_i - O_i| \qquad (3.3)$$

and the correlation coefficient (*R*).

$$R = \frac{\sum_{i=1}^{N}(M_i-\bar{M})(O_i-\bar{O})}{\sqrt{\sum_{i=1}^{N}(M_i-\bar{M})^2}\sqrt{\sum_{i=1}^{N}(O_i-\bar{O})^2}} \qquad (3.4)$$

In the equations (3.2) to (3.4), M represents simulated model values and O observed values, the time step is indicated with subscript i and the length of the total time series is N:

$$\bar{M} = \frac{1}{N}\sum_{i=1}^{N} M_i, \quad \bar{O} = \frac{1}{N}\sum_{i=1}^{N} O_i \qquad (3.5)$$

The Perkins Skill Score (PSS) (Perkins et al., 2007) quantifies the overlap area (percent) between two empirical frequency distributions. Z_m and Z_o are the normalised frequencies of a bin for the frequency distributions of simulations and observations, respectively, see equation (3.6). In this study, the respective bin width for the PSS calculation for sfcWind, rsds, and tas are 1 m s^{-1}, 30 W m^{-2}, and 1 °C. PSS calculation for pr is not applicable as data is only available at a monthly temporal resolution.

$$PSS = \sum_{1}^{n} \min(Z_m - Z_o) \qquad (3.6)$$

In the spatial comparison, variables of rsds and pr are not available from ICON-GL, and sfcWind as well as tas are based on the lowermost model level (10 m) of ICON-GL simulated u and v, and air temperature, respectively. Additionally, different satellite and composite data products corresponding to the variables of interest are used to compensate for the discrete and unevenly distributed station-based observations. As these data products come on grids which differ from the ICON-LAM triangular model grid, data on different grids are resampled to a common grid for comparison, using a conservative remapping approach (Suklitsch et al., 2008). We downsample fine grid data according to their relative spatial contribution to the same grid as the coarse resolution comparison grid is available on. The conservative mapping approach has been used in comparisons which are displayed in Figures 3.8, Figure 3.13, and Figure A.3.

Understanding the capacity of ICON-LAM model to simulate rsds under different sky clearness conditions is crucial for solar energy applications. We use the sky clearness index (K_t) and categorize the observed rsds into distinct atmospheric conditions of all-sky, clear-sky, and cloudy-sky. All observational data are used to evaluate simulations under all-sky condition. Cloudy-sky as well as clear-sky cases are identified on the basis of the observed rsds, and the corresponding time steps from the simulation are taken and simulated rsds for those time steps are compared with observed rsds. K_t is defined as the ratio of the rsds to the extraterrestrial solar radiation at the top of the atmosphere (G_0) according:

$$K_t = \frac{rsds}{G_0} \tag{3.7}$$

The extraterrestrial solar radiation at a given location for a specific day depends only on the latitude and the day of the year, and the daily extraterrestrial radiation G_0 (MJ m^{-2} day^{-1}) is calculated according to (Allen et al., 1998). The daily observed rsds is derived from hourly rsds under the condition that there is no single missing hourly observation value during the day.

This sky clearness index has been applied in many studies but the thresholds used to differentiate distinct sky conditions vary with the focus area: 0.82 was recognized as the boundary threshold between clear- and cloudy-sky for studies in China (Du et al., 2022; Shi et al., 2021), $K_t \geqslant 0.6$ was accepted as clear-sky and cloudy-sky was treated as $0.12 \leqslant K_t < 0.35$ in another study focusing on western Africa (Sawadogo, Bliefernicht, Fersch, Salack, Guug, Diallo, et al., 2023). Here we follow studies for South Africa (Apeh et al., 2021; Govindasamy & Chetty, 2018) and determine clear-sky as $K_t > 0.7$ and cloudy-sky as $K_t < 0.3$.

The capability of the ICON-LAM model to simulate the diurnal variation of sfcWind and rsds is further investigated. The average diurnal variation of sfcWind for all-year, austral winter, and austral summer as well as the average diurnal variation of rsds under the sky conditions all-sky, clear-sky, and cloudy-sky are compared between in-situ observations and ICON-LAM simulations for three representative stations.

3.3 Results and discussion

To evaluate the performance of our ICON-LAM simulations over southern Africa, we compare simulated sfcWind and rsds with in-situ station point measurements, as well as with spatially distributed data products. The focus of the evaluation is on the entire model domain. In a first step, seasonal means are compared with the state-of-the-art global reanalysis product ERA5, the forcing data ICON-GL, and satellite observations, to see whether the mean atmospheric states can be reproduced by this new ICON-LAM setup; in addition, the spatial distribution of the mean states is also investigated.

3.3.1 Seasonal mean comparison

The seasonal means of sfcWind and rsds in austral summer (December-January-February, DJF) and austral winter (June-July-August, JJA) from ERA5, ICON-GL, ICON-LAM, and the reference datasets OSB-CDR and SARAH-3 are illustrated in Figure 3.3. The spatial patterns of sfcWind over the ocean are similar for the different simulation datasets. In comparison, OSB-CDR shows in general lower sfcWind in both seasons. This is possibly due to the passive microwave sensor with coarse spatial resolution that cannot capture fine spatial wind speed details. Over the land area of the domain, increasing the spatial resolution from ERA5 (31 km) to ICON-GL (13 km), and ICON-LAM (3.3 km) allows to depict finer spatial details of the wind speed field. The southern Africa Great Escarpment altered wind speeds, which are clearly visible in the high-resolution ICON-LAM simulations, especially in austral winter, where the

higher wind speed belt (mean sfcWind > 6 m/s) coincides with the steep slopes at the central southern African Plateau. The western branch of the Great Escarpment, which is predominantly located in Namibia, can be identified in ICON-LAM with increased wind speeds, which are not in the simulated wind speeds by the ICON-GL and ERA5 models. On the other hand, it is found that ICON-LAM systematically simulates higher wind speeds over land compared with ERA5 and ICON-GL in both seasons. It should be noted that in this study the focus is not on an evaluation of the added value of the km-scale simulation with reference to the lower resolution model runs, this is the reason why we do not resample the high-resolution data to the coarse resolution grids.

Rsds from ICON-GL is not included in this study (empty sub-plot in Figure 3.3). ERA5, ICON-LAM, and SARAH-3 agree with each other on the rsds magnitude of the differences between the summer and winter seasons and the spatial patterns of rsds in both seasons. With a low cloud coverage (see also the pr maps in Figure A.1) in the austral winter, averaged rsds decreases meridionally according to the mean solar zenith angle from north to south. During austral summer, the hot desert climates of South Africa and Namibia clearly stand out.

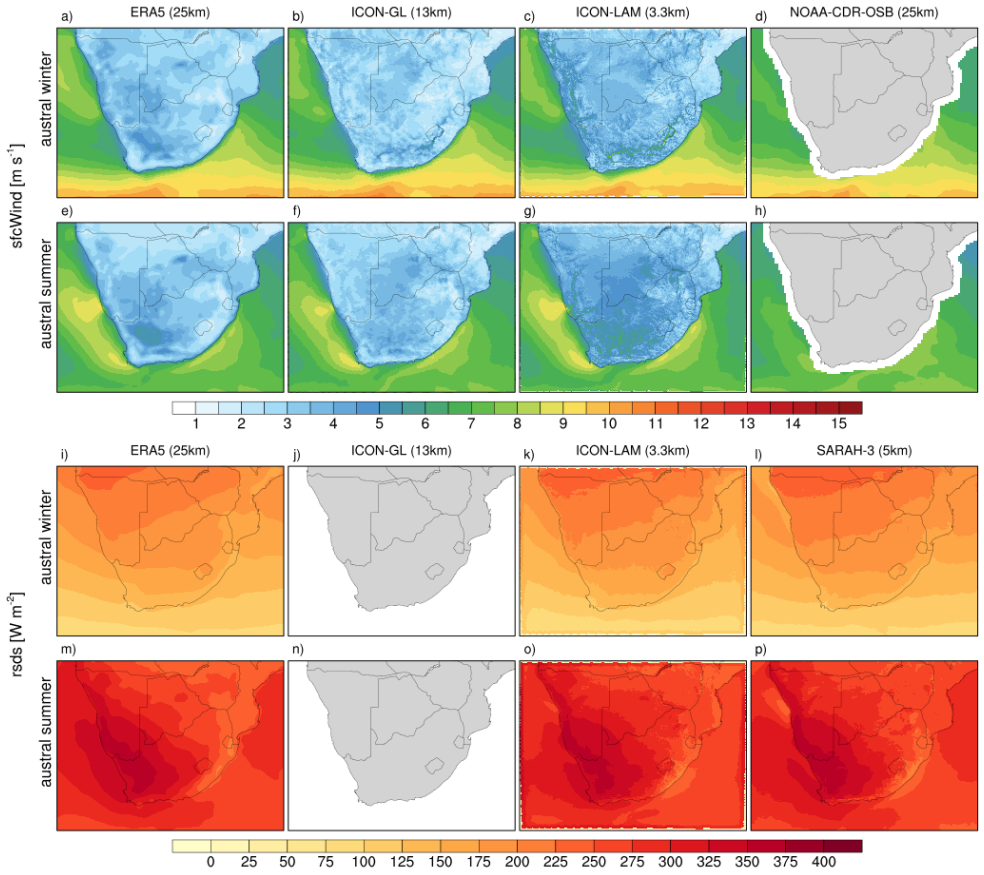

Figure 3.3 Average sfcWind [m s^{-1}] (top multi-panel) and rsds [W m^{-2}] (lower multi-panel) for

the period 2017 to 2019 and austral winter (JJA) (upper row) and austral summer (DJF) (lower row), for ERA5 (1st column), driving ICON-GL (2nd column), ICON-LAM (3rd column), and the reference data (4th column), OSB-CDR for sfcWind, SARAH-3 for rsds. The sfcWind of ICON-GL is derived from the lowest model level (10 m) of u and v and the rsds of ICON-GL is not available. All the datasets are presented on their respective native grids.

3.3.2 Simulated wind speed evaluation

3.3.2.1 Wind speed over station points

Figure 3.4 shows the spatial distribution of the metrics MAE, ME, R, and PSS for the evaluation of ICON-LAM sfcWind simulation results against the meteorological stations. The associated summary statistics per metric and network are presented in Figure 3.5. ICON-LAM simulated sfcWind has for many stations a positive bias and the spatial average (standard deviation) of MAE and ME are 1.7 (± 0.51) and 1.12 (± 0.83) m s^{-1}, respectively (Figure 3.5 a and b). Here, 92.2% of a total 217 considered in-situ observations are found with positive sfcWind ME biases, and 40% of the total scatter are in the range of +/-1 m s^{-1}, based on hourly data for the period 2017 to 2019. Additionally, 69% of the stations show a correlation > 0.6 between observations and simulation. PSS is larger than 0.8 for 39% of the station locations. The metrics are similar for the three measurement networks. Despite the observation data quality control procedures (see Section 3.2.4), some stations were retained, which show large deviations from simulations and are consequently also treated as outliers (defined as points out of the range minimum, 1st quartile - 1.5 * (3rd quartile - 1st quartile), and maximum, 3rd quartile + 1.5 * (3rd quartile - 1st quartile), of the box-whisker) in the plots. For the sake of completeness, outliers are plotted in the summary statistics box-whisker plots.

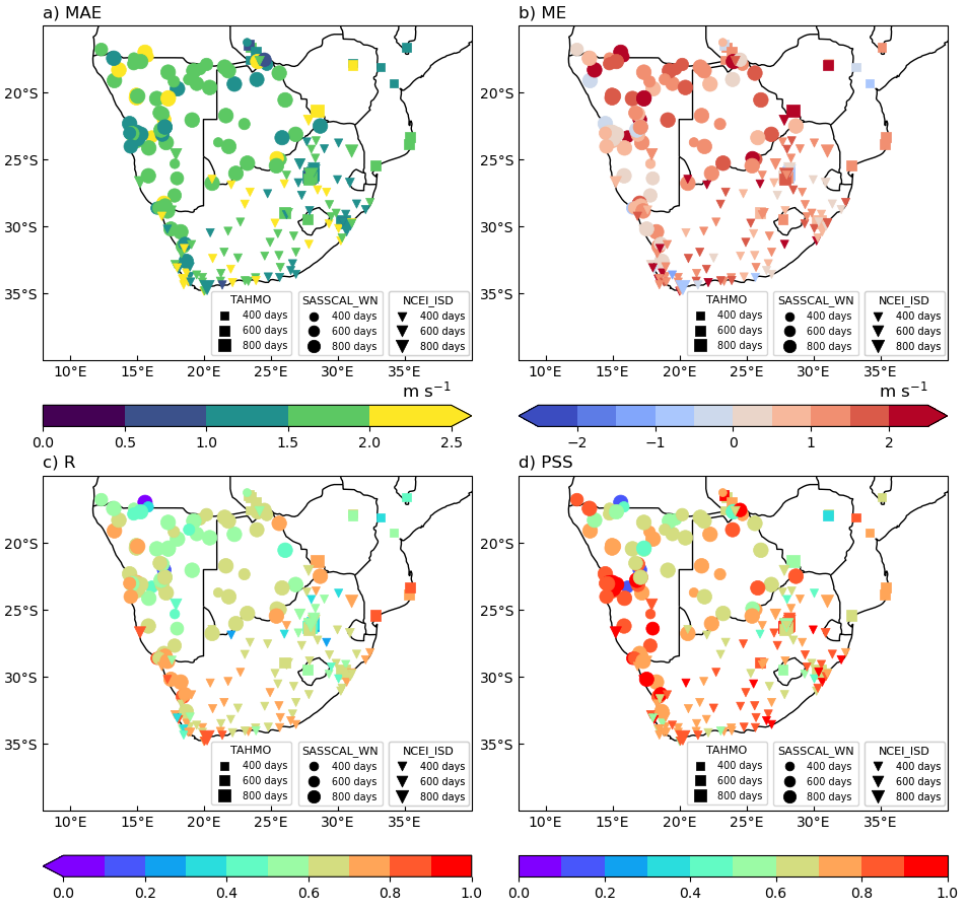

Figure 3.4 Spatial distribution of MAE, ME, R, and PSS of hourly sfcWind for the period 2017 to 2019 at ground meteorological stations. Statistics are calculated comparing simulated sfcWind by ICON-LAM and observed sfcWind by ground meteorological stations. Symbols identify different observational networks. Rectangles: TAHMO, circles: SASSCAL_WN, triangles: NCEI_ISD. The symbol sizes represent the number of valid measurement days during 2017 to 2019.

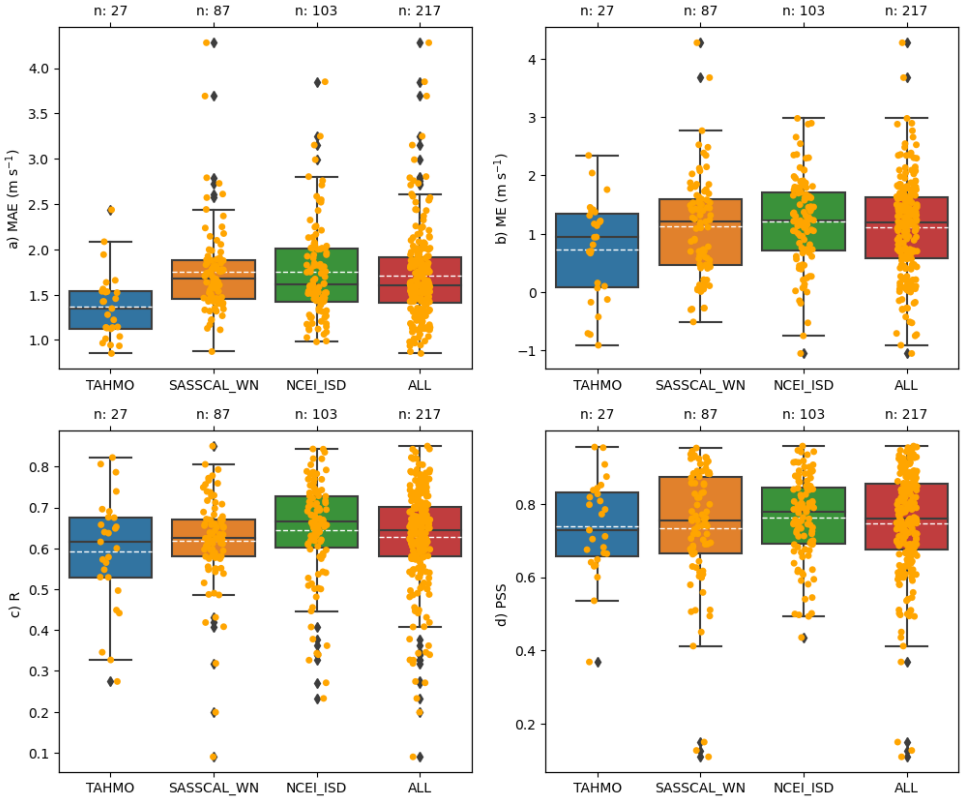

Figure 3.5 Summary statistics of the metrics presented in Figure 3.4 per meteorological station network and combined. Each box-whisker plot shows the minimum, 0.25 percentile, median, 0.75 percentile, and maximum values of each evaluation measure per network, and in addition the mean (white dashed line) and the outliers (black diamonds). Yellow dots: individual data points (one dot corresponds to one station in Figure 3.4), n is the number of stations with valid data.

3.3.2.2 Wind speed over representative station points

Aside from the summarising metrics of Figure 3.4 and 3.5, we illustrate model performance for three representative stations (see Table 3.2 for details), which are located in different areas of the model domain, at different altitudes above mean sea level, through scatter plots, percentile plots, frequency distributions, and monthly mean annual cycles for ICON-LAM simulated and observed sfcWind (Figure 3.6), and also through the average diurnal variation analysis (Figure 3.7). The selected stations have hourly observational data records with less than 24 missing data points in three years.

Station 68325 locates at the centre of the model domain and also the centre of the Plateau at an altitude of 1275m. ICON-LAM shows on average higher wind speeds than in the observations

with more frequent wind speeds above 5 m s^{-1} as illustrated by the scatter, percentile, and histograms plots. On the other hand, ICON-LAM captures the sfcWind with a correlation coefficient of 0.75, the measured annual cycle and also the diurnal variations are well represented.

Station E7625 is a coastal station at a height of 405m. For this station, the scatter plot indicates an underestimation by ICON-LAM simulated larger wind speed. Generally, biases are small, as illustrated by the percentiles, histograms, and annual cycles. The time series in sfcWind are well captured by ICON-LAM. The observed trend in diurnal variation has been reproduced although with overestimation during daytime and underestimation during nighttime in the austral summer and also in the complete year; Overestimations also happen in the midday of the austral winter.

Station 858596 at a height of 606m is chosen to represent a transition zone from the coastal area to the Plateau. Similar to station 68325, for this observation site ICON-LAM overestimates wind speeds and simulates much more often elevated wind speeds (> 6-8 m s^{-1}) than measured at the site, despite the fact, that the shape of the annual sfcWind cycle and diurnal variation are reproduced well.

Table 3.2 Three selected representative stations with location, altitude, and the altitude of the corresponding ICON-LAM grid cell.

Station id used by the networks	Station name	Country	Longitude [decimal degrees]	Latitude [decimal degrees]	Network identifier	Altitude from station metadata [m]	ICON-LAM altitude [m]
68325	Goodhope	Botswana	25.43	-25.46	SASSCAL_WN	1275	1275.07
E7625	Aussinanis	Namibia	15.05	-23.44	SASSCAL_WN	405	426.09
858596	Eksteenfontein	South Africa	17.29	-28.84	SASSCAL_WN	606	634.39

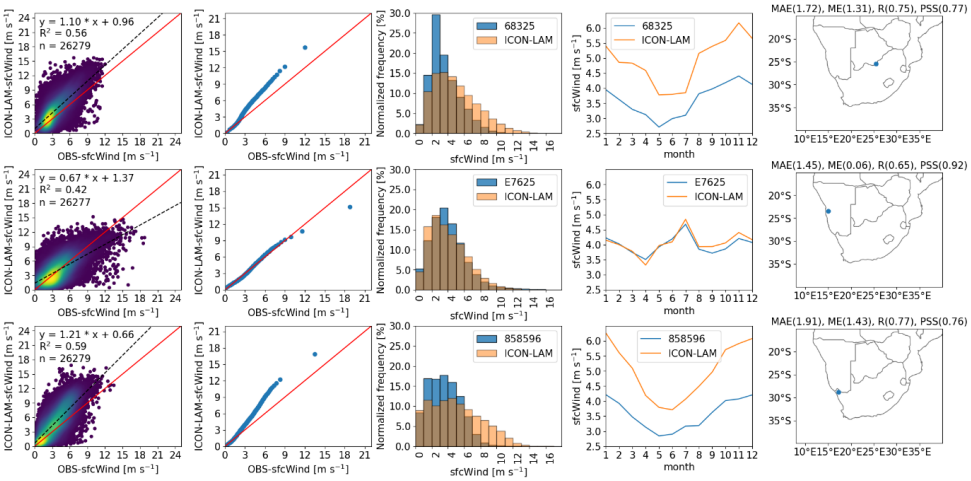

Figure 3.6 Overview of sfcWind characteristics, ICON-LAM vs meteorological station observations, for three selected stations (rows) for hourly 10 m wind speed [m s^{-1}]. Columns from left to right: scatter plots, percentile plots, histograms (bin width 1 m s^{-1}), monthly mean annual cycles, and the location of each station. Colours in the scatter plots: point density estimated by a Gaussian Kernel (brighter colour means higher density). Percentiles in the percentile plot are at every 1% interval. Histogram plot has a bin size of 1 m s^{-1}.

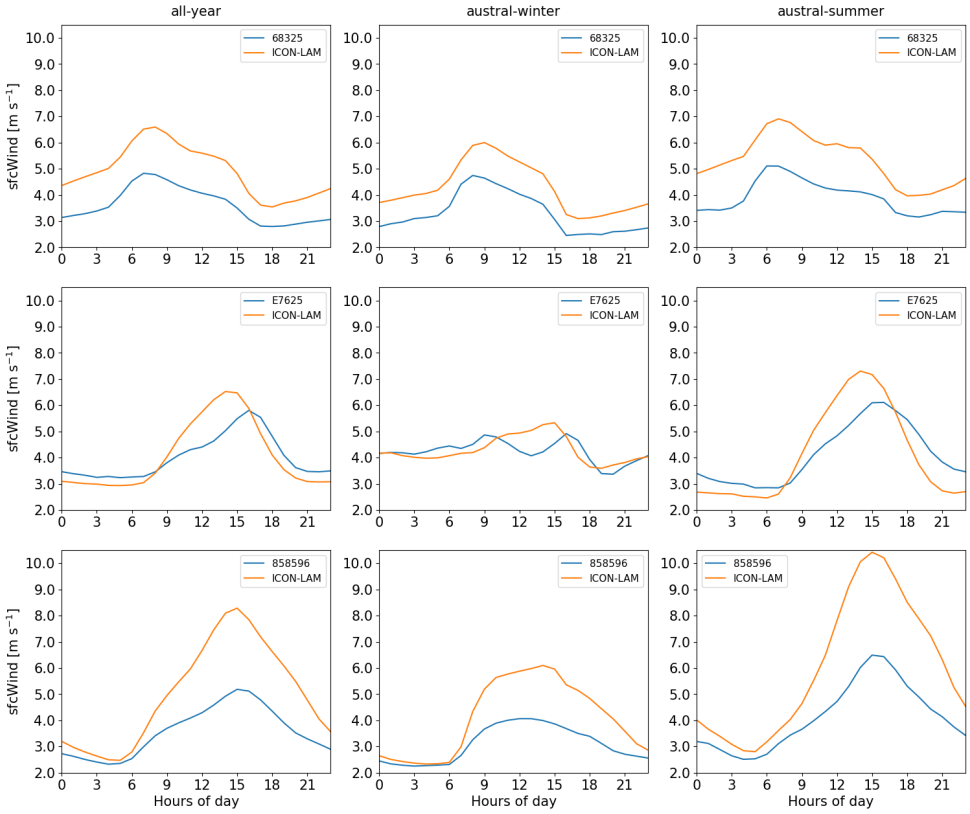

Figure 3.7 Average diurnal cycle of hourly sfcWind [m s^{-1}] at three selected stations (rows). Results are shown for in-situ observations (blue line) and ICON-LAM simulations (orange line) for the period 2017 to 2019 (all-year), austral winter (JJA), and austral summer (DJF) (columns).

3.3.2.3 Wind speed over ocean

The comparison over the oceans in Figure 3.3 indicates that ICON-LAM shows higher seasonal mean sfcWind than OSB-CDR. In order to compare sfcWind over the oceans in more detail, despite the fact that offshore wind energy potentials are not a focus and would be too close to the coastline to be captured in our data comparison, Figure 3.8 shows differences in the percentiles and the mean. ICON-LAM overestimates sfcWind off the coast of Namibia. The overestimation is more pronounced for higher sfcWind with the highest overestimation for extreme sfcWind of the 0.95 percentile. For the 0.05 percentile there is a widespread underestimation of sfcWind by ICON-LAM. For the mean sfcWind over the ocean (Figure 3.8f) differences range from -0.5 to 1.5 m s^{-1}.

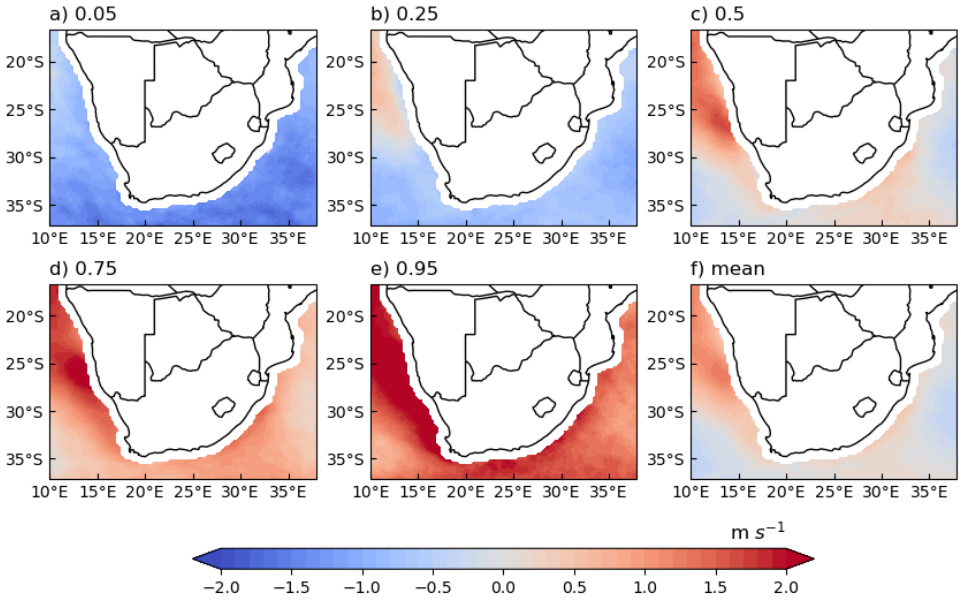

Figure 3.8 Differences in 3-hourly sfcWind [m s^{-1}] between (ICON-LAM minus OSB-CDR) for corresponding percentiles (0.05, 0.25, 0.5, 0.75, 0.95) over the ocean for the period 2017 to 2019. The mean difference is also plotted.

3.3.2.4 Wind speed evaluation discussion

In our comparison of ICON-LAM sfcWind with a large compiled station dataset we find a clear tendency towards positive sfcWind ME biases (Section 3.3.2.1.). At the same time the observational reference data (as big a wind speed data set as we could compile at the time of writing) shows various deficiencies: Despite the quality control of the in-situ sfcWind observations (section 3.2.4), outliers in Figure 3.5 are an indication of problems with data quality, that is difficult to fully evaluate without knowing the local setup. Although we tried to compile an observation dataset with as many sites as possible, the spatial heterogeneity is very much undersampled. Finally, the station-to-model grid comparison even at km-scale resolution, means the local measurement condition could differ from the model's land cover and terrain.

Through the sfcWind seasonal mean biases analysis (Figure 3.3 a to h), systematic overestimations compared with ERA5 and ICON-GL are found with ICON-LAM simulated austral winters and summers average sfcWind. Studies in Sweden (Minola et al., 2020), US and Iran (Gualtieri, 2021) have documented an underestimation of the simulated sfcWind for mountain sites with ERA5 due to its coarse spatial resolution. Given our study domain with a complex topography with features such as the Plateau and the Great Escarpment, the overestimation from ICON-LAM with reference to ERA5 still needs to be further investigated to evaluate the true added value from the high-resolution dynamical downscaling. With respect to ICON-GL (Figure 3.3 b and f) the model setup also plays a role, as, e.g., the roughness

lengths are lower in ICON-LAM by about 20.9% on average over the central southern mountainous part of the model domain (data not shown).

As data from this experiment are to be used for REP estimates, the entire evaluation is done with hourly wind speeds. A similar near-surface wind speed evaluation study (Molina et al., 2021) showed with decreased temporal resolution, from hourly to 6-hourly to daily, that the correlation coefficients and skill scores increase. In an evaluation with hourly temporal resolution for sfcWind (Minola et al., 2020), they showed an overestimation of up to 1.5 and 2 m s^{-1} from ERA5 over Sweden, when comparing to coastal and inland stations, respectively. A study (D'Isidoro et al., 2020) conducted an atmospheric dynamical downscaling study using the Weather Research and Forecasting (WRF) model over Lesotho at 1 km resolution. The study was driven by the ECMWF ERA5 reanalysis dataset. The authors found that the simulated hourly surface wind speed biases were generally between 0.5 and 1.7 m s^{-1} using three different physics combinations. These biases are comparable to the average hourly surface wind ME of 1.12 (± 0.83) m s^{-1}, as determined from 217 stations in this study.

3.3.3 Simulated solar irradiance evaluation

3.3.3.1 Solar irradiance over station points

Figure 3.9 shows the spatial distribution of 4 evaluation metrics comparing ICON-LAM simulated and station observed rsds in [W m^{-2}] under various sky conditions of all-sky, clear-sky, and cloudy-sky and also the associated available observation days number. Figure 3.10 shows the statistical summary of the corresponding metrics. Under all skies (Figure 3.9 a to e), the average MAE (± standard deviation) over the considered stations is 118.6 (± 30.87) W m^{-2} and the average ME is 50.8 (± 42.21) W m^{-2}. Often a positive ME is observed in the study domain. In the deserts along the west coast of Namibia and South Africa biases are often close to 0 W m^{-2}. The absolute biases underlying MAE show an increasing trend from coast to inland and from south to north; this coincides with areas of higher precipitation and hence cloudiness (see Figure A.1). On the other hand, the correlation coefficient and frequency distribution illustrate that the simulated values by ICON-LAM are close to observations. The average of R is 0.87 with a standard deviation of 0.05, and for 95% of the stations PSS > 0.8. When considering the TAHMO and SASSCAL_WN networks, for which rsds data are available, they show systematic differences in their comparison with the ICON-LAM. The SASSCAL_WN sites show for all metrics a better agreement with ICON-LAM simulated rsds especially in terms of ME and PSS. The newly integrated weather sensor type of the TAHMO network could be a reason for this behaviour. Grouping according to station networks in Figure 3.5 and Figure 3.10 allows to identify network-related effects in the evaluation.

ICON-LAM simulates rsds under clear skies well (see Figure 3.9 f to j), the average MAE over all stations is about 60 W m^{-2} and the estimate is almost unbiased with an average R across all stations above 0.95. The PSS values for clear-sky rsds show a large spread with average PSS around 0.75. Simulating rsds is challenging under cloudy skies, which occurs less than 109 days for all the used stations (except one station, Figure 3.9o). For cloudy skies MAE and ME are higher (stations average about 210 W m^{-2} and 175 W m^{-2}, respectively), average R is about

0.52 and PSS 0.65.

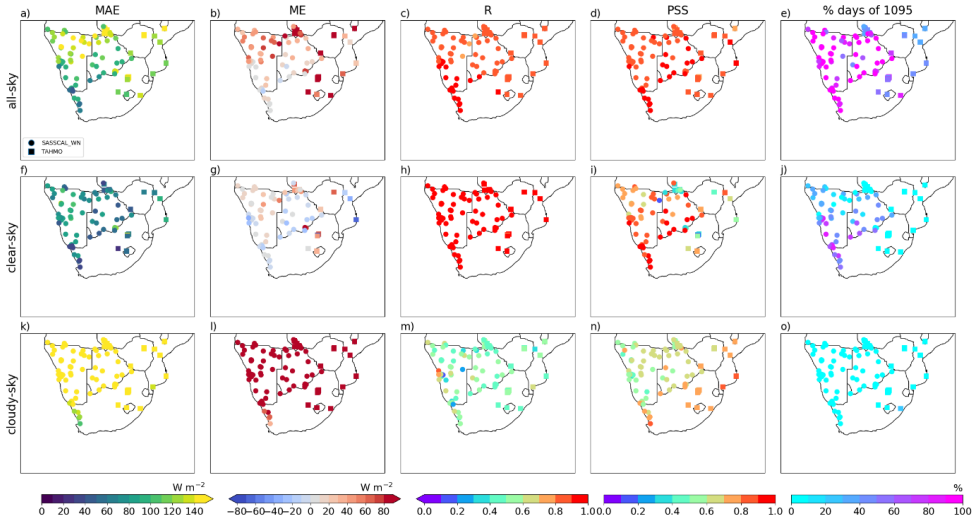

Figure 3.9 As in Figure 3.4, but for daytime hourly rsds [W m^{-2}] under sky conditions of all-sky, clear-sky, and cloudy-sky (rows). The last column "% days of 1095" indicates the percentage of days out of the full three years (1095 days) that are available with the corresponding sky condition over each station.

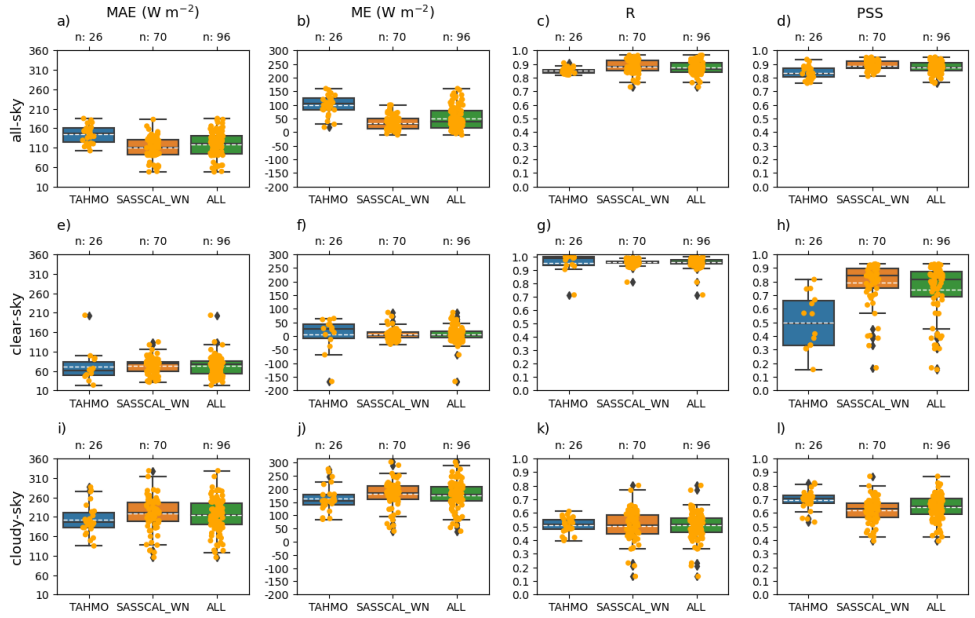

Figure 3.10 As in Figure 3.5, but for the summary statistics of the metrics presented in Figure

3.9.

3.3.3.2 Solar irradiance over representative station points

The same three representative stations from Section 3.3.2.2. are also analysed in terms of rsds in Figure 3.11 and their average rsds diurnal variation under all-sky, clear-sky, and cloudy-sky are showed in Figure 3.12. In general, ICON-LAM simulates rsds in close agreement with the station network observations, which is especially obvious in the scatter and percentile plots. Higher scores of R with a minimum of 0.88 and a PSS of 0.87 are found for all three stations. The simulated and observed diurnal cycles of all-sky rsds and clear-sky rsds agree nearly perfectly. On the other hand, ICON-LAM strongly overestimates rsds for cloudy skies conditions, especially during the rsds peak hours. However, it is important to stress that cloudy skies conditions only occur 34 days in three simulation years at station 68325, and 4 days and 5 days for stations E7625 and 858596, respectively.

Station 68325 is actually one of the stations, to which we apply the offset correction during daytime (about 33 W m^{-2}). The observed rsds frequency distribution of station 68325 is reproduced by ICON-LAM with a PSS of 0.95. An overestimation is found in one austral summer month while underestimation exist during one month in austral spring based on the mean annual cycle comparison between simulation and observation.

If we compare simulated solar irradiance with measured solar irradiance for the stations E7625 and 858596 high R (0.94 and 0.96 respectively) and low ME (4.35 and -10.71 W m^{-2} respectively) are found. ICON-LAM underestimates solar irradiance in the austral winter at station 858596 and overestimates in September for station E7625. There is no obvious systematic bias except a small shift for ICON-LAM simulated clear sky rsds at station E7625.

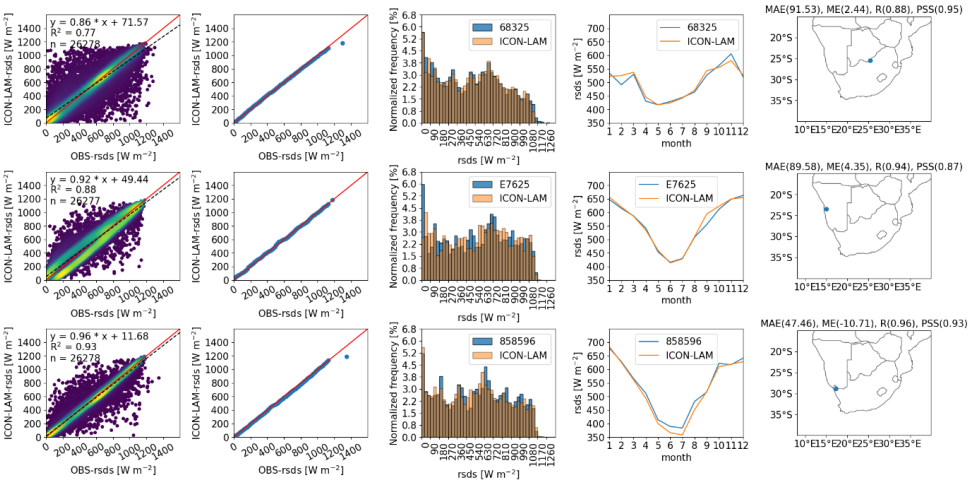

Figure 3.11 As in Figure 3.6, but for daytime hourly rsds statistics [W m^{-2}] and histogram plot has a bin size of 30 [W m^{-2}].

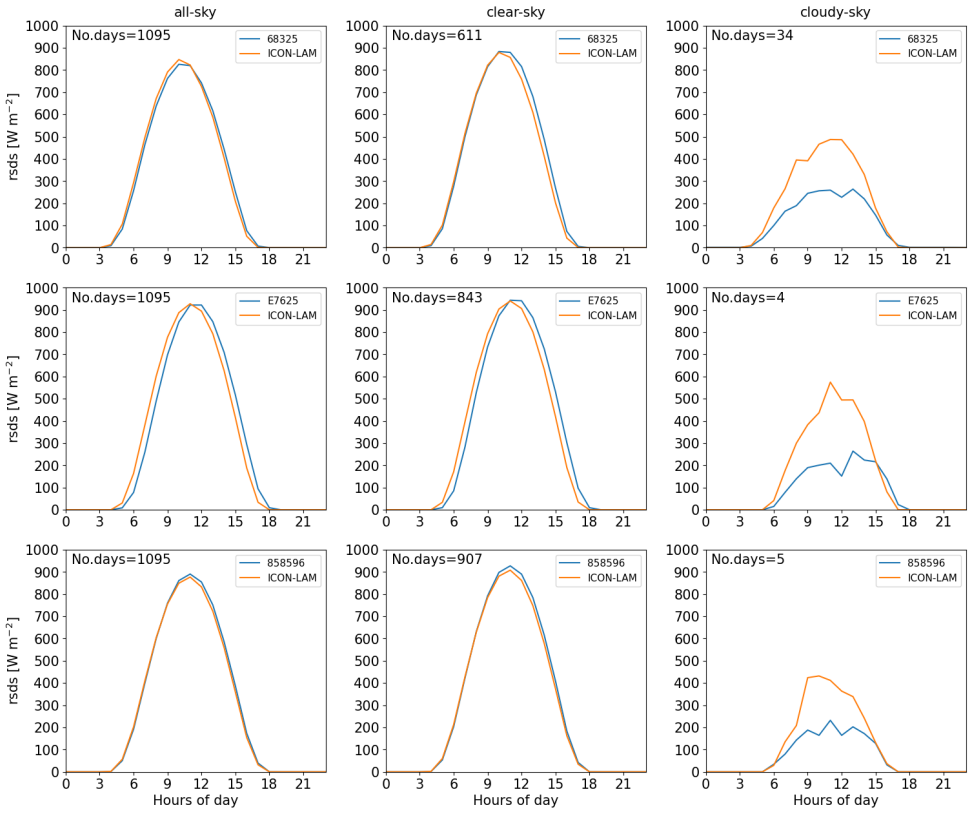

Figure 3.12 Average diurnal cycles for hourly rsds [W m^{-2}] at three selected stations (rows). Results are shown for in-situ observations (blue line) and ICON-LAM simulations (orange line) under all-sky, clear-sky, and cloudy-sky conditions (columns). "No.days" is the number of days found with the corresponding sky condition.

3.3.3.3 Solar irradiance over the whole study domain

In Figure 3.13 we show the difference between ICON-LAM and SARAH-3 simulated rsds for several percentiles as well as the mean differences. These differences are again based on daytime data. In general, both datasets show a good agreement at all the percentiles and also the mean states. Major differences in two models for simulating rsds exist over ocean. ICON-LAM simulated higher rsds compared with SARAH-3 at the coasts of Namibia and the ocean west of Namibia particularly for percentiles 0.75 and 0.5, and an area of underestimation of ICON-LAM also occurs at the northern part of the Indian Ocean. The difference between the simulated and observed mean is between -30 and 30 W m^{-2}.

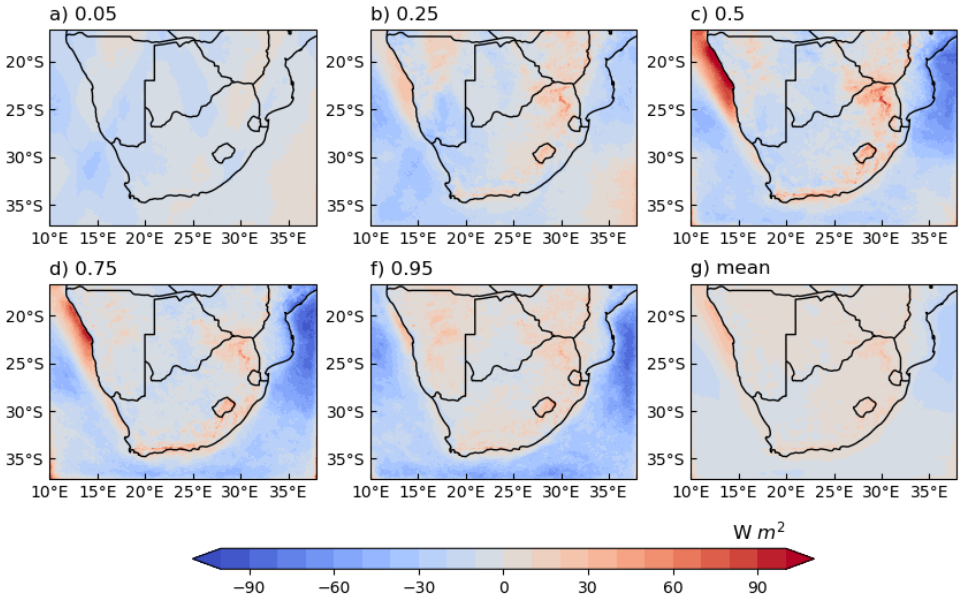

Figure 3.13 As in Figure 3.8, but for daytime hourly rsds [W m^{-2}].

3.3.3.4 Solar irradiance evaluation discussion

Generally, ICON-LAM simulates rsds in southern Africa in good accordance with observations especially under clear sky, delivers an almost unbiased clear sky rsds simulation. Biases are relatively small over the desert areas in the west, related to the strong anticyclonic circulation with subsidence which prevents that a cloud cover develops in the ICON-LAM, altering radiation. The larger biases can be found in the northern parts, which are characterized by more cloudiness and rainfall, as shown in Figure A.1, a shared challenge as with reanalysis data (Babar et al., 2019).

Actually, large discrepancies in the rsds under cloudy skies are also found between reanalysis and the in-situ observations as well as satellite products and the in-situ observations. A study (Sawadogo, Bliefernicht, Fersch, Salack, Guug, Diallo, et al., 2023) reported that the MAE varies from 153 to 232 W m^{-2} for the rsds under cloudy skies for the reanalysis (ERA5 and MERRA-2) and satellite (CAMS and SARAH-2) products, compared to 37 observing stations over western Africa. Evaluation of satellite-estimated rsds over South Africa (Mabasa et al., 2022) showed excellent performance under clear skies with rMAE smaller than 6.5% and poorer performance under cloudy skies with rMAE 29%, whereas satellite-based rsds estimate outperform the reanalysis-based estimate over South Africa (Mabasa et al., 2021). In addition, a dynamical downscaling study (Sawadogo, Bliefernicht, Fersch, Salack, Guug, Ogunjobi, et al., 2023) using the WRF-solar model driven by ERA5 also documented large overestimations for rsds under cloudy skies. The evaluation of ICON-LAM simulated cloudy-sky rsds over 96 stations shows an average MAE of 210 W m^{-2} which is within the typical margin of error.

When evaluating model performance, systematic differences become apparent between the two local observation networks we use. Evaluation results using observations from the SASSCAL_WN show a better overall agreement with the ICON-LAM model results at all times under all sky conditions. The average ME decreases from 50.8 W m^{-2} to 26 W m^{-2} if only SASSCAL_WN observations are used.

In our comparison, we apply a strict daytime hourly simulated rsds evaluation. Using longer averaging intervals, e.g., a daily temporal aggregation, would lead to a more favourable comparison for the ICON-LAM simulation (Cao et al., 2022). Daily averaged rsds evaluation with overestimation of 4.1 W m^{-2} and monthly 4.5 W m^{-2} are found from ERA5 at high latitudes (> 58°N) (Babar et al., 2019). Including nighttime rsds would also for sure increase the model skill scores for ICON-LAM. However, due to the study's goal of providing data for REP estimation, we have to stick to daytime hourly evaluation. In a study (Yang & Bright, 2020) done with worldwide 57 stations and a 27 years validation time span, the validation of hourly rsds from ERA5 shows a global average ME of 23.95 W m^{-2}. In their study, two stations in southern Africa are included, located in the coastal desert of Namibia and the desert of South Africa, with a ME of 4.14 and 11.11 W m^{-2}, respectively. In a comparison over China, ERA5 overestimates the hourly surface solar irradiance by about 30.87 W m^{-2} (Jiang et al., 2019). Hence the performance of ICON-LAM simulated daytime hourly rsds is comparable with ERA5 all-day comparisons.

When considering a high-resolution COSMO-REA6 reanalysis product, study shows that it is able to mitigate the limitation of ERA5 over complex terrain, e.g., coastal areas, in simulating rsds (Urraca et al., 2018). The coastal station E7625 in section 3.3.3. proves ICON-LAM can capture solar irradiance over complex terrain.

3.3.4 Simulated precipitation and 2 m air temperature evaluation

We additionally evaluate pr and tas for this novel model implementation over the study domain.

In Figure A.1, seasonal means of pr and tas from ERA5, ICON-GL, ICON-LAM, and GPM/CRU are presented. Pr of ICON-GL is not available for Figure A.1 b and f. The spatial patterns of pr, Figure A.1 a to h, are similar for the three datasets. Austral winter is the dry season in southern Africa, very little (< 5 mm) or no rainfall occurs over land except along the southern coast and western part of South Africa associated with the Benguela current; most of the pr is located over the oceans of the southern part of the study domain. In austral summer (wet season), rainfall expands over almost all land areas with a southerly shifted ITCZ and the northerly winds of the East African Monsoon (Geppert et al., 2022), except for the deserts in the western part. This pronounced seasonal pr cycle with its local features is, e.g., in accordance with other studies (Engelbrecht et al., 2015; Geppert et al., 2022; Weldon & Reason, 2014). The deserts along the west coast of Namibia and South Africa are related to the combination of the cold Benguela ocean current and the subsidence of the South Atlantic Anticyclone. Aside from reproducing the large-scale patterns, the high-resolution ICON-LAM shows small-scale local pr maxima associated, e.g., with orographic features such as the mountains in Lesotho.

Towards the Southern Ocean ICON-LAM pr amounts are smaller when compared to ERA5 and GPM.

Tas in Figure A.1 show good agreement among the different datasets in both seasons, again, with a pronounced seasonal cycle. The distribution of tas over the ocean follows a thermal north-south gradient, altered by the warm Agulhas current over the Indian Ocean and the cold Benguela current along the Atlantic coastline. Land surface heterogeneity over southern Africa characterises the pattern of tas; mountain ranges and the Plateau are clearly visible in the ICON-LAM high-resolution simulation.

Pr is further evaluated on a monthly time scale. Figure A.2 shows MAE and ME of simulated pr, compared to in-situ observed pr. ICON-LAM simulated monthly pr biases decrease from the North-East to the deserts in the South-East of the study domain, which follows the prevailing rainfall patterns. The average of MAE for pr (± standard deviation) is 16.56 (± 16.89) mm month^{-1} and the average for ME is 3.75 (± 12.57) mm month^{-1}. A very pronounced and much documented added value of convection-permitting RCM simulations is an improved reproduction of pr characteristics (amounts, intensities, spatial patterns, etc.) (Ban et al., 2021; Lucas‐Picher et al., 2021; Prein et al., 2015). We therefore analyse the difference of the 0.95 percentile of daily pr between ICON-LAM and GPM, for the three simulation years and austral winters and summers (see Figure A.3). Pr in southern Africa shows a high seasonality with an obvious contrast between austral winter (dry) and austral summer (wet). In line with the experiment setup of regular re-initialisations, ICON-LAM reproduces the observed seasonality of pr by GPM and also the spatial pattern of extreme pr. However, ICON-LAM simulates a too small amount of extreme daily pr compared with GPM over the Indian ocean, and also over the country of Mozambique during austral summer (see Figure A.3k). This lack of ICON-LAM simulated pr over the Indian ocean is also found in the monthly mean pr comparison, on the contrary, ICON-LAM has more monthly pr over land than GPM except for the area of Mozambique (Figure A.3l).

The simulated ICON-LAM tas shows, depending on the spatial location, positive and negative biases throughout the simulation domain without a clear spatial pattern, although western Namibia and western Southern Africa tend to have more often negative ME, and other areas positive ME. See also Figure A.4b. The average ME is 0.23 (± 0.99) °C and the MAE is 1.97 (± 0.55) °C. The R and PSS illustrate the high correspondence between simulated and measured values with spatial means above 0.9 and standard deviations below 0.05. Figure A.5 compares again for individual stations simulated values and measurements. The measured data are in general well reproduced, but two of the three stations show some systematic bias. For station E7625 tas is overestimated about 1.49 °C (ME) and for station 858596 there is an underestimation with a mean error of -1.45 °C.

3.4 Summary and conclusions

Our study presents a high-resolution physically consistent dataset over southern Africa to serve as input for spatially and temporally highly resolved REP estimates. The dedicated convection-

permitting 3.3 km atmospheric simulations are run with the ICON-LAM, driven by initialised analysis based on the global deterministic ICON-NWP forecasts, and using the operational km-scale weather prediction ICON configuration of DWD. The simulations cover three meteorologically contrasting years from 2017 to 2019. They help fill the scarcity of high-resolution datasets over this part of Africa. Subsequently, these results can help to foster the development of renewable energy expansion in Africa, where three quarters of the global population without reliable access to electricity are located and where renewable energy is considered one of the vital solutions.

Our high-resolution ICON-LAM setup and simulations are to our knowledge unprecedented for the study area; they show overall a good performance in reproducing REP-related sfcWind and rsds fields and near surface essential climate variables, albeit with some limitations.

The detailed hourly sfcWind evaluation indicates overall a good reproduction of station observations, and biases of 1.12 (± 0.83) m s^{-1} are well comparable to other work (D'Isidoro et al., 2020). There is, however, a tendency to an overestimation over land. The reason behind this model behaviour is unclear; more in-depth assessment of the surface and boundary layer schemes as implemented and configured and a dedicated model parameter optimisation study for the area might after all be necessary to further reduce the biases. This is beyond the scope of this analysis.

The error level of the ICON-LAM hourly daytime rsds is similar to what is found in other studies. Those studies were evaluating daily mean rsds (daytime and nighttime); such that comparisons however are less rigorous and tend to result in smaller error metric values of ME or MAE, because for instance the 0 W m^{-2} nighttime rsds is usually correctly simulated. Additionally, ICON-LAM simulates rsds well under clear skies, while overestimating rsds under cloudy skies, although within the typical margin of error compared to other existing high-resolution products. Furthermore, ICON-LAM correctly simulates the background weather and typical climatological features, investigated through tas and pr fields.

In an ensuing step, this evaluation will be expanded by an evaluation of the same model runs for wind speeds at higher altitudes above the land surface, as the wind energy field is in a height range between 80 to 140 m (Jung & Schindler, 2021), with bigger hub heights in the future wind turbines underway (Martin et al., 2020). This leads to much fewer evaluation datasets (Drechsel et al., 2012).

Most importantly, the added value of using a km-scale meteorological input dataset as opposed to the conventionally used coarse-resolution reanalysis in REP estimates for wind and solar power will be investigated. We consider our methodology of a km-scale dynamical downscaling with a state-of-the-art atmospheric NWP model system a viable approach to complement existing datasets in the field of REP estimation. Aside from an immediate use of the dataset for other REP-related studies, the experiment design can also be applied in studies on the impact of climate change on REP estimates.

Chapter 4. Higher onshore wind energy potentials revealed by kilometre-scale atmospheric modelling

*adapted from: Chen, S., Goergen, K., Hendricks Franssen, H. J., Winkler, C., Poll, S., Houssoukri Zounogo Wahabou, Y., ... & Heinrichs, H. (2024). Higher onshore wind energy potentials revealed by kilometer‐scale atmospheric modeling. Geophysical Research Letters, 51(19), e2024GL110122. https://doi.org/10.1029/2024GL110122

4.1 Introduction

Wind energy is one of the most promising renewable energy technologies for achieving carbon neutrality (Lei et al., 2023; Zhao & You, 2020). Its globally installed total capacity has steadily increased and reached about 900 GW at the end of 2022, this is 27% of the global renewable energy capacity; 93% of which is from onshore wind power farms (International Renewable Energy Agency, 2023). To make the most efficient use of onshore wind energy within the energy system transition, its energy potential needs to be known with sufficient spatial and temporal resolution (McKenna et al., 2022), including wind feed-in time series to optimize the energy mix.

Africa is the world's least-electrified continent, even facing an increasing lack of access to electricity as of 2022 (International Energy Agency, 2023). Given half of the population in southern Africa is without electricity supply (International Energy Agency, 2023), along with the abundant untapped technical potential for onshore wind energy of approximately 14 TWpeak (Ishmam et al., 2024; Winkler et al., 2025), reliable estimates of southern Africa's onshore wind energy potential (WEP) are important for the region.

Assessments of onshore WEP with an hourly resolution are state-of-the-art for energy system studies (Caglayan, Ryberg, et al., 2019; McKenna et al., 2022; Ryberg et al., 2019). While spatially highly fluctuating wind speeds are difficult to capture, especially over complex terrain (Qiao et al., 2022), reanalysis products, typically utilized for assessing WEP in energy system studies, have relatively coarse spatial resolutions. For example, ERA5 (Hersbach et al., 2020), a state-of-the-art global reanalysis, has a spatial resolution of 31 km. Regional reanalyses over Europe with higher spatial resolutions such as COSMO-REA6 (Bollmeyer et al., 2015) at 6 km and CERRA (Schimanke et al., 2021) at 5.5 km, have been shown to outperform global reanalyses especially for winds at marginal frequency distributions, near the ground, and over complex terrain (Frank et al., 2020; Jourdier, 2020; Jourdier et al., 2023). In general, the added value of kilometre-scale (km-scale), convection-permitting, atmospheric (regional) climate simulations, e.g., in the resolution of surface heterogeneities, the reproduction of atmospheric processes, or land-atmosphere interactions, has been documented in several overviews (Lucas‐Picher et al., 2021; Prein et al., 2015; Schär et al., 2020). However, to our knowledge, no regional atmospheric reanalysis is available for any region over the African continent.

In this work, we first evaluate simulated wind speeds against measured wind speeds from

weather masts at a height of 60 m, which is the highest available wind speed observations over southern Africa. We use three simulation data products: (i) A dedicated atmospheric simulation with the ICON model (Zängl et al., 2015) (Zängl et al., 2015) in hindcast mode at a convection-permitting high-resolution of 3.3 km (ICON-LAM) over southern Africa, as documented in a validation study (Chen, Poll, et al., 2024), (ii) the ERA5 (Hersbach et al., 2020) atmospheric reanalysis with a resolution of 31 km as a commonly used dataset in renewable energy assessments (ERA5_ori), and (iii) the ERA5's wind speed statistical downscaling using the Global Wind Atlas (GWA) version 3 (GWA, 2019) (ERA5_GWA). Secondly, the WEP is computed with the renewable energy simulation model RESKit (GitHub repository, 2019) from ICON-LAM, ERA5_ori, and ERA5_GWA wind speed products to investigate the benefit of the km-scale spatial resolution. The WEP is first calculated over existing weather mast locations. In a further step, 1.8 million eligible wind turbine placements over southern Africa (Franzmann et al., 2023; Ishmam et al., 2024; Winkler et al., 2025) are exploited to simulate the hourly power time series of the WEP. The differences between the estimated wind turbine power time series from ICON-LAM, ERA5_ori, and ERA5_GWA and the corresponding annual average of WEP for each of 1.8 million eligible wind turbines over southern Africa are further inspected to derive the impact of higher resolution input data for WEP assessments on estimated wind energy yields over our pilot study region over southern Africa.

4.2 Data and methods

4.2.1 Wind Speed Data and Height Scaling

To evaluate the simulated wind speeds, in-situ observations at 60 m height from 18 weather masts over South Africa are used (Wind Atlas for South Africa, 2010). To our knowledge, these are the only publicly available observations for southern Africa that measure wind speeds relatively close to real-world wind turbine hub heights. The details of the observation data quality are documented in Appendix B.1.1.

ERA5 reanalysis data from the European Centre for Medium-Range Weather Forecasts (ECMWF) (Hersbach et al., 2020) has an hourly temporal and 31 km spatial resolution, and it provides wind speed for 13 vertical model levels up to 500 m above ground level (AGL) (ERA5_ori). In addition, ERA5 also provides the interpolated eastward and northward components of 100 m AGL wind speed. The ERA5 100 m wind speeds have been widely used in WEP studies (Görmüş et al., 2022; Gruber et al., 2022; Jung & Schindler, 2022) as they are often considered as the most representative for hub heights of modern wind turbines (von Krauland et al., 2021).

The convection-permitting atmospheric model runs used here are done with a regional setup of the ICON atmospheric model (Zängl et al., 2015) (ICON-LAM) for the years 2017 to 2019. This dynamically downscaled one-way single nest ICON run over southern Africa has a convection-permitting high spatial resolution of 3.3 km; the initial and lateral boundary conditions are from the German Weather Service (DWD) initialized analysis based on global ICON weather forecasts; the atmosphere is reinitialized every six days. In an extensive

validation study (Chen, Poll, et al., 2024), they provide a detailed overview of the setup and configuration, based on the operational DWD numerical weather forecast simulations. ICON-LAM has 11 vertical model levels below 500 m AGL. The 15-minute instantaneous wind speed outputs are averaged to hourly resolution for comparison to the ERA5 and the weather mast measurements.

Simulated wind speeds for 60 m height from ERA5_ori and ICON-LAM at the weather mast locations are interpolated from the nearest model grid cells and the closest two model vertical levels above and below 60 m using the wind speed power law (Devis et al., 2014; Devis et al., 2018; Pryor et al., 2005), see Appendix B.1.2 for details.

In some renewable energy potential studies (Gruber et al., 2022; Murcia et al., 2022), the coarse spatial resolution of ERA5 is addressed by a combination with wind speeds from GWA through a statistical downscaling, where the ratio of the long-term mean 100 m wind speed of GWA and ERA5 is multiplied by the time series of ERA5 100 m wind speed to obtain a nominal spatial resolution of 250 m as in GWA version 3 (ERA5_GWA). GWA itself is also based on a dynamical downscaling (Davis et al., 2023). Studies (González-Aparicio et al., 2017; Ryberg et al., 2019) have applied this procedure also to the MERRA-2 reanalysis. For comparison with these previous studies, the same approach is also applied in our study to the ERA5 100 m wind speed. Hence, aside from ICON-LAM and ERA5_ori a third simulation-based dataset ERA5_GWA is used. ERA5_GWA 100 m wind speed is logarithmically extrapolated to the observed wind speed height of 60 m for evaluation.

4.2.2 Wind Power Calculation

Wind speed (m s^{-1}) is the key parameter for the wind power (kWh) calculation. Usually, the wind power density, half of the constant air density multiplied by the cube of the wind speed, is used as the typical measure of WEP (Pryor & Barthelmie, 2011) in the meteorological realm, e.g., (Lei et al., 2023). In this study, however, we conduct a more realistic WEP estimate by using the wind turbine-specific power curve (Ryberg et al., 2019), which relates the actual electrical power production generated by the wind turbine to the wind speed, and by calculating wind power for individual potential wind turbine placements that are eligible for wind energy, including a sufficient horizontal distance between the placements (Franzmann et al., 2023; Ishmam et al., 2024; Winkler et al., 2025).

The wind power calculations are done with the RESKit renewable energy simulation model (GitHub repository, 2019). RESKit calculates the wind power based on the 100 m wind speed while considering the effects of air temperature and pressure from the meteorological input data. The 100 m wind speed is logarithmically extrapolated to the hub height of the turbine and the generated wind power is found by identifying the corresponding wind speed on the power curve, which is determined by the wind turbine's specific power—the installed capacity per rotor swept area—as a synthetic power curve in RESKit (Ryberg et al., 2019). RESKit is also able to provide optimized wind turbine parameters capacity, rotor diameter, and hub height for a given turbine placement based on the long-term averaged 100 m wind speed from the GWA

version 3 dataset (GWA, 2019) to harvest wind energy resources with maximum efficiency (Ryberg et al., 2019).

To examine the impact on WEP estimates from ERA5_ori, ERA5_GWA, and ICON-LAM, we choose the technical parameters from the wind turbine NTK1500/60 (Nordtank, 1997) with 1.5 MW rated capacity, 60 m rotor diameter, and 60 m hub height (hereafter H60m) to match the height of the observed wind speeds. We then compute the wind power for these three different wind speed products over the 18 locations with weather masts for comparison.

The turbine H60m is actually a small turbine and wind turbines have developed rapidly in recent decades, such that smaller wind turbines are successively replaced by larger and more efficient turbines (Martin et al., 2020). In order to deliver up-to-date WEP estimates, the expected median onshore wind turbine size in 2035 of 5.5 MW capacity, 174 m rotor diameter, and 130 m hub height (hereafter H130m)—from a survey conducted by (Wiser et al., 2021) oriented to the world's leading experts in the wind energy industry—is additionally used as a baseline turbine with RESKit to find the optimal future turbine design (hereafter HOpt) for each wind turbine placement. A total of 1,829,467 eligible individual wind turbine placements have been identified over southern Africa (Franzmann et al., 2023; Ishmam et al., 2024; Winkler et al., 2025). The onshore WEP across entire southern Africa is then estimated using RESKit with the turbine HOpt over these 1.8 million eligible wind turbine placements, with approximately 99.4% of them using different turbine technologies, i.e., different values of capacity, rotor diameter, and hub height. For example, the spatial distribution of wind turbine hub heights used in HOpt is shown in Figure B.1. A similar HOpt determination is also conducted over 18 weather mast locations with detailed output parameters documented in Table B.1. Please note that whenever spatial plots are shown, values for each of the 1.8 million placements are plotted, providing eventually a continuous map.

4.2.3 Wind Speed Evaluation and Wind Power Comparison

The three data products are evaluated against observations by employing various statistical metrics. While the Mean Error (ME) indicates the systematic over- or under-estimation when comparing the simulation with the observation, the Mean Absolute Error (MAE) reveals the absolute biases between them. To assess the similarity in both wind speed magnitude and the variation in direction between simulations and observations over time, the Pearson Correlation Coefficient (R) is employed. Additionally, the Perkins Skill Score (PSS) (Perkins et al., 2007) is used to quantify the extent to which the simulation reproduces the observed frequency distribution of wind speed at a frequency distribution bin size of 1 m s^{-1}.

To compare the WEP derived from three wind speed products, the Capacity Factor (CF), as an indicator of WEP, is calculated for all eligible 1.8 million wind turbine placements. CF represents the ratio of actual power generation of a wind turbine to its nominal power generation capacity (Bolson et al., 2022).

$$Capacity\ Factor\ (CF) = \frac{generated\ power}{nominal\ power\ generation\ capacity} \quad (4.1)$$

4.3 Results

4.3.1 Comparison of Simulated 60 m Wind Speeds from ERA5 and ICON-LAM to Observations

Figure 4.1 shows the comparison of observed hourly wind speed at 60 m height and simulated wind speed by ICON-LAM, ERA5_ori, and ERA5_GWA. From the ME subplot (Figure 4.1a), it is evident that ERA5_ori underestimates the 60 m wind speeds by up to 4 m s^{-1} with an average underestimation of 1.8 m s^{-1} (-27%). ERA5_GWA has only a slight underestimation of 0.32 m s^{-1} (-4.7%). In comparison, ICON-LAM 60 m wind speeds show an even smaller underestimation of only 0.12 m s^{-1} (-1.8%). The average MAE (Figure 4.1b) across all the weather mast sites is roughly 2.2 m s^{-1} (33%), 1.6 m s^{-1} (24%), and 1.7 m s^{-1} (25%) for ERA5_ori, ERA5_GWA, and ICON-LAM, respectively. The percentages in parentheses are percentage errors of each metric when divided by the average 60 m wind speed of 6.68 m s^{-1} over all weather masts. All datasets reproduce the observed 60 m wind speed variations over time similarly well (Figure 4.1c), with an averaged R over all the masts of 0.78 and 0.79 for ERA5_ori and ERA5_GWA, and 0.75 for ICON-LAM. ICON-LAM shows closer agreement with observations than the ERA5 variants in simulating the frequency distributions of 60 m wind speeds (see Figure 4.1d) with an average PSS for all weather mast locations of 0.93 for ICON-LAM, 0.74 for ERA5_ori, and 0.84 for ERA5_GWA, respectively.

The simulated 60 m wind speeds at the different wind speed ranges of the baseline wind turbine's power curve (see Figure B.2) are compared separately with the observations in Appendix B.3. The result of the full range wind speed comparison (Figure 4.1) is confirmed by the additional comparisons of the wind turbine's usable (from 3 to 25 m s^{-1}, see Figure B.3) and ramping phase (from 3 to 11 m s^{-1}, see Figure B.4) wind speed ranges of the power curve. However, ICON-LAM outperforms the other two by a big margin in simulating the rated wind speed (Figure B.5) from 11 to 25 m s^{-1} in terms of ME, MAE, and PSS, and with quite similar R among the three data sets.

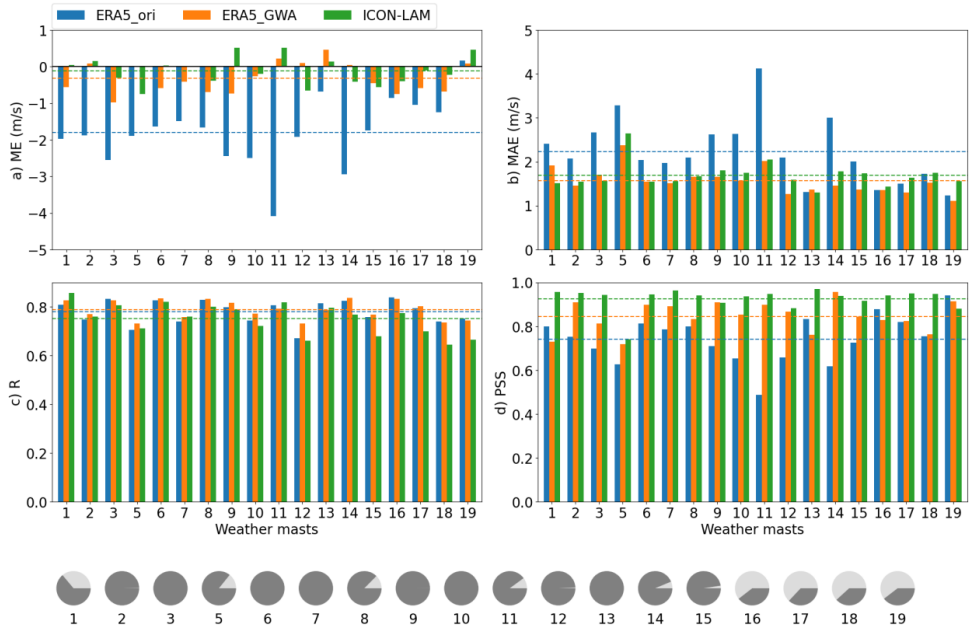

Figure 4.1 Comparison of simulated 60 m wind speeds from ERA5 (EAR5_ori and ERA5_GWA) and ICON-LAM against weather mast observations: a) ME, b) MAE, c) R, and d) PSS. Dashed lines correspond to the average of the respective metric per dataset. The pie charts indicate the temporal data coverage of 60 m observed wind speeds for each weather mast; dark grey indicates the percentage of available data from 2017 to 2019. The masts are labelled according to their identifier in the Wind Atlas of South Africa (2010); weather mast "WM04" has no data from 2017 to 2019 and is therefore not included in the comparison. For the mast locations see Figure 4.2b.

4.3.2 Contrasts in Wind Power Generation Driven from ERA5 and ICON-LAM Over Weather Mast Locations

The estimated wind power for the 18 weather mast locations is expressed through CF and shown in Figure 4.2. CFs are calculated from the ERA5_ori, ERA5_GWA, and ICON-LAM wind speed products and the H60m and HOpt wind turbine technologies (see Table B.1 for detailed wind turbine parameters). Converting 60 m wind speed into wind power by using the H60m turbine, the averaged CFs for all the masts are 0.11, 0.16, and 0.21 for ERA5_ori, ERA5_GWA, and ICON-LAM, respectively. When considering the optimal turbine HOpt for each of the 18 weather mast locations, CF shows a similar behaviour, albeit with a clear positive offset; the corresponding averaged CFs are 0.28, 0.35, and 0.44 for ERA5_ori, ERA5_GWA, and ICON-LAM. Significant increases in average CFs—perceived as the power generation efficiency—are found from the H60m turbine as typically manufactured in 1997 to the HOpt turbine expected for 2035. The average CF difference from different wind speed products is consistent with the evaluation of simulated CFs against power measurements for existing wind

farms in South Africa (see B.4.2 for details) using the real-world installed turbine parameters; the corresponding averaged CFs are 0.25, 0.30, and 0.38, whilst the observed averaged CF is 0.37.

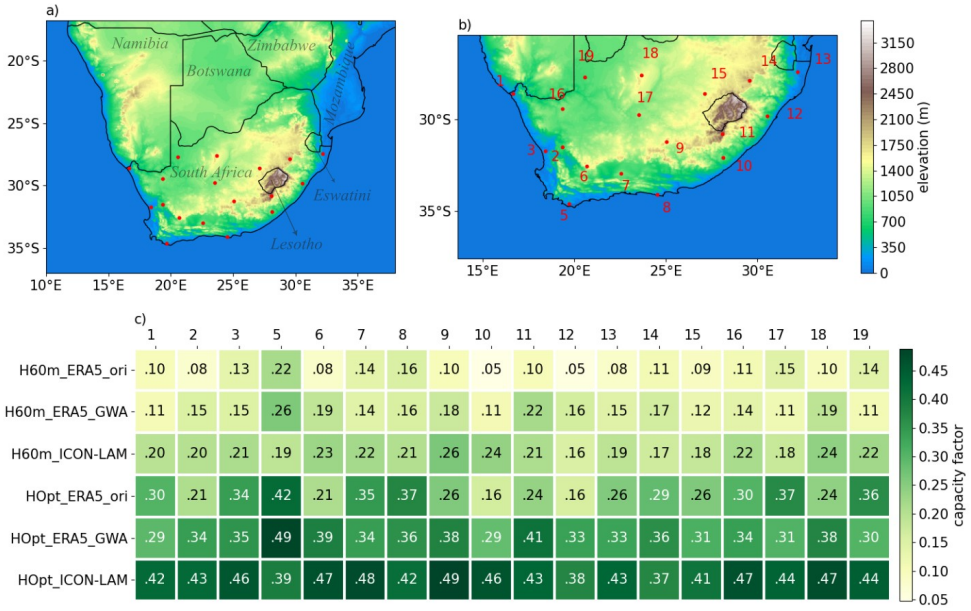

Figure 4.2 a) Locations of the weather masts (red dots) with topography over the entire study area and ICON-LAM model domain. b) As in a), but zoomed into the area where the masts (with index) are located. c) Averaged CFs from 2017 to 2019 over weather mast locations estimated from ERA5_ori, ERA5_GWA, and ICON-LAM under two wind turbine technologies of H60m and HOpt.

4.3.3 Spatially Distributed Wind Energy Potential

Examining the CF time series differences derived from ERA5_ori, ERA5_GWA, and ICON-LAM over all the eligible placements (see B.5.1 for details) shows that most placements have larger CFs derived from ICON-LAM than from ERA5_ori and ERA5_GWA, with few exceptions for placements over flat terrain from ERA5_ori and over steep terrain from ERA5_GWA. The spatial patterns of the correlation coefficient between ICON-LAM and ERA5_ori on the one hand and between ICON-LAM and ERA5_GWA on the other hand are similar, and larger correlation coefficients occur in the southwest and northeast of the study area.

The annual average CF is further inspected in Figure 4.3, comparing the 2017 to 2019 averages of the CF derived from ERA5_ori, ERA5_GWA, and ICON-LAM. The interannual variation of CF within one dataset is relatively small (see the annual maps in Figures B.11 and B.12), albeit the spatial variation of the CF is very pronounced, within each dataset and among

ERA5_ori, ERA5_GWA and ICON-LAM.

ICON-LAM reveals more spatial details (Figure 4.3a) in CFs compared to ERA5_ori. The added value of the ICON-LAM runs is evident, as the surface topography with 3.3 km spatial resolution is much better represented than in ERA5 with 31 km spatial resolution. In total, 58.6% and 9.2% of the ICON-LAM placements show larger CFs of more than 30% and 100%, respectively, compared to ERA5_ori (Figure 4.3d), indicating a higher WEP from ICON-LAM. In addition, only 5% of all the placements show smaller CFs from ICON-LAM compared to ERA5_ori, mostly located in the inland plateau and the coastal plain of Mozambique.

Local details can barely be seen in the ERA5_ori-based CFs (Figure 4.3c). A low CF (< 0.2) belt is found in the strong-relief (Figure 4.2a and 4.2b) southern and eastern part of South Africa, where significant differences in terrain heterogeneity between the high and coarse resolution data exist, that impact the wind speeds. This results in larger CFs from ICON-LAM compared to ERA5_ori, even exceeding 100% for some placements in this region (Figure 4.3d).

By combining GWA information into ERA5_ori, much more heterogeneous CFs are found from ERA5_GWA (Figure 4.3e) compared to ERA5_ori (Figure 4.3c). The larger CFs of ICON-LAM compared to ERA5_ori in the topographically complex belt disappear when comparing ICON-LAM to ERA5_GWA, and slightly larger CFs are found by ERA5_GWA (Figure 4.3f). In fact, GWA version 3 has reported a tendency to overestimate mean wind speeds over steep terrains such as ridges and hilltops (Davis et al., 2023), which is consistent with the slightly larger CFs compared to ICON-LAM found from ERA5_GWA in this study over the extremely contrasting terrain in and/or around Lesotho. Spatially distributed CFs from ICON-LAM are generally closer to ERA5_GWA than ERA5_ori, except for placements over the northeastern plateau of the study area. Overall, 81.8% of the placements from ICON-LAM show more than 30% and 11.4% more than 100% larger CFs, respectively, compared to ERA5_GWA, and 3% of the placements indicate smaller CFs from ICON-LAM compared to ERA5_GWA (Figure 4.3f).

The comparison of spatially distributed average CFs derived from different wind speed products is summarized in the CF frequency distribution analysis (Figure 4.3b). ERA5_ori and ERA5_GWA perform quite similarly for CFs below 0.2 and reach the CF peak near CF 0.25, but ERA5_GWA shows more CFs occurrences in the CF range [0.2, 0.3] and ERA5_ori in the range [0.3, 0.475]. ICON-LAM has a similar shape of the frequency distribution compared to ERA5_GWA but with a CF peak near 0.4 instead of 0.25. These results are consistent with the evaluation of the simulated power over existing wind farms in South Africa (see B.4.2) that ERA5 variants tend to deliver smaller CFs and miss the larger ones. Splitting placements by country, as shown in B.6, also indicates similar patterns.

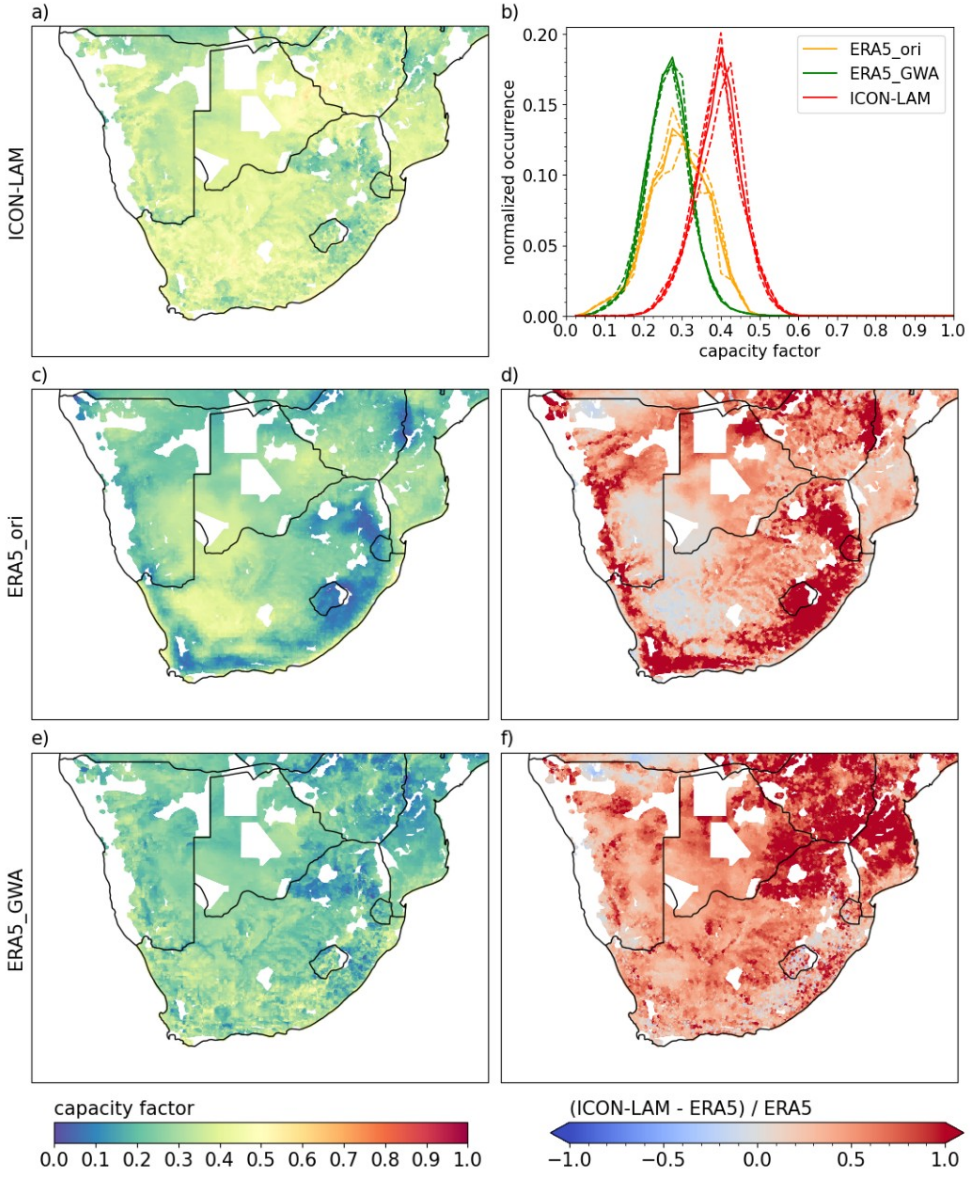

Figure 4.3 Averaged CF of 2017 to 2019 for each eligible wind turbine placement across southern Africa derived from a) ICON-LAM, c) ERA5_ori, and e) ERA5_GWA and their relative differences in CF of d) (ICON-LAM minus ERA5_ori) / ERA5_ori and f) (ICON-LAM minus ERA5_GWA) / ERA5_GWA. The frequency distributions of spatially distributed 3-year (solid lines) and annually (dashed lines) averaged CFs across all eligible placements derived from three wind speed products are shown in b) with a CF bin size of 0.025.

4.4 Discussion and conclusions

In this chapter we assessed the quality of wind speed simulation products against in-situ observations and compared WEP over southern Africa.

ERA5_ori underestimates the 60 m wind speed by 27%. Other wind speed evaluations at wind energy-related heights in Europe (Jourdier, 2020; Olsen et al., 2019), America and Iran (Gualtieri, 2021) confirm our finding and this indicates ERA5_ori limits in providing a reliable assessment of WEP. ERA5_GWA, based on statistical downscaling of ERA5_ori, performs well compared to ICON-LAM in terms of ME, MAE, and R. However, ICON-LAM reproduces the observed wind speed frequency distribution with PSS of 0.93, and ERA5_GWA 0.84. Wind speed evaluation at the cut-in and cut-out range against measurements shows similar results (see Figure B.3) to the full range, however, ICON-LAM clearly outperforms the two ERA5 variants in simulating the wind speed in the rated wind speed range of the wind turbine's power curve (Figure B.5), which is the most productive wind speed range for the wind energy.

The evaluation of simulated wind power for the existing 25 wind farms in three provinces in South Africa for the year 2019 shows ICON-LAM generally reproduces the observed CFs better than ERA5_GWA and ERA5_ori (see B.4.2). The WEP, using CF as an indicator, is further estimated over 1.8 million eligible wind turbine placements across southern Africa. Spatially, ICON-LAM has larger CFs over mountainous regions, and it agrees better with ERA5_GWA than with ERA5_ori over these regions. ERA5_ori tends to provide slightly larger CFs over part flat terrain, which is missing in the other products. ICON-LAM (with larger CFs) differs most with ERA5_GWA for the northeastern part of the southern African Plateau. The respective spatial mean CFs derived from ERA5_ori, ERA5_GWA, and ICON-LAM are 0.28 (annual power 12.39 GWh/turbine, see Figure B.15), 0.25 (11.37 GWh/turbine), and 0.38 (17.02 GWh/turbine). These CFs are corroborated by comparing wind speeds from the different products used to calculate CFs over all the eligible wind turbine placements (Figure B.14).

More than half of the eligible placements show a larger CF of more than 30% when comparing ICON-LAM to both ERA5 variants, and this translates into an increased average annual power of 6 GWh/turbine according to ICON-LAM; it is compelling when compared to South Africa's electricity consumption of 203 TWh in 2022. This calls for more suitable (high resolution and physically consistent) datasets for future WEP studies for southern Africa and beyond. It is an important finding for the optimization of the energy transition towards net zero carbon emission, i.e., it hints to the possibility that the renewable WEP may for large areas be widely underestimated.

Note that the different performances of the wind speed products, evaluated against 18 masts, may not be directly transferable to the comparison of the corresponding derived CFs across 1.8 million eligible wind turbine placements due to: 1) The non-linear conversion from wind speed to wind power. 2) Different scale of 18 wind speed evaluation masts versus 1.8 million eligible placements-based CFs in southern Africa, with very pronounced heterogeneity of surface topography and calculated wind power. 3) The wind atlas workflow related with ERA5_GWA

is possibly tuned over the weather masts as the evaluation is applied there iteratively (Davis et al., 2023; Mortensen, 2021; Mortensen et al., 2017), which is not the case for ICON-LAM.

A particular strength of the study is the higher level of applicability of our results as we employ a state-of-the-art WEP calculation workflow adapted from the energy assessment realm (Ryberg et al., 2019), which considers land eligibility and variable turbine technology to maximize generation for each eligible turbine placement, and also uses the turbine-specific power curve for wind to power conversion. This more realistic calculation of WEP is usually missing in similar other works (Lei et al., 2023; Lu et al., 2009; Reyers et al., 2016), which often consider only meteorological variables.

Meanwhile, WEP derived from high-resolution, convection-permitting, physically consistent wind speed products, especially over Africa, is usually missing in the energy realm (Fasihi & Breyer, 2020; McKenna et al., 2022). The spatial patterns of CFs derived from coarse wind speed products in studies (Fasihi & Breyer, 2020; Lu et al., 2009) over southern Africa are similar to our ERA5_ori-based CFs, highlighting the importance of using the high-resolution wind speed product for WEP estimates. Higher fidelity of wind speed simulation and wind power calculation are found with our high-resolution physically consistent wind speed product, revealing higher wind power (see B.7) and helping to attract investment in the local onshore wind energy industry.

Onshore wind energy is expected to play a major role in the energy transition and underestimated onshore WEP estimates would ultimately affect its efficient use. However, a direct transferability of our findings to other regions may not be feasible due to the particular ocean-land distribution and the complex topography with complex circulation patterns in the analysed region (Chen, Poll, et al., 2024).

Given the substantially larger estimated WEP revealed by ICON-LAM, our next step is to investigate the impact these increased WEPs have on the design of the renewable energy system over southern Africa as a contribution to the energy security discussion in the region.

Chapter 5. High-resolution atmospheric modelling reveals lower costs for renewable energy systems in southern Africa

*adapted from: Chen, S., Goergen, K., Hendricks Franssen, H.-J., Franzman, D., Winkler, C., Ishmam, S., Poll, S., Linssen, J., Vereecken, H., & Heinrichs, H. (2025). High-resolution atmospheric modelling reveals lower costs for renewable energy systems in southern Africa. In preparation for submission to Energy.

5.1 Introduction

Africa remains the least electrified continent in the world (International Energy Agency, 2022). Renewable energy presents a crucial opportunity to bridge this electricity supply gap, given the continent's vast, untapped renewable energy resources (Ishmam et al., 2024; Winkler et al., 2025). The feasibility of distributed renewable energy systems further strengthens this case, as they offer a cost-effective and technically viable alternative to centralized fossil-fuelled power plants, particularly in reaching un-electrified rural areas (Nyarko et al., 2023). The ongoing global transition to carbon-neutral energy systems in response to global climate change (Oteng et al., 2024) further underscores the urgency of a renewable energy-driven transformation in Africa. Expanding renewable energy within African energy systems is therefore a decision that yields multiple benefits.

Wind and solar are the most widely accessible renewable energy sources for electricity generation compared to others such as biomass (biofuels and wastes), water (hydro and tidal), or geothermal heat (López Prol & Schill, 2021). However, both are variable renewable energy (VRE) resources, as they are highly dependent on weather conditions (Wang et al., 2023). Energy systems in general consist of interconnected networks of components involved in the production, conversion, delivery, and use of energy across various sectors, including power generation, heating/cooling, transportation, and industry (Mancarella, 2014; Martínez-Gordón et al., 2021). Such energy systems are complex, as they consist of heterogeneous, spatio-temporally interconnected multi-scalar and multi-dimensional system components (Bale et al., 2015). Incorporating power generated by VRE further complicates the energy systems design, implementation, and operation. Analysing complex energy systems with respect to VRE at a sufficient, decision-relevant level of detail is challenging.

How to deal with the internal fluctuation of power supply from VRE in an energy system has therefore been a long-standing and widespread discussion (Cochran et al., 2012; Deguenon et al., 2023; Sinsel et al., 2020). Proposed viable solutions are, e.g., the self-complementarity of VRE, or the inclusion of backup systems, such as a storage system using battery or "power-to-x" (Franzmann et al., 2023; Ishmam et al., 2024; Müller et al., 2025; Palys & Daoutidis, 2022; Winkler et al., 2025), as well as dispatchable power systems like fossil-fired power plants and hydropower plants. To build reliable energy systems, the key lies in successfully identifying the self-complementarity of VRE sources, specifically, how their total power generation varies within the energy systems. As part of the VRE complementarity topic, the geophysical constraints of the reliability of solar and wind energy in terms of their hybridization, i.e. how both sources may complement each other, have been studied globally (Tong et al., 2021) or

locally like in the United States (Shaner et al., 2018). The identification of solar and wind energy "droughts" under the influence of different weather conditions and climate modes has been investigated for Australia (Richardson et al., 2023). The complementarity of wind and solar energy has been for example analysed for historical periods based on MERRA-2 reanalysis (Ren et al., 2019) and dynamical downscaling simulations with regional climate models (D'Isidoro et al., 2020). For the investigation of future periods of wind and solar energy complementarity, simulations from the sixth phase of the Coupled Model Intercomparison Project (CMIP6) have been used by Costoya et al. (Costoya et al., 2023). In this study, the self-complementarity of VRE is defined as the hybridization of solar and wind power generation within a given region, emphasizing its role in optimizing energy balance at a local scale. For a comprehensive review of complementarity analysis of VRE, readers are referred to Jurasz et al. (Jurasz et al., 2020), where different types of complementarity – temporal, spatial, and spatiotemporal – between renewable energy sources are introduced, along with metrics for assessing complementarity.

To build an affordable, reliable, and sustainable energy system in Africa, in accordance with the United Nations Sustainable Development Goals (SDG) goal seven, the spatial and temporal variability of VRE potential and the self-complementarity of VRE feed-in power time series need to be accurately resolved to optimize the energy system design. This energy system optimization implies the necessity of accurate meteorological data from which reliable VRE information can be derived. However, existing meteorological data sets over Africa used for this purpose are often characterized by a coarse spatial resolution or data gaps (Chen, Goergen, et al., 2024; Chen, Poll, et al., 2024; Michael R Davidson & Dev Millstein, 2022; McKenna et al., 2022).

This study therefore aims to examine the impacts of using different meteorological data products at different spatial resolutions on the energy systems design. The state-of-the-art global reanalysis ERA5 (referred to as ERA5_ori) (Hersbach et al., 2020), its statistical downscaling variants ERA5_GWA (using the Global Wind Atlas (GWA, 2019)) and ERA5_GSA (using the Global Solar Atlas (GSA, 2019)), collectively referred to as ERA5_adpt, and a dedicated high-resolution dynamically downscaled product based on ICON simulations in limited area mode (ICON-LAM) (Chen, Poll, et al., 2024) are examined. A previous study already indicated higher onshore wind energy potentials using high-resolution meteorological data from ICON-LAM simulations compared to ERA5_ori and ERA5_GWA (Chen, Goergen, et al., 2024). Based on these results, this study explores the data sets' impact on energy systems design. Southern Africa is chosen as the focus area due to the availability of the high-resolution ICON-LAM simulations. The region may serve as a pilot area for the entire African continent.

The level of detail that model-based energy systems planning can incorporate is not only dependent on the quality of the VRE information, which is constrained by meteorological data sets, but also on computational capacity, computational methods for optimisation, and energy system-related data availability (Martínez-Gordón et al., 2021). In large-scale energy systems models, typically at the national level, it is usual to use clustered or aggregated spatial data due

to the high computational cost (Martínez-Gordón et al., 2021). The spatial granularity of energy systems, often referred to as energy system nodes, is predefined, with calculations performed at the level of these nodes. The internal structure of the components within these nodes is typically disregarded. Likewise, in this study, we define administrative provinces as the energy system nodes and the energy system modelling is performed for each such province in southern Africa.

This study starts the analysis by comparing the wind and solar potential maps derived from ICON-LAM and ERA5 data. The motivation is to illustrate the maximum possible amount of VRE potential in southern Africa. We then move to the complementarity analysis of solar and wind energy over southern Africa by incorporating the representative future electricity demand time series projected for the year 2050 for southern Africa. A cost-optimized renewable energy system is designed for each province in southern Africa, with power generation from VRE and power storage from batteries considered to meet the projected regional electricity demand. The underlying VRE complementarity designed in this cost-optimized energy system is able to address both reliable electricity supply and minimum overall costs. To evaluate the direct impact on local energy systems, it is assumed that power transmission from generation to consumers is lossless within a region and that there is no power exchange between regions, following the works in Ishmam et al. (Ishmam et al., 2024) and Winkler et al. (Winkler et al., 2025). The cost and design of the energy system is compared based on the wind and solar VRE from different meteorological data sets. Finally, the daily time series of the renewable energy systems in terms of meeting the electricity demand shares of wind energy, solar energy, and battery (dis)charge are further investigated and compared.

5.2 Materials and methods

5.2.1 Meteorological data sets

ERA5 (Hersbach et al., 2020) is a state-of-the-art global reanalysis product (ERA5_ori). With a temporal resolution of 1 hour and a spatial resolution of 31 km, it has been widely used in Renewable Energy Potential (REP) assessments (Bloomfield et al., 2020; Ruiz et al., 2021; Sakuru & Ramana, 2023). The new ERA6 reanalysis is expected to replace ERA5 in 2027, with grid space reduced to half (close to 15 km) that of ERA5 (European Centre for Medium-Range Weather Forecasts (ECMWF), 2024). The Global Wind Atlas (GWA, 2019) and Global Solar Atlas (GSA, 2019), both with a nominal spatial resolution of 250 m and long-term mean temporal averages are also frequently used information for REP analysis (Gruber et al., 2022; Neupane et al., 2022; Ryberg et al., 2019). These global atlases (Wind: GWA, Solar: GSA) are integrated with a statistical downscaling approach (Peña-Sánchez et al., 2025; Ryberg, 2020; Ryberg et al., 2019) to overcome the coarse spatial resolution in ERA5. The long-term mean ratios of the global atlases to ERA5_ori, i.e., GWA/ERA5_ori and GSA/ERA5_ori, are first calculated and then multiplied with the ERA5_ori time series to obtain ERA5_GWA and ERA5_GSA (collectively referred to as ERA5_adpt).

High-resolution, i.e., convection-permitting or, interchangeably, kilometre-scale,

meteorological data are scarce for Africa. Pan-African simulations are, e.g., by Stratton et al. (Stratton et al., 2018) and Kendon et al. (Kendon et al., 2019) at 4.5 km resolution. For our study a dedicated high-resolution dynamical downscaling atmospheric simulation experiment over southern Africa was performed by Chen et al. (Chen, Poll, et al., 2024) using the ICON model (Zängl et al., 2015) in Limited Area Mode (ICON-LAM) at a convection-permitting resolution of 3.3 km. The ICON-LAM simulation is driven by the global initialized analysis from the German Weather Service (DWD) and uses a numerical weather prediction configuration of DWD. Chen et al. (Chen, Poll, et al., 2024) gives a detailed overview on the experiment setup and configuration including an extensive evaluation of near-surface wind and solar irradiance, which demonstrates the suitability of the ICON-LAM 2017 to 2019 data for REP analysis. In Chen et al. (Chen, Goergen, et al., 2024), further evaluations show that ICON-LAM more accurately reproduces observed wind speed closer to the wind turbine height, as well as the derived wind power, when using a state-of-the-art renewable energy simulation model, compared to commonly used data sets.

The model domain of the ICON-LAM simulations defines the spatial focus of this study; it encompasses southern Africa below about 16 degrees south, i.e., countries Namibia, Botswana, South Africa, Lesotho, Eswatini are fully covered, and Zimbabwe and Mozambique are partially covered, and hence included in the study with a total of 65 provinces. This is referred to as southern Africa. The location and details of these countries and their provinces are shown in Figure C.1 and Table C.1.

5.2.2 The wind and solar power calculation and the REP estimation

The renewable energy simulation model RESKit (GitHub repository, 2019) is employed to calculate wind and solar power in this study. In the RESKit model wind workflow (Peña-Sánchez et al., 2025; Ryberg et al., 2019), the 100 m wind speed is logarithmically scaled to the wind turbine hub height, and the wind power generated by the wind turbine is then derived according to a synthetic power curve – wind power as a function of wind speed. In the RESKit solar workflow (Ryberg, 2020), the solar irradiance received on top of the solar photovoltaic (PV) panels is first determined, and then the solar power generated by the solar PV panels is calculated accordingly using the law of photoelectric conversion. Other system-level loss factors are also considered, such as drops in PV panel photoelectric conversion efficiency due to the unfavourable ambient air temperature, losses from the inverter when converting direct current (DC) to alternating current (AC), and losses from soiling on the solar PV panels.

Based on the land eligibility and placement identification analyses performed by Winkler et al. (Winkler et al., 2025), we calculate in total 1,829,467 wind turbines and 748,388 km^2 solar PV panels in southern Africa that are eligible for the installation of the onshore wind and open-field solar PV energy placements. Advanced wind turbines and solar PV panel modules, which are available from laboratory or manufacturer and are barely installed now but may be widely used in the future, are selected to be simulated with the RESKit model. Specifically, the baseline wind turbine with turbine parameters predicted for 2035 (Chen, Goergen, et al., 2024; Wiser et al., 2021) and the solar PV module with solar power conversion efficiency projected

for 2050 (Ryberg, 2020) are used, see Table 5.1 for details. Utilizing all the eligible placements for the installation of wind and solar farms with advanced wind and solar energy technologies, the onshore wind and open-field solar PV energy potentials are estimated using the RESKit model over southern Africa with the ERA5_ori, ERA5_adpt, and ICON-LAM datasets.

Table 5.1 Key parameters of anticipated advanced wind turbine and PV panel technologies. Note that all simulated wind turbines have deviating parameters from the baseline configuration that lead to a maximum wind resource harvesting efficiency.

Design	**Value**
Baseline wind turbine:	
Hub Height	130 m
Root Diameter	174 m
Capacity	5500 kW
Specific Power	231.3 W m^{-2}
Solar PV panel design:	
Solar PV module	WINAICO WSx-240P6 (Ryberg, 2020)
Conversion rate	Projected for 2050
Capacity	Proportionate to the available land area at 20 m^2/kWpeak

5.2.3 Spatially resolved electricity demand and time series for 2050

A basis for any energy system optimization is electricity demand data. The annual sub-national disaggregated electricity demand data for the study region of southern Africa is sourced from Ishmam (Ishmam, unpublished yet). The annual electricity demand projections are built upon the national energy demand projections from the Net Zero 2050 scenario provided by the Network for Greening the Financial System (NGFS) Scenario Framework (O Richters et al., 2022; Oliver Richters et al., 2022). These projections consider electricity demand from residential, commercial, agriculture, manufacturing, service, and transportation sectors. Geospatial proxies such as level of access to electricity, population density, CO2 emissions distribution, gross domestic product (GDP) distribution, etc., corresponding to these sectors are then utilized to disaggregate the annual national electricity demand to the administrative level 1 (GID-1), i.e., provinces.

Hourly load curve data was then obtained from Toktarova et al. (Toktarova et al., 2019) for each country and adjusted to the UTC time zone to match the time zone of the generation time series. It is important to note that the shapes of these load curves may change over time as

access to electricity improves, and as the industrial and service sectors of countries grow, along with advancements in energy efficiency. However, for the purposes of this study, the load profiles have been retained in their current form and then scaled to align with the projected annual disaggregated demand in 2050. For in-depth information regarding the demand disaggregation methodology, please refer to Ishmam (Ishmam, unpublished yet).

To illustrate the electricity demand, the spatially resolved hourly electricity demand time series for 2050 have been summed up over the entire southern Africa study domain as well as over individual countries in the study region (Figure 5.1). All time series utilized in this study are in UTC. The annual cycle for the whole region shows highest values during the austral winter (Figure 5.1a), the country of South Africa is projected to exhibit the highest electricity demand in southern Africa by 2050, estimated at 342 TWh year^{-1}, about 86% of the total annual electricity demand in the region. Due to scale, for better visibility, the electricity demand time series of remaining study area countries are also shown in Figure 5.1b with highest values during austral spring and summer when cooling demand is highest.

Hourly fluctuations in electricity demand for all of southern Africa, South Africa, and the Western Cape province, which is the economic hub of South Africa, are shown in Figure 5.2. The hourly electricity demand displays a discernible diurnal cycle, with a reduced nighttime demand from approximately 02:00 to 07:00. Expectedly, there is a contrast in energy demand between weekdays and weekends; also public holidays stand out. A slight seasonal cycle is visible with an increased electricity demand during Austral winter months and evenings.

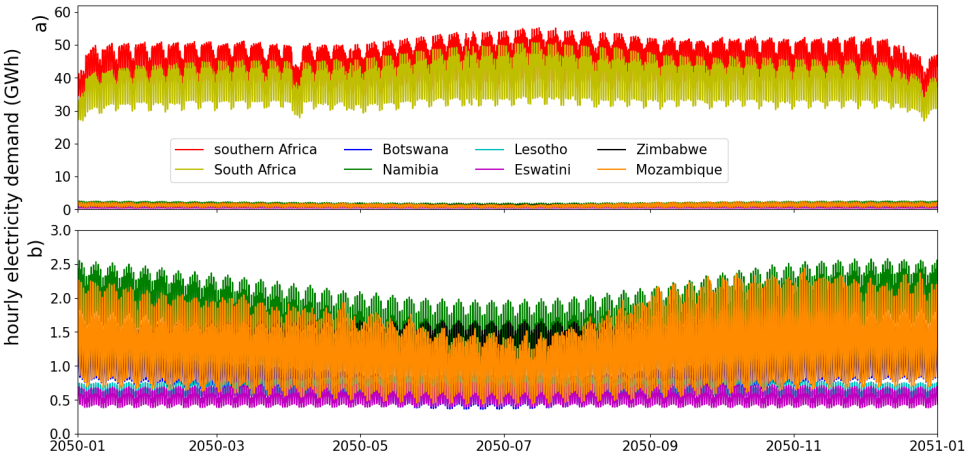

Figure 5.1 a) Projected total hourly electricity demand for 2050 for the entire southern Africa and those countries that are fully or partly covered by the ICON-LAM model domain, b) Same as in a) but zoomed in for countries with relatively lower electricity demand (Ishmam, unpublished yet).

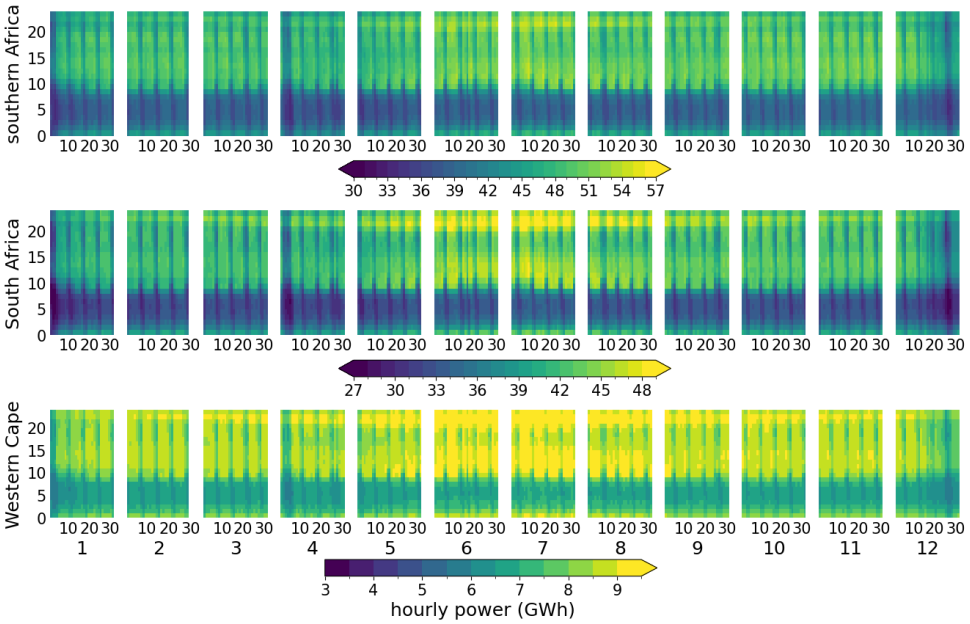

Figure 5.2 Hourly electricity demand time series for a) southern Africa, b) South Africa, and c) Western Cape as projected for 2050, with days of the year aggregated by month shown on the x-axis and hours of the day shown on the y-axis. Please note the different scales of the colour bars used in the figure.

5.2.4 Energy systems modelling

The power time series calculated by the RESKit (Peña-Sánchez et al., 2025; Ryberg, 2020; Ryberg et al., 2019) model for onshore wind energy and open-field solar PV energy serve as the basis for designing optimal energy systems. Our study focuses on a future 2050 electricity demand scenario as introduced in the previous section. To alleviate the computational burden in the energy system modelling, power time series of wind and solar energy are clustered over each energy system node (province). Following studies of Ryberg (Ryberg, 2020) and Franzmann et al. (Franzmann et al., 2023), segmented average clustering is used in this study: For each of the energy system nodes, the annual Full Load Hours (FLH) of every individual wind and solar placement within an analysis region is calculated and ordered from the highest to the lowest. They are further serially divided into N groups with similar FLH members. The power time series belonging to the same FLH group are averaged as the group representative. The class number used as N is set to 10 and 3 for wind and solar power time series clustering, respectively (Franzmann et al., 2023; Ryberg, 2020).

After getting the representative wind and solar power time series in each energy system node, the energy system framework ETHOS.FINE (GitHub repository, 2018; Klütz et al., 2025) and the solver gurobi (Gurobi Optimizer, 2018) is used to derive cost-optimized energy systems based on wind energy, solar energy, and battery storage for each province independently the

year of 2050. ETHOS.FINE minimizes the total annual costs while fulfilling the aforementioned provincial electricity demand based on the restricted maximum operation time series of renewable energy generation and on the ability to use curtailment. Due to the one node spatial resolution of the energy systems, power transmission losses from power plants to power consumers and power transmission between provinces are not considered to solely focus on the impact of different weather data products. The techno-economic parameters for calculating the total annual costs follow published works (Schöb et al., 2023; Schöb, 2024).

5.3 Results

5.3.1 ICON-LAM reveals higher onshore wind and similar open-field solar PV energy potential

Considerable differences are found between the maximum harvestable wind energy potentials estimated from the three data sets, as shown in Figure 5.3. These results are consistent with the findings of Chen et al. (Chen, Goergen, et al., 2024). In contrast, similar maximum harvestable solar energy potentials are shown in Figure 5.3 estimated from different data sets. They are actually almost identical, with few detectable differences, and very similar spatial distributions of solar irradiance for the data sets were shown in Chen et al. (Chen, Poll, et al., 2024). Comparable results for wind and solar energy potential, as indicated by the capacity factor – the ratio of actual power generated to the nominal generation capacity – are shown in Figure C.2. The solar and wind energy potential maps in Figure 5.3 and C.2 are produced based on a total 1.8 million eligible wind turbine placements and 0.74 million km^2 solar photovoltaic (PV) panel placements in southern Africa, respectively; values for each of these eligible placements are plotted, resulting in eventually a continuous map made up of many individual data points.

When comparing wind energy potentials derived from the three data sets, the coarse spatial resolution of ERA5_ori (31 km) becomes obvious, as details of wind energy potentials are hardly visible compared to the other two high spatial resolution data sets. However, the general patterns of contrasting high and low wind energy potentials are consistent between the data sets. In addition, ICON-LAM shows generally a higher wind energy potential over the entire study domain, while ERA5_GWA partially agrees with ICON-LAM. The respective spatial mean annual wind energy potential derived from ERA5_ori, ERA5_GWA, and ICON-LAM are 12.39 GWh/turbine, 11.37 GWh/turbine, and 17.02 GWh/turbine, with all 1.8 million eligible wind turbine placements considered.

Relatively large solar energy potentials within our study area exist in western South Africa and small parts of southern Namibia and Botswana (Figure 5.3b, 5.3d, and 5.3f). Locations along the south coast, eastern South Africa, Zimbabwe, and southern Mozambique are more unfavourable for solar energy installations. These locations correspond to the general atmospheric circulation patterns and the spatial patterns of precipitation in southern Africa (Figure S1 in Chen et al. (Chen, Poll, et al., 2024)), where clouds reduce the incoming solar radiation. The agreement in the spatial patterns of solar energy potentials derived from three data sets indicates that large-scale anticyclonic circulation patterns with high pressure clear-

sky conditions in the southwest of the domain are well represented by ERA5 and ICON-LAM.

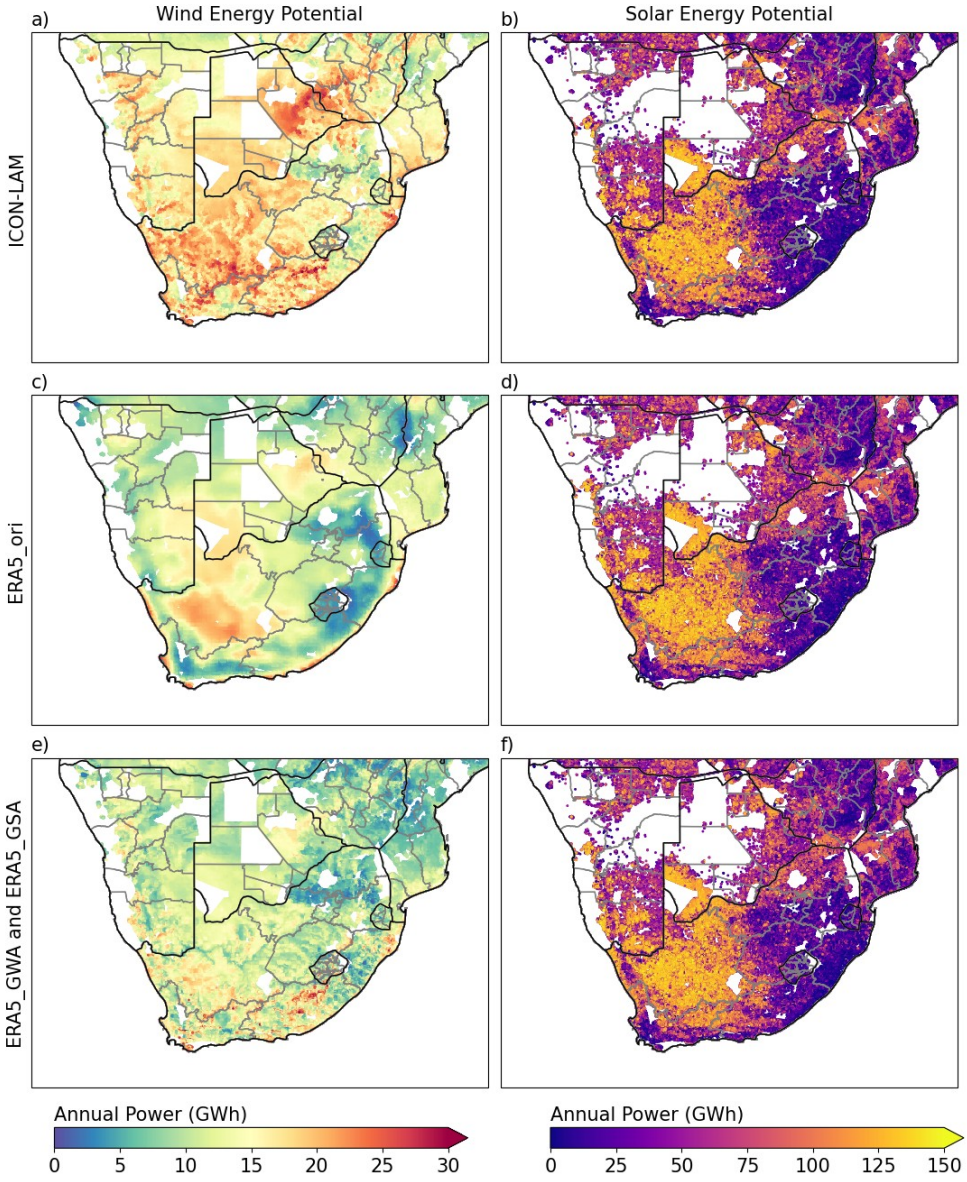

Figure 5.3 Comparison of estimated 2017-2019 average annual total power derived from ERA5_ori, ERA5_GWA/_GSA, and ICON-LAM simulated by the RESKit model wind and solar workflows across all eligible wind turbine and solar PV panel placements in southern Africa. Black lines are country borders and grey lines are provinces in southern Africa used as energy system nodes in the study. Names of the countries and provinces included in this study are shown in Figure C.1 and Table C.1. All maps are made up of multiple colour-coded site-

specific information, where each data point represents one wind turbine (total 1.8 million turbines) in Figure 5.3a, 5.3c, and 5.3e and one area of solar PV panels (total 0.74 million km^2 panels) in Figure 5.3b, 5.3d, and 5.3f, visually appearing as continuous data fields.

5.3.2 Lower annual costs in energy systems derived from ICON-LAM

In this study, the impact of three different meteorological data sets on the design of a renewable energy system over southern Africa is investigated. For this, an energy system considering wind energy, solar energy, and battery storage is designed in a cost-optimized way to meet 100% of the provincial 2050 electricity demand scenario in the 65 provinces over southern Africa. Three meteorological data sets for 2017 to 2019, are used to calculate the solar and wind power generation serving as input for the design of the cost-optimized energy system.

The total annual costs and the individual shares of different technologies (wind, solar, battery) of these cost-optimized energy systems in southern Africa, derived from different meteorological data sets, are shown in Figure 5.4. A scaled axis is additionally provided in Figure 5.4, since values of provinces from South Africa, due to its dominant electricity demand in all of southern Africa (see Figure 5.1), exceed the other countries as outliers. Out of the 65 provinces of our southern African study domain, 52 are considered capable of supporting a cost-optimized energy system that meets 100% of the regional 2050 scenario electricity demand by exploiting only renewable energy sources, i.e., the local wind and solar energy potentials per region, combined with battery installations. Table C.1 details the basic information for each province and indicates whether the cost-optimized energy system would be feasible to build or not. If the cost-optimized energy system cannot be built, the reasons are also documented, which are usually rooted in no eligible wind and solar placements at all or the optimization being proven infeasible or unbounded.

In general, cost-optimized energy systems designed based on the ICON-LAM data set have lower total annual costs compared to the other two data sets. The annual cost from ICON-LAM is 11% Euros/a less than from ERA5_adpt and 16% Euros/a less than from ERA5_ori, averaged over three years for all provinces. Cost-optimized energy systems derived from ICON-LAM have more wind energy capacity (comparable to ERA5_adpt and 9% more than ERA5_ori) and less solar energy capacity (13% less than ERA5_adpt and 23% less than ERA5_ori) compared to the two ERA5 variants. In addition, the required battery capacity of cost-optimized energy systems derived from ICON-LAM is less than the other two (9% less than ERA5_adpt and 17% less than ERA5_ori).

To investigate the reasons behind the lower annual costs of energy systems designed with ICON-LAM, a comprehensive analysis of annual operational characteristics of energy systems derived from different meteorological data sets is presented in Figure 5.5. The figure shows the full load hours (FLHs), levelized cost of electricity (LCOE), potential utilization rate, and curtailment rate for wind and solar technologies, and (dis)charge frequency and levelized cost of storage for battery technology, used in the energy systems. More FLHs of wind energy (Figure 5.5a), pointing to cheaper wind energy (Figure 5.5d), are available for use in the cost-

optimized energy systems designed with ICON-LAM, which is consistent with the findings of Chen et al. (Chen, Goergen, et al., 2024) that high-resolution kilometre-scale atmospheric modelling over southern Africa yields higher wind energy potentials. Meanwhile, lower required battery capacity (Figure 5.4) indicates that wind and solar power estimated from ICON-LAM better complement each other in meeting demand, as less backup (battery) capacity is needed, leading to lower system cost. This is further confirmed by the lowest average battery (dis)charge frequency (Figure 5.5c) of energy systems designed with ICON-LAM, as compared to with other ERA5 variants.

Generally, all three data sets agree with each other that a low potential utilization rate with a maximum around 7% from the total wind and solar potentials (Figure 5.5 g and h), combined with an appropriate amount of installed battery capacity, is sufficient to meet the electricity demand for all provinces in southern Africa. Furthermore, on average more than half of the solar energy is curtailed (Figure 5.5k), while a relatively higher proportion of wind energy is utilized (Figure 5.5j), due to the nature of their generation, where solar energy is almost only available during the day and wind energy does not have a relatively strong periodic signal. Little interannual variation is observed regarding the cost and design (Figure 5.4) and the operational characteristics (Figure 5.5) of cost-optimized energy systems based on data from 2017 to 2019.

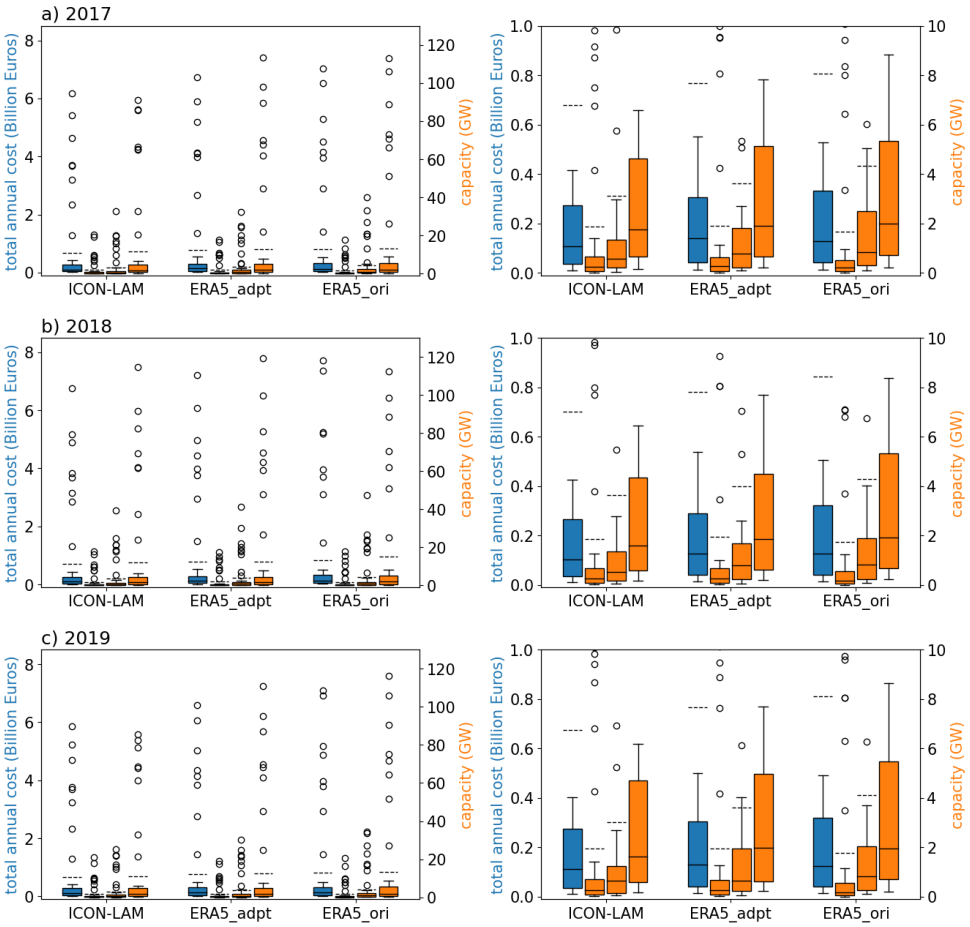

Figure 5.4 The energy system's total annual cost (Billion Euros) (blue bar) and the installed capacity (GW) of wind energy, solar energy, and battery (respective orange bars from left to right) for the cost-optimized regional energy system derived from different meteorological products for the three weather reference years a) 2017, b) 2018, and c) 2019. The first column contains all data points, while the second column zooms in on a range from 0 to 1 billion Euros and 0 to 10 GW capacity for a better presentation of the data. Each box extends from the first quartile (25th percentile) to the third quartile (75th percentile) of the data, with the median shown as a solid line inside. The whiskers are set at 1.5 times the interquartile range (IQR, the difference between the 75th and 25th percentiles) above the 75th percentile and below the 25th percentile, i.e., a box ends at ± 1.5*IQR. Data points are marked as outliers if they exceed the range defined by two whiskers. Dashed lines are the averages of all underlying data points for the corresponding box plots.

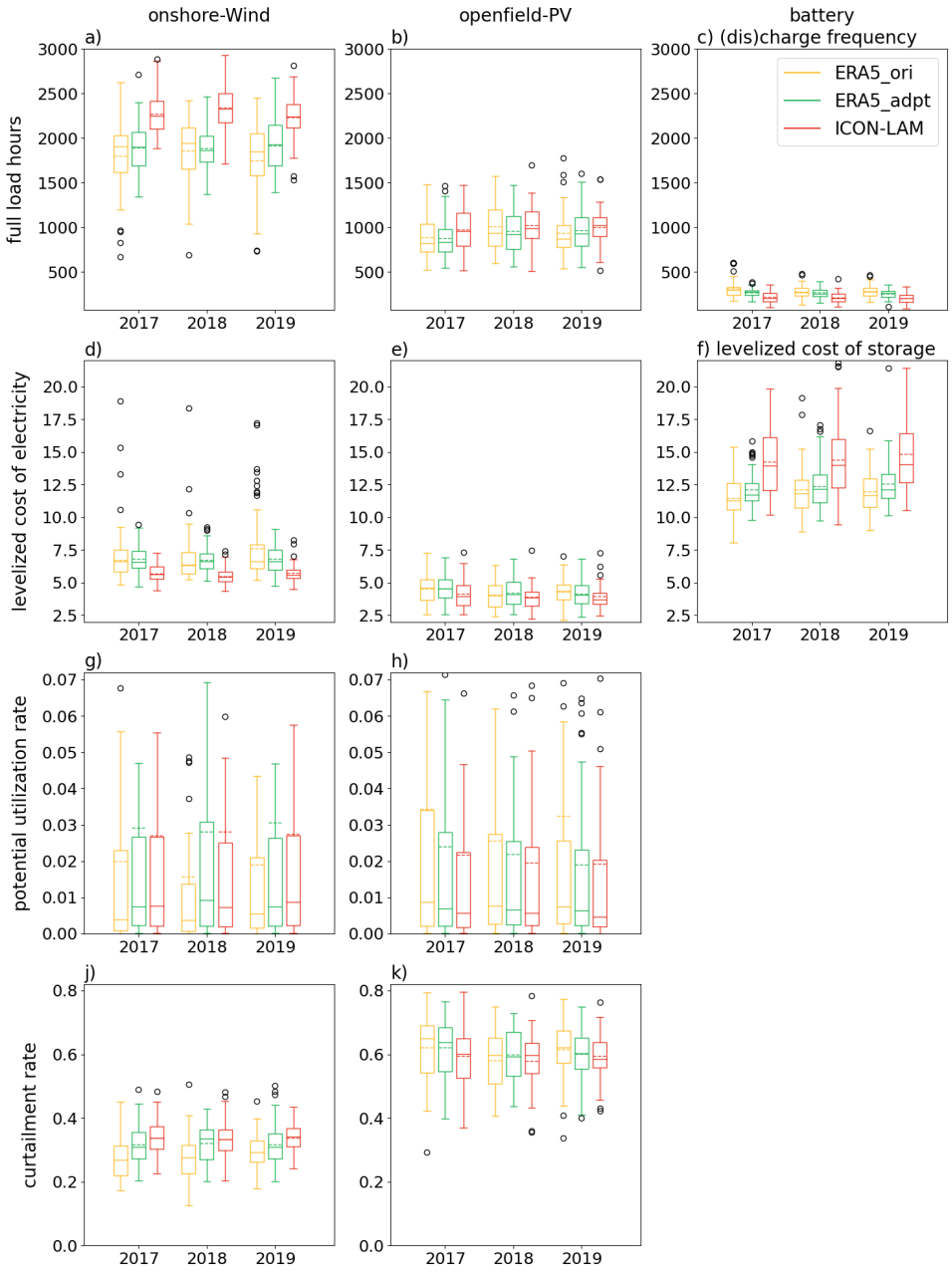

Figure 5.5 Annual operational characteristics, including full load hours (FLH, [hours]) (1st row), levelized cost of electricity (LCOE, cents per kilowatt-hour [€/kWh]) (2nd row), potential utilization rate (3rd row), and curtailment rate (4th row), for onshore wind (1st column), open-field PV (2nd column), and battery (3rd column) technologies used in cost-optimized energy systems designed from different meteorological datasets. Please note that terminology changes

when it comes to battery technology. The (dis)charge frequency is the total energy delivered by the battery divided by its capacity, and the levelized cost of storage is the total annual cost of the battery divided by the total energy delivered by the battery. A blank subplot indicates that the corresponding metric does not apply to that particular technology. For the description of the components of boxplots please refer to Figure 5.4.

5.3.3 Spatially varied costs and design of energy systems using different meteorological inputs

Figure 5.6 presents the cost-optimized energy system for each southern African province in 2017, derived from three meteorological data sets. Results for 2018 and 2019 are shown in Figure C.3 and C.4, which display in essence the same patterns. South African provinces, especially Western Cape and KwaZulu-Natal, have the highest total annual costs compared to other provinces in southern Africa, but ICON-LAM lowers the average costs by 11% and 16% compared to ERA5_adpt and ERA5_ori, respectively. The cost differences between energy systems derived from two ERA5 variants are relatively small, around 5%. Given the significantly lower electricity demand compared to South African provinces, other provinces in southern Africa beyond South Africa show insignificant variations in terms of energy system design and costs. The following analysis therefore focuses on South Africa.

The southern coastal provinces of South Africa exhibit greater wind energy capacity installation according to ICON-LAM (Figure 5.6b) compared to both ERA5 (Figure 5.6f and 5.6j), particularly Western Cape and KwaZulu-Natal, which are the biggest electricity demand provinces and have higher wind energy potential from ICON-LAM (Figure 5.3a) compared to ERA5 variants (Figure 5.3c and 5.3e). Meanwhile, the northern four provinces of South Africa demonstrate slightly lower wind energy capacity installation from ICON-LAM compared to ERA5_adpt and similar to ERA5_ori. In contrast, the energy systems derived from ICON-LAM (Figure 5.6c) require less solar energy capacity compared to ERA5_adpt (Figure 5.6g) and especially ERA5_ori (Figure 5.6k). A similar behaviour is observed for the required battery capacities, with a slight increase only in the northernmost province using ICON-LAM (Figure 5.6d) compared to ERA5_adpt (Figure 5.6h). This is mainly due to the cheaper wind energy as well as better complemented wind and solar energy that ICON-LAM delivers compared with ERA5 variants, as indicated in Figure 5.4 and Figure 5.5.

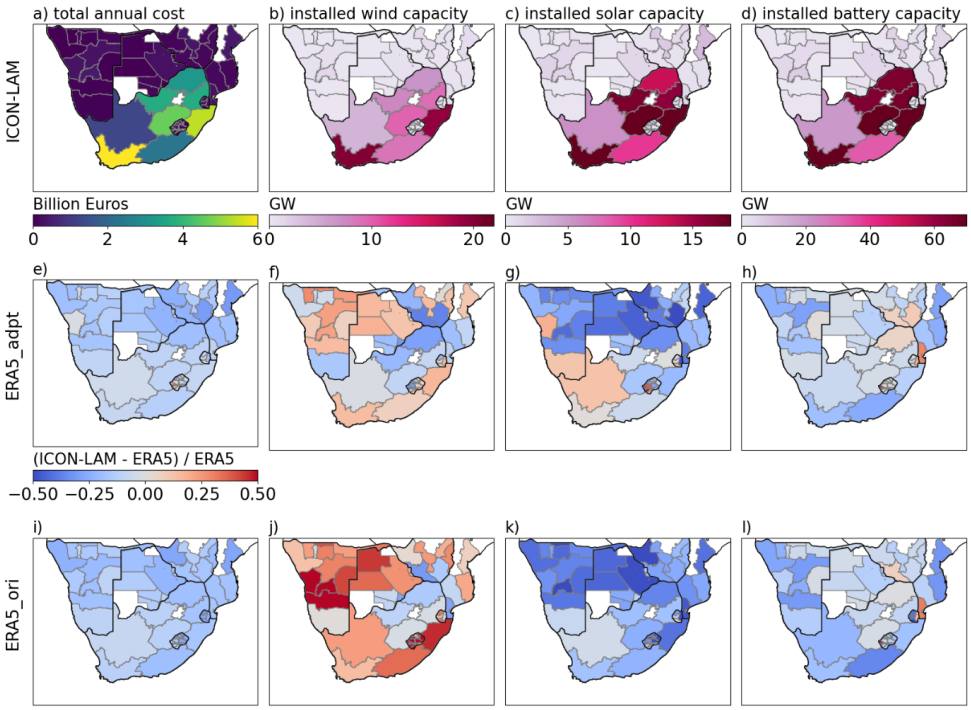

Figure 5.6 The costs and design of cost-optimized energy systems in southern Africa derived from meteorological data sets of ICON-LAM (1st row), ERA5_adpt (2nd row), and ERA5_ori (3rd row) based on 2017. For the other years, the reader is directed to Figure C.3 and C.4. Energy systems optimized with ERA5 data sets are depicted as relative differences compared to results obtained from ICON-LAM. The regions coloured in white indicate that a cost-optimized energy system incorporating wind, solar, and battery technologies is not feasible in that region without connections to neighbouring regions.

5.3.4 ICON-LAM: Increased wind and reduced solar energy contribution for meeting demand over time

To illustrate how hourly electricity demand is met using a combination of technologies and how the energy system is cost-optimized through the curtailment of VRE power generation, a random subset of time series data is selected from the cost-optimized energy system in the Western Cape province of South Africa. Figure 5.7 shows energy systems cost-optimized by energy system modelling based on VRE potentials derived from ICON-LAM, ERA5_adpt, and ERA5_ori. The total power available in the system is the combined generation from wind energy and solar energy, as well as the charging (negative) or discharging (positive) from the battery. The electricity demand is depicted in an inverse manner, representing demand as an energy sink. Since the electricity demand is met 100% on an hourly basis, as illustrated in Figure 5.7, the lines representing the total power available in the system and the electricity demand are two symmetric lines with respect to the zero line. The energy system limits the

amount of wind and solar power it generates to balance costs and operational efficiency. The maximum possible wind and solar power are higher than the actual power generated, and the difference is curtailment. This curtailment helps the system to minimize costs.

To investigate how different energy systems optimized with different meteorological data sets behave over time, the time series of cost-optimized energy systems are examined, focusing on the shares of electricity demand met by wind energy, solar energy, and batteries. Although the time series is simulated on an hourly basis, as shown in Figure 5.7, daily data is analysed to present more condensed information, which nevertheless delivers consistent results, as demand is fully met each hour.

The projected 2050 yearly cycle of daily total electricity demand for the southern African provinces is shown in Figure 5.8, and Figure 5.9 compares daily electricity demand shares met by wind energy, solar energy, and batteries in energy systems. ICON-LAM generally shows higher shares of wind energy and lower shares of solar energy. Exceptions are found in Lesotho, where ERA5_adpt uses more wind energy (Figure 5.9b LSO) and less solar energy (Figure 5.9e LSO), while ERA5_ori shows an extremely low wind share with a correspondingly higher solar share (Figure 5.9c and 5.9f LSO). This result is consistent with the findings of Chen et al. (Chen, Goergen, et al., 2024), who show that ICON-LAM has the highest skill of simulating wind speeds over complex terrain, such as over Lesotho, where ERA5_GWA tends to overestimate, especially over extremely contrasting terrain features such as hilltops and ridges. In contrast, ERA5_ori cannot resolve this type of terrain and tends to underestimate due to its coarse spatial resolution.

Wind and solar energy shares, in meeting the electricity demand, vary throughout the year but complement each other, as the system is designed to fully meet electricity demand (see Figure 5.1, 5.2, and 5.8) at minimal cost. Slightly different temporal patterns of met electricity shares are observed between the years 2017 to 2019 (see Figure C.5 for 2018 results and Figure C.6 for 2019). The contribution of wind and solar energy to meet the electricity demand on a specific day may vary between years, as it is influenced by the local weather on that day, or even over multiple days depending on the weather pattern. This interannual variability is therefore expected, but no significant year-to-year changes are noted in the comparison columns of Figure 5.9, Figure C.5, and Figure C.6, indicating consistent results.

In all the cost-optimized energy systems, the total generated power from wind and solar energy most of the time meets the local electricity demand with only a small contribution of battery power. The spatio-temporal average battery discharge rates – the fraction of time when the battery is discharging – are 27.7%, 32.6%, and 36.5% for the cost-optimized energy systems derived from ERA5_ori, ERA5_adpt, and ICON-LAM, respectively, while the corresponding total electricity demand met by the battery is only 6.4%, 5.3%, and 5.8%.

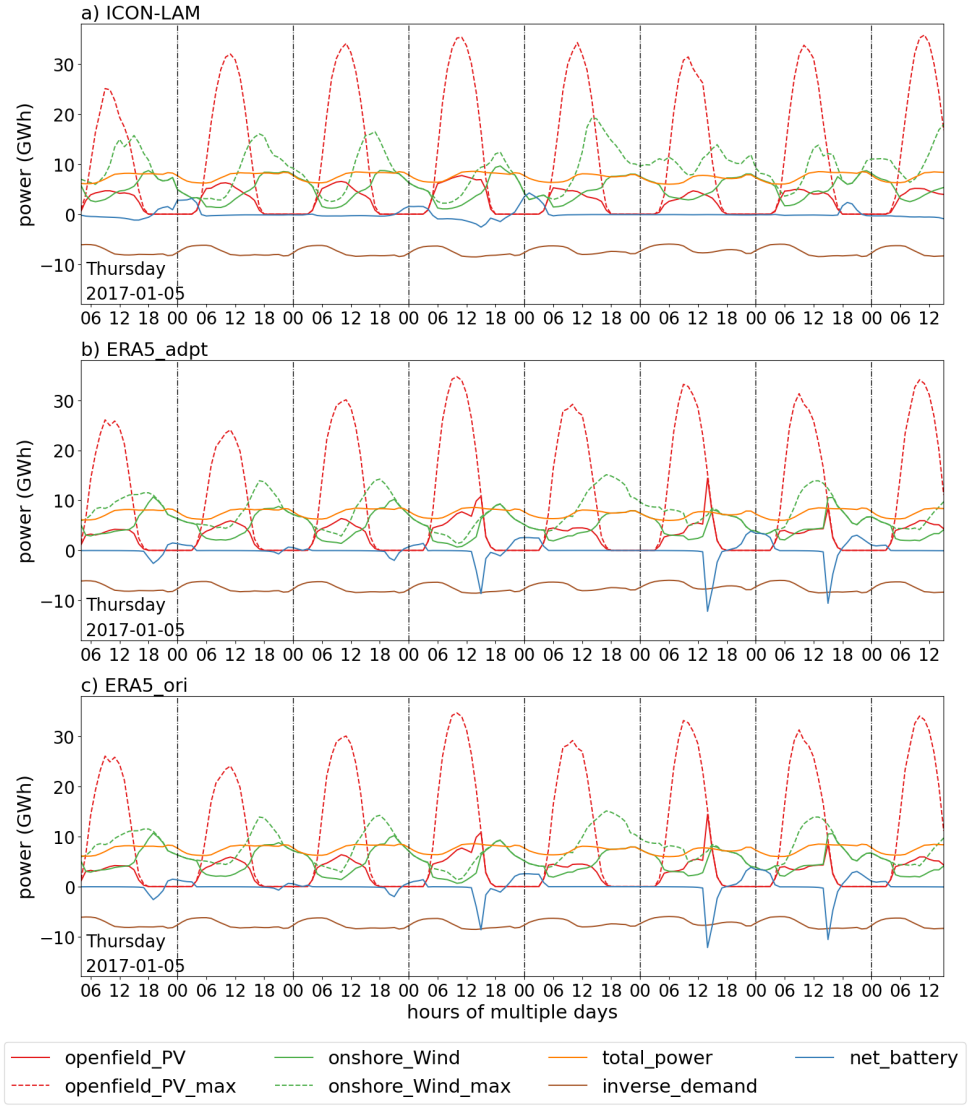

Figure 5.7 The time series subset of the cost-optimized energy system of the province Western Cape derived from three different meteorological data sets based on the 2017 weather year. The orange solid line represents the total power generation in the energy system, which is made up of contributions from open-field PV (solar energy) in the red solid line, onshore wind energy in the green solid line, and batteries in the blue solid line. The electricity demand, or energy sink, is presented in the brown solid line. The maximum harvestable solar and wind energy generation is shown in the red and green dashed lines, respectively.

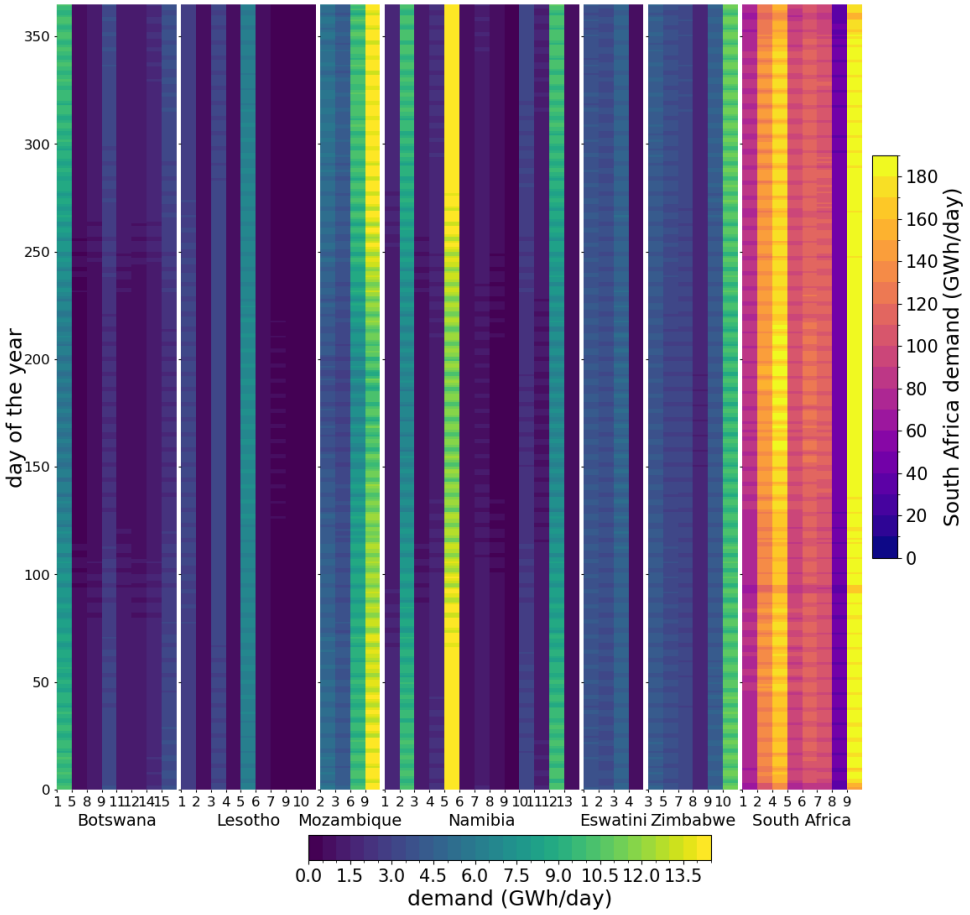

Figure 5.8 The projected 2050 daily total electricity demand of the southern African provinces (numbers), where a feasible cost-optimized energy system can be built. The colour bar on the right of the figure, with a different scale, is used exclusively for the electricity demand of South African provinces. This is necessary due to the large difference in electricity demand between provinces from South Africa and other Southern African countries considered in this study. All provinces are arranged by country and sorted ascending by name index, i.e., their identical GID numbers, which are shown in the ticks on the x axis. For the correspondence between the identical GID numbers and the exact province, please refer to Table C.1, column "Province code (GID_1 code)".

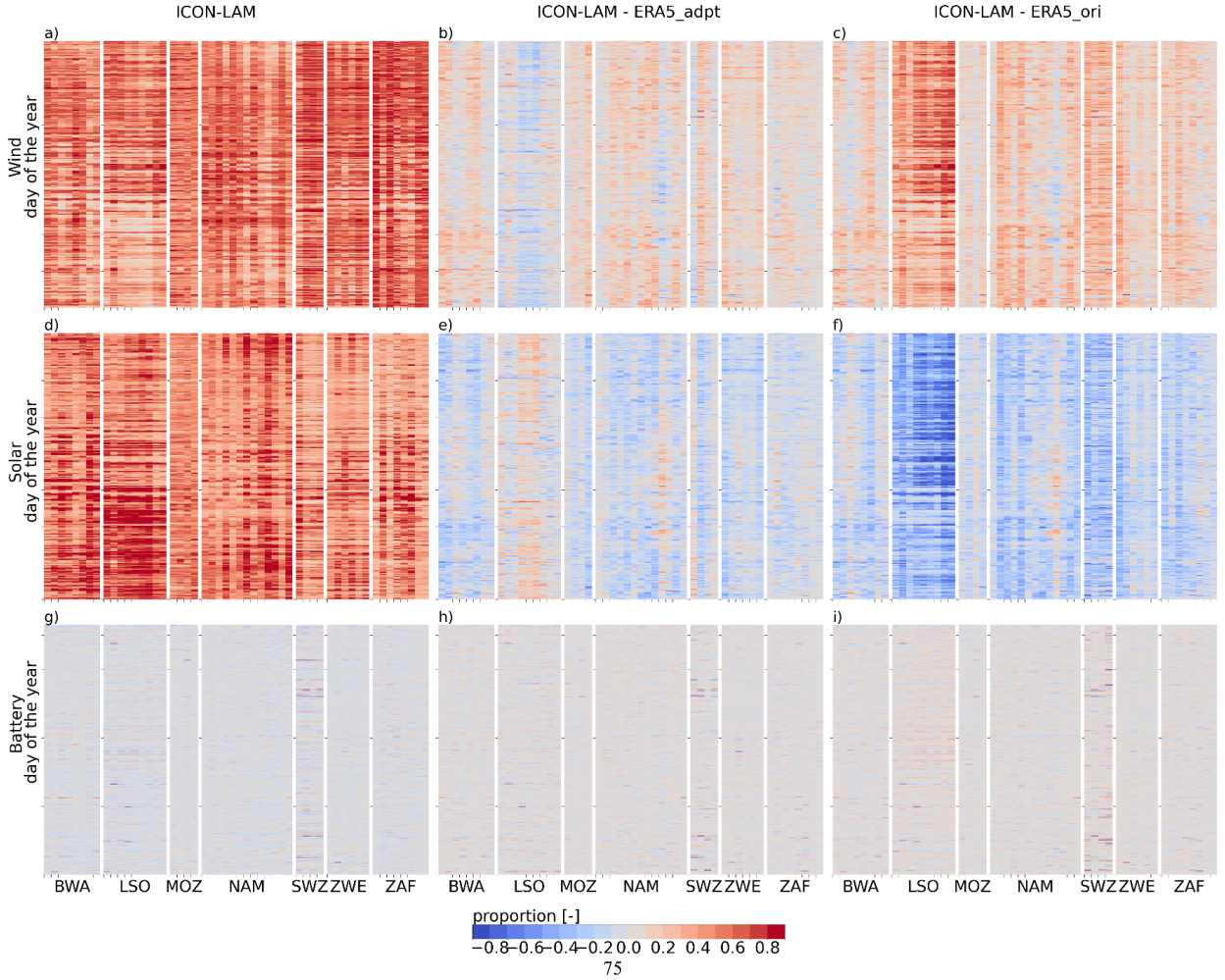
ICON-LAM
ICON-LAM - ERA5_adpt
ICON-LAM - ERA5_ori
a)
b)
c)
d)
e)
f)
g)
h)
i)
Wind
day of the year
Solar
day of the year
Battery
day of the year
BWA
LSO
MOZ
NAM
SWZ
ZWE
ZAF
proportion [-]
−0.8
−0.6
−0.4
−0.2
0.0
0.2
0.4
0.6
0.8

Figure 5.9 The time series comparison of daily demand (with reference to the 2050 demand projection) fraction met by wind, solar, and battery technologies in the cost-optimized energy systems derived from meteorological data sets ICON-LAM, ERA5_adpt, and ERA5_ori for 2017. The 1st column is the result derived from ICON-LAM, and the 2nd and 3rd columns are the comparison of ICON-LAM to the ERA5 variants, ICON-LAM minus ERA5_adpt and ICON-LAM minus ERA5_ori, respectively. The structure of the x- and y-axis of each subplot in this figure is the same as in Figure 5.8, i.e., the y-axis contains the day of the year, and the x-axis shows different provinces grouped by country; the country names are abbreviated (Table C.1) for better visualization. In the "ICON-LAM" column, only positive or 0 values are present in the "Wind" and "Solar" rows, meaning the corresponding fraction of electricity demand is met; both positive and negative values are present in the "Battery" row, indicating battery discharge and charge, respectively. In the columns "ICON-LAM - ERA5_adpt" and "ICON-LAM - ERA5_ori" positive and negative values represent the comparison between ICON-LAM and ERA5 for each technology. The results for years 2018 and 2019 are shown in Figures C.5 and C.6.

5.4 Discussion and conclusions

This study indicates that the cost-optimized energy systems in southern Africa, designed based on ICON-LAM meteorological input data, reduces the estimated total annual cost on average by about 14% (16% less than ERA5_adpt and 11% less than ERA5_ori) compared to the commonly used data set for this task, the ERA5 products, and cuts the required battery capacity by 13% (9% less than ERA5_adpt and 17% less than ERA5_ori). In detail, cost-optimized energy systems derived from ICON-LAM, compared to other alternatives, deploy more wind energy, less solar energy, and less battery, primarily due to the cheaper wind energy revealed by ICON-LAM. Under such circumstances, this would facilitate the development of regional renewable net-zero energy systems. This finding further underlines the necessity of using high-resolution physically consistent model-based data to plan for a cost-optimized energy system.

This study also shows significant differences in wind energy potentials, with ICON-LAM producing, on average, about 5 GWh per turbine (approximately 50%) more annual wind power compared to other ERA5 products. The additional wind energy per year revealed by ICON-LAM for only one single wind turbine averaged out of the 1.8 million eligible turbines across the study area could power approximately 1,736 typical British three-person households, the size of a small town, with an annual electricity consumption of 2,880 kWh/household (IRSAP, 2023), for one year. In contrast, the solar energy potentials are similar (almost identical) across all data sets. This suggests that solar irradiance under clear-sky conditions over southern Africa primarily controlled by large-scale anticyclonic atmospheric circulation patterns are well-resolved in all the data sets. The simulation of wind speed remains challenging, particularly for the coarser spatial resolution of ERA5. Local surface properties cannot be resolved in such detail as with the kilometre-scale ICON-LAM, the simulation of planetary boundary layer mixing or surface friction, and ultimately the accuracy of near-surface wind speed simulations is affected.

Regarding the role of batteries in renewable energy systems, the three meteorological data sets of the study agree with each other that wind and solar can supply most of the electricity demand, with minimal battery use – averaged only about 5.8% of the annual demand have to be covered by batteries, for about 68% of the time no battery discharge is required. Batteries remain essential, however, for times without sufficient wind and solar power. This is in accordance with the global 100% renewable or net-zero emission scenarios, where batteries are projected to be a critical energy system component to achieving high levels of reliability, although their contribution to electricity demand may vary depending on local conditions and specific system designs (International Renewable Energy Agency, 2024).

The complementarity of wind and solar energy that this study focus here is actually a frequently raised topic in literature. However, many of these studies as mentioned in the introduction section tend to address the complementarity of wind and solar energy from a theoretical and strategic perspective, and do not consider the latest developments in the field of renewable energy assessment. Compared to our study, these studies do not consider the suitability of the land to build wind turbines or solar power plants or the specific placement of the renewable energy sources, and only include spatially distributed (gridded) meteorological information. Also, the energy system, which includes the complementarity of wind and solar energy, often does not consider the system costs and the battery capacity, or only includes a predefined constant battery capacity. However, these are important factors that need to be carefully considered in the design and operation of real-world energy systems. Our study also clearly demonstrates that any future design of VRE based energy systems should include assessments based on high-resolution, dedicated modelling and not only rely on readily available data products.

It should be noted, however, that the impact of different meteorological data sets on the cost-optimized design of energy systems is specific to our study area in southern Africa. The complex land-atmosphere interactions, given the complex terrain with some highly contrasting features in southern Africa, or ocean-land circulation patterns, play a role in the simulation of VRE variables and may limit the transferability of the study's findings.

As for the energy systems modelling, this study assumes lossless power transmission and no power exchange between provinces to examine the direct impact on the local energy system. Dealing with a real-world power grid is more complex and would alter the outcome of our study. Furthermore, research by Blanco and Faaij (Blanco & Faaij, 2018) suggests that including more energy sectors reduces the need for battery capacity in the energy systems even further. By modelling energy systems with only wind and solar energy and without interprovincial transmission, our study may overestimate battery needs. Modelling a real-world full energy system with all the energy sectors integrated and power exchanged would likely lower both battery requirements and overall costs, but the relative differences in VRE contributions derived from different meteorological data sets should remain the same as this study presents.

Furthermore, this study considers annual variations in designing the cost-optimized energy system. Multi-decadal simulations that capture interannual VRE variabilities, as shown by Caglayan et al. (Caglayan, Heinrichs, et al., 2019), could yield more robust results and, therefore, deserve attention in future decades-scale applications of the current study.

Chapter 6. Discussion, conclusions, and outlook

A significant deficit exists in the provision of electrical energy across Africa. Renewable energy is recognized as a crucial solution, given the continent's abundant untapped potential and the low greenhouse gas emissions associated with harnessing these resources. However, planning energy systems using Africa's most widely accessible renewable energy sources—wind and solar—faces challenges due to limitations in available meteorological data sets from both measurements and simulations. The identified limitations include relatively coarse spatial resolution, data gaps in both space and time, and general data quality issues in simulated meteorological data sets.

This doctoral thesis presents a comprehensive interdisciplinary study between Earth System Modelling and Energy System Design and aims to alleviate the meteorological data strains in Africa, focusing on southern Africa as a prototype. First, a dedicated dynamical downscaling using the ICON model is performed to produce a high-resolution, physically consistent, model-based data set ICON-LAM. The capability of ICON-LAM to simulate wind and solar energy related variables is then evaluated, and the estimated wind power derived from ICON-LAM is also evaluated and compared with those derived from alternative data sets. Finally, the impact of ICON-LAM on cost-optimised energy system design in southern Africa compared to other alternatives is investigated. The entire energy system modelling chain is addressed in this study, starting with the production of the meteorological data set. The broad scope of fundamental expertise required for this work represents a significant departure from the approaches taken in previous studies.

6.1 Discussion

Achieving higher spatio-temporal resolution in meteorological data sets is a clear trend in geoscience, as small-scale phenomena can be explicitly resolved without parameterization, providing more detailed insights compared to coarser models (Schär et al., 2020). Determined by the target of the research, many studies in geoscience with a focus on renewable energy assessment tend to approach the subject from a theoretical and strategic perspective. Idealised assumptions are typically made, and state-of-the-art developments in the renewable energy assessment field are often not considered. For example, studies focused on estimating renewable energy potentials (Antonini et al., 2024; Lu & McElroy, 2023; Yang et al., 2024), on investigating the impact of climate change on renewable energy potentials (Feron et al., 2021; Reyers et al., 2016), and on examining the complementarity of wind and solar energy (Lei et al., 2023; Richardson et al., 2023; Tong et al., 2021). Land eligibility, technical constraints within the power plant, and social acceptance of the installation of renewable energy power plants are not taken into account, despite being addressed in the state-of-the-art renewable energy assessment field, which aims to really look at how much energy is available to harness for practical use, as reviewed by (McKenna et al., 2022). And these are non-negligible factors that highly affect the feasibility of the project and, subsequently, on the accuracy of the estimated total renewable energy potential.

At the same time, high-resolution, physically consistent, model-based meteorological data sets through dynamical downscaling are rarely used in the renewable energy assessment field. Typically, global reanalyses with coarse spatial resolution in the range of 30 km to 60 km, such as MERRA-2 and ERA5, are used in renewable energy assessment (Gonzalez-Aparicio et al., 2017; Ruiz et al., 2021; Sakuru & Ramana, 2023). Regional reanalyses also play a role (Gualtieri, 2022; Kenny & Fiedler, 2022), e.g., COSMO-REA2 and COSMO-REA6. Although it is better resolved in terms of spatial resolution, ranging from 2 km to 12 km, to the best of the author's knowledge there is no regional analysis available for all or part of the African continent. Other products such as the Global Wind Atlas (GWA, 2019) and the Global Solar Atlas (GSA, 2019) with high-resolution of 250 m do exist, but without information on temporal variation, which is crucial for the energy systems modelling (Caglayan et al., 2021; Lund et al., 2015). High-resolution, physically consistent meteorological data sets for renewable energy assessment especially over Africa are missing, and the impact of using high-resolution versus coarse-resolution data sets on renewable energy assessment remains unknown.

In this thesis, a linkage between the fields of geoscience and renewable energy assessment is established. The wind and solar energy potential estimated in this work integrates state-of-the-art developments from both fields into a single project, delivering new results. Dedicated dynamical downscaling using the ICON model is performed to provide high-resolution physically consistent data set over southern Africa. Existing results of land eligibility and power plant siting are included from the starting point of this thesis. Maximum resource harvesting is ensured as the technical parameters of the renewable energy units are not constant but varied to achieve the best generation efficiency at each eligible location. In the energy system modelling, an optimization solver is employed to consider an energy system that first meets 100% of the electricity demand, which is the top priority for a real-world power supply system. The best combination of wind energy, solar energy, and batteries for the energy system is then solved in a cost-optimised way. As a result, energy systems can be designed for southern Africa. This is in accordance with the Sustainable Development Goal 7 proposed by the United Nations (United Nations, 2015) and is of great practical value for the local energy system development in Africa.

While this thesis has done its best to fill the identified research gaps, some aspects need further consideration to improve renewable energy potential estimates and energy system design in southern Africa. In the atmospheric modelling step, the ICON model is used to dynamically downscale the forcing data—the global initialized analysis—from 13 km to a convection-permitting scale of 3.3 km. The ICON model configuration used for this atmospheric modelling over southern Africa is taken from the operational Numerical Weather Prediction (NWP) runs for Germany in DWD. The sensitivity of the physical parameterization schemes used in this configuration over southern Africa has not been analysed, although it has been carefully tuned by DWD for the German domain. A sensitivity study of the high-resolution ICON model has been performed for Italy (De Lucia et al., 2022) and the ICON model was found to be sensitive to changes in the physical parameterization schemes. A similar sensitivity analysis can be carried out for southern Africa, with the aim of selecting suitable parameterization schemes to

properly represent local weather and climate features.

Constrained by the availability of forcing data from 2015 onwards, three simulation years from 2017 to 2019 are selected in this study. Although average and extreme wind and solar conditions are best considered in the selection of simulation years, a climate scale simulation such as 30 years would be more reliable for robust energy systems design; this is only possible when the corresponding forcing data will be available. Beyond historical weather patterns, it is also important to account for weather variability under climate change and explore how this will impact the robust design of energy systems. In addition, a higher level of accuracy is found with sub-hourly energy system modelling (Omoyele et al., 2024). It is suggested to extend the current hourly temporal resolution used in energy system modelling to sub-hourly intervals, such as 30 mins, 15 mins, or even 1 min. This would require more temporally detailed meteorological data sets and the allocation of additional computational resources, which, although resource-intensive, is a potentially indispensable endeavour for achieving more accurate energy system modelling.

Although real-world restrictions such as land eligibility were taken into account, the renewable energy potentials estimated in this study may still be overestimated. This is mainly due to social factors limiting the installation of wind and solar power plants, such as local resistance to placing solar/wind power plants, which is difficult to quantify and was not considered in this study. A recent review on quantifying social factors for onshore wind energy planning (Tsani et al., 2024) documented that landscape impacts, proximity to settlements, and justice are important social factors and indicated that further improvements are needed to better reflect social concerns in planning models. Nonetheless, since normally only a fraction of the estimated technical potential is already sufficient to meet local electricity demand, it might be possible to circumvent at least parts of the overlooked social factors in this study. In addition, the regional energy system that we analyse only considers wind energy, solar energy, and batteries, based on the Copper Plate scenario — assuming an ideal, unlimited power flow exchange in the region (Hess et al., 2018). It is highly simplified compared to the real-world energy systems facing grid constraints, although it is a reasonable scenario to use here to compare the results of different designed energy systems derived from different meteorological data sets.

6.2 Conclusions

The high-resolution atmospheric simulations performed by the ICON model have been shown to reproduce the basic atmospheric conditions and the underlying large-scale atmospheric circulations in southern Africa, and the wind and solar energy-related atmospheric variables have also been shown to be well captured. This supports the reliability of the ICON model for use over southern Africa and makes it a viable candidate for other related applications, such as investigating the impacts of variable weather conditions on renewable energy. Testing the performance of the ICON model beyond southern Africa is of interest to assess its simulation accuracy across different terrain types, land-atmosphere interactions, and dominant large-scale

atmospheric circulations.

Higher and different spatially distributed wind energy potentials are revealed by the ICON model over southern Africa, compared to other commonly used meteorological data sets like ERA5. It is the first time that the higher onshore wind energy potential has been revealed by km-scale convection-permitting atmospheric modelling. Underestimation of wind energy yields may hinder further expansion of wind energy, as lower economic performance is expected, highlighting the importance of highly resolved weather data. Attention is also drawn to further investigate the local wind energy potential in order to better inform and attract local investment, and ultimately assist in the planning and construction of local energy systems. Whether the same trend of wind energy potential underestimation would be observed in other parts of the world remains unknown, making it an important topic for ensuing studies to explore.

The southern African cost-optimised energy systems under the 100% renewable energy scenario derived from ICON-LAM show lower total annual costs and lower required battery capacity compared to those derived from other available data sets. This is vital information for planning the local energy system in southern Africa. It implies that the previous local energy system design may have been overestimated in terms of cost, thus hindering the local energy system development. This further emphasises the importance of using convection-permitting km-scale high-resolution meteorological data sets in energy system analysis. Considering the impacts of weather variability on energy systems would further increase the robustness of the analysis, including long-term historical weather years, uncertainty in future weather years under climate change, and the feedback on weather from huge wind power plants.

6.3 Outlook

As mentioned above, a sensitivity analysis of the ICON model is suggested to find the best performance combination of physical parameterization schemes over southern Africa. Given the complex atmospheric circulations and highly contrasting topography present in southern Africa, this sensitivity analysis of the ICON model is expected to further improve the current model simulation performance. To derive robust regional energy system designs for southern Africa, the simulation time span should be increased to a longer period like 30 years.

Potential improvements are also identified for the RESKit wind and solar power simulation workflows. For the RESKit wind workflow, the wind power calculation is based on the 100 m wind speed and logarithmically extrapolates this 100 m wind speed to the hub height of the wind turbine. Actually, both the ICON and ERA5 models utilise a terrain-following vertical model discretization, which allows for fine vertical resolution of the planetary boundary layer, where wind turbine rotors are situated. A wind speed extrapolation based on the wind speed at the model vertical level closest to the wind turbine hub height is more straightforward and has less uncertainty. In addition, the wake effect—the trail left by each wind turbine after it has extracted kinetic energy—has been shown to affect the performance of nearby wind turbines and sometimes even neighbouring wind farms (Porté-Agel et al., 2020). The wind workflow used in this study does not account for this wake effect. Future studies should include wake

effects to simulate wind power more realistically.

For the RESKit solar workflow, the uncertainty lies in the photoelectric conversion efficiency and the applied system-level losses. The solar photovoltaic industry has grown dramatically over the last 10 years (Allouhi et al., 2022). The cost of solar photovoltaic panels has drastically declined, and the photoelectric conversion efficiency of solar photovoltaic panels continues to improve (Manisha et al., 2022). The photoelectric conversion efficiency used in this study is projected to 2050 based on the observed trends (Ryberg, 2020), most assuming a further cost decrease. Different development scenarios of the solar photovoltaic industry—the underlying changes in photoelectric conversion efficiency—could be formulated and included in the future analyses. Besides, an approximate system-level overall loss factor based on first-hand industry experience is applied to represent all inevitable losses in the solar photovoltaic system in this study. A detailed quantification of each of these losses in the system may also be helpful as a next step to better quantify different loss factors in the photovoltaic system.

Social factors are not included in the wind and solar energy potential estimates of this study. These social factors, which impede the implementation of renewable energy projects, are more complex than they may initially appear. The recent review on quantifying social factors for onshore wind planning (Tsani et al., 2024) showcases this and highlights the need for interdisciplinary approaches. Further work building on the current study should consider dealing with this topic.

Aspects to improve the energy system modelling are also worthy of attention. The inclusion of realistic grid constraints in the energy system modelling and the possibility to exchange electricity between regions/provinces are of high interest. Apart from that, the inclusion of other existing energy sectors such as heating and cooling, transport, residential, and industry, to achieve a realistic energy system modelling, is also of great importance. Sub-hourly temporal resolution should also be considered when optimising the energy system modelling. Having all these aspects on board would certainly increase the accuracy of the energy system design, but it also exponentially increases the computational burden and challenge for the optimization procedure. The corresponding data availability and data uncertainty are also the limitations here. The trade-off between modelling accuracy and the required efforts must be carefully evaluated.

The higher onshore wind energy potentials and the lower costs of cost-optimised energy systems are revealed by the ICON simulations in this study, compared to other commonly used meteorological data sets. It is of great interest to apply high-resolution atmospheric simulations in the context of renewable energy potential also for other regions, to see if the same results are observed/ revealed.

Climate change is likely to become more severe and extreme if the mitigation measures currently under discussion are not implemented as they should be for all countries in the world. Investigating the impact of climate change on wind and solar energy potentials, and subsequently on the robust design of energy systems, is of paramount importance for the

regions most vulnerable to climate change like the African continent.

Appendix

A. Appendix A

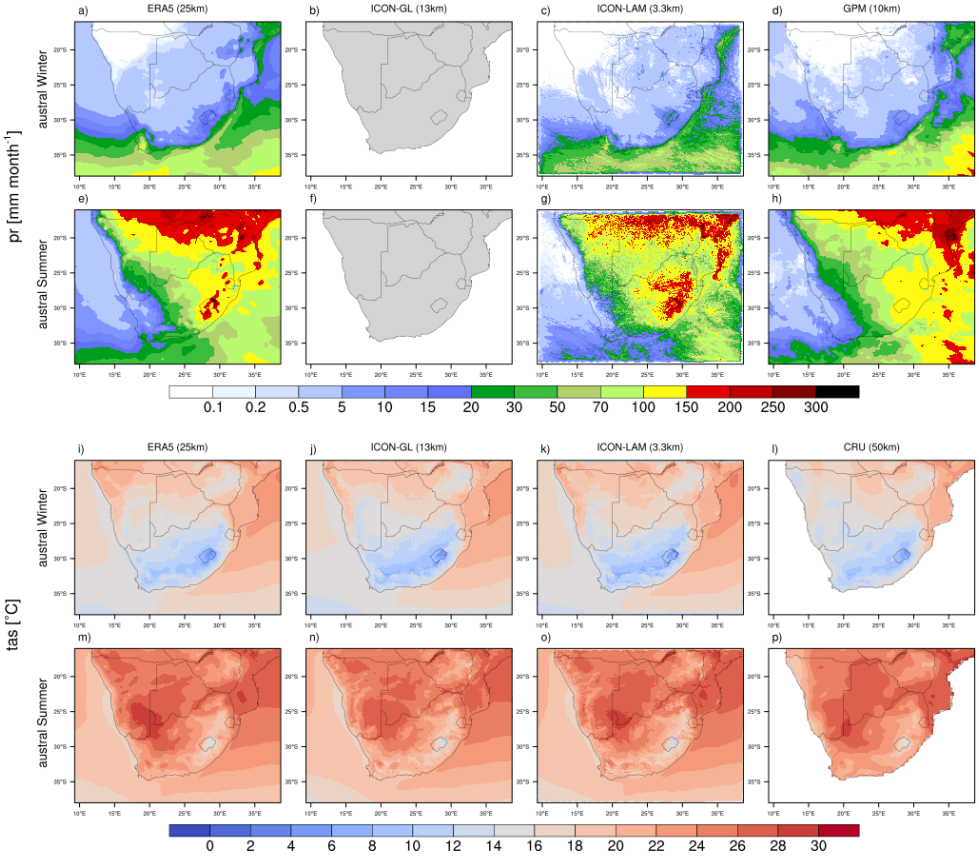

Figure A.1 Average total precipitation [mm month^{-1}] (top multi-panel) and 2 m air temperature [°C] (lower multi-panel) for the period 2017 to 2019 and austral winter (JJA) (upper row) and austral summer (DJF) (lower row), for ERA5 (1st column), driving ICON-GL (2nd column), ICON-LAM (3rd column), and the reference data (4th column), GPM for pr, and CRU for tas. The tas of ICON-GL is based on the lowermost model level (10 m) of air temperature. All the datasets are presented on their respective native grids.

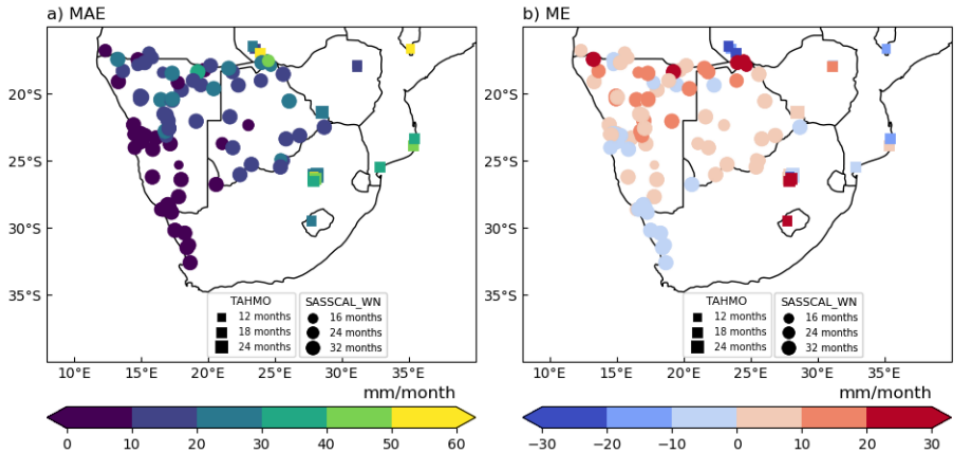

Figure A.2 Spatial distribution of a) MAE and b) ME of monthly precipitation [mm] from 2017 to 2019 from ICON-LAM compared with ground meteorological stations.

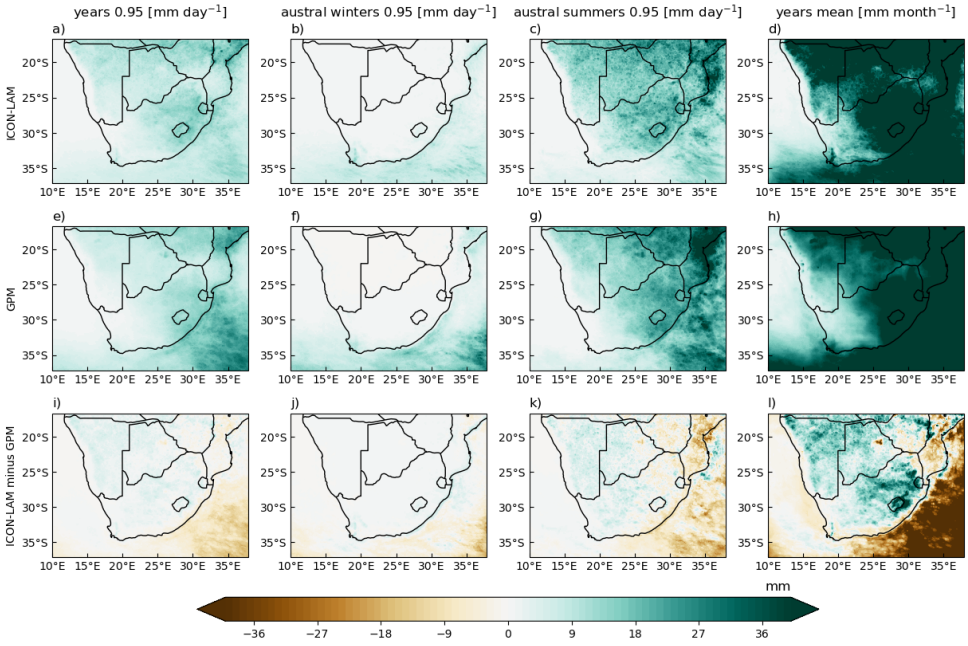

Figure A.3 Precipitation comparison: 0.95 percentile of daily precipitation [mm day^{-1}] (1st column), daily precipitation in austral winters [mm day^{-1}] (2nd column), daily precipitation in austral summers [mm day^{-1}] (3rd column), and monthly mean precipitation [mm month^{-1}] (4th column) from ICON-LAM (1st row) and GPM (2nd row); difference ICON-LAM minus GPM (3rd row), for the years from 2017 to 2019. Simulated precipitation from ICON-LAM is resampled to the GPM grid using conservative remapping.

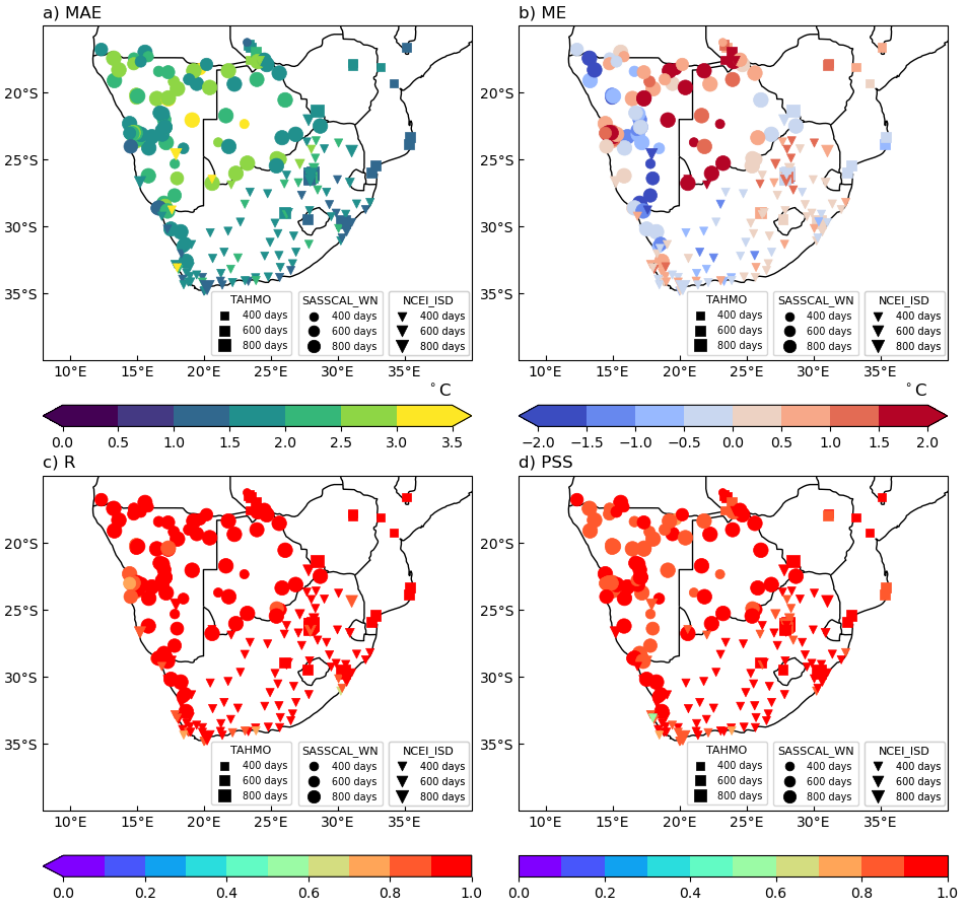

Figure A.4 Spatial distribution of MAE, ME, R, and PSS of hourly air temperature at 2 m height for the period from 2017 to 2019. Statistics are calculated for simulated air temperature by ICON-LAM compared with ground meteorological stations. Rectangles are stations from the TAHMO network, circles are SASSCAL_WN stations, and triangles represent NECI_ISD stations. The symbol size represents the number of valid measurement days.

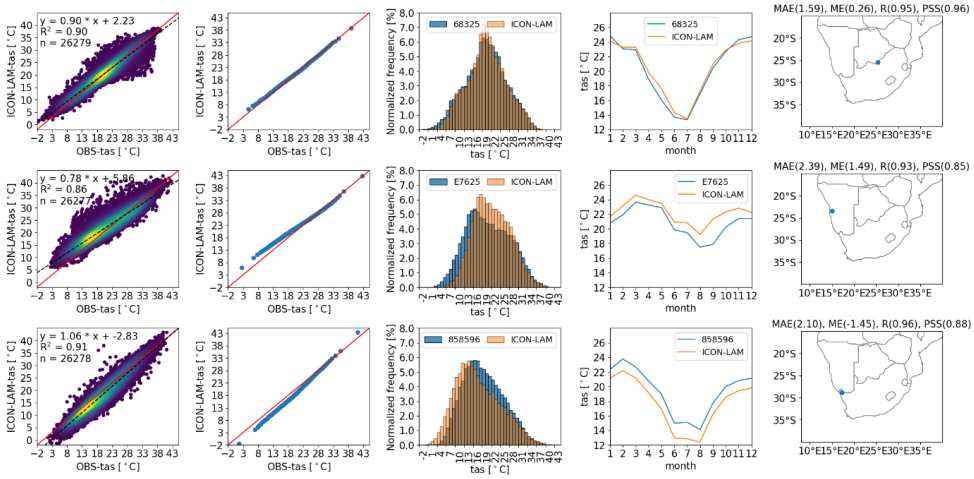

Figure A.5 For three selected stations hourly 2 m air temperature statistics [°C] are shown (one row per station). The columns from left to right show: scatter plot, percentile plot, histograms, mean annual cycles, and spatial location. In these plots ICON-LAM simulated values are compared with measurements. Colours in the scatter plot represent the point density estimated by the Gaussian Kernel, the brighter the colour is, the higher the density is. Percentiles for every 1% are plotted in the percentile plot. The histogram plot has a bin size of 1 [°C].

B. Appendix B

B.1 Data preparation for wind speed evaluation and wind energy potential estimation

B.1.1 Data quality of observed wind speeds at weather masts in South Africa

The data quality of the wind speed observations is the cornerstone of the simulated wind speed evaluation. A total of 19 weather masts (Wind Atlas for South Africa, 2010) over South Africa are, to our knowledge, the only publicly available observations for southern Africa that measure wind speeds at bigger heights near real wind turbine heights. The detailed description of each mast can be found on the website: https://wasadata.csir.co.za/wasa1/WASAData. Wind speeds over the mast locations are recorded at 10 m, 20 m, 40 m, 60 m, and 62 m, and with wind directions observed at 20 m and 60 m. The mean, minimum, maximum, and standard deviation of the wind speeds are recorded at 10-minute intervals. All the weather masts were carefully installed, and all site-specific adjustments were well documented. The properties of the sensors and how they are structured on the standing tower are also available. Calibrations are performed on the collected raw data according to the calibration certificates of each sensor. Further quality control procedures recommended by the instrument supplier are also performed before the data are officially released. All the data/times are provided in local time (UTC+2), the transformation to the UTC time has been applied in this study.

B.1.2 Wind speed scaling using power law

$$WS_H = WS_{ref}\left(\frac{H}{H_{ref}}\right)^{\alpha} \qquad \text{(B.1)}$$

WS_H is the wind speed of interest, here H=60 m; WS_{ref} is the wind speed at the reference height H_{ref}, always using the closest available simulated wind speed. Empirically, α is 1/7 under a neutrally stable atmosphere without considering surface roughness (Bratton & Womeldorf, 2011). As simulated wind speeds are available on multiple vertical model levels of the terrain following grids, we follow the approach in the study (Devis et al., 2018) and make use of the wind speed of the upper (H + 1) and lower (H - 1) vertical model levels around 60 m to determine α individually:

$$\alpha = \frac{ln\frac{WS_{(H+1)}}{WS_{(H-1)}}}{ln\frac{(H+1)}{(H-1)}} \qquad \text{(B.2)}$$

This allows us to describe α dynamically to account for temporal variations in atmospheric stability and variations in surface roughness. Additionally, incorporating the nearest two wind speeds around the target height, the interpolated wind speed is internally consistent with the vertical wind shear in the models.

B.1.3 The wind turbine hub heights designed in the HOpt wind turbine

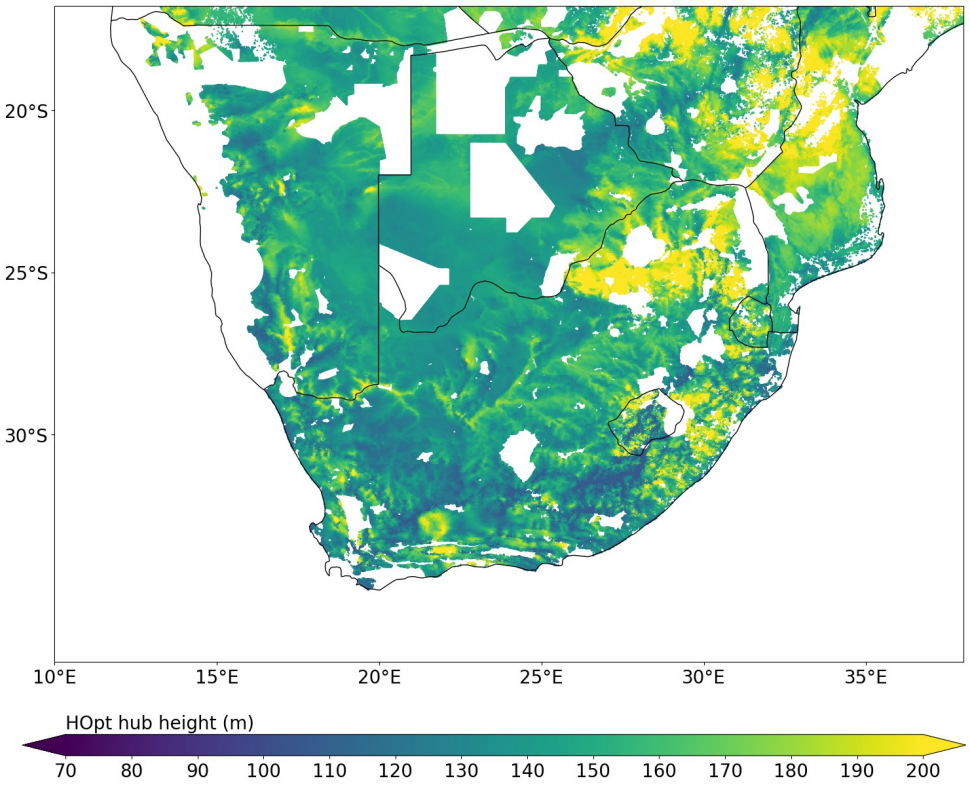

Figure B.1 Spatial distribution of wind turbine hub heights used in the HOpt wind turbine setting across all 1.8 million eligible wind turbine placements in southern Africa. Note that values are plotted for each of the 1.8 million placements, providing eventually a continuous map; white spots are areas where no wind turbine placement is possible according to (Franzmann et al., 2023; Ishmam et al., 2024; Winkler et al., 2025).

B.2 Details of wind turbine technologies used to simulate wind power over weather mast locations

Table B.1 Wind turbine technologies details for the 60 m hub height wind turbine H60m, the baseline wind turbine H130m, and the optimal wind turbine HOpt over weather mast locations. H60m is included to quantify the impact of the different data sets on wind energy potential calculation for the observation height of the weather masts. H130m represents the wind turbine development in 2035 and it is used as the baseline turbine to derive HOpt turbine parameters in the RESKit model.

Name	Capacity (kW)	Hub height (m)	Rotor diameter (m)	Specific power (W/m^2)
H60m	1500	60	60	530.8
H130m	5500	130	174	231.3
HOpt-WM01	5316.3	137.2	174	223.6
HOpt-WM02	5577.6	127.2	174	234.6
HOpt-WM03	5524.4	129.1	174	232.3
HOpt-WM05	6245.5	107.0	174	262.7
HOpt-WM06	5996.2	113.4	174	252.2
HOpt-WM07	5744.7	121.4	174	241.6
HOpt-WM08	5766.9	120.6	174	242.5
HOpt-WM09	6251.8	107.0	174	262.9
HOpt-WM10	5707.5	122.6	174	240.0
HOpt-WM11	6708.6	107.0	174	282.1
HOpt-WM12	4933.4	154.4	174	207.5
HOpt-WM13	5057.8	148.4	174	212.7
HOpt-WM14	6325.7	107.0	174	266.0
HOpt-WM15	5252.4	139.8	174	220.9
HOpt-WM16	5668.7	123.9	174	238.4
HOpt-WM17	5488.7	130.4	174	230.8
HOpt-WM18	5242.4	140.2	174	220.5
HOpt-WM19	5257.1	139.6	174	221.1

B.3 Evaluation of wind speeds at the different wind speed ranges of the wind turbine's power curve

According to the synthetic power curve (Ryberg et al., 2019), the cut-in, rated, and cut-out wind speeds of the baseline wind turbine (turbine H130m, see Table B.1) are set to 3, 11, and 25 m s^{-1}. The corresponding exemplary power curve is shown in Figure B.2. These cut-in, rated, and

cut-out wind speeds are also consistent with most of the wind turbines installed in South Africa (see Table B.2).

The evaluation of the simulated wind speed in the usable, cut-in to rated (ramping phase), and rated to cut-out wind speed ranges of the wind turbine is shown in Figure B.3, Figure B.4, and Figure B.5, respectively. The simulated wind speed beyond the usable wind speed range of the wind turbine is not the focus of this study, but it may be interesting for other applications, so we also show it in Figure B.6.

ERA5_ori performs best at simulating wind speeds beyond the usable wind speed range of the wind turbine. Most of the wind speeds beyond the usable wind speed range are small wind speeds below 3 m s^{-1}. The upper limit of the wind speed for the current wind energy industry is due to the material constraint and the lower limit is due to the size of the wind turbine. Readers will need to reconsider the results of this study if there is a major advancement in the wind energy industry that dramatically changes the usable wind speed range of wind turbines in the future.

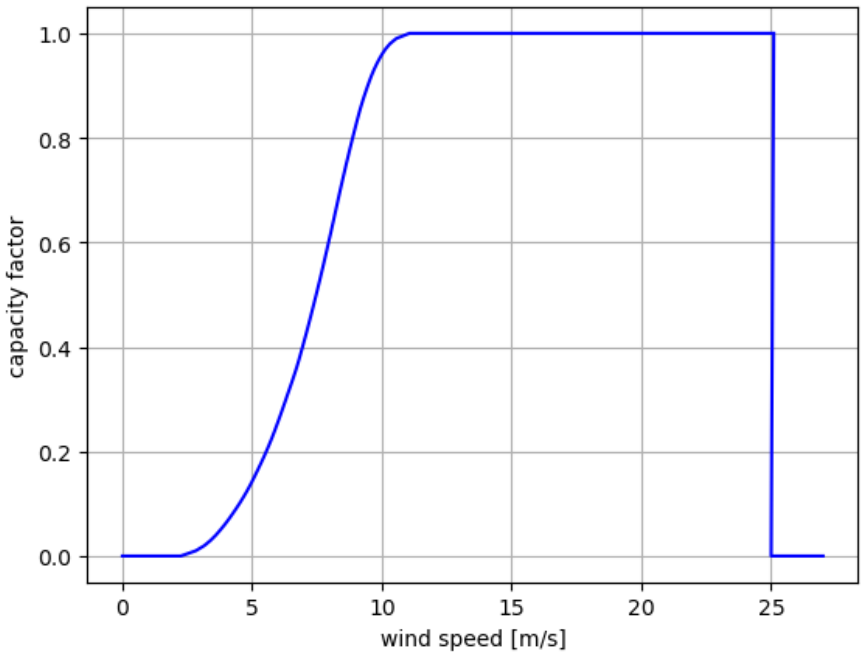

Figure B.2 The exemplary power curve used in this study for determining different investigated wind speed ranges in the wind speed evaluation.

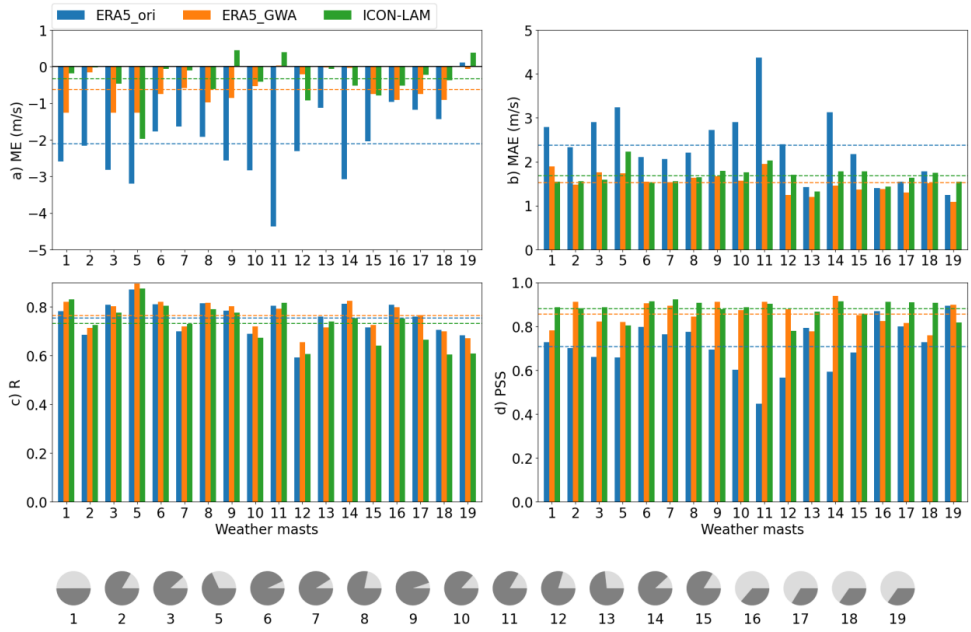

Figure B.3 As in Figure 4.1, but for the observed 60 m wind speed in the range of the 3 m s^{-1} cut-in to the 25 m s^{-1} cut-out wind speeds, concentrating on the usable wind speed range for wind turbines.

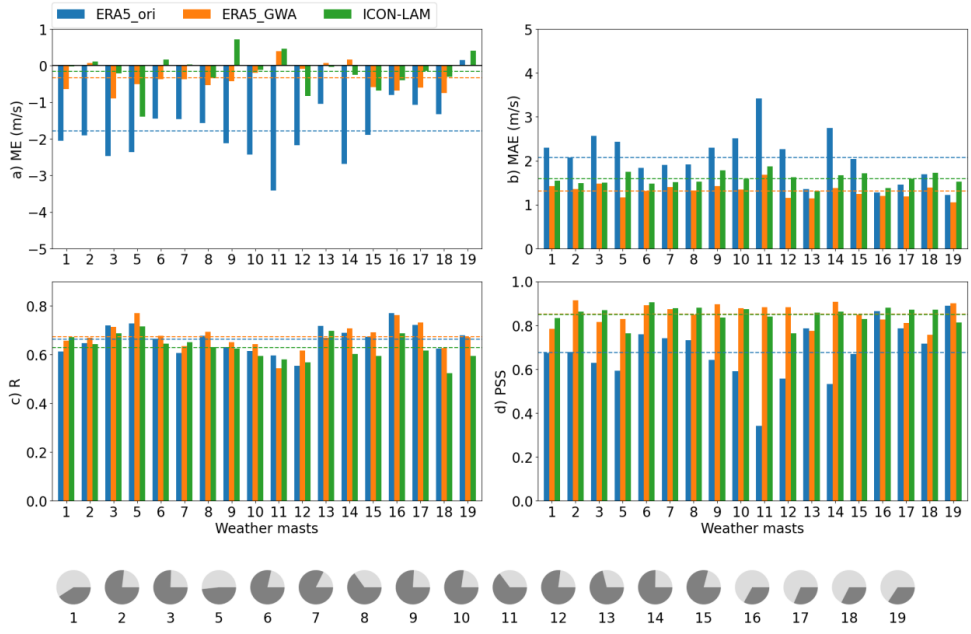

Figure B.4 As in Figure B.3, but for the observed 60 m wind speed in the range of 3 m s^{-1} to 11 m s^{-1} wind speeds, concentrating on the wind speed range during the ramping phase of a wind turbine's power curve. Note the nearly equal mean PSS values of ERA5_GWA and ICON_LAM.

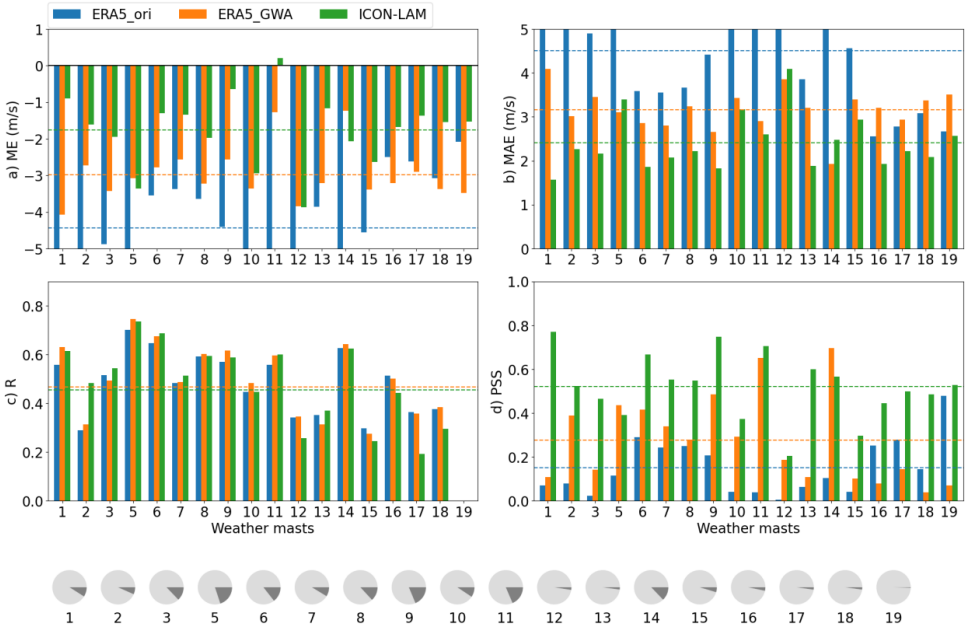

Figure B.5 As in Figure B.3, but for the observed 60 m wind speed in the range of 11 m s^{-1} to 25 m s^{-1} wind speeds, concentrating on the wind speed range from the rated wind speed to the cut-out wind speed of a wind turbine's power curve. Note that ERA5_ori, ERA5_GWA, and ICON-LAM all experience negative R at mast number 19 of -0.06, -0.07, and -0.04, respectively.

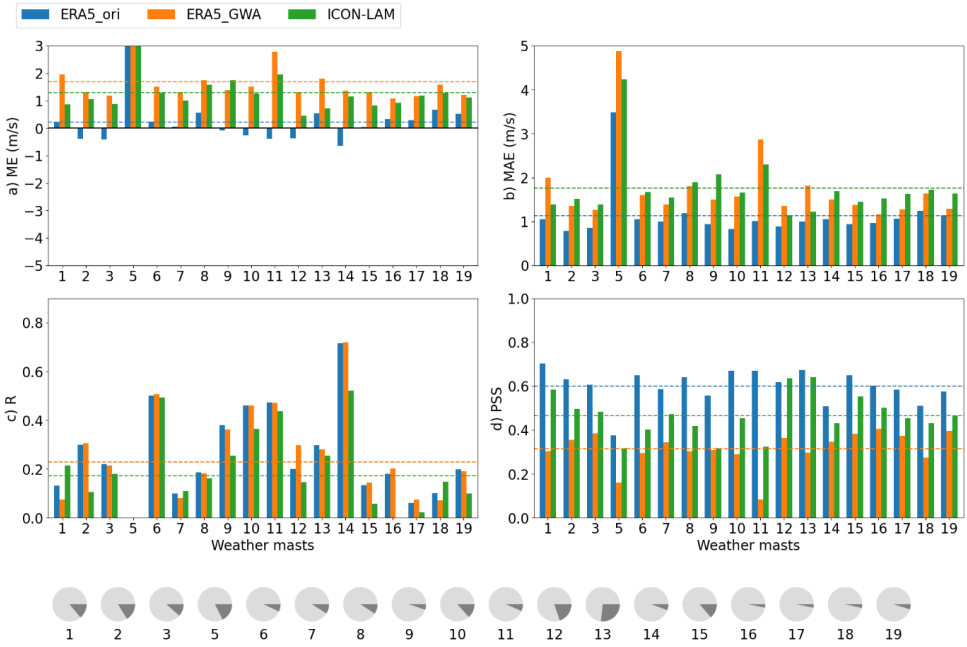

Figure B.6 As in Figure B.3, but for the observed 60 m wind speeds that cannot be harvested by the wind turbine—wind speeds outside the cut-in (3 m s^{-1}) and cut-out (25 m s^{-1}) wind speed range of the wind turbine's power curve. Note the extended y-axis range in subplot a) and the nearly equal mean MAE values of ERA5_GWA and ICON_LAM as well as the nearly equal mean R values of ERA5_ori and ERA5_GWA in subplot c).

B.4 Comparison of simulated wind power to measured wind power for three provinces in South Africa

In this section, in order to justify the credibility of the estimated CFs, besides the wind speed evaluation, a further evaluation of the wind power simulation against measurements is performed. Since no individual wind turbine power measurements are publicly available in southern Africa, the wind power measurements from three provinces in South Africa are utilized and compared to the simulated wind power using the RESKit model with the real installed wind turbine parameters. Through this comparison, we gain insights into which wind power derived from the wind speed product is more reliable, and therefore the corresponding derived wind energy potential.

B.4.1 The wind power measurement in South Africa

The Department of Mineral Resources and Energy from South Africa developed, hosted, and operated the Renewable Energy Data and Information Service (REDIS, 2022) to provide access to renewable energy data and information. Three provinces of South Africa, Western Cape,

Eastern Cape, and Northern Cape, have wind farms, see Figure B.7. The measured hourly CFs of wind power at the provincial level for each of the three provinces are provided by REDIS, and the location of these wind farms and the parameters of the installed wind turbines such as hub height, rotor diameter, and capacity are extracted from The Wind Power database (The Wind Power, 2005).

As our focus time period is 2017-2019, the wind farms with the commissioning date after 2019 and the dismantling date before 2017 are not included. Since some wind farms were commissioned in 2017, we choose 2019 as our focus year to be on the safe side, i.e., away from the commission date. After completing the missing information, 3 missing hub heights and 1 missing turbine model, in The Wind Power database by searching the project name online, we finally get 25 wind farms in South Africa for the year 2019. The location map and the detailed information of these wind farms are shown in Figure B.7 and Table B.2. It is worth mentioning that the installed capacity in each province extracted from the Wind Power database is quite close to the installed capacity provided by REDIS (see Table B.2): the respective installed capacity for Eastern Cape, Northern Cape, and Western Cape from the Wind Power are 1020.25, 673.4, and 436.6 MW, and, 1010.31, 665.46, and 418.72 MW from REDIS.

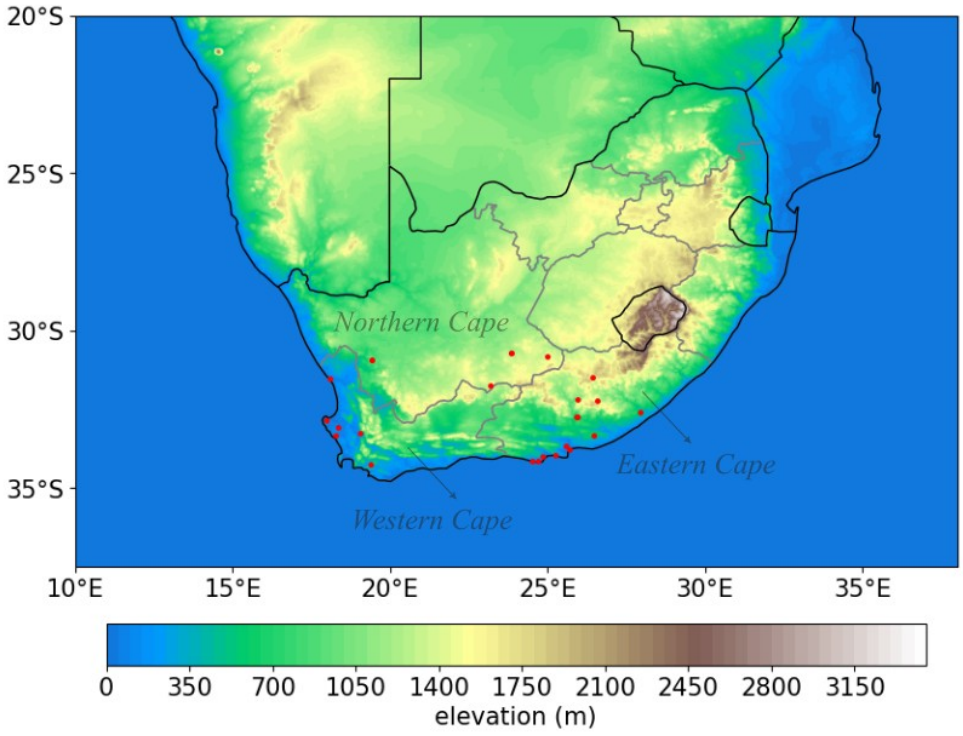

Figure B.7 Spatial distribution of 25 wind farms in South Africa in 2019.

Table B.2 Detailed information on the 2019 wind farms in South Africa. The comparison of the province's installed capacity, derived from The Wind Power (black) and REDIS (blue), is shown in the rows next to each province.

wind farm (ID)	latitude	longitude	Status	Capacity (kW)	Number of turbines	hub height	rotor diameter	Cut-in wind	Cut-out wind	Rated wind	province
10655	-33.75	25.67	Production	1800	1	90.0	90.0	3.00	25	13.0	Eastern Cape
20215	-34.00	24.83	Production	138000	60	80.0	101.0	3.00	20	12.0	Eastern Cape
21724	-32.74	25.93	Production	138600	66	79.0	88.0	3.50	25	14.0	Eastern Cape
23989	-33.96	25.25	Production	27000	9	90.0	113.0	3.00	25	11.5	Eastern Cape
20879	-33.66	25.58	Production	60000	20	84.0	112.0	3.50	25	15.5	Eastern Cape
21733	-31.48	26.44	Production	100000	40	50.0	100.0	4.00	20	12.5	Eastern Cape
22461	-34.14	24.70	Production	80000	32	80.0	90.0	3.00	25	13.5	Eastern Cape
22705	-32.59	27.96	Production	21525	7	84.0	112.0	2.50	25	13.0	Eastern Cape
23002	-33.33	26.46	Production	24600	8	84.0	112.0	2.50	25	13.0	Eastern Cape
21757	-32.18	25.96	Production	134400	56	91.0	117.0	3.00	20	11.0	Eastern Cape
23318	-32.22	26.58	Production	95325	31	101.5	112.0	2.50	25	13.0	Eastern Cape
23819	-32.72	25.94	Production	88000	44	80.0	100.0	3.50	22	12.0	Eastern Cape
22331	-34.15	24.52	Production	111000	37	116.0	116.8	2.50	25	12.5	Eastern Cape
			sum	1020.25 (MW)	1010.31 (MW)						13 wind farms
20822	-31.73	23.18	Production	73800	41	95.0	100.0	4.00	20	12.0	Northern Cape
22618	-30.81	25.00	Production	80500	35	99.0	108.0	3.00	20	11.0	Northern Cape
26144	-30.72	23.85	Production	94500	63	72.5	86.0	2.50	25	10.5	Northern Cape
29612	-30.72	23.85	Production	144000	96	80.0	76.2				Northern Cape
22659	-30.94	19.43	Production	140300	61	99.5	108.0	3.00	20	11.0	Northern Cape
22660	-30.94	19.43	Production	140300	61	99.5	108.0	3.00	20	11.0	Northern Cape
			sum	673.4 (MW)	665.46 (MW)						6 wind farms
4098	-33.32	18.26	Production	5200	4	50.0	62.0	5.00	25	17.0	Western Cape

21107	-33.06	18.35	Production	66600	37	95.0	100.0	4.00	20	12.0	Western Cape
21730	-34.23	19.38	Production	27000	9	90.0	90.0	3.50	25	13.0	Western Cape
20103	-31.53	18.09	Production	105800	46	115.0	108.0	3.00	20	11.0	Western Cape
16810	-32.83	18.00	Production	94000	47	80.0	90.0	3.00	25	13.5	Western Cape
22276	-33.26	19.03	Production	138000	46	100.0	100.0	4.00	25	11.7	Western Cape
			sum	436.6 (MW)	418.72 (MW)						6 wind farms

B.4.2 Simulation of wind power and comparison to measurements

Using the wind farms' information shown in the Table B.2 with the RESKit model driven by wind speed products from ERA5_ori, ERA5_GWA, and ICON-LAM, hourly CFs in 2019 are simulated over all the wind farms in South Africa. When averaging all CFs of simulated wind power over all wind farms in a province, for comparison with the measured CFs at the province level, a weighted average is performed by weighting each wind farm according to its share of installed capacity in the province.

The frequency distribution comparisons between simulated and measured CFs for different provinces are shown in Figure B.8. The averaged CFs derived from ERA5_ori, ERA5_GWA, and ICON-LAM are 0.25, 0.30, and 0.38 for existing wind farms in South Africa, and the observed averaged CF is 0.37. Regionally, ICON-LAM better captures mean CFs, see the average CFs in the legend of Figure B.8, and also better reproduces the frequency distribution of measured CFs, compared to ERA5_ori and ERA5_GWA in Northern and Eastern Capes. ERA5_ori- and ERA5_GWA-based CFs show similar problems of simulating too many (largest discrepancy 11%) low CFs (< 0.375) and too few (largest discrepancy 2%) high CFs (> 0.375), although ERA5_GWA-based CFs are generally better than ERA5_ori-based CFs. In Western Cape, ERA5_GWA better resolves the simulated CFs above 0.7 and delivers the closest mean CF compared to measurements; ICON-LAM better reproduce CFs below 0.2 and all data sets fail to catch CFs in the range about [0.2, 0.7]; too many (largest discrepancy 1.8%) and too few (largest discrepancy 1%) CF occurrences above 0.7 are found with ICON-LAM and ERA5_ori, respectively. Further examination of the wind speed distribution in Figure B.9 confirms and/or explains our findings for CFs, ICON-LAM simulates more often wind speeds in the range of 9 to 15 m/s and less around the mean wind speed of approximately 6 m s^{-1} than the ERA5 products, although the general shape of the wind speed frequency distributions is similar, i.e., one modal distribution with changes in magnitude of central height and overall width, among the different wind speed products.

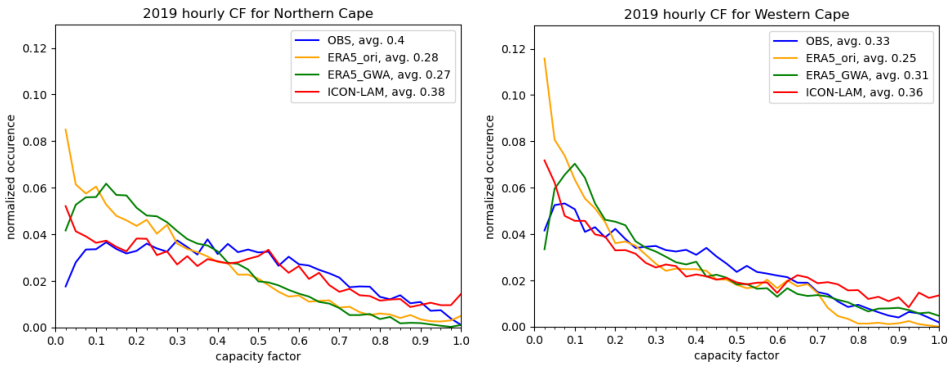

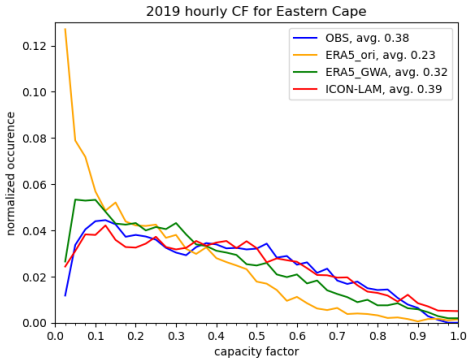

Figure B.8 Frequency distributions of measured (OBS) and simulated CFs from ERA5_ori, ERA5_GWA, and ICON-LAM with a bin size of 0.025 for three provinces in South Africa (Northern Cape, Western Cape, and Eastern Cape). Averaged CF are presented next to the legend of each product.

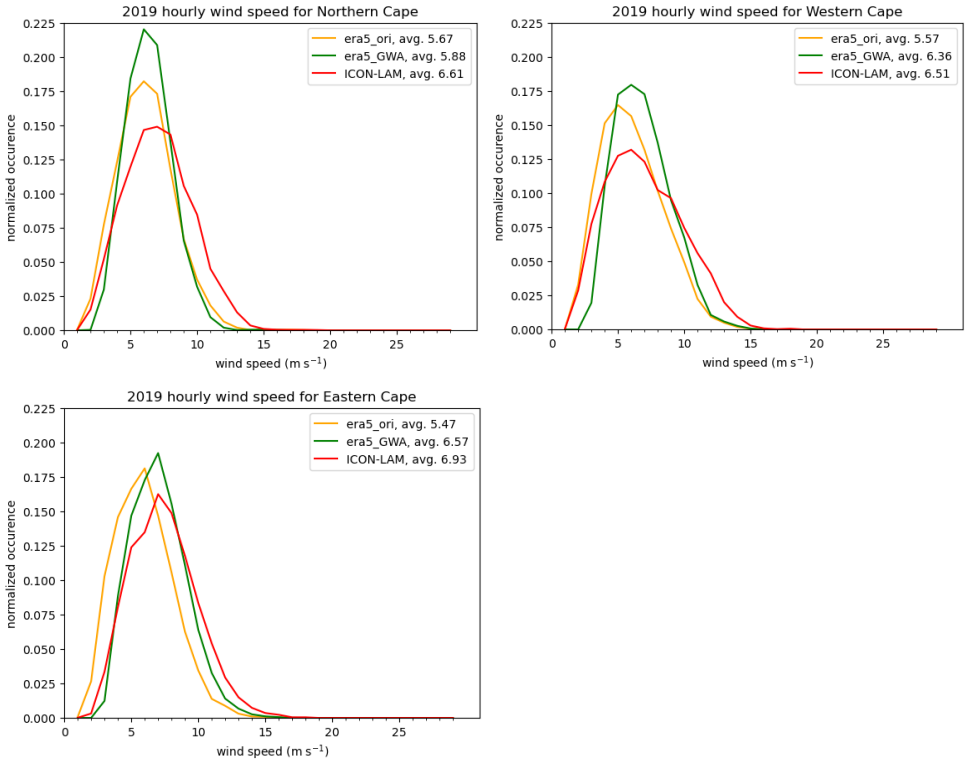

Figure B.9 As in Figure B.8, but for the corresponding wind speed frequency distribution with bin size of 1 m s^{-1}.

B.5 Comparison of CF time series, annual and average CF derived from different wind speed products

B.5.1 Investigation of time series differences in CF between ICON-LAM and ERA5

With the aim of investigating the time series' similarity and differences between ERA5 (EAR5_ori and ERA5_GWA) and ICON-LAM derived CFs for each of the about 1.8 million southern African eligible wind turbine placements, a Detrended Cross Correlation Analysis (DCCA) (Podobnik & Stanley, 2008) is performed. Although DCCA indicates the correlation between two variables like R, DCCA removes the inherent trend from the analyzed time series and is able to provide insights regarding how two time series are related, which might not be captured by simple correlation metrics like R. Additionally, ME, MAE, and R are also calculated for the comparison of CFs time series derived from ICON-LAM against those from ERA5 products.

Figure B.10 examines the differences in the CF time series derived from ERA5_ori, ERA5_GWA, and ICON-LAM across the 1.8 million eligible wind turbine placements in the ICON-LAM domain. In most cases, ICON-LAM shows larger CF compared to ERA5 (Figure B.10a and B.10b) with some exceptions over flat terrain in western South Africa and southern Namibia (Figure B.10a) and steep terrain, e.g., in the Drakensberg region in South Africa and Lesotho (Figure B.10b) (see Figure 4.2a for the topography and place names in the model domain). Spatially, the mean absolute differences (MAE) between ICON-LAM-based and ERA5-based (ERA5_ori in Figure B.10c and ERA5_GWA in Figure B.10d) CFs over all the placements are generally below 0.3 for most of the placements (>98%). Quite similar patterns in correlation coefficients are found between ICON-LAM and ERA5_ori on one hand and ICON-LAM and ERA5_GWA on the other hand; larger correlation coefficient values exist in the southwest and northeast. The DCCA metric gives a similar signal.

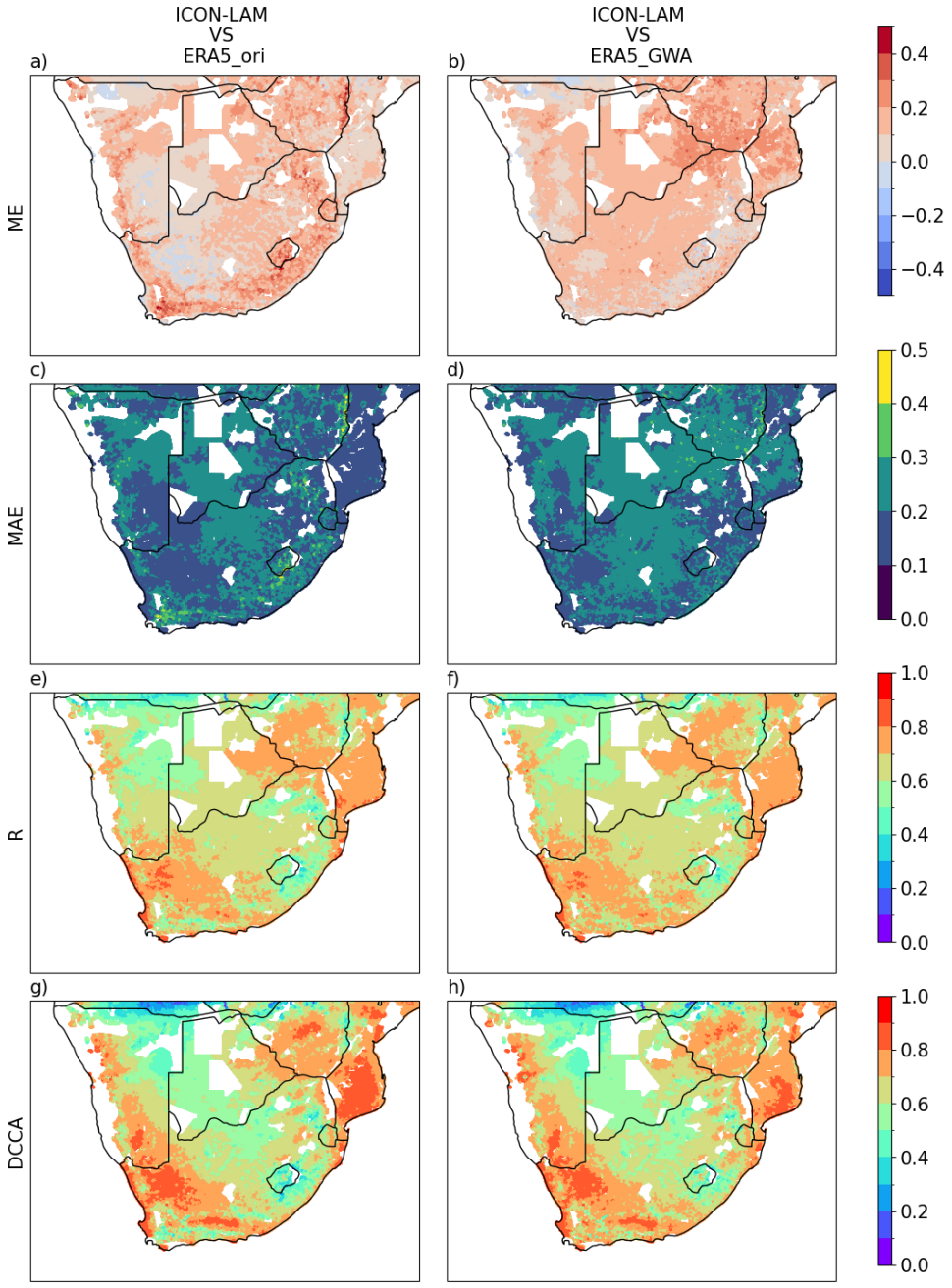

Figure B.10 Comparison of time series of estimated CFs between ICON-LAM-based and ERA5-based wind energy potentials for all 1.8 million eligible wind turbine placements in southern Africa; 1st column ICON-LAM vs ERA5_ori; 2nd column ICON-LAM vs ERA5_GWA for ME, MAE, R, and DCCA. White spots are areas where no wind turbine

placement is possible according to (Franzmann et al., 2023; Ishmam et al., 2024; Winkler et al., 2025).

B.5.2 Comparison of different wind speed products derived annual and 3-year average CF

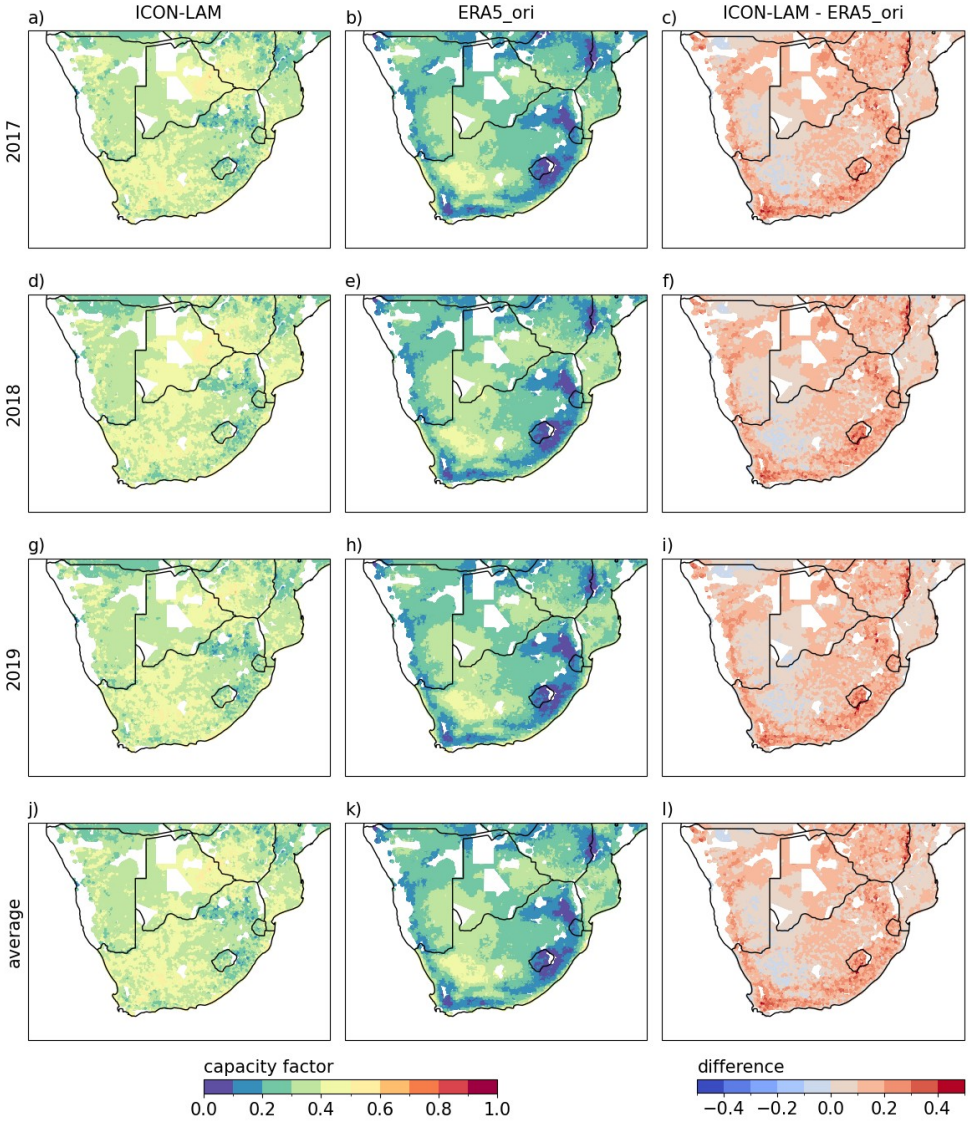

Figure B.11 Differences (3rd column) of averaged CF derived from ICON-LAM (1st column) and ERA5_ori (2nd column) mapped across all the eligible wind turbine placements southern Africa for the years 2017, 2018, and 2019, and 3 years average.

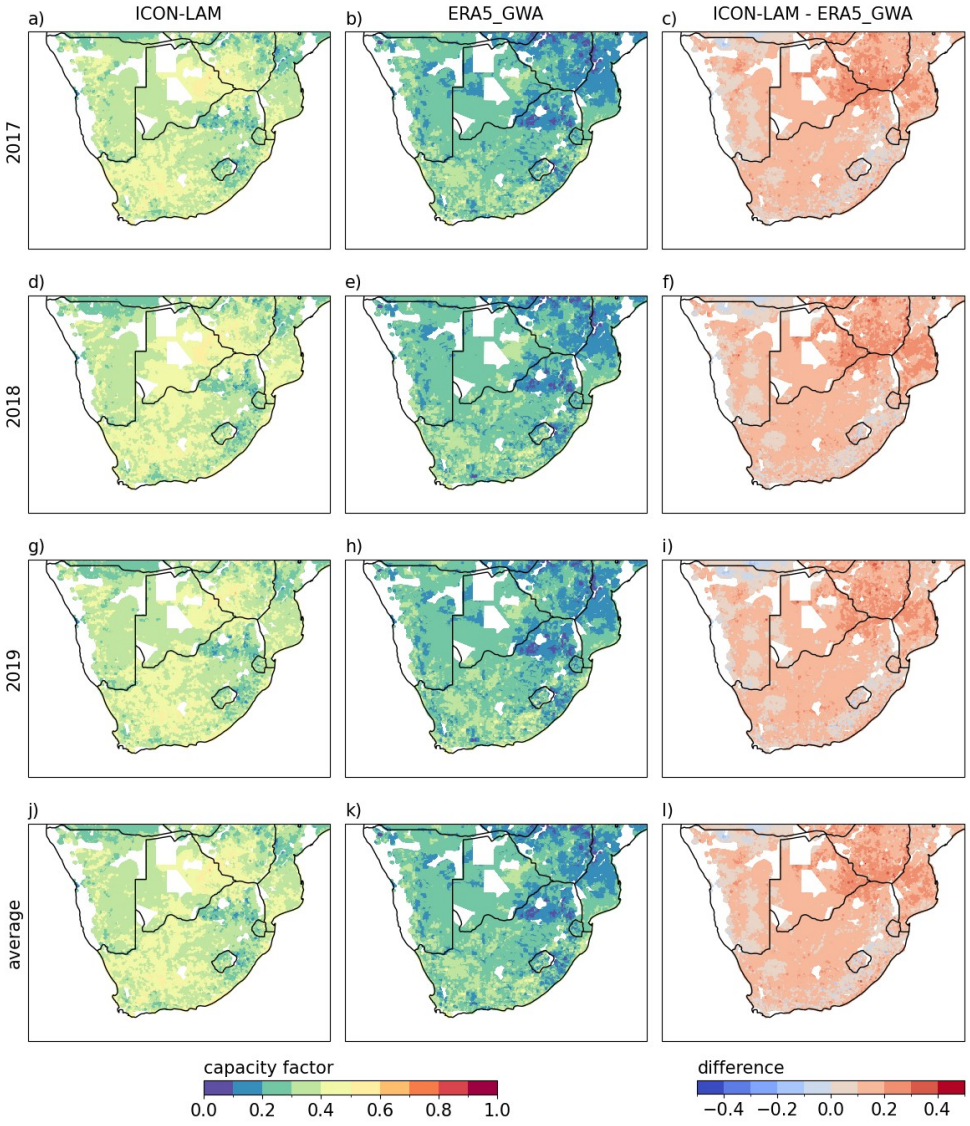

Figure B.12 As in Figure B.11, but for the ERA5_GWA.

B.6 Exploration of the frequency distribution of simulated wind speeds and its derived CFs across eligible wind turbine placements country by country

The frequency distribution comparisons between simulated hourly CFs averaged over all the eligible wind turbine placements for different countries derived from ERA5_ori, ERA5_GWA, and ICON-LAM are shown in Figure B.13, and the corresponding wind speeds frequency distributions are in Figure B.14. Similar to the distribution pattern of simulated CFs derived

from ERA5_ori, ERA5_GWA, and ICON-LAM found in Figure B.11, the CFs simulated by two ERA5 variants have more low CFs and few high CFs compared to by ICON-LAM over all eligible wind turbine placements in southern Africa, but the differences between products intensified compared to Figure B.11. In general, CFs from ERA5_ori agree more with ICON-LAM over relatively flat terrain countries such as Mozambique and Botswana, while ERA5_GWA CFs are more consistent with ICON-LAM over contrasting terrain such as Lesotho. The frequency distributions of wind speed (Figure B.14) show a similar pattern but in a more condensed form when compared to the CFs in Figure B.13. The cube of the wind speed when converting wind speed to wind power could be the underlying reason.

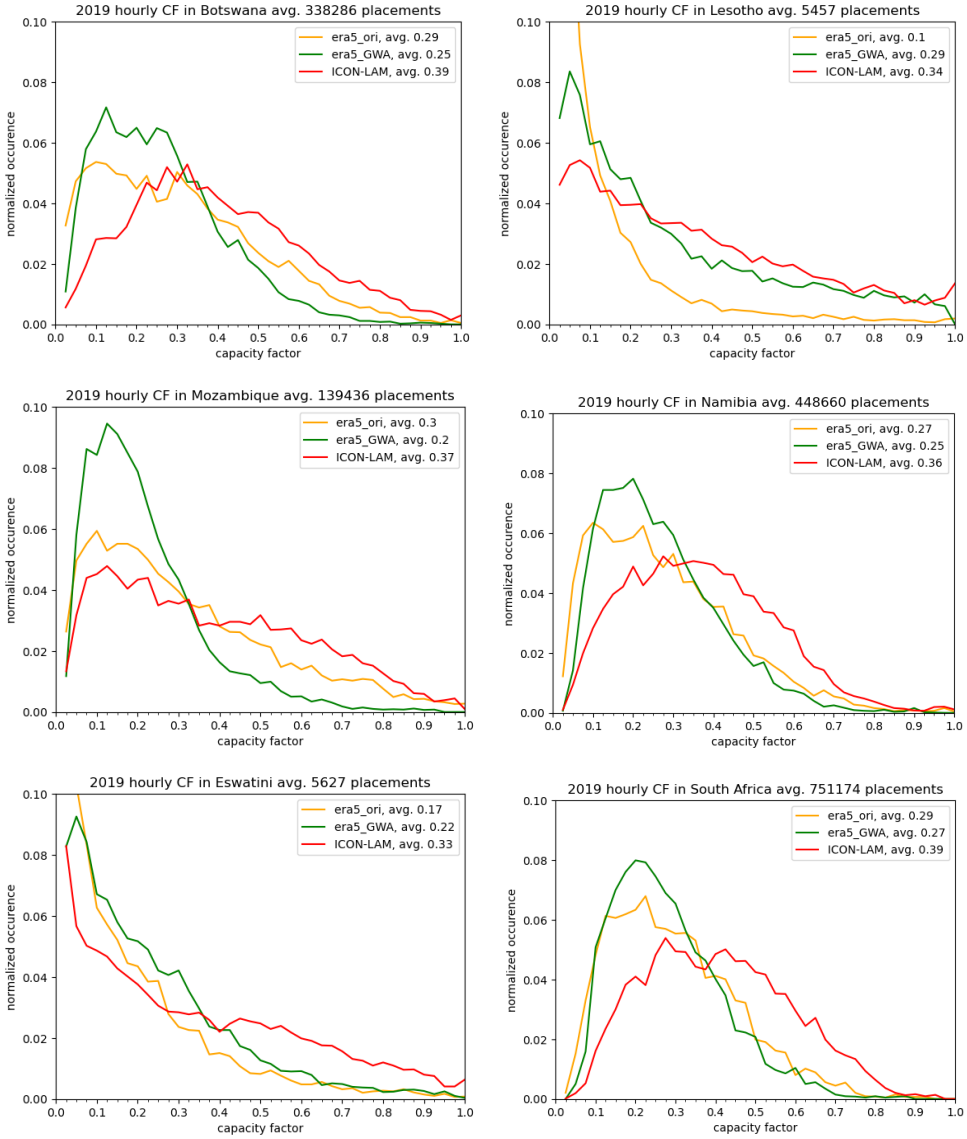

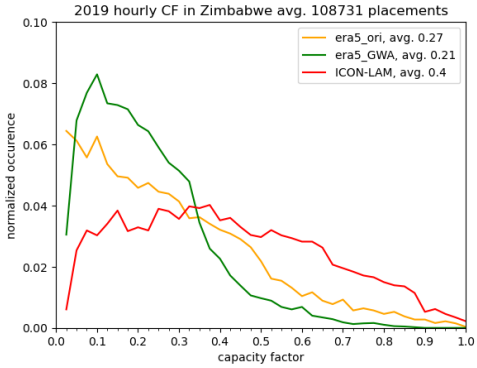

Figure B.13 As in Figure B.8, but over the eligible wind turbine placements for seven countries in southern Africa.

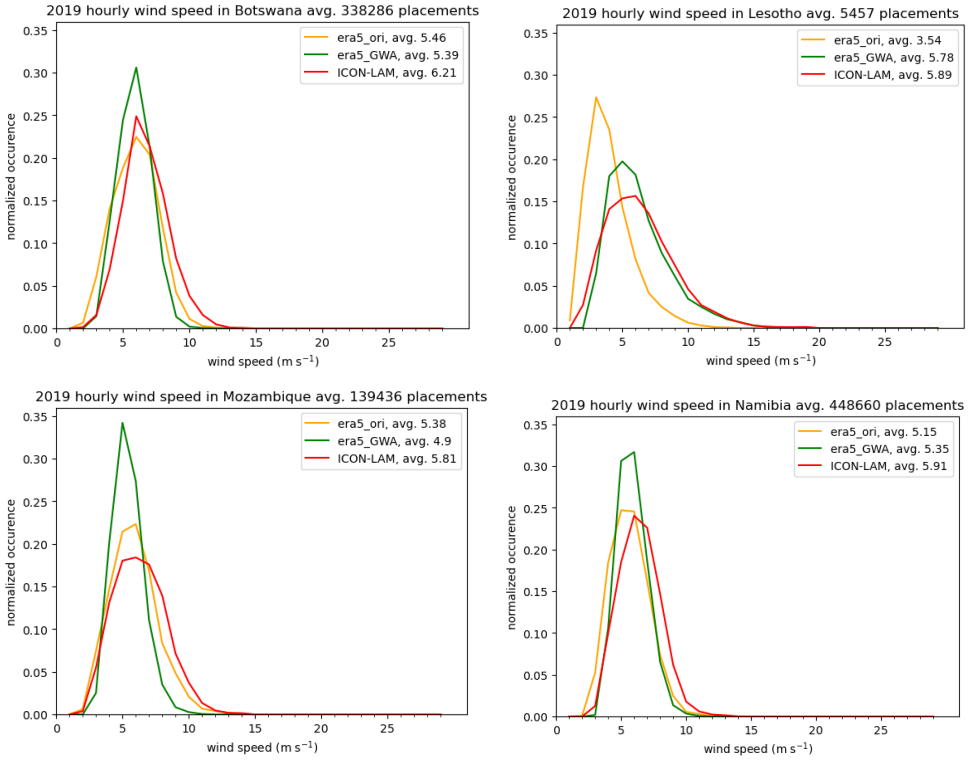

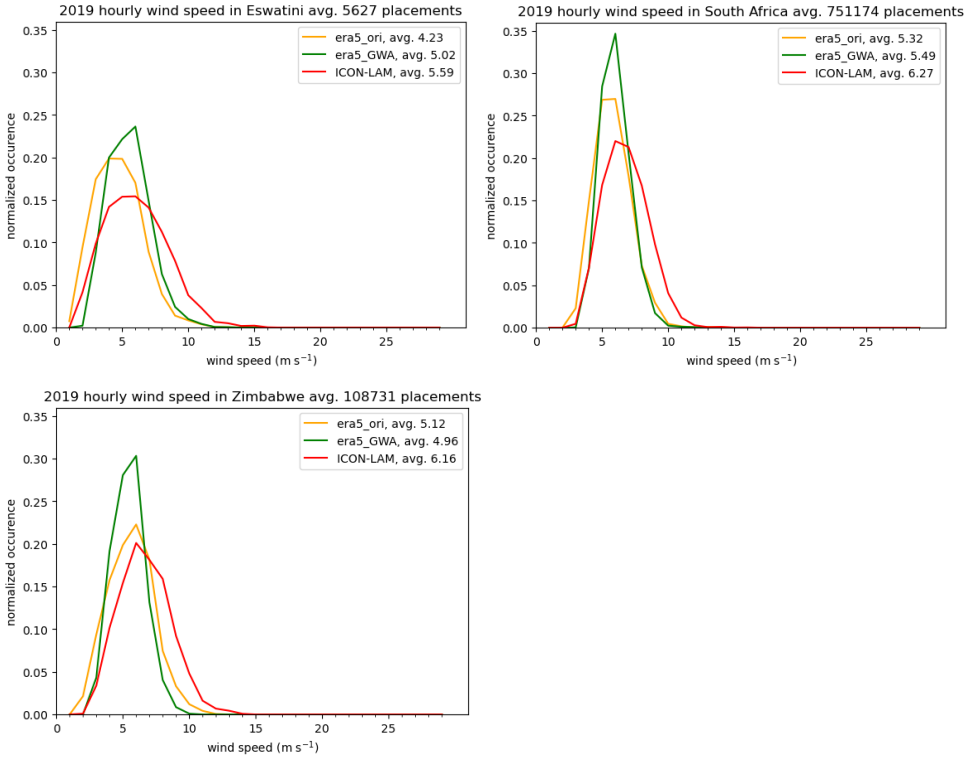

Figure B.14 As in Figure B.13, but for the corresponding wind speed frequency distribution with bin size of 1 m s^{-1} over the eligible wind turbine placements for seven countries in southern Africa.

B.7 The estimated wind power over eligible placements across southern Africa

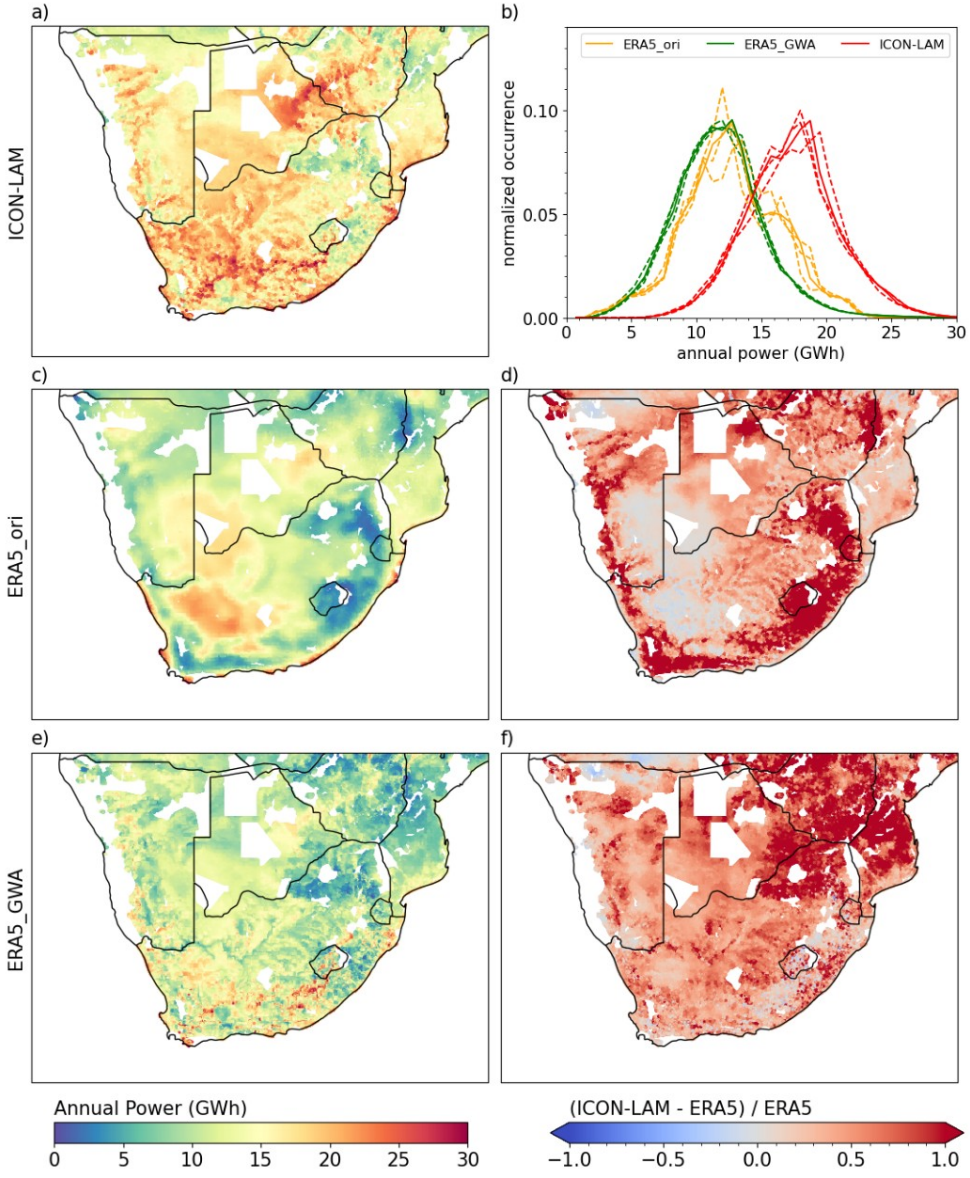

Figure B.15 As in Figure 4.3, but for the estimated average annual total power for 2017-2019, simulated by the RESKit model with the HOpt wind turbine, across all eligible wind turbine placements in southern Africa. The used bin size of power in subplot b) is 0.75 GWh.

C. Appendix C

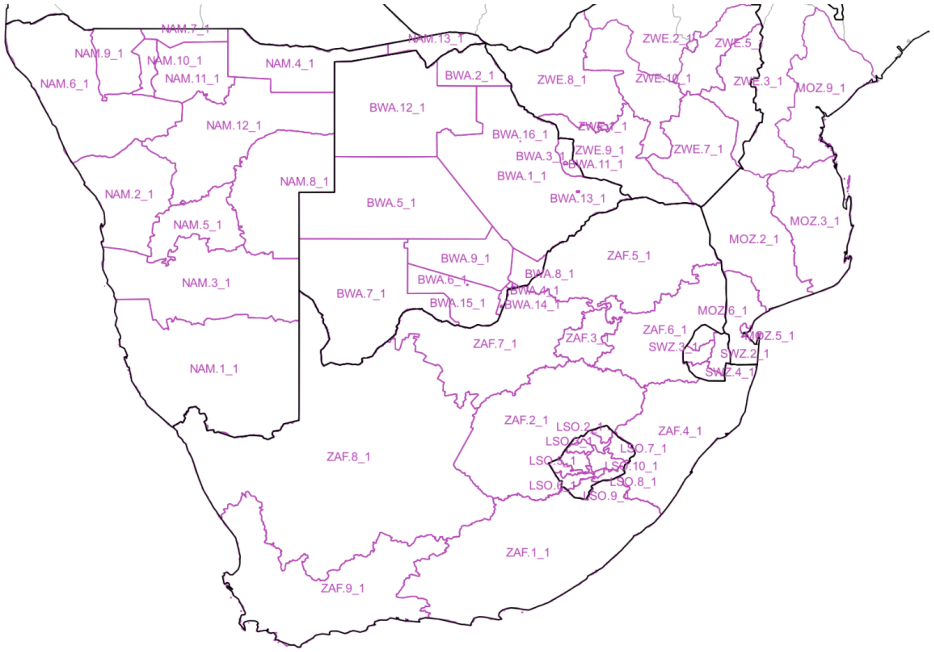

Figure C.1 Location of the 65 fully covered provinces by the ICON-LAM domain over southern Africa. Provincial boundaries are coloured purple and country boundaries are coloured black. For country names and the reference of the indexed province name to the full name, readers are forwarded to Table C.1.

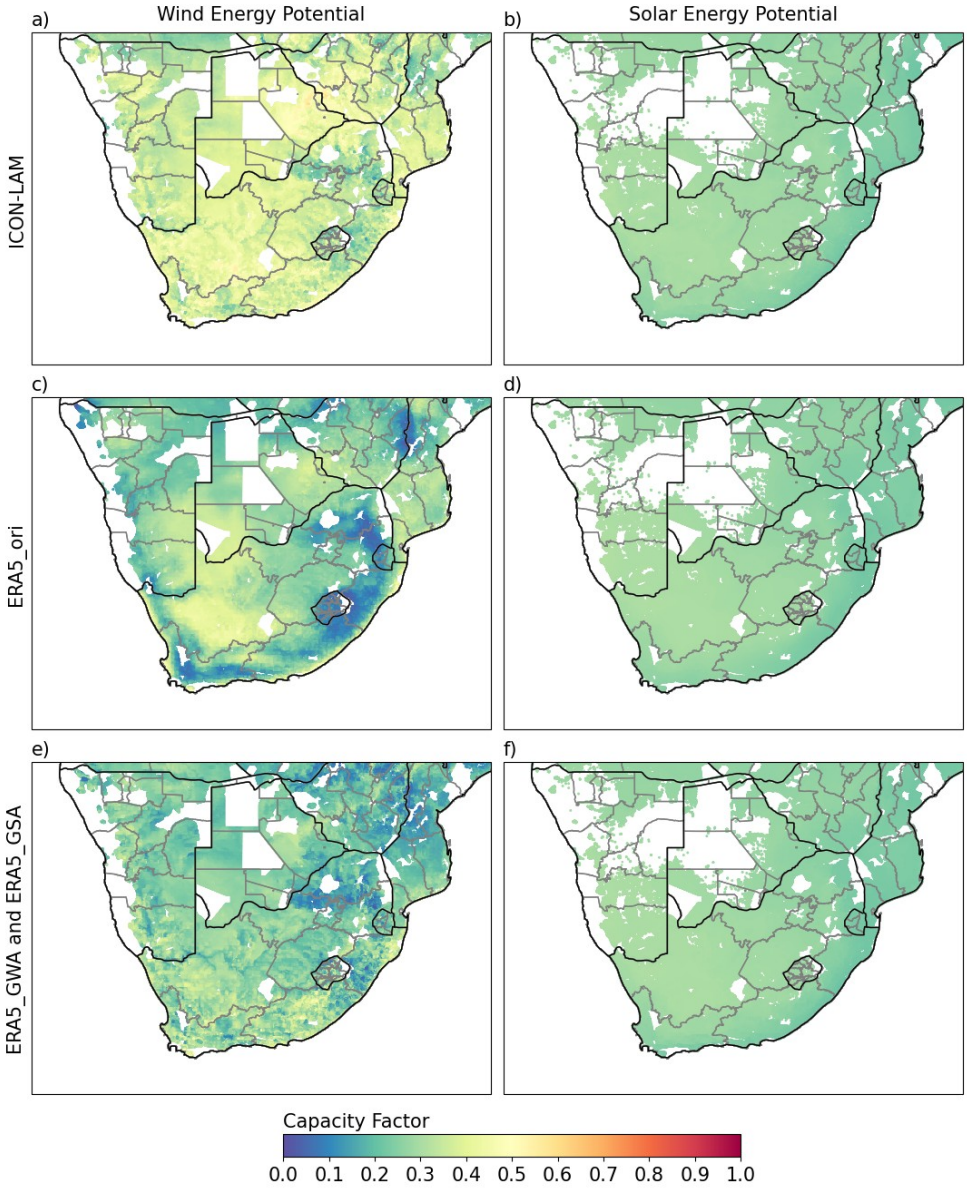

Figure C.2 As in Figure 5.3, but comparison of the capacity factor.

Table C.1 Information on all provinces in southern Africa fully covered by this study and their feasibility to build a cost-optimized energy system.

No.	Country	Country code (ISO-3166-1 alpha 3 code)	Province code (GID_1 code)	Province	Area (km^2)	Cost-optimized energy system feasible to build or not?	If not, why?
1	Botswana	BWA	BWA.1_1	Central	146579.22	yes	
2	Botswana	BWA	BWA.2_1	Chobe	20963.93	no	no valid energy system provided
3	Botswana	BWA	BWA.3_1	Francistown	92.86	no	no eligible solar or wind placements found
4	Botswana	BWA	BWA.4_1	Gaborone	281.35	no	problem proven to be infeasible or unbounded
5	Botswana	BWA	BWA.5_1	Ghanzi	114402.57	yes	
6	Botswana	BWA	BWA.6_1	Jwaneng	14.06	no	no eligible solar or wind placements found
7	Botswana	BWA	BWA.7_1	Kgalagadi	105128.85	no	no valid energy system provided
8	Botswana	BWA	BWA.8_1	Kgatleng	7786.39	yes	
9	Botswana	BWA	BWA.9_1	Kweneng	36938.09	yes	
10	Botswana	BWA	BWA.10_1	Lobatse	23.79	no	no eligible solar or wind placements found
11	Botswana	BWA	BWA.11_1	North-East	5249.15	yes	
12	Botswana	BWA	BWA.12_1	North-West	111333.66	yes	
13	Botswana	BWA	BWA.13_1	Selibe Phikwe	46.16	no	no eligible solar or wind placements found
14	Botswana	BWA	BWA.14_1	South-East	1690.56	yes	
15	Botswana	BWA	BWA.15_1	Southern	27334.43	yes	

16	Botswana	BWA	BWA.16_1	Sowa	4.43	no	no eligible solar or wind placements found
17	Lesotho	LSO	LSO.1_1	Berea	1992.05	yes	
18	Lesotho	LSO	LSO.2_1	Butha-Buthe	1789.24	yes	
19	Lesotho	LSO	LSO.3_1	Leribe	2818.12	yes	
20	Lesotho	LSO	LSO.4_1	Mafeteng	2650.36	yes	
21	Lesotho	LSO	LSO.5_1	Maseru	3767.99	yes	
22	Lesotho	LSO	LSO.6_1	Mohale's Hoek	3439.60	yes	
23	Lesotho	LSO	LSO.7_1	Mokhotlong	4169.05	yes	
24	Lesotho	LSO	LSO.8_1	Qacha's Nek	2122.69	no	no valid energy system provided
25	Lesotho	LSO	LSO.9_1	Quthing	2964.57	yes	
26	Lesotho	LSO	LSO.10_1	Thaba-Tseka	4831.60	yes	
27	Mozambique	MOZ	MOZ.2_1	Gaza	75467.55	yes	
28	Mozambique	MOZ	MOZ.3_1	Inhambane	68708.24	yes	
29	Mozambique	MOZ	MOZ.6_1	Maputo	22903.42	yes	
30	Mozambique	MOZ	MOZ.5_1	Maputo City	701.58	no	problem proven to be infeasible or unbounded
31	Mozambique	MOZ	MOZ.9_1	Sofala	68071.81	yes	
32	Namibia	NAM	NAM.1_1	!Karas	161182.45	yes	
33	Namibia	NAM	NAM.2_1	Erongo	63612.63	yes	
34	Namibia	NAM	NAM.3_1	Hardap	109698.00	yes	
35	Namibia	NAM	NAM.4_1	Kavango	48687.34	yes	

36	Namibia	NAM	NAM.5_1	Khomas	37074.03	yes	
37	Namibia	NAM	NAM.6_1	Kunene	115329.68	yes	
38	Namibia	NAM	NAM.7_1	Ohangwena	10649.00	yes	
39	Namibia	NAM	NAM.8_1	Omaheke	84749.19	yes	
40	Namibia	NAM	NAM.9_1	Omusati	26601.96	yes	
41	Namibia	NAM	NAM.10_1	Oshana	8652.19	yes	
42	Namibia	NAM	NAM.11_1	Oshikoto	38638.39	yes	
43	Namibia	NAM	NAM.12_1	Otjozondjupa	104631.88	yes	
44	Namibia	NAM	NAM.13_1	Zambezi	14354.56	yes	
45	Swaziland	SWZ	SWZ.1_1	Hhohho	3642.62	yes	
46	Swaziland	SWZ	SWZ.2_1	Lubombo	5851.45	yes	
47	Swaziland	SWZ	SWZ.3_1	Manzini	4124.36	yes	
48	Swaziland	SWZ	SWZ.4_1	Shiselweni	3764.82	yes	
49	South Africa	ZAF	ZAF.1_1	Eastern Cape	168905.15	yes	
50	South Africa	ZAF	ZAF.2_1	Free State	129825.16	yes	
51	South Africa	ZAF	ZAF.3_1	Gauteng	18178.31	no	problem proven to be infeasible or unbounded
52	South Africa	ZAF	ZAF.4_1	KwaZulu-Natal	93282.88	yes	
53	South Africa	ZAF	ZAF.5_1	Limpopo	125754.01	yes	
54	South Africa	ZAF	ZAF.6_1	Mpumalanga	76492.34	yes	
55	South Africa	ZAF	ZAF.7_1	North West	104881.67	yes	

56	South Africa	ZAF	ZAF.8_1	Northern Cape	372916.54	yes	
57	South Africa	ZAF	ZAF.9_1	Western Cape	129472.96	yes	
58	Zimbabwe	ZWE	ZWE.1_1	Bulawayo	458.31	no	no valid energy system provided
59	Zimbabwe	ZWE	ZWE.2_1	Harare	897.17	no	problem proven to be infeasible or unbounded
60	Zimbabwe	ZWE	ZWE.3_1	Manicaland	35598.68	yes	
61	Zimbabwe	ZWE	ZWE.5_1	Mashonaland East	32096.32	yes	
62	Zimbabwe	ZWE	ZWE.7_1	Masvingo	56280.09	yes	
63	Zimbabwe	ZWE	ZWE.8_1	Matabeleland North	75500.54	yes	
64	Zimbabwe	ZWE	ZWE.9_1	Matabeleland South	54675.71	yes	
65	Zimbabwe	ZWE	ZWE.10_1	Midlands	49440.09	yes	

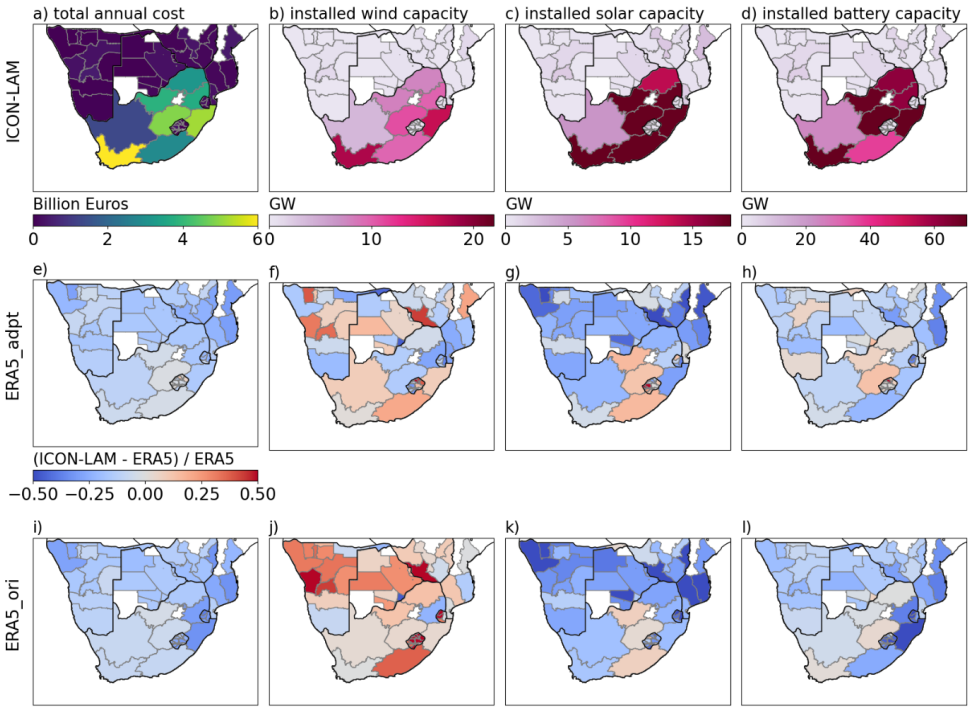

Figure C.3 As in Figure 5.6 but based on the weather year 2018.

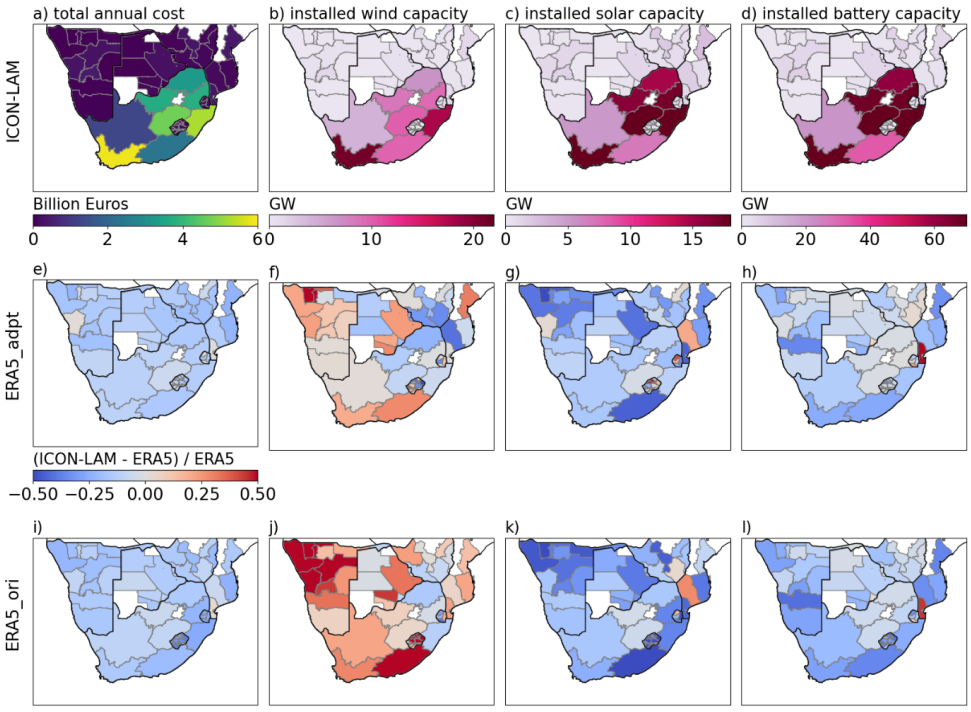

Figure C.4 As in Figure C.3 but for the weather year 2019.

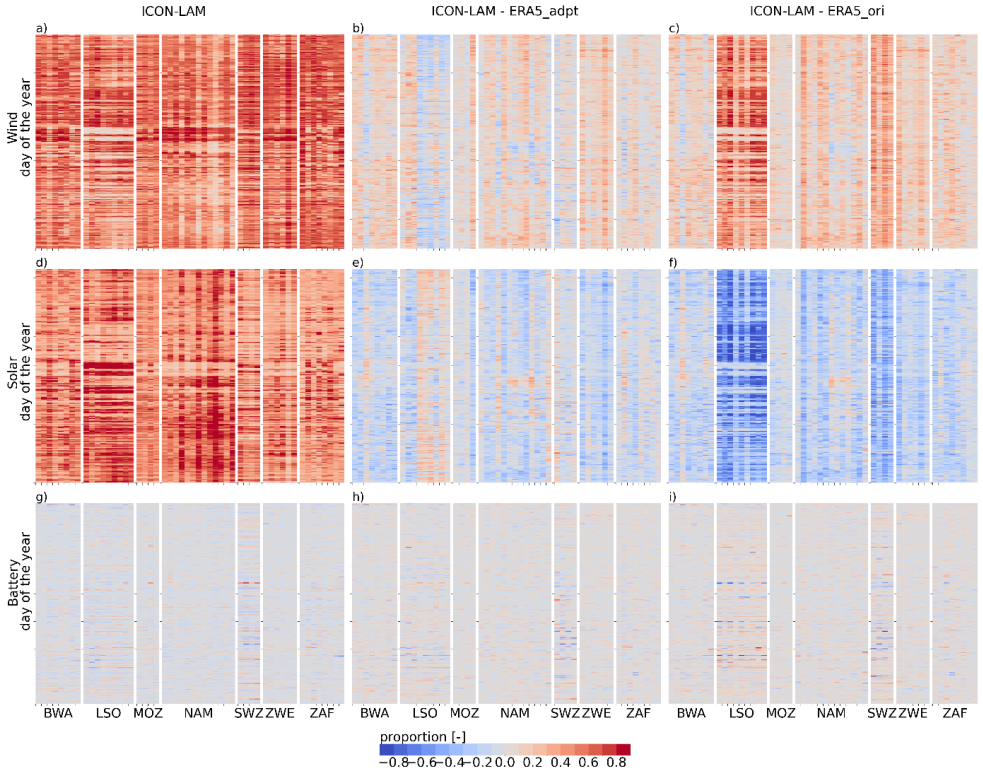

Figure C.5 As in Figure 5.9 but based on the weather year 2018.

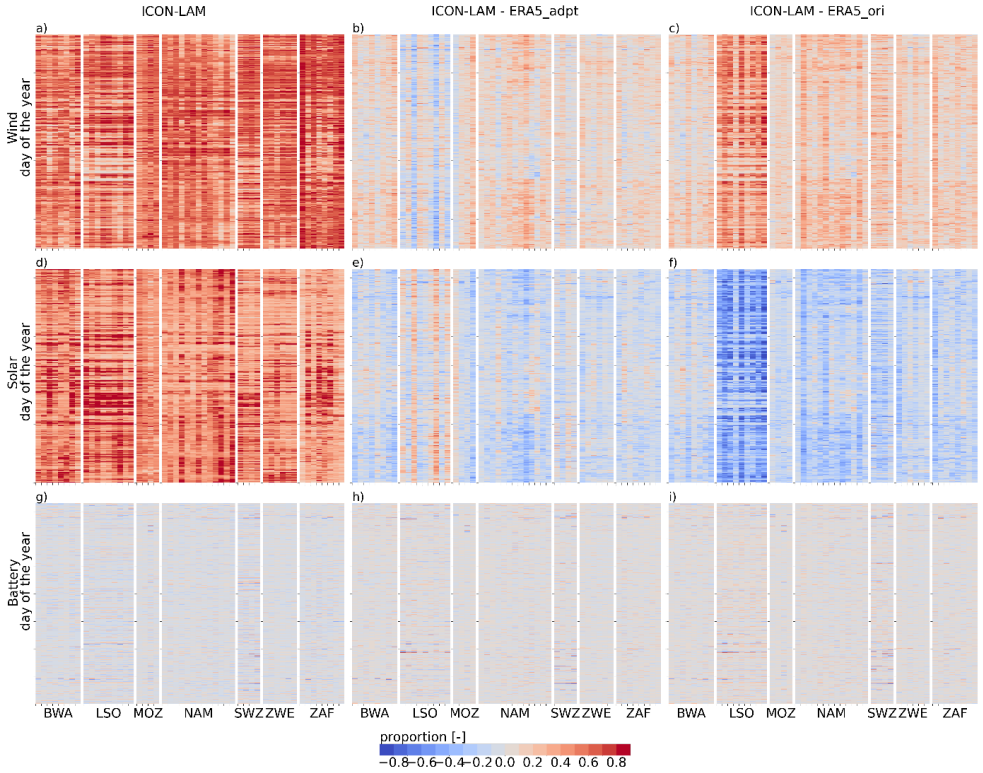

Figure C.6 As in Figure C.5 but for the weather year 2019.

Acknowledgements

I would like to thank Prof. Dr. Harrie-Jan Hendricks Franssen for promoting and coordinating this interdisciplinary PhD project in the fields of “Earth System Modelling” and “Energy Systems Design” as a joint work of the Institute of Bio- and Geosciences - Agrosphere (IBG-3) and the Institute of Climate and Energy Systems - Jülich Systems Analysis (ICE-2), Forschungszentrum Jülich GmbH, for three and three-quarter years. His broad knowledge and perceptive insights are impressive, and he always helps to keep this project on track.

I would also like to express my great gratitude to Dr. Klaus Görgen, as a professional climatologist he provided many excellent and helpful ideas during the tough moments of this project. His passion for scientific research and his rigorous and meticulous work ethic were deeply imprinted in this project and in me.

I am also very grateful for the solid support I received from Prof. Dr. Heidi Ursula Heinrichs, an energy systems expert. She brought the knowledge of energy systems into this project and actively pushed this project forward. Her spirit of scientific critical thinking and her successful way of time management shaped this project and me.

I also gratefully knowledge Dr. Stefan Poll, who is a meteorologist and an expert of the ICON atmospheric model. He dedicated lots of effort to make the 1st time running of ICON NWP core happen in the institute, helped me solve the technical issues that arose when running the ICON model, and generously shared his experience in working with the ICON model as well as with the High Performance Computing (HPC) at the Jülich Supercomputing Centre (JSC).

I am also thankful to Christoph Winkler for he conducted the land eligibility and placements identification analysis that is the basis for the Renewable Energy Potential (REP) estimates carried out in this project, for working with me to perform the REP calculations on the ICE-2 cluster, and for the interesting scientific ideas he proposed and the fruitful discussions we had.

I thank David Franzmann for his help in adapting me to the ICE-2 cluster, our discussions for using the RESKit model, and guiding me through the energy system modelling. I also thank Dr. David Severin Ryberg who initially built the RESKit model and the ICE-2 RESKit team, Philipp Dunkel, Edgar Ubaldo Pena Sanchez, and Shitab Ishmam, who actively maintained the RESKit model.

I appreciate all the interesting and inspiring discussions I had with IBG-3 Directors Prof. Dr. Harry Vereecken and Prof. Dr. Jan Vanderborght and the inputs I received from ICE-2 Deputy Director Prof. Dr. Jochen Linßen.

Thanks to Dr. Ruben Borgers who works on wind energy at KU Leuven for all the helpful discussions we had and to Dr. Trentmann Jörg from DWD for his patient support in using SARAH-3 dataset for this project. Special thanks to my other colleagues from IBG-3 and ICE-2, my dear friends, and my family, for being with me through all the painful, peaceful, and joyful PhD moments.

Bibliography

Adelaja, A. O. (2020). Barriers to national renewable energy policy adoption: Insights from a case study of Nigeria. Energy Strategy Reviews, 30, 100519.

Akinbami, O. M., Oke, S. R., & Bodunrin, M. O. (2021). The state of renewable energy development in South Africa: An overview. Alexandria Engineering Journal, 60(6), 5077-5093.

Allen, R. G., Pereira, L. S., Raes, D., & Smith, M. (1998). Crop evapotranspiration-Guidelines for computing crop water requirements-FAO Irrigation and drainage paper 56 - Chapter 3 Meteorological data. Fao, Rome, 300(9), D05109.

Allouhi, A., Rehman, S., Buker, M. S., & Said, Z. (2022). Up-to-date literature review on Solar PV systems: Technology progress, market status and R&D. Journal of Cleaner Production, 362, 132339.

Amir, M., & Khan, S. Z. (2021). Assessment of renewable energy: Status, challenges, COVID-19 impacts, opportunities, and sustainable energy solutions in Africa. Energy and Built Environment.

Anis, W. R., & Nour, M. A.-S. (1995). Energy losses in photovoltaic systems. Energy Conversion and Management, 36(11), 1107-1113.

Antonini, E. G., Virgüez, E., Ashfaq, S., Duan, L., Ruggles, T. H., & Caldeira, K. (2024). Identification of reliable locations for wind power generation through a global analysis of wind droughts. Communications Earth & Environment, 5(1), 103.

Apeh, O. O., Overen, O. K., & Meyer, E. L. (2021). Monthly, seasonal and yearly assessments of global solar radiation, clearness index and diffuse fractions in alice, South Africa. Sustainability, 13(4), 2135.

Arias, P., Bellouin, N., Coppola, E., Jones, R., Krinner, G., Marotzke, J., Naik, V., Palmer, M., Plattner, G.-K., & Rogelj, J. (2021). Climate Change 2021: the physical science basis. Contribution of Working Group I to the Sixth Assessment Report of the Intergovernmental Panel on Climate Change; technical summary.

Aurora Solar. (2023). Aurora's PV System Losses Series: Part 1 Nameplate, Mismatch, and LID Losses, Part 2 Wiring, Connections, and System Availability, Part 3 Soiling, Snow, System Degradation, and Part 4 Tilt & Orientation, Incident Angle Modifier, Environmental Conditions, and Inverter Losses & Clipping. https://aurorasolar.com/blog/understanding-pv-system-losses-part-1/

Ayompe, L. M., Davis, S. J., & Egoh, B. N. (2021). Trends and drivers of African fossil fuel CO2 emissions 1990–2017. Environmental Research Letters, 15(12), 124039.

Babar, B., Graversen, R., & Boström, T. (2019). Solar radiation estimation at high latitudes: Assessment of the CMSAF databases, ASR and ERA5. Solar Energy, 182, 397-411.

Bale, C. S., Varga, L., & Foxon, T. J. (2015). Energy and complexity: New ways forward. Applied Energy, 138, 150-159.

Ban, N., Caillaud, C., Coppola, E., Pichelli, E., Sobolowski, S., Adinolfi, M., Ahrens, B., Alias, A., Anders, I., Bastin, S., Belušić, D., Berthou, S., Brisson, E., Cardoso, R. M., Chan, S. C., Christensen, O. B., Fernández, J., Fita, L., Frisius, T., . . . Zander, M. J. (2021). The first multi-model ensemble of regional climate simulations at kilometer-scale

resolution, part I: evaluation of precipitation. Climate Dynamics, 57(1-2), 275-302. https://doi.org/10.1007/s00382-021-05708-w

Benasla, M., Allaoui, T., Brahami, M., Denai, M., & Sood, V. K. (2018). HVDC links between North Africa and Europe: Impacts and benefits on the dynamic performance of the European system. Renewable and sustainable energy reviews, 82, 3981-3991.

Bichet, A., Hingray, B., Evin, G., Diedhiou, A., Kebe, C. M. F., & Anquetin, S. (2019). Potential impact of climate change on solar resource in Africa for photovoltaic energy: analyses from CORDEX-AFRICA climate experiments. Environmental Research Letters, 14(12), 124039.

Birch, C. E., Parker, D. J., Marsham, J. H., Copsey, D., & Garcia-Carreras, L. (2014). A seamless assessment of the role of convection in the water cycle of the West African Monsoon. Journal of Geophysical Research: Atmospheres, 119(6), 2890-2912. https://doi.org/10.1002/2013jd020887

Blamey, R., & Reason, C. (2009). Numerical simulation of a mesoscale convective system over the east coast of South Africa. Tellus A: Dynamic Meteorology and Oceanography, 61(1), 17-34.

Blanco, H., & Faaij, A. (2018). A review at the role of storage in energy systems with a focus on Power to Gas and long-term storage. Renewable and sustainable energy reviews, 81, 1049-1086.

Bloomfield, H., Brayshaw, D., & Charlton-Perez, A. (2020). ERA5 derived time series of European country-aggregate electricity demand, wind power generation and solar power generation: hourly data from 1979-2019.

Bloomfield, H. C., Wainwright, C. M., & Mitchell, N. (2022). Characterizing the variability and meteorological drivers of wind power and solar power generation over Africa. Meteorological Applications, 29(5), e2093.

Blunden, J., & Boyer, T. (2022). State of the Climate in 2021. Bulletin of the American Meteorological Society, 103(8), S1-S465.

Bollmeyer, C., Keller, J. D., Ohlwein, C., Wahl, S., Crewell, S., Friederichs, P., Hense, A., Keune, J., Kneifel, S., & Pscheidt, I. (2015). Towards a high‐resolution regional reanalysis for the European CORDEX domain. Quarterly Journal of the Royal Meteorological Society, 141(686), 1-15.

Bolson, N., Prieto, P., & Patzek, T. (2022). Capacity factors for electrical power generation from renewable and nonrenewable sources. Proceedings of the National Academy of Sciences, 119(52), e2205429119.

Bratton, D. C., & Womeldorf, C. A. (2011). The wind shear exponent: Comparing measured against simulated values and analyzing the phenomena that affect the wind shear. Energy Sustainability,

Bucciarelli Jr, L. L. (1984). Estimating loss-of-power probabilities of stand-alone photovoltaic solar energy systems. Solar Energy, 32(2), 205-209.

Caglayan, D. G., Heinrichs, H. U., Linssen, J., Robinius, M., & Stolten, D. (2019). Impact of different weather years on the design of hydrogen supply pathways for transport needs. International Journal of Hydrogen Energy, 44(47), 25442-25456.

Caglayan, D. G., Heinrichs, H. U., Robinius, M., & Stolten, D. (2021). Robust design of a future 100% renewable european energy supply system with hydrogen infrastructure. International Journal of Hydrogen Energy. https://doi.org/10.1016/j.ijhydene.2020.12.197

Caglayan, D. G., Ryberg, D. S., Heinrichs, H., Linßen, J., Stolten, D., & Robinius, M. (2019). The techno-economic potential of offshore wind energy with optimized future turbine designs in Europe. Applied Energy, 255, 113794.

Caldwell, P., Chin, H.-N. S., Bader, D. C., & Bala, G. (2009). Evaluation of a WRF dynamical downscaling simulation over California. Climatic change, 95(3), 499-521.

Cao, Q., Liu, Y., Sun, X., & Yang, L. (2022). Country-level evaluation of solar radiation data sets using ground measurements in China. Energy, 241, 122938.

Caretta, A. M. M. A., Arfanuzzaman, R. B. M., Morgan, S. M. R., & Kumar, M. (2022). Water. In: Climate Change 2022: Impacts, Adaptation, and Vulnerability. Contribution of Working Group II to the Sixth Assessment Report of the Intergovernmental Panel on Climate Change.

Carta, J. A., & Mentado, D. (2007). A continuous bivariate model for wind power density and wind turbine energy output estimations. Energy Conversion and Management, 48(2), 420-432.

Chamberlain, J., Bain, C., Boyd, D., McCourt, K., Butcher, T., & Palmer, S. (2014). Forecasting storms over Lake Victoria using a high resolution model. Meteorological Applications, 21(2), 419-430.

Chen, S., Goergen, K., Hendricks Franssen, H. J., Winkler, C., Poll, S., Houssoukri Zounogo Wahabou, Y., Linssen, J., Vereecken, H., Stolten, D., & Heinrichs, H. (2024). Higher Onshore Wind Energy Potentials Revealed by Kilometer‐Scale Atmospheric Modeling. Geophysical Research Letters, 51(19). https://doi.org/10.1029/2024gl110122

Chen, S., Hamdi, R., Ochege, F. U., Du, H., Chen, X., Yang, W., & Zhang, C. (2019). Added Value of a Dynamical Downscaling Approach for Simulating Precipitation and Temperature Over Tianshan Mountains Area, Central Asia. Journal of Geophysical Research: Atmospheres, 124(21), 11051-11069. https://doi.org/10.1029/2019jd031016

Chen, S., Poll, S., Hendricks Franssen, H. J., Heinrichs, H., Vereecken, H., & Goergen, K. (2024). Convection‐Permitting ICON‐LAM Simulations for Renewable Energy Potential Estimates Over Southern Africa. Journal of Geophysical Research: Atmospheres, 129(6). https://doi.org/10.1029/2023jd039569

Choi, S.-J., & Klemp, J. B. (2021). A new hybrid sigma-pressure vertical coordinate with smoothed coordinate surfaces. Monthly Weather Review, 149(12), 4077-4089.

Clayson, C., Brown, J., & Program, N. C. (2016). NOAA Climate Data Record Ocean Surface Bundle (OSB) Climate Data Record (CDR) of Ocean Heat Fluxes, Version 2. Clim. Algorithm Theor. Basis Doc. C-ATBD Asheville NC NOAA Natl. Cent. Environ. Inf. Doi, 10, V59K4885. https://doi.org/https://doi.org/10.7289/V55T3HH0

Cochran, J., Bird, L., Heeter, J., & Arent, D. J. (2012). Integrating variable renewable energy in electric power markets. best practices from international experience.

Cook, K. H. (2000). The South Indian convergence zone and interannual rainfall variability over southern Africa. Journal of Climate, 13(21), 3789-3804.

Costoya, X., deCastro, M., Carvalho, D., & Gómez-Gesteira, M. (2023). Assessing the complementarity of future hybrid wind and solar photovoltaic energy resources for North America. Renewable and sustainable energy reviews, 173. https://doi.org/10.1016/j.rser.2022.113101

D'Isidoro, M., Briganti, G., Vitali, L., Righini, G., Adani, M., Guarnieri, G., Moretti, L., Raliselo, M., Mahahabisa, M., & Ciancarella, L. (2020). Estimation of solar and wind energy resources over Lesotho and their complementarity by means of WRF yearly simulation at high resolution. Renewable Energy, 158, 114-129.

Davidson, M. R., & Millstein, D. (2022). Limitations of reanalysis data for wind power applications. Wind Energy. https://doi.org/10.1002/we.2759

Davidson, M. R., & Millstein, D. (2022). Limitations of reanalysis data for wind power applications. Wind Energy, 25(9), 1646-1653.

Davis, N. N., Badger, J., Hahmann, A. N., Hansen, B. O., Mortensen, N. G., Kelly, M., Larsén, X. G., Olsen, B. T., Floors, R., Lizcano, G., Casso, P., Lacave, O., Bosch, A., Bauwens, I., Knight, O. J., Potter van Loon, A., Fox, R., Parvanyan, T., Krohn Hansen, S. B., . . . Drummond, R. (2023). The Global Wind Atlas: A High-Resolution Dataset of Climatologies and Associated Web-Based Application. Bulletin of the American Meteorological Society, 104(8), E1507-E1525. https://doi.org/10.1175/bams-d-21-0075.1

De Lucia, C., Bucchignani, E., Mastellone, A., Adinolfi, M., Montesarchio, M., Cinquegrana, D., Mercogliano, P., & Schiano, P. (2022). A Sensitivity Study on High Resolution NWP ICON—LAM Model over Italy. Atmosphere, 13(4), 540.

Dee, D. P., Uppala, S. M., Simmons, A., Berrisford, P., Poli, P., Kobayashi, S., Andrae, U., Balmaseda, M., Balsamo, G., & Bauer, d. P. (2011). The ERA‐Interim reanalysis: Configuration and performance of the data assimilation system. Quarterly Journal of the Royal Meteorological Society, 137(656), 553-597.

Deguenon, L., Yamegueu, D., & Gomna, A. (2023). Overcoming the challenges of integrating variable renewable energy to the grid: A comprehensive review of electrochemical battery storage systems. Journal of Power Sources, 580, 233343.

Dehghan, M., Rashidi, S., & Waqas, A. (2022). Modeling of soiling losses in solar energy systems. Sustainable Energy Technologies and Assessments, 53, 102435.

Devis, A., van Lipzig, N. P., & Demuzere, M. (2014). A height dependent evaluation of wind and temperature over Europe in the CMIP5 Earth System Models. Climate research, 61(1), 41-56.

Devis, A., Van Lipzig, N. P. M., & Demuzere, M. (2018). Should future wind speed changes be taken into account in wind farm development? Environmental Research Letters, 13(6). https://doi.org/10.1088/1748-9326/aabff7

Dhass, A., Beemkumar, N., Harikrishnan, S., & Ali, H. M. (2022). A review on factors influencing the mismatch losses in solar photovoltaic system. International Journal of Photoenergy, 2022, 1-27.

Doddy Clarke, E., Griffin, S., McDermott, F., Monteiro Correia, J., & Sweeney, C. (2021). Which reanalysis dataset should we use for renewable energy analysis in Ireland? Atmosphere, 12(5), 624.

Doms, G., Förstner, J., Heise, E., Herzog, H., Mironov, D., Raschendorfer, M., Reinhardt, T., Ritter, B., Schrodin, R., & Schulz, J.-P. (2011). A description of the nonhydrostatic regional COSMO model. Part II: Physical Parameterization, 154.

Drechsel, S., Mayr, G. J., Messner, J. W., & Stauffer, R. (2012). Wind speeds at heights crucial for wind energy: measurements and verification of forecasts. Journal of Applied Meteorology and Climatology, 51(9), 1602-1617.

Du, Y., Shi, H., Zhang, J., Xia, X., Yao, Z., Fu, D., Hu, B., & Huang, C. (2022). Evaluation of MERRA-2 hourly surface solar radiation across China. Solar Energy, 234, 103-110.

Duah, N. T., & Asamoah, P. K. (2018). Renewable energy in Africa; Potential, impact and the way forward. ELEKTRIKA-Journal of Electrical Engineering, 17(1), 16-20.

Dubey, S., Sarvaiya, J. N., & Seshadri, B. (2013). Temperature dependent photovoltaic (PV) efficiency and its effect on PV production in the world–a review. Energy Procedia, 33, 311-321.

DWD. (2024). ICON model. Website, https://www.dwd.de/EN/research/weatherforecasting/num_modelling/01_num_weather_prediction_modells/icon_description.html?nn=484268

Edwards, M. R., Holloway, T., Pierce, R. B., Blank, L., Broddle, M., Choi, E., Duncan, B. N., Esparza, Á., Falchetta, G., & Fritz, M. (2022). Satellite Data Applications for Sustainable Energy Transitions. Frontiers in Sustainability, 64.

Ekici, S., & Kopru, M. A. (2017). Investigation of PV system cable losses. International Journal of Renewable Energy Research (IJRER), 7(2), 807-815.

Elsner, P. (2019). Continental-scale assessment of the African offshore wind energy potential: Spatial analysis of an under-appreciated renewable energy resource. Renewable and sustainable energy reviews, 104, 394-407. https://doi.org/10.1016/j.rser.2019.01.034

Ember. (2024). Electricity Data Explorer. https://ember-climate.org/data/data-tools/data-explorer/

Engelbrecht, C. J., Landman, W. A., Engelbrecht, F. A., & Malherbe, J. (2015). A synoptic decomposition of rainfall over the Cape south coast of South Africa. Climate Dynamics, 44, 2589-2607.

Epstein, A. (2014). The moral case for fossil fuels. Penguin.

European Centre for Medium-Range Weather Forecasts (ECMWF). (2024). New climate reanalysis: ERA6. https://www.ecmwf.int/en/about/media-centre/news/2024/copernicus-climate-change-service-provides-new-tools-users

European Commission. (2019). The European green deal. Eur. Comm., 53(9), 24.

Fasihi, M., & Breyer, C. (2020). Baseload electricity and hydrogen supply based on hybrid PV-wind power plants. Journal of Cleaner Production, 243, 118466.

Feron, S., Cordero, R. R., Damiani, A., & Jackson, R. B. (2021). Climate change extremes and photovoltaic power output. Nature Sustainability, 4(3), 270-276.

Fetting, C. (2020). The European green deal. ESDN Report, December, 2(9).

Frank, C. W., Pospichal, B., Wahl, S., Keller, J. D., Hense, A., & Crewell, S. (2020). The added value of high resolution regional reanalyses for wind power applications. Renewable Energy, 148, 1094-1109. https://doi.org/10.1016/j.renene.2019.09.138

Franzmann, D., Heinrichs, H., Lippkau, F., Addanki, T., Winkler, C., Buchenberg, P., Hamacher, T., Blesl, M., Linßen, J., & Stolten, D. (2023). Green hydrogen cost-potentials for global trade. International Journal of Hydrogen Energy.

Gal-Chen, T., & Somerville, R. C. (1975). On the use of a coordinate transformation for the solution of the Navier-Stokes equations. Journal of Computational Physics, 17(2), 209-228.

Gates, W. L. (1955). Results of numerical forecasting with the barotropic and thermotropic atmospheric models (Vol. 56). Geophysics Research Directorate, Air Force Cambridge Research Center.

Gelaro, R., McCarty, W., Suárez, M. J., Todling, R., Molod, A., Takacs, L., Randles, C. A., Darmenov, A., Bosilovich, M. G., & Reichle, R. (2017). The modern-era retrospective analysis for research and applications, version 2 (MERRA-2). Journal of Climate, 30(14), 5419-5454.

Geppert, M., Hartmann, K., Kirchner, I., Pfahl, S., Struck, U., & Riedel, F. (2022). Precipitation over southern Africa: Moisture sources and isotopic composition. Journal of Geophysical Research: Atmospheres, 127(21), e2022JD037005.

Geyer, B., Weisse, R., Bisling, P., & Winterfeldt, J. (2015). Climatology of North Sea wind energy derived from a model hindcast for 1958–2012. Journal of Wind Engineering and Industrial Aerodynamics, 147, 18-29.

Giorgi, F. (2019). Thirty Years of Regional Climate Modeling: Where Are We and Where Are We Going next? Journal of Geophysical Research: Atmospheres. https://doi.org/10.1029/2018jd030094

Giorgi, F. (2020). Regional Dynamical Downscaling. In Oxford Research Encyclopedia of Climate Science.

GitHub repository. (2018). ETHOS.FINE - Framework for Integrated Energy System Assessment. https://github.com/FZJ-IEK3-VSA/FINE?tab=readme-ov-file

GitHub repository. (2019). RESKit—Renewable Energy Simulation Toolkit for Python. https://github.com/FZJ-IEK3-VSA/RESKit

Gnedin, N. Y., Semenov, V. A., & Kravtsov, A. V. (2018). Enforcing the Courant–Friedrichs–Lewy condition in explicitly conservative local time stepping schemes. Journal of Computational Physics, 359, 93-105.

Gonzalez-Aparicio, I., Monforti, F., Volker, P., Zucker, A., Careri, F., Huld, T., & Badger, J. (2017). Simulating European wind power generation applying statistical downscaling to reanalysis data. Applied Energy, 199, 155-168.

González-Aparicio, I., Monforti, F., Volker, P., Zucker, A., Careri, F., Huld, T., & Badger, J. (2017). Simulating European wind power generation applying statistical downscaling to reanalysis data. Applied Energy, 199, 155-168. https://doi.org/10.1016/j.apenergy.2017.04.066

Good, J., & Johnson, J. X. (2016). Impact of inverter loading ratio on solar photovoltaic system

performance. Applied Energy, 177, 475-486.
Görmüş, T., Aydoğan, B., & Ayat, B. (2022). Offshore wind power potential analysis for different wind turbines in the Mediterranean Region, 1959–2020. Energy Conversion and Management, 274, 116470.
Govindasamy, T. R., & Chetty, N. (2018). Quantifying the global solar radiation received in Pietermaritzburg, KwaZulu-Natal to motivate the consumption of solar technologies. Open Physics, 16(1), 786-794.
Gruber, K., Regner, P., Wehrle, S., Zeyringer, M., & Schmidt, J. (2022). Towards global validation of wind power simulations: A multi-country assessment of wind power simulation from MERRA-2 and ERA-5 reanalyses bias-corrected with the global wind atlas. Energy, 238, 121520.
GSA. (2019). Data obtained from the "Global Solar Atlas 2.0," a free, web‐based application is developed and operated by the company Solargis s.r.o. on behalf of the World Bank Group, utilizing Solargis data, with funding provided by the Energy Sector Management Assistance Program (ESMAP). https://globalsolaratlas.info
Gualtieri, G. (2021). Reliability of ERA5 Reanalysis Data for Wind Resource Assessment: A Comparison against Tall Towers. Energies, 14(14). https://doi.org/10.3390/en14144169
Gualtieri, G. (2022). Analysing the uncertainties of reanalysis data used for wind resource assessment: A critical review. Renewable and sustainable energy reviews, 167, 112741.
Gurobi Optimizer, L. (2018). Gurobi Optimizer Reference Manual.
Gutowski, W. J., Ullrich, P. A., Hall, A., Leung, L. R., O'Brien, T. A., Patricola, C. M., Arritt, R., Bukovsky, M., Calvin, K. V., & Feng, Z. (2020). The ongoing need for high-resolution regional climate models: Process understanding and stakeholder information. Bulletin of the American Meteorological Society, 101(5), E664-E683.
GWA. (2019). Data obtained from the "Global Wind Atlas 3.0," a free, web‐based application developed, owned and operated by the Technical University of Denmark (DTU). The Global Wind Atlas 3.0 is released in partnership with the World Bank Group, utilizing data provided by Vortex, using funding provided by the Energy Sector Management Assistance Program (ESMAP). https://globalwindatlas.info
Hafner, M., Tagliapietra, S., & de Strasser, L. (2018). Prospects for Renewable Energy in Africa. In Energy in Africa: Challenges and Opportunities (pp. 47-75). Springer International Publishing. https://doi.org/10.1007/978-3-319-92219-5_3
Hall, C. A. (2017). Energy Return on Investment: A Unifying Principle for Biology, Economics, and Sustainability.
Hargreaves, J. K. (1992). The solar-terrestrial environment: an introduction to geospace-the science of the terrestrial upper atmosphere, ionosphere, and magnetosphere. Cambridge university press.
Harris, I., Osborn, T. J., Jones, P., & Lister, D. (2020). Version 4 of the CRU TS monthly high-resolution gridded multivariate climate dataset. Scientific Data, 7(1), 109. https://doi.org/10.1038/s41597-020-0453-3
Hashemi, B., Taheri, S., Cretu, A.-M., & Pouresmaeil, E. (2021). Systematic photovoltaic system power losses calculation and modeling using computational intelligence

techniques. Applied Energy, 284, 116396.
He, G., & Kammen, D. M. (2014). Where, when and how much wind is available? A provincial-scale wind resource assessment for China. Energy Policy, 74, 116-122.
He, Y., Monahan, A. H., Jones, C. G., Dai, A., Biner, S., Caya, D., & Winger, K. (2010). Probability distributions of land surface wind speeds over North America. Journal of Geophysical Research: Atmospheres, 115(D4).
Heikkilä, U., Sandvik, A., & Sorteberg, A. (2011). Dynamical downscaling of ERA-40 in complex terrain using the WRF regional climate model. Climate Dynamics, 37, 1551-1564.
Heinze, R., Dipankar, A., Henken, C. C., Moseley, C., Sourdeval, O., Trömel, S., Xie, X., Adamidis, P., Ament, F., Baars, H., Barthlott, C., Behrendt, A., Blahak, U., Bley, S., Brdar, S., Brueck, M., Crewell, S., Deneke, H., Di Girolamo, P., . . . Quaas, J. (2017). Large‐eddy simulations over Germany using ICON: a comprehensive evaluation. Quarterly Journal of the Royal Meteorological Society, 143(702), 69-100. https://doi.org/10.1002/qj.2947
Hellmann, G. (1919). Über die Bewegung der Luft in den untersten Schichten der Atmosphäre. Kgl. Akademie der Wissenschaften [G.] Reimer.
Hersbach, H., Bell, B., Berrisford, P., Hirahara, S., Horányi, A., Muñoz‐Sabater, J., Nicolas, J., Peubey, C., Radu, R., & Schepers, D. (2020). The ERA5 global reanalysis. Quarterly Journal of the Royal Meteorological Society, 146(730), 1999-2049.
Hess, D., Wetzel, M., & Cao, K.-K. (2018). Representing node-internal transmission and distribution grids in energy system models. Renewable Energy, 119, 874-890.
Hogan, R. J., & Bozzo, A. (2018). A flexible and efficient radiation scheme for the ECMWF model. Journal of Advances in Modeling Earth Systems, 10(8), 1990-2008.
Hohenegger, C., Korn, P., Linardakis, L., Redler, R., Schnur, R., Adamidis, P., Bao, J., Bastin, S., Behravesh, M., & Bergemann, M. (2023). ICON-Sapphire: simulating the components of the Earth System and their interactions at kilometer and subkilometer scales. Geoscientific Model Development, 16(2), 779-811.
Holmgren, W. F., Hansen, C. W., & Mikofski, M. A. (2018). pvlib python: A python package for modeling solar energy systems. Journal of Open Source Software, 3(29), 884.
Holton, J. R., & Hakim, G. J. (2013). An introduction to dynamic meteorology (Vol. 88). Academic press.
Huang, G., Li, Z., Li, X., Liang, S., Yang, K., Wang, D., & Zhang, Y. (2019). Estimating surface solar irradiance from satellites: Past, present, and future perspectives. Remote Sensing of Environment, 233, 111371.
Huffman, G. J., Bolvin, D. T., Braithwaite, D., Hsu, K., Joyce, R., Xie, P., & Yoo, S.-H. (2015). NASA global precipitation measurement (GPM) integrated multi-satellite retrievals for GPM (IMERG). Algorithm theoretical basis document (ATBD) version, 4(26), 2020-2005.
Ineichen, P., & Perez, R. (2002). A new airmass independent formulation for the Linke turbidity coefficient. Solar Energy, 73(3), 151-157.
Intergovernmental Panel on Climate Change. (2021). Climate change widespread, rapid, and

intensifying—IPCC. https://www.ipcc.ch/2021/08/09/ar6-wg1-20210809-pr/
International Energy Agency. (2021). World energy outlook 2020. Available online: https://www.iea.org/reports/world-energy-outlook-2020?mode=overview (last accessed on 26 June 2023).
International Energy Agency. (2022). Africa Energy Outlook 2022. https://www.iea.org/reports/africa-energy-outlook-2022/
International Energy Agency. (2023). Sustainable Development Goal 7 (SDG7): Data and projections, access to affordable, reliable, sustainable and modern energy for all. Available online: https://www.iea.org/reports/sdg7-data-and-projections/access-to-electricity
International Renewable Energy Agency (IRENA). (2023). Renewable capacity statistics 2023, Abu Dhabi.
International Renewable Energy Agency. (2024). 100% renewable energy scenarios: Supporting ambitious policy targets. https://www.irena.org/Publications/2024/Mar/100pc-renewable-energy-scenarios-Supporting-ambitious-policy-targets
IRSAP. (2023). How much energy does an average household use? https://www.irsap.com/en/blog/average-energy-consumption
Ishmam, S. (unpublished yet). Implications of energy cooperation in fully renewable energy systems for African regions Dissertation, RWTH Aachen University].
Ishmam, S., Heinrichs, H., Winkler, C., Bayat, B., Lahnaoui, A., Agbo, S., Sanchez, E. P., Franzmann, D., Oijeabou, N., & Koerner, C. (2024). Mapping local green hydrogen cost-potentials by a multidisciplinary approach. International Journal of Hydrogen Energy, 87, 1155-1170.
Jacobson, M. Z. (2002). Fundamentals of atmospheric modeling. Atmosphere, 50, 60.
Jain, A., & Kapoor, A. (2004). Exact analytical solutions of the parameters of real solar cells using Lambert W-function. Solar Energy Materials and Solar Cells, 81(2), 269-277.
Jánosi, I. M., Medjdoub, K., & Vincze, M. (2021). Combined wind-solar electricity production potential over north-western Africa. Renewable and sustainable energy reviews, 151, 111558.
Jiang, H., Yang, Y., Bai, Y., & Wang, H. (2019). Evaluation of the total, direct, and diffuse solar radiations from the ERA5 reanalysis data in China. IEEE Geoscience and Remote Sensing Letters, 17(1), 47-51.
Jourdier, B. (2020). Evaluation of ERA5, MERRA-2, COSMO-REA6, NEWA and AROME to simulate wind power production over France. Advances in Science and Research, 17, 63-77. https://doi.org/10.5194/asr-17-63-2020
Jourdier, B., Diaz, C., & Dubus, L. (2023). Evaluation of CERRA for wind energy applications.
Jung, C., & Schindler, D. (2021). The role of the power law exponent in wind energy assessment: A global analysis. International Journal of Energy Research, 45(6), 8484-8496. https://doi.org/10.1002/er.6382
Jung, C., & Schindler, D. (2022). On the influence of wind speed model resolution on the global technical wind energy potential. Renewable and sustainable energy reviews, 156.

https://doi.org/10.1016/j.rser.2021.112001

Jurasz, J., Canales, F. A., Kies, A., Guezgouz, M., & Beluco, A. (2020). A review on the complementarity of renewable energy sources: Concept, metrics, application and future research directions. Solar Energy, 195, 703-724. https://doi.org/10.1016/j.solener.2019.11.087

Jurasz, J., Mikulik, J., Dąbek, P. B., Guezgouz, M., & Kaźmierczak, B. (2021). Complementarity and 'resource droughts' of solar and wind energy in poland: An era5-based analysis. Energies, 14(4), 1118.

Kalnay, E. (2003). Atmospheric modeling, data assimilation and predictability. Cambridge university press.

Kanwal, A., Tahir, Z. u. R., Asim, M., Hayat, N., Farooq, M., Abdullah, M., & Azhar, M. (2022). Evaluation of reanalysis and analysis datasets against measured wind data for wind resource assessment. Energy & Environment, 0958305X221084078.

Kendon, E. J., Stratton, R. A., Tucker, S., Marsham, J. H., Berthou, S., Rowell, D. P., & Senior, C. A. (2019). Enhanced future changes in wet and dry extremes over Africa at convection-permitting scale. Nat Commun, 10(1), 1794. https://doi.org/10.1038/s41467-019-09776-9

Kenny, D., & Fiedler, S. (2022). Which gridded irradiance data is best for modelling photovoltaic power production in Germany? Solar Energy, 232, 444-458.

King, D. L., Kratochvil, J. A., & Boyson, W. E. (2004). Photovoltaic array performance model (Vol. 8). Citeseer.

Klemp, J. B. (2011). A terrain-following coordinate with smoothed coordinate surfaces. Monthly Weather Review, 139(7), 2163-2169.

Klütz, T., Knosala, K., Behrens, J., Maier, R., Hoffmann, M., Pflugradt, N., & Stolten, D. (2025). ETHOS. FINE: A Framework for Integrated Energy System Assessment. Journal of Open Source Software, 10(105), 6274.

Kotlarski, S., Keuler, K., Christensen, O. B., Colette, A., Déqué, M., Gobiet, A., Goergen, K., Jacob, D., Lüthi, D., van Meijgaard, E., Nikulin, G., Schär, C., Teichmann, C., Vautard, R., Warrach-Sagi, K., & Wulfmeyer, V. (2014). Regional climate modeling on European scales: a joint standard evaluation of the EURO-CORDEX RCM ensemble. Geoscientific Model Development, 7(4), 1297-1333. https://doi.org/10.5194/gmd-7-1297-2014

Kumar, N. M., Gupta, R. P., Mathew, M., Jayakumar, A., & Singh, N. K. (2019). Performance, energy loss, and degradation prediction of roof-integrated crystalline solar PV system installed in Northern India. Case Studies in Thermal Engineering, 13, 100409.

Labriji, H., Herscovici-Schiller, O., & Cassaing, F. (2022). Computation of the lateral shift due to atmospheric refraction. Astronomy & Astrophysics, 662, A61.

Laing, A. G., & Fritsch, M. J. (1997). The global population of mesoscale convective complexes. Quarterly Journal of the Royal Meteorological Society, 123(538), 389-405.

Laprise, R. (2008). Regional climate modelling. Journal of Computational Physics, 227(7), 3641-3666. https://doi.org/10.1016/j.jcp.2006.10.024

Lean, H. W., Clark, P. A., Dixon, M., Roberts, N. M., Fitch, A., Forbes, R., & Halliwell, C.

(2008). Characteristics of high-resolution versions of the Met Office Unified Model for forecasting convection over the United Kingdom. Monthly Weather Review, 136(9), 3408-3424.

Lei, Y., Wang, Z., Wang, D., Zhang, X., Che, H., Yue, X., Tian, C., Zhong, J., Guo, L., & Li, L. (2023). Co-benefits of carbon neutrality in enhancing and stabilizing solar and wind energy. Nature Climate Change, 13(7), 693-700.

Leuenberger, D., Koller, M., Fuhrer, O., & Schär, C. (2010). A generalization of the SLEVE vertical coordinate. Monthly Weather Review, 138(9), 3683-3689.

Long, C. N., & Dutton, E. G. (2010). BSRN Global Network recommended QC tests, V2. x.

López Prol, J., & Schill, W.-P. (2021). The economics of variable renewable energy and electricity storage. Annual Review of Resource Economics, 13, 443-467.

Lu, X., & McElroy, M. B. (2023). Global potential for wind-generated electricity. In Wind energy engineering (pp. 47-61). Elsevier.

Lu, X., McElroy, M. B., & Kiviluoma, J. (2009). Global potential for wind-generated electricity [Article]. Proceedings of the National Academy of Sciences of the United States of America, 106(27), 10933-10938. https://doi.org/10.1073/pnas.0904101106

Lucas‐Picher, P., Argüeso, D., Brisson, E., Tramblay, Y., Berg, P., Lemonsu, A., Kotlarski, S., & Caillaud, C. (2021). Convection‐permitting modeling with regional climate models: Latest developments and next steps. WIREs Climate Change, 12(6). https://doi.org/10.1002/wcc.731

Lund, P. D., Mikkola, J., & Ypyä, J. (2015). Smart energy system design for large clean power schemes in urban areas. Journal of Cleaner Production, 103, 437-445.

Lynch, P. (2008). The origins of computer weather prediction and climate modeling. Journal of Computational Physics, 227(7), 3431-3444.

Mabasa, B., Lysko, M. D., & Moloi, S. J. (2021). Validating Hourly Satellite Based and Reanalysis Based Global Horizontal Irradiance Datasets over South Africa. Geomatics, 1(4), 429-449. https://doi.org/10.3390/geomatics1040025

Mabasa, B., Lysko, M. D., & Moloi, S. J. (2022). Comparison of Satellite-Based and Ångström–Prescott Estimated Global Horizontal Irradiance under Different Cloud Cover Conditions in South African Locations. Solar,

Magnusson, L., Ackerley, D., Bouteloup, Y., Chen, J.-H., Doyle, J., Earnshaw, P., Kwon, Y., Köhler, M., Lang, S. K., & Lim, Y.-J. (2022). Skill of medium-range forecast models using the same initial conditions. Bulletin of the American Meteorological Society, 103(9), E2050-E2068.

Mancarella, P. (2014). MES (multi-energy systems): An overview of concepts and evaluation models. Energy, 65, 1-17.

Manisha, Pinkey, Kumari, M., Sahdev, R. K., & Tiwari, S. (2022). A review on solar photovoltaic system efficiency improving technologies. Applied Solar Energy, 58(1), 54-75.

Marsham, J. H., Dixon, N. S., Garcia-Carreras, L., Lister, G. M. S., Parker, D. J., Knippertz, P., & Birch, C. E. (2013). The role of moist convection in the West African monsoon system: Insights from continental-scale convection-permitting simulations.

Geophysical Research Letters, 40(9), 1843-1849. https://doi.org/10.1002/grl.50347
Martin, S., Jung, S., & Vanli, A. (2020). Impact of near-future turbine technology on the wind power potential of low wind regions. Applied Energy, 272, 115251.
Martínez-Gordón, R., Morales-España, G., Sijm, J., & Faaij, A. (2021). A review of the role of spatial resolution in energy systems modelling: Lessons learned and applicability to the North Sea region. Renewable and sustainable energy reviews, 141, 110857.
McKenna, R., Pfenninger, S., Heinrichs, H., Schmidt, J., Staffell, I., Bauer, C., Gruber, K., Hahmann, A. N., Jansen, M., Klingler, M., Landwehr, N., Larsén, X. G., Lilliestam, J., Pickering, B., Robinius, M., Tröndle, T., Turkovska, O., Wehrle, S., Weinand, J. M., & Wohland, J. (2022). High-resolution large-scale onshore wind energy assessments: A review of potential definitions, methodologies and future research needs. Renewable Energy, 182, 659-684. https://doi.org/10.1016/j.renene.2021.10.027
Medina-Lopez, E., McMillan, D., Lazic, J., Hart, E., Zen, S., Angeloudis, A., Bannon, E., Browell, J., Dorling, S., & Dorrell, R. (2021). Satellite data for the offshore renewable energy sector: synergies and innovation opportunities. Remote Sensing of Environment, 264, 112588.
Meenal, R., Binu, D., Ramya, K., Michael, P. A., Vinoth Kumar, K., Rajasekaran, E., & Sangeetha, B. (2022). Weather forecasting for renewable energy system: a review. Archives of Computational Methods in Engineering, 29(5), 2875-2891.
Mejia, F., Kleissl, J., & Bosch, J. (2014). The effect of dust on solar photovoltaic systems. Energy Procedia, 49, 2370-2376.
Mejia, F. A., & Kleissl, J. (2013). Soiling losses for solar photovoltaic systems in California. Solar Energy, 95, 357-363.
Minola, L., Zhang, F., Azorin-Molina, C., Pirooz, A. S., Flay, R., Hersbach, H., & Chen, D. (2020). Near-surface mean and gust wind speeds in ERA5 across Sweden: towards an improved gust parametrization. Climate Dynamics, 55(3-4), 887-907.
Mironov, D., Ritter, B., Schulz, J.-P., Buchhold, M., Lange, M., & MacHulskaya, E. (2012). Parameterisation of sea and lake ice in numerical weather prediction models of the German Weather Service. Tellus A: Dynamic Meteorology and Oceanography, 64(1), 17330.
Mironov, D. V. (2005). Parameterization of lakes in numerical weather prediction. Part 1: Description of a lake model. German Weather Service, Offenbach am Main, Germany.
Moemken, J., Reyers, M., Feldmann, H., & Pinto, J. G. (2018). Future Changes of Wind Speed and Wind Energy Potentials in EURO-CORDEX Ensemble Simulations. Journal of Geophysical Research: Atmospheres, 123(12), 6373-6389. https://doi.org/10.1029/2018jd028473
Molina, M. O., Gutiérrez, C., & Sánchez, E. (2021). Comparison of ERA5 surface wind speed climatologies over Europe with observations from the HadISD dataset. International Journal of Climatology, 41(10), 4864-4878. https://doi.org/10.1002/joc.7103
Moore, A., Blenkinsop, T., & Cotterill, F. (2009). Southern African topography and erosion history: plumes or plate tectonics? Terra Nova, 21(4), 310-315.
Mortensen, N. G. (2021). Global Wind Atlas 1, 2 & 3–validations and uncertainties.

WindEurope Electric City 2021,
Mortensen, N. G., Davis, N., Badger, J., & Hahmann, A. N. (2017). Global Wind Atlas–validation and uncertainty. WindEurope Resource Assessment Workshop 2017,
Müller, G., Kullmann, F., Linssen, J., & Stolten, D. (2025). The costs of future energy technologies: A comprehensive review of power-to-X processes. Journal of CO2 Utilization, 92, 103019.
Murcia, J. P., Koivisto, M. J., Luzia, G., Olsen, B. T., Hahmann, A. N., Sørensen, P. E., & Als, M. (2022). Validation of European-scale simulated wind speed and wind generation time series. Applied Energy, 305. https://doi.org/10.1016/j.apenergy.2021.117794
Nagarajan, A., Thiagarajan, R., Repins, I. L., & Hacke, P. L. (2019). Photovoltaic inverter reliability assessment.
Neher, I., Crewell, S., Meilinger, S., Pfeifroth, U., & Trentmann, J. (2020). Photovoltaic power potential in West Africa using long-term satellite data. Atmospheric Chemistry and Physics, 20(21), 12871-12888. https://doi.org/10.5194/acp-20-12871-2020
Neupane, D., Kafle, S., Karki, K. R., Kim, D. H., & Pradhan, P. (2022). Solar and wind energy potential assessment at provincial level in Nepal: Geospatial and economic analysis. Renewable Energy, 181, 278-291.
Nordtank (now Vestas). (1997). Model: NTK1500/60. Access with https://www.thewindpower.net/turbine_en_362_nordtank_ntk1500-60.php
Nyarko, K., Whale, J., & Urmee, T. (2023). Drivers and challenges of off-grid renewable energy-based projects in West Africa: A review. Heliyon, 9(6).
Olsen, B. T., Hahmann, A., Žagar, M., Hristov, Y., Mann, J., Kelly, M., & Badger, J. (2019). Mapping the European wind climate: validation of the New European Wind Atlas. EMS Annual Meeting,
Omoyele, O., Hoffmann, M., Koivisto, M., Larraneta, M., Weinand, J. M., Linßen, J., & Stolten, D. (2024). Increasing the resolution of solar and wind time series for energy system modeling: A review. Renewable and sustainable energy reviews, 189, 113792.
Ortiz-Imedio, R., Caglayan, D. G., Ortiz, A., Heinrichs, H., Robinius, M., Stolten, D., & Ortiz, I. (2021). Power-to-Ships: Future electricity and hydrogen demands for shipping on the Atlantic coast of Europe in 2050. Energy, 228, 120660.
Oteng, C., Gamette, P., Peprah, J. A., & Obeng, C. K. (2024). Towards a carbon neutral Africa: A review of the linkages between financial inclusion and renewable energy. Social Sciences & Humanities Open, 10, 100923.
Oyewo, A. S., Sterl, S., Khalili, S., & Breyer, C. (2023). Highly renewable energy systems in Africa: Rationale, research, and recommendations. Joule.
Palys, M. J., & Daoutidis, P. (2022). Power-to-X: A review and perspective. Computers & Chemical Engineering, 165, 107948.
Patil, S., Kotzur, L., & Stolten, D. (2022). Advanced spatial and technological aggregation scheme for energy system models. Energies, 15(24), 9517.
Peña-Sánchez, E. U., Dunkel, P., Winkler, C., Heinrichs, H., Prinz, F., Weinand, J., Maier, R., Dickler, S., Chen, S., & Gruber, K. (2025). Towards high resolution, validated and open global wind power assessments. arXiv preprint arXiv:2501.07937.

Pena Sanchez, E. U., Ryberg, S. D., Heinrichs, H. U., Stolten, D., & Robinius, M. (2021). The potential of variable renewable energy sources in Mexico: a temporally evaluated and geospatially constrained techno-economical assessment. Energies, 14(18), 5779.

Perez, R., Ineichen, P., Seals, R., Michalsky, J., & Stewart, R. (1990). Modeling daylight availability and irradiance components from direct and global irradiance. Solar Energy, 44(5), 271-289.

Perkins, S. E., Pitman, A. J., Holbrook, N. J., & McAneney, J. (2007). Evaluation of the AR4 Climate Models' Simulated Daily Maximum Temperature, Minimum Temperature, and Precipitation over Australia Using Probability Density Functions. Journal of Climate, 20(17), 4356-4376. https://doi.org/10.1175/jcli4253.1

Pfeifroth, U., Kothe, S., Drücke, J., Trentmann, J., Schröder, M., Selbach, N., & Hollmann, R. (2023). Surface Radiation Data Set - Heliosat (SARAH) - Edition 3. Satellite Application Facility on Climate Monitoring. https://doi.org/10.5676/EUM_SAF_CM/SARAH/V003

Pfeifroth, U., Kothe, S., Müller, R., Trentmann, J., Hollmann, R., Fuchs, P., & Werscheck, M. (2017). Surface Radiation Data Set - Heliosat (SARAH) - Edition 2. Satellite Application Facility on Climate Monitoring. https://doi.org/10.5676/EUM_SAF_CM/SARAH/V002

Pham, T. V., Steger, C., Rockel, B., Keuler, K., Kirchner, I., Mertens, M., Rieger, D., Zängl, G., & Früh, B. (2021). ICON in Climate Limited-area Mode (ICON release version 2.6.1): a new regional climate model. Geoscientific Model Development, 14(2), 985-1005. https://doi.org/10.5194/gmd-14-985-2021

Pielke Sr, R. A. (2013). Mesoscale meteorological modeling. Academic press.

Podobnik, B., & Stanley, H. E. (2008). Detrended cross-correlation analysis: a new method for analyzing two nonstationary time series. Physical review letters, 100(8), 084102.

Porté-Agel, F., Bastankhah, M., & Shamsoddin, S. (2020). Wind-turbine and wind-farm flows: a review. Boundary-layer meteorology, 174(1), 1-59.

Potrč, S., Čuček, L., Martin, M., & Kravanja, Z. (2021). Sustainable renewable energy supply networks optimization–The gradual transition to a renewable energy system within the European Union by 2050. Renewable and sustainable energy reviews, 146, 111186.

Prein, A. F., Langhans, W., Fosser, G., Ferrone, A., Ban, N., Goergen, K., Keller, M., Tolle, M., Gutjahr, O., Feser, F., Brisson, E., Kollet, S., Schmidli, J., van Lipzig, N. P., & Leung, R. (2015). A review on regional convection-permitting climate modeling: Demonstrations, prospects, and challenges. Rev Geophys, 53(2), 323-361. https://doi.org/10.1002/2014RG000475

Prill, F., Reinert, D., Rieger, D., & Zängl, G. (2022). ICON Tutorial - working with the ICON model https://doi.org/10.5676/DWD_pub/nwv/icon_tutorial2022

Pryor, S., & Barthelmie, R. (2011). Assessing climate change impacts on the near-term stability of the wind energy resource over the United States. Proceedings of the National Academy of Sciences, 108(20), 8167-8171.

Pryor, S., Schoof, J. T., & Barthelmie, R. (2005). Empirical downscaling of wind speed probability distributions. Journal of Geophysical Research: Atmospheres, 110(D19).

Pryor, S. C., Barthelmie, R. J., Bukovsky, M. S., Leung, L. R., & Sakaguchi, K. (2020). Climate change impacts on wind power generation. Nature Reviews Earth & Environment, 1(12), 627-643. https://doi.org/10.1038/s43017-020-0101-7

Pueblas, R., Kuckertz, P., Weinand, J. M., Kotzur, L., & Stolten, D. (2023). ETHOS. PASSION: An open-source workflow for rooftop photovoltaic potential assessments from satellite imagery. Solar Energy, 265, 112094.

Qiao, D., Wu, S., Li, G., You, J., Zhang, J., & Shen, B. (2022). Wind speed forecasting using multi-site collaborative deep learning for complex terrain application in valleys. Renewable Energy, 189, 231-244.

Raj, A., Gupta, M., & Panda, S. (2016). Design simulation and performance assessment of yield and loss forecasting for 100 KWp grid connected solar PV system. 2016 2nd International Conference on Next Generation Computing Technologies (NGCT),

Ramirez-Vergara, J., Bosman, L., Leon-Salas, W. D., & Wollega, E. (2023). Predicting on-site solar energy generation using off-site weather stations and deep neural networks. International Journal of Energy and Environmental Engineering, 14(1), 1-13.

Raschendorfer, M. (2001). The new turbulence parameterization of LM. COSMO Newsletter, 1, 89-97.

Raupach, M., & Fraser, P. (2011). Climate and greenhouse gases. In Climate change: science and solutions for Australia (pp. 15-34).

Reda, I., & Andreas, A. (2004). Solar position algorithm for solar radiation applications. Solar Energy, 76(5), 577-589.

REDIS, 2022. Department of Energy, The IPP Office, and Eskom. Location and contracted capacites, link: http://redis.energy.gov.za/power-producers/; Load factors for provincial data, link: http://redis.energy.gov.za/electricity-production-details/

Ren, G., Wan, J., Liu, J., & Yu, D. (2019). Spatial and temporal assessments of complementarity for renewable energy resources in China. Energy, 177, 262-275. https://doi.org/10.1016/j.energy.2019.04.023

Reyers, M., Moemken, J., & Pinto, J. G. (2016). Future changes of wind energy potentials over Europe in a large CMIP5 multi-model ensemble. International Journal of Climatology, 36(2).

Richardson, D., Pitman, A., & Ridder, N. (2023). Climate influence on compound solar and wind droughts in Australia. npj Climate and Atmospheric Science, 6(1), 184.

Richters, O., Bertram, C., Kriegler, E., Al Khourdajie, A., Cui, R., Edmonds, J., Hackstock, P., Holland, D., Hurst, I., & Kikstra, J. (2022). NGFS Climate Scenarios Data Set Version 3.0.

Richters, O., Bertram, C., Kriegler, E., Anz, J., Beck, T., Bresch, D. N., Charles, M., Clarke, L., Cui, R., & Edmonds, J. (2022). NGFS Climate Scenarios Database: Technical Documentation V3. 1.

Roy, D. P., Huang, H., Houborg, R., & Martins, V. S. (2021). A global analysis of the temporal availability of PlanetScope high spatial resolution multi-spectral imagery. Remote Sensing of Environment, 264, 112586.

Ruiz, S. A. G., Barriga, J. E. C., & Martínez, J. A. (2021). Wind power assessment in the

Caribbean region of Colombia, using ten-minute wind observations and ERA5 data. Renewable Energy, 172, 158-176.

Rummukainen, M. (2015). Added value in regional climate modeling. WIREs Climate Change, 7(1), 145-159. https://doi.org/10.1002/wcc.378

Ryberg, D. S. (2020). Generation Lulls from the Future Potential of Wind and Solar Energy in Eutope (Publication Number ISBN 978-3-95806-513-0) RWTH Aachen University]. Energie & Umwelt / Energy & Environment.

Ryberg, D. S., Caglayan, D. G., Schmitt, S., Linßen, J., Stolten, D., & Robinius, M. (2019). The future of European onshore wind energy potential: Detailed distribution and simulation of advanced turbine designs. Energy, 182, 1222-1238. https://doi.org/10.1016/j.energy.2019.06.052

Saeed, F., & Zohaib, A. (2022). Quantification of Losses in a Photovoltaic System: A Review. Engineering Proceedings, 11(1), 35.

Sakuru, S. K. V., & Ramana, M. (2023). Wind power potential over India using the ERA5 reanalysis. Sustainable Energy Technologies and Assessments, 56, 103038.

Samal, R. K. (2021). Assessment of wind energy potential using reanalysis data: A comparison with mast measurements. Journal of Cleaner Production, 313, 127933.

Santos-Alamillos, F., Pozo-Vázquez, D., Ruiz-Arias, J., Lara-Fanego, V., & Tovar-Pescador, J. (2014). A methodology for evaluating the spatial variability of wind energy resources: Application to assess the potential contribution of wind energy to baseload power. Renewable Energy, 69, 147-156.

Sarkodie, S. A., & Adams, S. (2020). Electricity access and income inequality in South Africa: evidence from Bayesian and NARDL analyses. Energy Strategy Reviews, 29, 100480.

Sawadogo, W., Bliefernicht, J., Fersch, B., Salack, S., Guug, S., Diallo, B., Ogunjobi, K. O., Nakoulma, G., Tanu, M., Meilinger, S., & Kunstmann, H. (2023). Hourly global horizontal irradiance over West Africa: A case study of one-year satellite- and reanalysis-derived estimates vs. in situ measurements. Renewable Energy, 216. https://doi.org/10.1016/j.renene.2023.119066

Sawadogo, W., Bliefernicht, J., Fersch, B., Salack, S., Guug, S., Ogunjobi, K. O., Meilinger, S., & Kunstmann, H. (2023). Global horizontal irradiance in West Africa: evaluation of the WRF-solar model in convection-permitting mode with ground measurements. Journal of Applied Meteorology and Climatology, 62(7), 835-851.

Sawadogo, W., Reboita, M. S., Faye, A., da Rocha, R. P., Odoulami, R. C., Olusegun, C. F., Adeniyi, M. O., Abiodun, B. J., Sylla, M. B., & Diallo, I. (2021). Current and future potential of solar and wind energy over Africa using the RegCM4 CORDEX-CORE ensemble. Climate Dynamics, 57(5-6), 1647-1672.

Schaber, K., Steinke, F., & Hamacher, T. (2012). Transmission grid extensions for the integration of variable renewable energies in Europe: Who benefits where? Energy Policy, 43, 123-135.

Schär, C., Fuhrer, O., Arteaga, A., Ban, N., Charpilloz, C., Di Girolamo, S., Hentgen, L., Hoefler, T., Lapillonne, X., Leutwyler, D., Osterried, K., Panosetti, D., Rüdisühli, S., Schlemmer, L., Schulthess, T. C., Sprenger, M., Ubbiali, S., & Wernli, H. (2020).

Kilometer-Scale Climate Models: Prospects and Challenges. Bulletin of the American Meteorological Society, 101(5), E567-E587. https://doi.org/10.1175/bams-d-18-0167.1

Schär, C., Leuenberger, D., Fuhrer, O., Lüthi, D., & Girard, C. (2002). A new terrain-following vertical coordinate formulation for atmospheric prediction models. Monthly Weather Review, 130(10), 2459-2480.

Schaub, P., Mermoud, A., & Guisan, O. (1994). Evaluation of the different losses involved in two photovoltaic systems. 12th European Photovoltaic Solar Energy Conference,

Schimanke S., Ridal M., Le Moigne P., Berggren L., Undén P., Randriamampianina R., Andrea U., Bazile E., Bertelsen A., Brousseau P., Dahlgren P., Edvinsson L., El Said A., Glinton M., Hopsch S., Isaksson L., Mladek R., Olsson E., Verrelle A., Wang Z.Q., (2021). CERRA sub-daily regional reanalysis data for Europe on height levels from 1984 to present. Copernicus Climate Change Service (C3S) Climate Data Store (CDS), DOI: 10.24381/cds.38b394e6

Schöb, T., Kullmann, F., Linßen, J., & Stolten, D. (2023). The role of hydrogen for a greenhouse gas-neutral Germany by 2045. International Journal of Hydrogen Energy, 48(99), 39124-39137.

Schöb, T. F. (2024). Model-based analysis of greenhouse gas neutral transformation strategies for Germany Dissertation, RWTH Aachen University].

Schrodin, R., & Heise, E. (2001). The multi-layer version of the DWD soil model TERRA_LM. DWD.

Schulz, J.-P., Vogel, G., Becker, C., Kothe, S., Rummel, U., & Ahrens, B. (2016). Evaluation of the ground heat flux simulated by a multi-layer land surface scheme using high-quality observations at grass land and bare soil. Meteorologische Zeitschrift, 607-620.

Seifert, A. (2008). A revised cloud microphysical parameterization for COSMO-LME. COSMO Newsletter, 7, 25-28.

Senior, C. A., Marsham, J. H., Berthou, S., Burgin, L. E., Folwell, S. S., Kendon, E. J., Klein, C. M., Jones, R. G., Mittal, N., & Rowell, D. P. (2021). Convection-permitting regional climate change simulations for understanding future climate and informing decision-making in Africa. Bulletin of the American Meteorological Society, 102(6), E1206-E1223.

Shaner, M. R., Davis, S. J., Lewis, N. S., & Caldeira, K. (2018). Geophysical constraints on the reliability of solar and wind power in the United States. Energy & Environmental Science, 11(4), 914-925.

Shi, H., Zhang, J., Zhao, B., Xia, X., Hu, B., Chen, H., Wei, J., Liu, M., Bian, Y., & Fu, D. (2021). Surface brightening in eastern and central China since the implementation of the Clean Air Action in 2013: Causes and implications. Geophysical Research Letters, 48(3), e2020GL091105.

Siegel, F. R. (2021). Global Warming and Water 2050: More People, Yes; Less Ice, Yes; More Water, Yes; More Fresh Water, Probably; More Accessible Fresh Water?

Simmons, A. J., & Burridge, D. M. (1981). An energy and angular-momentum conserving vertical finite-difference scheme and hybrid vertical coordinates. Monthly Weather Review, 109(4), 758-766.

Sinsel, S. R., Riemke, R. L., & Hoffmann, V. H. (2020). Challenges and solution technologies for the integration of variable renewable energy sources—a review. Renewable Energy, 145, 2271-2285.

Sterl, S., Hussain, B., Miketa, A., Li, Y., Merven, B., Ben Ticha, M. B., Elabbas, M. A. E., Thiery, W., & Russo, D. (2022). An all-Africa dataset of energy model "supply regions" for solar photovoltaic and wind power. Scientific Data, 9(1), 664.

Stratton, R. A., Senior, C. A., Vosper, S. B., Folwell, S. S., Boutle, I. A., Earnshaw, P. D., Kendon, E., Lock, A. P., Malcolm, A., & Manners, J. (2018). A Pan-African convection-permitting regional climate simulation with the met office unified model: CP4-Africa. Journal of Climate, 31(9), 3485-3508.

Strikwerda, J. C. (2004). Finite difference schemes and partial differential equations. SIAM.

Suklitsch, M., Gobiet, A., Leuprecht, A., & Frei, C. (2008). High resolution sensitivity studies with the regional climate model CCLM in the Alpine Region. Meteorologische Zeitschrift, 467-476.

Tadross, M., Hewitson, B., & Usman, M. (2005). The interannual variability of the onset of the maize growing season over South Africa and Zimbabwe. Journal of Climate, 18(16), 3356-3372.

Tadross, M., Jack, C., & Hewitson, B. (2005). On RCM‐based projections of change in southern African summer climate. Geophysical Research Letters, 32(23).

Tahir, Z. U. R., Asim, M., Jamil, S., Shad, R., & Safyan, M. (2018). Comparison of Reanalysis, Analysis and Forecast datasets with measured wind data for a Wind Power Project in Jhimpir, Pakistan. Journal of Physics Conference Series, 1102(1), 012004.

Tang, C., Morel, B., Wild, M., Pohl, B., Abiodun, B., & Bessafi, M. (2019). Numerical simulation of surface solar radiation over Southern Africa. Part 1: Evaluation of regional and global climate models. Climate Dynamics, 52, 457-477.

Tapiador, F. J., Navarro, A., Moreno, R., Sánchez, J. L., & García-Ortega, E. (2020). Regional climate models: 30 years of dynamical downscaling. Atmospheric Research, 235, 104785.

Tegen, I., Hollrig, P., Chin, M., Fung, I., Jacob, D., & Penner, J. (1997). Contribution of different aerosol species to the global aerosol extinction optical thickness: Estimates from model results. Journal of Geophysical Research: Atmospheres, 102(D20), 23895-23915.

The White House. (2021). President Biden Sets 2030 Greenhouse gas pollution reduction target aimed at creating good-paying union jobs and securing US leadership on clean energy technologies.

The Wind Power, 2005. Wind energy market intelligence. Link: https://www.thewindpower.net/index.php

Tizgui, I., Bouzahir, H., El Guezar, F., & Benaid, B. (2017). Wind speed extrapolation and wind power assessment at different heights. 2017 International Conference on Electrical and Information Technologies (ICEIT),

Tobin, I., Jerez, S., Vautard, R., Thais, F., Van Meijgaard, E., Prein, A., Déqué, M., Kotlarski, S., Maule, C. F., & Nikulin, G. (2016). Climate change impacts on the power generation

potential of a European mid-century wind farms scenario. Environmental Research Letters, 11(3), 034013.

Todd, M. C., Washington, R., & Palmer, P. I. (2004). Water vapour transport associated with tropical–temperate trough systems over southern Africa and the southwest Indian Ocean. International Journal of Climatology: A Journal of the Royal Meteorological Society, 24(5), 555-568.

Toktarova, A., Gruber, L., Hlusiak, M., Bogdanov, D., & Breyer, C. (2019). Long term load projection in high resolution for all countries globally. International Journal of Electrical Power & Energy Systems, 111, 160-181.

Tong, D., Farnham, D. J., Duan, L., Zhang, Q., Lewis, N. S., Caldeira, K., & Davis, S. J. (2021). Geophysical constraints on the reliability of solar and wind power worldwide. Nature communications, 12(1), 6146.

Trieb, F., Kern, J., Caldés, N., de la Rua, C., Frieden, D., & Tuerk, A. (2016). Rescuing the concept of solar electricity transfer from North Africa to Europe. International Journal of Energy Sector Management.

Trisos, C., Adelekan, I., Totin, E., Ayanlade, A., Efitre, J., Gemeda, A., Kalaba, K., Lennard, C., Masao, C., & Mgaya, Y. (2022). Africa. In: Climate Change 2022: Impacts, Adaptation and Vulnerability. Contribution of Working Group II to the Sixth Assessment Report of the Intergovernmental Panel on Climate Change.

Tsani, T., Weinand, J. M., Linßen, J., & Stolten, D. (2024). Quantifying social factors for onshore wind planning–A systematic review. Renewable and sustainable energy reviews, 203, 114762.

Turbines—Part, W. (2005). 12-1: Power Performance Measurements of Electricity Producing Wind Turbines. British Standard, IEC, 61400-61412.

United Nations. (2015). Transforming our world: The 2030 agenda for sustainable development. New York: United Nations, Department of Economic and Social Affairs, 1, 41.

Upstill‐Goddard, R., Watson, A., Liss, P., & Liddicoat, M. (1990). Gas transfer velocities in lakes measured with SF6. Tellus B, 42(4), 364-377.

Urraca, R., Huld, T., Gracia-Amillo, A., Martinez-de-Pison, F. J., Kaspar, F., & Sanz-Garcia, A. (2018). Evaluation of global horizontal irradiance estimates from ERA5 and COSMO-REA6 reanalyses using ground and satellite-based data. Solar Energy, 164, 339-354. https://doi.org/10.1016/j.solener.2018.02.059

Valmassoi, A., Keller, J. D., Kleist, D. T., English, S., Ahrens, B., Ďurán, I. B., Bauernschubert, E., Bosilovich, M. G., Fujiwara, M., & Hersbach, H. (2023). Current challenges and future directions in data assimilation and reanalysis. Bulletin of the American Meteorological Society, 104(4), E756-E767.

Vautard, R., Thais, F., Tobin, I., Bréon, F.-M., De Lavergne, J.-g. D., Colette, A., Yiou, P., & Ruti, P. M. (2014). Regional climate model simulations indicate limited climatic impacts by operational and planned European wind farms. Nature communications, 5(1), 3196.

von Krauland, A.-K., Permien, F.-H., Enevoldsen, P., & Jacobson, M. Z. (2021). Onshore wind energy atlas for the United States accounting for land use restrictions and wind speed

thresholds. Smart Energy, 3, 100046.
Wahl, S., Bollmeyer, C., Crewell, S., Figura, C., Friederichs, P., Hense, A., Keller, J. D., & Ohlwein, C. (2017). A novel convective-scale regional reanalysis COSMO-REA2: Improving the representation of precipitation. Meteorologische Zeitschrift, 26(4), 345-361.
Wald, L. (2018). Basics in solar radiation at Earth surface.
Waliser, D. E., & Gautier, C. (1993). A satellite-derived climatology of the ITCZ. Journal of Climate, 6(11), 2162-2174.
Wan, H., Giorgetta, M. A., Zängl, G., Restelli, M., Majewski, D., Bonaventura, L., Fröhlich, K., Reinert, D., Rípodas, P., Kornblueh, L., & Förstner, J. (2013). The ICON-1.2 hydrostatic atmospheric dynamical core on triangular grids – Part 1: Formulation and performance of the baseline version. Geoscientific Model Development, 6(3), 735-763. https://doi.org/10.5194/gmd-6-735-2013
Wang, J., Chen, L., Tan, Z., Du, E., Liu, N., Ma, J., Sun, M., Li, C., Song, J., & Lu, X. (2023). Inherent spatiotemporal uncertainty of renewable power in China. Nature communications, 14(1), 5379.
Wang, Y., Guo, C.-h., Chen, X.-j., Jia, L.-q., Guo, X.-n., Chen, R.-s., Zhang, M.-s., Chen, Z.-y., & Wang, H.-d. (2021). Carbon peak and carbon neutrality in China: Goals, implementation path and prospects. China Geology, 4(4), 720-746.
Weber, T., Haensler, A., & Jacob, D. (2017). Sensitivity of the atmospheric water cycle to corrections of the sea surface temperature bias over southern Africa in a regional climate model. Climate Dynamics, 51(7-8), 2841-2855. https://doi.org/10.1007/s00382-017-4052-8
Wedi, N. P., & Malardel, S. (2010). Non-hydrostatic modelling at ECMWF. Retrieved from https://www.ecmwf.int/sites/default/files/elibrary/2010/17457-non-hydrostatic-modelling-ecmwf.pdf
Weickmann, K., Whitaker, J., Roubicek, A., & Smith, C. (2007). The Use of Ensemble Forecasts to Produce Improved Medium Range (3-15 days) Weather Forecasts. Climate Diagnostics Center. Retrieved, 02-16.
Weissman, D., Stiles, B., Hristova-Veleva, S., Long, D., Smith, D., Hilburn, K., & Jones, W. (2012). Challenges to satellite sensors of ocean winds: Addressing precipitation effects. Journal of Atmospheric and Oceanic Technology, 29(3), 356-374.
Weldon, D., & Reason, C. (2014). Variability of rainfall characteristics over the South Coast region of South Africa. Theoretical and Applied Climatology, 115, 177-185.
Wenham, S. R., Green, M. A., Watt, M. E., Corkish, R., & Sproul, A. (2013). Applied photovoltaics. Routledge.
Wind Atlas for South Africa (WASA). (2010). Installed meteorological masts for the WASA project. Wind speeds observed data retrieved from website: http://wasadata.csir.co.za/wasa1/WASAData
Winkler, C., Heinrichs, H., Ishmam, S., Bayat, B., Lahnaoui, A., Agbo, S., Peña Sanchez, E. U., Franzmann, D., Oijeabou, N., Koerner, C., Michael, Y., Oloruntoba, B., Montzka, C., Vereecken, H., Hendricks Franssen, H., Brendt, J., Brauner, S., Kuckshinrichs, W.,

Venghaus, S., . . . Stolten, D. (2025). Participatory mapping of local green hydrogen cost-potentials in Sub-Saharan Africa. International Journal of Hydrogen Energy, 112, 289-321. https://doi.org/https://doi.org/10.1016/j.ijhydene.2025.02.015

Wiser, R., Rand, J., Seel, J., Beiter, P., Baker, E., Lantz, E., & Gilman, P. (2021). Expert elicitation survey predicts 37% to 49% declines in wind energy costs by 2050. Nature Energy, 6(5), 555-565.

World Meteorological Organization. (2021). Guide to instruments and methods of observation. Available online: https://library.wmo.int/index.php?lvl=notice_display&id=12407.

Xu, Z., Han, Y., & Yang, Z. (2019). Dynamical downscaling of regional climate: A review of methods and limitations. Science China Earth Sciences, 62, 365-375.

Yang, D., & Bright, J. M. (2020). Worldwide validation of 8 satellite-derived and reanalysis solar radiation products: A preliminary evaluation and overall metrics for hourly data over 27 years. Solar Energy, 210, 3-19.

Yang, X., Delworth, T. L., Jia, L., Johnson, N. C., Lu, F., & McHugh, C. (2024). Skillful seasonal prediction of wind energy resources in the contiguous United States. Communications Earth & Environment, 5(1), 313.

Yang, Y., Javanroodi, K., & Nik, V. M. (2022). Climate Change and Renewable Energy Generation in Europe—Long-Term Impact Assessment on Solar and Wind Energy Using High-Resolution Future Climate Data and Considering Climate Uncertainties. Energies, 15(1), 302.

Yu, L., Zhong, S., Bian, X., & Heilman, W. E. (2015). Temporal and spatial variability of wind resources in the United States as derived from the climate forecast system reanalysis. Journal of Climate, 28(3), 1166-1183.

Yu, S. L., Hamrick, J. M., & Lee, D.-s. (1984). Wind effects on air-water oxygen transfer in a lake. In Gas transfer at water surfaces (pp. 357-367). Springer.

Yuan, X., Su, C.-W., Umar, M., Shao, X., & LobonŢ, O.-R. (2022). The race to zero emissions: Can renewable energy be the path to carbon neutrality? Journal of Environmental Management, 308, 114648.

Zängl, G., Reinert, D., Rípodas, P., & Baldauf, M. (2015). The ICON (ICOsahedral Non-hydrostatic) modelling framework of DWD and MPI-M: Description of the non-hydrostatic dynamical core. Quarterly Journal of the Royal Meteorological Society, 141(687), 563-579. https://doi.org/10.1002/qj.2378

Zhang, C., Chen, X., Shao, H., Chen, S., Liu, T., Chen, C., Ding, Q., & Du, H. (2018). Evaluation and Intercomparison of High-Resolution Satellite Precipitation Estimates—GPM, TRMM, and CMORPH in the Tianshan Mountain Area. Remote Sensing, 10(10). https://doi.org/10.3390/rs10101543

Zhang, L., Xu, Y., Meng, C., Li, X., Liu, H., & Wang, C. (2020). Comparison of statistical and dynamic downscaling techniques in generating high-resolution temperatures in China from CMIP5 GCMs. Journal of Applied Meteorology and Climatology, 59(2), 207-235.

Zhang, Y., Ren, J., Pu, Y., & Wang, P. (2020). Solar energy potential assessment: A framework to integrate geographic, technological, and economic indices for a potential analysis. Renewable Energy, 149, 577-586. https://doi.org/10.1016/j.renene.2019.12.071

Zhang, Y., Sun, K., Gao, Z., Pan, Z., Shook, M. A., & Li, D. (2020). Diurnal Climatology of Planetary Boundary Layer Height Over the Contiguous United States Derived From AMDAR and Reanalysis Data. Journal of Geophysical Research: Atmospheres, 125(20). https://doi.org/10.1029/2020jd032803

Zhao, N., & You, F. (2020). Can renewable generation, energy storage and energy efficient technologies enable carbon neutral energy transition? Applied Energy, 279, 115889.

Zhou, Y. (2023). Worldwide carbon neutrality transition? Energy efficiency, renewable, carbon trading and advanced energy policies. Energy Reviews, 100026.

Band / Volume 649
Prospektive Lebenszyklusanalysen von Power-to-Gas-Optionen
J. C. Koj (2024), XVIII, 197 pp
ISBN: 978-3-95806-794-3

Band / Volume 650
Assimilation of groundwater level and cosmic-ray neutron sensor soil moisture measurements into integrated terrestrial system models for better predictions
F. Li (2024), xvii, 172 pp
ISBN: 978-3-95806-796-7

Band / Volume 651
Integration of a rib-channel design to improve air-side contacting in solid oxide cell (SOC) stacks
Y. S. Ayhan (2024), 82 pp
ISBN: 978-3-95806-797-4

Band / Volume 652
Modelling Secondary Circulation in Convective Boundary Layer Using Large Eddy Simulation
L. Zhang (2024), 84 pp
ISBN: 978-3-95806-799-8

Band / Volume 653
Optionen zur Umsetzung der Klimaschutzziele im Verkehrssektor
S. Kraus (2025), XI, 317 pp
ISBN: 978-3-95806-802-5

Band / Volume 654
Modellierung der flächendifferenzierten Grundwasserneubildung für Schleswig-Holstein im Beobachtungszeitraum 1961 – 2021 und für Klimaszenarien bis 2100
I. McNamara, B. Tetzlaff, F. Wendland, T. Wolters (2025), 191 pp
ISBN: 978-3-95806-803-2

Band / Volume 655
Entwicklung alternativer Brenngaselektroden für die Hochtemperatur-Elektrolyse
F. E. Winterhalder (2025), vii, 161 pp
ISBN: 978-3-95806-805-6

Band / Volume 656
Oxide-based All-Solid-State Batteries for and from Recycling Processes
V. M. Kiyek (2025), viii, 128 pp, xix
ISBN: 978-3-95806-806-3

Band / Volume 657
Investigation of current and future anthropogenic chemical regimes in simulation chamber experiments
M. Färber (2025), 213 pp
ISBN: 978-3-95806-809-4

Band / Volume 658
Dynamischer Betrieb von Polymer-Elektrolyt-Membran Wasserelektrolyseuren
E. Rauls (2025), XIV, 239 pp
ISBN: 978-3-95806-811-7

Band / Volume 659
Pore-scale reactive transport modeling in cementitious materials: Development and application of a high-performance computing code based on the Lattice-Boltzmann method
S. Rohmen (2025), X, 295 pp
ISBN: 978-3-95806-812-4

Band / Volume 660
Recyclingmöglichkeiten für die Keramikkomponenten einer Festoxidzelle
S. Sarner (2025), VIII, 122 pp
ISBN: 978-3-95806-816-2

Band / Volume 661
Methodological Approach Enabling the Two-phase Flow Investigation in Alkaline Electrolysis under Demanding Conditions
S. Renz (2025), IX, 252 pp
ISBN: 978-3-95806-821-6

Band / Volume 662
Variable renewable energy potential estimates based on high-resolution regional atmospheric modelling over southern Africa
S. Chen (2025), XIII, 141 pp
ISBN: 978-3-95806-822-3

Energie & Umwelt / Energy & Environment
Band / Volume 662
ISBN 978-3-95806-822-3

Mitglied der Helmholtz-Gemeinschaft

JÜLICH
Forschungszentrum